The potential of UAV-based sun-induced chlorophyll fluorescence in understanding crop photosynthesis

Na Wang

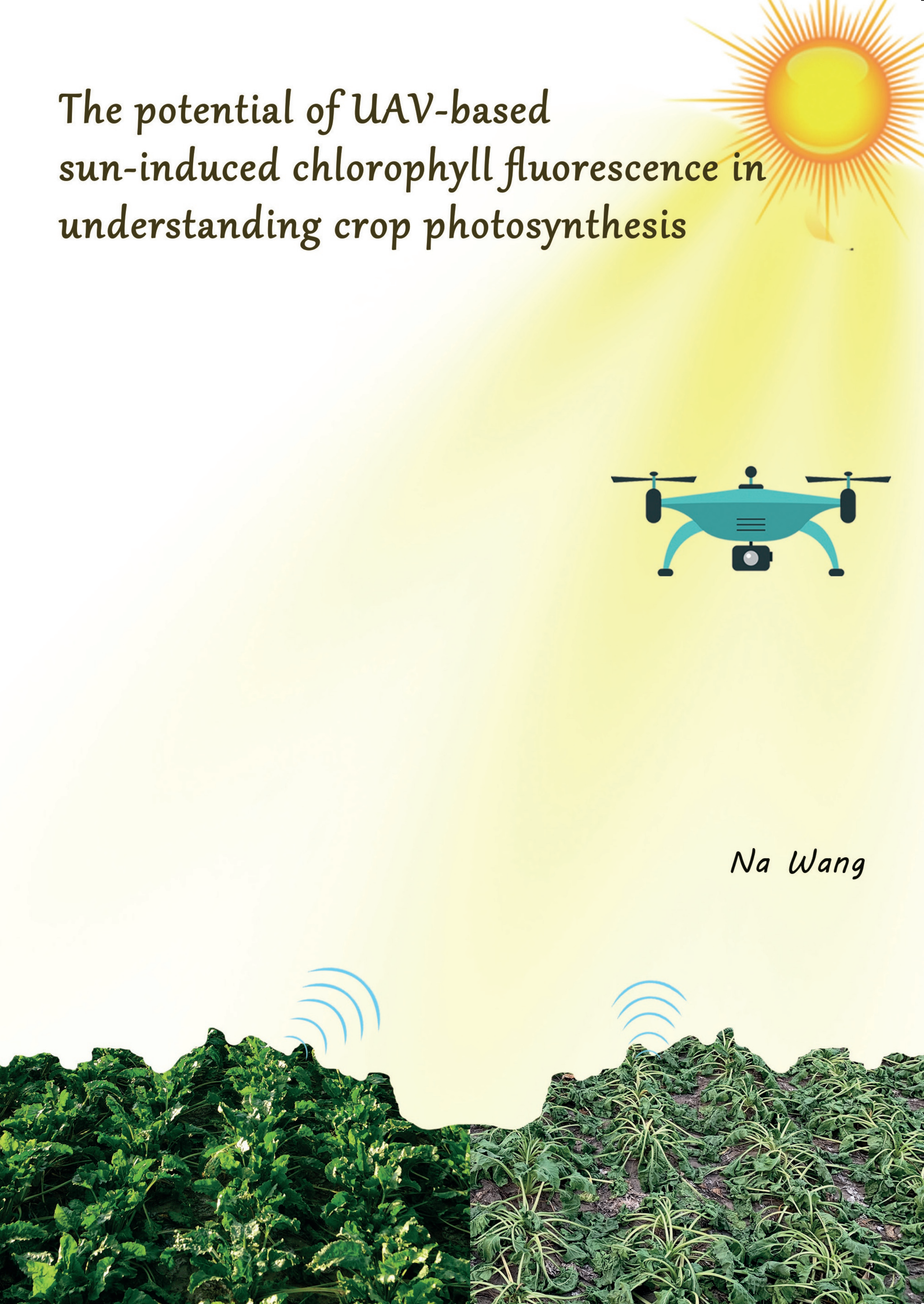

Propositions

1. A characterization of canopy structure is strongly needed to link sun-induced chlorophyll fluorescence and photosynthesis under severe water stress.
   (this thesis)
2. UAV-based sun-induced chlorophyll fluorescence will be the most widely used way for validation of satellite SIF.
   (this thesis)
3. Repeated studies lack novelty but advance science.
4. Too much critical thinking limits research publications.
5. Divergence from current findings is one way to get to the truth.
6. Having a positive attitude is more important than anything else.

Propositions belong to the thesis, entitled

The potential of UAV-based sun-induced chlorophyll fluorescence in understanding crop photosynthesis

Na Wang

Wageningen, 18 May 2022

The potential of UAV-based sun-induced chlorophyll fluorescence in understanding crop photosynthesis

Na Wang

Thesis committee

Promotor

Dr L. Kooistra
Associate Professor, Laboratory of Geo-information Science and Remote Sensing
Wageningen University & Research

Co-promotors

Dr J.G.P.W. Clevers
Associate Professor, Laboratory of Geo-information Science and Remote Sensing
Wageningen University & Research

Dr H. Bartholomeus
Assistant Professor, Laboratory of Geo-information Science and Remote Sensing
Wageningen University & Research

Other members

Dr K.F. Boersma, Wageningen University & Research
Dr M. Rossini, University of Milano-Bicocca, Italy
Dr S. Van Wittenberghe, University of Valencia, Spain
Dr C. Van der Tol, University of Twente, Enschede

This research was conducted under the auspices of the C. T. de Wit Graduate School for Production Ecology and Resource Conservation (PE&RC).

The potential of UAV-based sun-induced chlorophyll fluorescence in understanding crop photosynthesis

Na Wang

Thesis

submitted in fulfilment of the requirements for the degree of doctor

at Wageningen University

by the authority of the Rector Magnificus

Prof. Dr A. P. J. Mol,

in the presence of the

Thesis Committee appointed by the Academic Board

to be defended in public

on Wednesday 18 May 2022

at 11 a.m. in the Omnia Auditorium.

Na Wang
The potential of UAV-based sun-induced chlorophyll fluorescence in understanding crop photosynthesis, 184 pages.

PhD thesis, Wageningen University, Wageningen, the Netherlands (2022)
With references, with summary in English

ISBN: 978-94-6447-212-7
DOI: https://doi.org/10.18174/568807

TABLE OF CONTENTS

Chapter 1

General introduction

1.1 Food security and crop photosynthesis

One of the greatest challenges in the 21st century is to sustainably feed ten billion people on Earth by 2050 (Foley et al., 2011; Godfray et al., 2010). In the past century, crop production has been increased considerably, benefiting from the Green Revolution that contains the application of knowledge in plant breeding and genetic modification (Hawkesford et al., 2013). Despite that yield levels have improved considerably, photosynthesis places an upper limit on food production (Guanter et al., 2014). Long et al. (2006) also demonstrated that photosynthesis is the only remaining major factor available to further increase the potential yield. As one of the most fundamental processes on Earth, photosynthesis provides the raw materials for all plant products and supplies most of the energy necessary for life on Earth (Bryant and Frigaard, 2006). During the photosynthetic process in green plants, light energy is captured by leaf pigments and used to convert water (H_2O) and carbon dioxide (CO_2) into oxygen (O_2) and chemical energy in the form of glucose ($C_6H_{12}O_6$) (Equation 1.1).

$$6CO_2 + 6H_2O \xrightarrow[\substack{Light+\\ Chlorophyll}]{} C_6H_{12}O_6 + 6O_2 \tag{1.1}$$

Crop productivity is generally not determined by the potential activity of the photosynthetic system, but by the actual activity. The photosynthetic activities are affected by many adverse environmental stress factors, such as lack of water or nutrients. The stresses can weaken the photosynthetic apparatus, resulting in a decrease in plant productivity and overall crop yield (Kalaji et al., 2016, 2017). Abiotic stresses are one of the major constraints to crop production and food security worldwide (Lesk et al., 2016). The drastic and rapid changes in the global climate have aggravated this situation (Lobell et al., 2011). Among the abiotic stresses, water stress for plants has been exacerbated by reduced rainfall and changed precipitation patterns (Lobell et al., 2011). Severe water stress can cause a substantial decline in crop yields through a wide range of plant responses in crop physiology, biochemistry, and morphology that induce a reduction in photosynthesis (Barnabás et al., 2008; Yardanov et al., 2003). To minimize harmful effects on crop production, it is essential to understand crop photosynthetic machinery under environmental changes and detect the stress timely and accurately.

Modern precision agriculture is one way to ensure crop productivity and farm profitability through improved management of farm inputs (Zhang et al., 2002). The essence of precision agriculture is the management of spatial-temporal crop variation using real-time monitoring. For instance, the detection and quantification of plant water stress are of major interest to determine the right management practice at the right place and the right time (Mulla, 2013). Early and accurate detection of stress is required for the effective management of crops. Biotic stress causes photosynthetic changes before visual symptoms show up (Jones and Schofield, 2008). This encourages the application of a pre-visual indicator to assess the photosynthetic functioning state of plants and their vitality and to monitor the presence and intensity of the stress.

Overall, to meet the enormous demand for food, there is an urgent need to have a better understanding of photosynthesis under field conditions. Monitoring photosynthesis facilitates a better understanding of what limits photosynthesis (and to what extent), further supporting the decision-making to reach the optimal photosynthetic capacity (e.g. timely management by adapting production inputs site-specifically) and increase photosynthetic capacity in crops for a sustainable yield (e.g. breeding high yielding plants).

1.2 Remote sensing approach to understand photosynthesis

Plants respond to changing environmental conditions with various biochemical reactions that influence the passive remote sensing (RS) signal in different domains. RS has the unique ability to provide spatial-temporal monitoring of structural, biochemical, and physiological properties of crops at different scales (Atzberger, 2013). Vegetation indices (VIs), combinations of surface reflectance in different bands of the spectrum, have been exploited to derive vegetation parameters like chlorophyll content (C_{ab}), leaf area index (LAI), and the fraction of absorbed photosynthetically active radiation (fAPAR), which largely determine photosynthesis by providing information on vegetation structure and biochemistry. For example, the normalized difference vegetation index (NDVI) can be a good indicator of LAI (Carlson and Ripley, 1997). The ratio of the transformed chlorophyll absorption in reflectance index and the optimized soil-adjusted vegetation index (TCARI/OSAVI) and the modified triangular vegetation index (MTVI) can provide predictive relationships for leaf and canopy chlorophyll content (C_{ab}) with hyperspectral imagery in closed (Dash and Curran, 2004; Haboudane et al., 2002). The wide dynamic range vegetation index (WDRVI) is adopted to effectively estimate fAPAR (Liu et al., 2019; Viña and Gitelson, 2005). A limitation of this approach is that they do not provide a direct link to photosynthetic functioning. For instance, greenness-based VIs cannot capture rapid and short-term adaptations in the photosystems to changing environmental conditions (Meroni et al., 2009; Porcar-Castell et al., 2014; Wieneke et al., 2016; Xu et al., 2021). Calderón et al. (2013) suggested that structural and pigment indices are good to assess the damage. However, plants can be irreversibly affected before visible symptoms of stress appears (Jones and Schofield, 2008; Mahajan and Tuteja, 2005).

The photochemical reflectance index (PRI) is used to track changes in the xanthophyll cycle and is further used to predict non-photosynthetic quenching (NPQ) (Gamon et al., 1992). NPQ is a plant response to excess light energy de-excited by thermal dissipation processes in light reaction centres (Müller et al., 2001). Therefore, NPQ directly links to photosynthesis. PRI can be derived from two narrow-band reflectances at 530 nm and at 570 nm ((R570 - R530) / (R570 + R530)). Barton and North. (2001) suggested there are many potentially complex factors when trying to apply PRI to whole crop stands in a remote sensing context. Previous reports already stated that the limitation of PRI rests on the changes in pigment pools, leaf albedo (Filella et al., 2009; Wong and Gamon, 2015), and canopy structure (Barton and North, 2001; Gitelson et al., 2017).

Plant stomata closure occurs to prevent water vapor loss via transpiration under water deficit conditions and consequently increases NPQ and photorespiration (Voss et al., 2013; Porcar-Castell et al., 2014), affecting the photosynthetic rate. As the leaf stomal closure increases leaf temperature (Chaves et al., 2002; Jones and Schofield, 2008), thermal imagery has been established to detect pre-visual water stress. The major limitation of the temperature-based approach is that the use of leaf or canopy temperature values alone cannot directly estimate the physiological status of plants (Gerhards et al., 2019).

1.3 Chlorophyll fluorescence to understand photosynthesis

Chlorophyll fluorescence is considered to be a direct and potentially accurate measure of the photosynthetic rate (Lichtenthaler and Rinderle, 1988). Light energy absorbed by plant chlorophyll has three main dissipating pathways. The absorbed energy can be used to fuel photosynthetic reactions for photosynthesis (photochemical quenching, PQ), dissipated as heat (NPQ), or re-emitted as chlorophyll fluorescence (ChF). ChF emission occurs within the waveband 640 - 850 nm and has two maxima (at room temperature) - one in the red spectral region around 685-690 nm (ChF_{685}) and the other in the far-red around 730-740 nm (ChF_{740}) (Figure 1.1). Photosystem II (PSII) emits ChF in both red and far-red regions of the spectrum, and PSI mainly emits ChF in the far-red. At normal ambient temperature, ChF mainly originates from PSII, and the ChF emission is generally low (Krause and Weis, 1991). Due to this fundamental connection, ChF depends strongly on the regulatory and operational state of the two photosystems, and the activity of NPQ. ChF re-emitted is a small fraction of the absorbed light energy. It is determined by the amount of absorbed photosynthetically active radiation (i.e. APAR) and the conversion efficiency between APAR and ChF radiation. This efficiency is called fluorescence emission yield (ΦF). ChF can be expressed using Equation 1.2.

$$ChF = APAR \times \Phi F \tag{1.2}$$

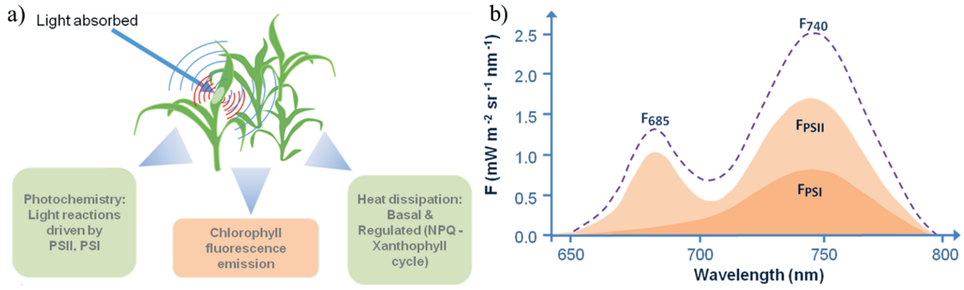

Figure 1.1. a) Distribution of energy of incident photons in green leaves under steady-state conditions, and b) conceptual figure of leaf fluorescence emission, with maxima in the red and far-red spectral regions, and arising from photosystems PSII and PSI. F represents chlorophyll fluorescence. The figure was modified from Mohammed et al. (2019).

A suite of measurement devices, such as fluorescence microscopes, spectrofluorimetric devices, portable fluorometers, and imaging tools have been utilized in fluorescence assessment in the laboratory, growth chamber, and greenhouse (Mohammed et al., 2019). These devices have facilitated the study of the quantifying photosynthesis in situ and the explanation of the relationship between ChF and photosynthetic CO_2 assimilation. Intensive studies at the leaf level have contributed significantly to our understanding of plant PQ and NPQ regulation mechanisms at the subcellular to leaf scales using active fluorometers (Cendrero-Mateo et al., 2015; Marrs et al., 2020; Porcar-Castell et al., 2014; Zarco-Tejada et al., 2000). However, this approach of artificially exciting fluorescence has been limited to the leaf or small canopy level and is impractical over large distances and large areas.

1.4 Sun-induced chlorophyll fluorescence to understand photosynthesis

Sun-induced chlorophyll fluorescence (SIF), a continuous emission signal from photosystem II and I produced by natural daylight, has been a widespread and exciting signal for quantifying the dynamics of photosynthesis and assessing plant photosynthetic functioning at different spatio-temporal scales (Bandopadhyay et al., 2020; Mohammed et al., 2019). SIF is a weak signal added to reflected radiation detected by a remote sensor. It only accounts for 1-

5% of the reflected radiation in the near-infrared (Frankenberg and Berry, 2018; Meroni et al., 2009). This SIF signal is comparably stronger and can be detected passively in narrow dark lines of the solar and atmospheric spectrum due to the atmospheric scattering and absorption (the so-called Fraunhofer lines). The commonly used atmospheric Fraunhofer lines are two oxygen absorption features at 687 nm (O_2-B, SIF_{687}) and 760 nm (O_2-A, SIF_{760}), representing red and far-red SIF.

SIF has been intensively studied to further understand vegetation photosynthesis from top of the canopy (TOC) to ecosystem levels. Innovative sensing efforts have shown the potential of SIF to indicate photosynthesis (Goulas et al., 2017; Porcar-Castell et al., 2014; Yang et al., 2021), to detect stress (Helm et al., 2020; Panigada et al., 2014; Zarco-Tejada et al., 2018) and to improve gross primary productivity (GPP) estimate (Tagliabue et al., 2019; Wieneke et al., 2016; Wohlfahrt et al., 2018). These studies were mainly carried out using ground-based platforms (e.g. FloX (Wohlfahrt et al., 2018), PICCOLO-DOPPIO (MacArthur and Robinson, 2015), S-FLUO box (Julitta et al., 2016), and the Fluorescence Auto-Measurement Equipment (FAME) (Gu et al., 2019), airborne platforms (e.g. HyPlant (Rascher et al., 2015), APEX (Damm et al., 2015), and AIRFLEX (Moya et al., 2006)), and spaceborne platforms (e.g. the Greenhouse Gases Observing Satellite (GOSAT) (Frankenberg et al., 2011), the Global Ozone Monitoring Experiment-2 satellite (GOME-2) (Joiner et al., 2013), the Orbiting Carbon Observatory satellite (OCO-2) (Frankenberg et al., 2014), TROPOspheric Monitoring Instrument (TROPOMI) (Guanter et al., 2015), Carbon Dioxide Observation Satellite (Tansat) (Du et al., 2018). The FLuorescence EXplorer (FLEX) mission equipped with the Fluorescence Imaging Spectrometer (FLORIS) is expected to be launched in 2024 to map terrestrial photosynthesis at the ecosystem scale with a 300 m spatial resolution. FLEX will provide global maps of vegetation fluorescence that can reflect photosynthetic activity and plant health and stress (Drusch et al., 2016).

Although substantial progress has been achieved in measuring SIF in field settings using the aforesaid platforms, there are some challenges to SIF acquisition and the mechanistic understanding of SIF response under stress conditions at the field level. Firstly, closing the gap between the proximal canopy and ecosystem level with field-based TOC SIF measurements is highly required (Mohammed et al., 2019; Rossini et al., 2016). The ground-based set-ups measure SIF at a distance between measured targets and instruments ranging from 0.1 m to 10 m above the canopy (Cheng et al., 2013; Cogliati et al., 2015; Pacheco-Labrador et al., 2019). As a result, the SIF signal can only be monitored over a few individual plants, making measurements at the field scale impossible. For current satellite observations, the observed signals are mixed due to the low spatial resolution (typically between a few up to tens of kilometers), which is an issue, especially for monitoring small-scale farmlands. Although airborne imaging spectroscopy is critical to bridge the existing gap between small-scale field measurements and global observations, airborne platforms can be costly for measuring SIF at a small-scale field level. Moreover, airborne platforms lack the flexibility of measuring SIF at a high temporal resolution, for example, to acquire timely information on crop photosynthesis over the day and the season. However, high spatio-temporal information is of great importance to understand photosynthetic processes in plant phenotyping and precision agriculture (Tsouros et al., 2019), where measuring certain plant traits every few days and managing crop performance related to different crop varieties and management practices is needed. Unmanned aerial vehicles (UAVs) are versatile platforms for such type of research, providing possibilities to making more frequent diurnal and seasonal measurements on specific areas. Furthermore, non-imaging spectrometers with advanced capabilities, including reduced size, high signal-to-noise ratio (SNR), high spectral and temporal resolutions, have facilitated the development of UAV-based SIF payloads (MacArthur and Robinson, 2015).

So far, only a few studies have focused on UAV-based SIF with non-imaging spectrometers (Bendig et al., 2019; Chang et al., 2020; Garzonio et al., 2017; MacArthur et al., 2014) and achieved valuable advances. However, SIF measurements from UAV-based non-imaging spectrometers lack robust validation (Bendig et al., 2021; Vargas et al., 2020). It is still unknown whether UAV-based SIF observations can provide reliable information within agricultural fields, challenging its potential applications in precision farming, phenotyping, and reducing the scale gap between ground measurements and airborne/satellite observations.

Given the advantages of UAV platforms (e.g. small size, the capability for highly-customized deployments, and quick response), UAV-based SIF applications are expected to increase drastically over the next few years to timely monitor, e.g. water stress within crop fields. However, SIF is a weak signal and can be strongly affected by a variety of physiological, biophysical and biochemical processes induced by water stress (Gerhards et al., 2019; Yang et al., 2019). Some studies found SIF at the leaf level or proximal level may not indicate the photosynthetic changes caused by water stress (Helm et al., 2020; Marrs et al., 2020), which are discrepant from some satellite SIF observations (Sun et al., 2015). Therefore, the direct effect of water stress on the SIF response in agricultural crops at the field level still needs further research to clearly understand the involved mechanisms.

Furthermore, variations in observed SIF values caused by water stress cannot be directly interpreted as physiological variations due to the confounding effects of vegetation structural, biochemical response, and incoming radiation (Damm et al., 2015; Porcar-Castell et al., 2014; Van der Tol et al., 2016). To better understand the actual crop photosynthetic status under water stress, it is necessary to make a distinction between physiological and non-physiological (crop biophysical and radiation) effects on TOC SIF and to quantify them separately.

1.5 Research Objective

The main objective of this thesis is to explore the potential of top of canopy (TOC) sun-induced chlorophyll fluorescence (SIF) measurements acquired by the UAV-based FluorSpec system in understanding crop photosynthesis under field conditions. This may bridge the gap between proximal TOC level and airborne/satellite SIF measurements and support the interpretation and validation of SIF products at larger scales (e.g. ecosystem). The FluorSpec consists of a non-imaging spectrometer, QE-pro, in the wavelength range of 630-800 nm at a subnanometer resolution of 0.3 nm. With this configuration, red SIF derived at the O_2-B absorption feature at 687 nm (SIF_{687}) and far-red SIF derived at the O_2-A absorption feature at 760 nm (SIF_{760}) can be derived from the reflected radiance. Based on the challenges proposed in section 1.4, this thesis aims to answer the following questions:

RQ1 Can the UAV-based FluorSpec system acquire SIF at the field level and characterize its diurnal variation?

RQ2 Can the SIF measurements from the UAV-based FluorSpec system provide reliable information within agricultural fields?

RQ3 Can UAV-based SIF and its indices detect water stress in a crop?

RQ4 What are the physiological and non-physiological effects on SIF variations caused by water stress and their respective contribution?

1.6 Thesis outline

Chapter 2 aimed to evaluate a UAV-based spectroscopy approach to understand crop sun-induced chlorophyll fluorescence (SIF) and photosynthesis in precision agriculture at the field level and its potential to bridge the gap in SIF measurements between different scales. Diurnal SIF measurements at ground and field level were collected over potato and sugar beet fields under clear sky conditions as case studies. It was expected to find a pronounced diurnal SIF pattern both at the ground and field level and variations in the spatial patterns of the two different crops.

Chapter 3 evaluated whether UAV-based FluorSpec can measure a reliable SIF signal within agricultural fields. To achieve this, the performance of the UAV-based FluorSpec was compared with a high-performance airborne system, HyPlant, in retrieving SIF over different crops. The two systems acquired data almost simultaneously four times following a diurnal pattern on one day over different crops under clear sky conditions. Similar diurnal and spatial patterns of SIF from both systems and a good correlation between the two systems per crop were expected.

Chapter 4 studied whether UAV-based SIF can detect water deficit within a sugar beet field. SIF measurements at the oxygen absorption bands A and B were acquired over irrigated and non-irrigated sugar beet plots using a UAV platform under clear sky conditions. Additional UAV-based hyperspectral and thermal data were acquired to better interpret the response of SIF indices to water stress. A significant difference was expected between the irrigated and non-irrigated plots in terms of SIF and its indices.

Chapter 5 adopted a modelling approach to quantify the physiological and non-physiological effects on SIF for a better understanding of the actual photosynthetic status of water-stressed crops at the field level. SIF and reflectance data were acquired over irrigated and non-irrigated plots using a UAV on two consecutive days under clear sky conditions. Non-physiological parameters of leaf biochemistry and canopy structure and the physiological factor (fluorescence emission yield, ΦF) were simulated using a radiative transfer model inversion approach, TOC hyperspectral reflectance, and SIF observations.

Chapter 6 summarized the findings reported in chapters 2 to 5 and the implications of these findings. Furthermore, this chapter indicated some challenges on the way ahead with UAV-based SIF and gave recommendations to improve the UAV-FluorSpec system and some future directions for its application.

Chapter 2

Diurnal variation of sun-induced chlorophyll fluorescence of agricultural crops observed from a point-based spectrometer on a UAV

This chapter is based on:
Wang, N., Suomalainen, J., Bartholomeus, H., Kooistra, L., Masiliūnas, D., Clevers, J.G., 2021. Diurnal variation of sun-induced chlorophyll fluorescence of agricultural crops observed from a point-based spectrometer on a UAV. *International Journal of Applied Earth Observation and Geoinformation*. 96, 102276

http://doi.org/10.1016/j.jag.2020.102276

Abstract

Unmanned Aerial Vehicle (UAV)-based measurements allow studying sun-induced chlorophyll fluorescence (SIF) at the field scale and can potentially upscale results from ground to airborne/satellite level. The objective of this paper is to present the FluorSpec system providing SIF measurements at the field level onboard a UAV, and to evaluate the potential of this system for understanding diurnal SIF patterns for different arable crops. The core components of FluorSpec are a point spectrometer configured to measure SIF in the O_2 absorption bands at sub-nanometer resolution, bifurcated fibre optics to switch between the downwelling irradiance and upwelling radiance measurements, and a laser range finder allowing accurate atmospheric correction. The processing chain was explained and the capability of the novel Spectral Shape Assumption Fraunhofer Line Discrimination (SSA-FLD) method to retrieve SIF was tested. To test the reliability of FluorSpec diurnal SIF measurements, near-canopy diurnal SIF was monitored during the growing season over potato and sugar beet plants with a ground-based setup. The two crops exhibited a clear diurnal SIF pattern, which positively correlated with the photosynthetically active radiation (PAR). The divergence in diurnal patterns between SIF and PAR indicated that the crops might be suffering from heat stress. A significant correlation between SIF and the Photosystem II Quantum Yield was obtained. By mounting the FluorSpec on a UAV, SIF measurements were obtained over the same crops during a clear day. UAV-based SIF also exhibited a pronounced diurnal pattern similar to the ground-based measurements and it showed clear spatial variation within different crop fields. The obtained results demonstrate the ability of the FluorSpec system to reliably measure plant fluorescence at ground and field level, and the possibility of the UAV-based FluorSpec to bridge the scale gap between different levels of SIF observations.

2.1. Introduction

The rapid increase in food demand will be one of the greatest challenges in the following decades (Foley et al., 2011). Although over the past decades, yield levels have improved considerably, the quantity of photosynthesis places an upper limit to food production (Guanter et al., 2014). Crop productivity is generally not determined by the potential activity of the photosynthetic system, but by the actual one since the photosynthetic activities are affected by many adverse environmental stress factors, such as lack of water or nutrients. These can weaken the photosynthetic apparatus, causing a decrease of plant productivity and overall crop yield (Kalaji et al., 2016, 2017). Light energy absorbed by leaf chlorophyll may be used for photochemistry, dissipated thermally, or is reemitted as chlorophyll fluorescence (ChF). Thus, as a by-product of photosynthesis, ChF has been proven to be a direct proxy for the instantaneous photosynthetic rate related to vegetation stress conditions (Smorenburg et al., 2002; Zarco-Tejada et al., 2016).

In the last decade, sun-induced chlorophyll fluorescence (SIF), which is produced in natural daylight and can be detected with remote sensing techniques, has been a research focus to understand vegetation photosynthesis at a large scale. Maier et al. (2004) showed the potential of SIF as a new tool for precision farming with remote sensing techniques. Intensive ground-based studies have shown the potential of SIF as an indicator of crop photosynthesis (Goulas et al., 2017; Rascher et al., 2009). Several SIF studies over crop canopies have confirmed a positive correlation between crop SIF and water stress (Daumard et al., 2010; Xu et al., 2018). The sensitivity of SIF to vegetation phenology and its diurnal and seasonal dynamics have also been explored in several studies (Cogliati et al., 2015; Daumard et al., 2012; Li et al., 2020; Meroni et al., 2011; Wyber et al., 2017).

Recently, important improvements in sensor capabilities and further understanding of the contribution from fluorescence to apparent reflectance have made it achievable to measure SIF from space, using platforms/instruments such as the Global Ozone Monitoring Instrument-2 (GOME-2) (Joiner et al., 2013), the Greenhouse Gases Observing Satellite (GOSAT) (Frankenberg et al., 2011), the Orbiting Carbon Observatory (OCO-2) (Frankenberg et al., 2014), and the TROPOspheric Monitoring Instrument (TROPOMI) (Guanter et al., 2015). A growing body of literature has recognized the potential of satellite-based SIF as an indicator of photosynthetic activities at large scale by monitoring global SIF patterns and dynamics (Frankenberg et al., 2014). Damm et al. (2010) showed that including SIF into gross primary productivity (GPP) modelling improves their results in predicting diurnal courses of GPP for agricultural fields. Similar conclusions were also found by Guan et al. (2016), who showed that spaceborne SIF retrievals from GOME-2 can improve the monitoring of crop productivity by including SIF into GPP models. Furthermore, airborne systems have been developed to upscale crop SIF from canopy to satellite level. For example, the airborne system HyPlant is able to map SIF at an intermediate spatial resolution (e.g. 0.5m*1m with a flying height of 350 m above ground level (AGL)), showing that there are large variations in SIF between different vegetation types (Rascher et al., 2015). Zarco-Tejada et al. (2016) found that, compared to other selected structural and physiological indices, SIF quantified from airborne hyperspectral imagery was the most robust indicator of photosynthesis measured by assimilation rates.

To further explore the potential of SIF in agriculture, especially in precision agriculture, a fine spatial resolution is playing a key role. For ground-based set-ups, the distance between measured targets and instruments ranges from 0.1 m to 10 m above the canopy (Cheng et al., 2013; Cogliati et al., 2015; Yang et al., 2018). Thus, with these set-ups, the SIF signal of only a few individual plants can be monitored, making measurements at the field, ecosystem, or global scales infeasible. For satellite observations, the signals observed are mixed due to the low spatial resolution (typically between a few up to tens of kilometers), which is an issue especially for the monitoring of small-scale farmlands. Although intermediate-scale observations using airborne imaging spectroscopy are critical to bridge the existing gap between small-scale field and global observations, the validation of airborne SIF products is still essential, as multiple factors can influence SIF measurements. Ground-based SIF observations, such as the FLOX system (FloX, JB Hyperspectral, Dusseldorf, Germany, PhotoSpec), provide a way to validate airborne SIF, but it is challenging to compare it with airborne SIF due to the large difference in their footprints. Additionally, imagery obtained from airborne sensors can only be evaluated at a limited number of locations measured by ground-based systems (Tagliabue et al., 2019).

Therefore, remotely sensed data acquired at the field level are highly needed to facilitate SIF interpretation in agricultural fields and to bridge the gap between the proximal level to the airborne level. Unmanned Aerial Vehicles (UAVs) are versatile platforms that have a potential to acquire SIF at a low flying altitude (from 10-120 m). UAVs can also acquire data at high temporal resolution on specific areas, e.g. diurnal measurements, and thus support airborne and satellite-based measurements through validation and interpretation. Additionally, UAVs can be more cost-effective at small scale and have great potential for applications in precision agriculture and phenotyping (Camino et al., 2019). Accurate SIF retrieval requires spectroradiometers with an ultrafine spectral resolution (less than 1 nm for far-red SIF and less than 0.5 nm for red SIF) and high signal-to-noise ratio (SNR) (Rossini et al., 2016). Simultaneous acquisitions of sunlight irradiance (downwelling) and target radiance (upwelling) also play a significant role in the precision of SIF measurements (MacArthur et al., 2014). Non-imaging spectrometers with technical advancements, including reduced size, high SNR, high spectral and temporal resolutions, has encouraged the development of UAV-based SIF payloads (MacArthur and Robinson, 2015).

So far, few studies have focused on UAV-based SIF with non-imaging spectrometers. Garzonio et al. (2017) developed the HyUAS equipped with a non-imaging instrument (USB4000) and a high-resolution RGB camera, based on a small rotary-wing UAV, to measure reflectance and SIF. Their study was mainly to test this new development and for provision of a more homogeneous footprint at a given flight height while flying over different vegetation canopies around solar noon. Piccolo Doppio, a dual-field-of-view spectrometer system consisting of two Ocean Insight spectrometers (QE Pro and FLAME) for reflectance and fluorescence measurements, was introduced by MacArthur et al. (2014) and was used aboard a DJI Matrice 600 pro UAV using a fly-and-hover approach (Maseyk et al., 2018) to gain insight into canopy-level photosynthetic responses to CO_2. However, this experiment was performed on woodland, not on crops. A case study of alfalfa and grass canopies was carried out with the AirSIF system, a dual-field-of-view spectroradiometer system in which sensor etaloning and platform motion correction was introduced to achieve accurate geolocation and shape reconstruction of the SIF measurements (Bendig et al., 2019). Aside from these studies, no studies have currently been done towards the application of this setup to measure SIF in precision agriculture and the diurnal cycles of SIF over different crop canopies to characterize variation of photosynthesis-related processes over the day.

This paper presents the FluorSpec system that includes a non-imaging sub-nanometer spectrometer operating across the visible and near-infrared spectral region. This system can be used both at a fixed location to acquire ground-based SIF measurements at the canopy level at high temporal frequency as well as be used as a UAV-based payload to acquire SIF data at the plot or field level. The main goal of this study is to evaluate the potential of this UAV-based spectroscopy approach for understanding crop SIF and photosynthesis in precision agriculture at the field level and to contribute to bridging the gap in SIF measurements between ground and airborne/spaceborne scales. Diurnal SIF measurements at ground and field level were collected over potato and sugar beet fields as case studies.

2.2. FluorSpec system

2.2.1. System Design

The FluorSpec system is composed of a non-imaging hyperspectral spectrometer (Ocean Insight QE-Pro), spectrometer optics, a simple USB connected Global Navigation Satellite System (GNSS) receiver, a laser rangefinder sensor (LightWare SF11C), a Raspberry Pi data sink, custom synchronization electronics, and a lithium polymer battery (3S, 500–1000 mA). Figure 2.1 shows the technical details of the system. We designed the FluorSpec to be mounted on board an octocopter UAV, but it is basically a stand-alone set-up that can be installed on any platform able to carry a 2.0 kg payload.

The QE-Pro is a compact, actively cooled, high-performance spectrometer that weighs 1.15 kg. The spectrometer unit selected for FluorSpec is configured to the wavelength range of 630--800 nm with a spectral resolution of 0.14 nm (FWHM). The spectrometer observes light through a bifurcated optical fibre, which has one tip connected to upward looking irradiance optics and the second one to downward looking custom radiance optics (Figure 2.1). The irradiance optics consist of an optical fibre mount, servo driven shutter, and a diffuser providing a near-Lambertian field-of-view (FOV). Similarly, the downward looking radiance optics consist of a fibre mount, a shutter, and an open "lens tube" (Thorlabs SM05 series) restricting the spectrometer FOV to 25° opening angle. Optionally, also a simple lens can be installed on the lens tube to limit the FOV to a narrower angle. With the servo-controlled shutters the system can automatically switch between irradiance, radiance, and dark current measurement modes.

The system is controlled in real time by a Raspberry Pi 2 computer. The control software of the FluorSpec is written in PHP as a customized version of the Ocean Optics STS Dev Kit software. In measurement mode, the FluorSpec repeats a loop where it measures a dark current spectrum, an irradiance spectrum, and a radiance spectrum. Simultaneously, it records the data streams from GNSS receiver and laser range finder. These metadata define the system geographical position, provide absolute timing, and provide an accurate above-ground altitude. To output the data, the raw spectra, geo-location data and metadata are written to a USB thumb drive as an ASCII file, which can then be post-processed to final SIF data according to the processing steps described in section 2.2.3.

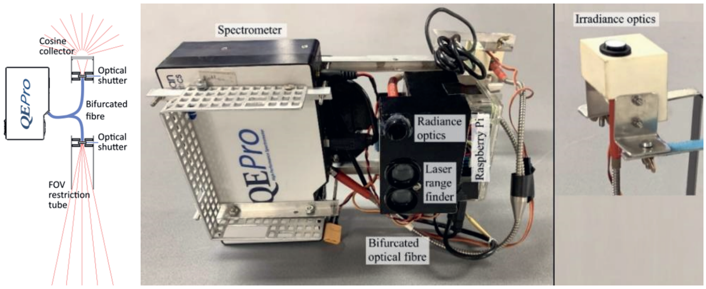

Figure 2.1. Schematic drawing of the FluorSpec optics and photos of the system.

2.2.2. Sensor calibration

Sensor calibration is required to produce absolute irradiance and radiance values. In addition, the accuracy of the reflectance factors and absolute values of reflected and fluorescent radiance are directly dependent on the accuracy of the radiance sensor calibration. The measured irradiance was calibrated using direct solar irradiance at sea level. Since pairing of the measured spectrum accurately is hard, the spectral resolutions of both sensors need to be the same to get a high calibration accuracy. Therefore, a spectral smoothing function on both spectra was performed by running a Gaussian averaging filter. After that, the radiance sensor can be calibrated with the radiometric measurements from a white Spectralon panel (99%) and from the calibrated irradiance sensor.

2.2.3. Processing Chain

The processing chain is based on MATLAB (v2018b, Mathworks) scripts, including steps for radiometric processing of spectra, merging each spectrum, processing laser rangefinder and GPS data, atmospheric correction, and SIF retrieval method.

2.2.3.1. Radiometric processing

As the ChF is a measurement in absolute radiance units, the first step of the FluorSpec processing chain is to convert the acquired raw spectra (digital numbers) to at-sensor irradiance (Wm^{-2} nm^{-1}) and radiance (Wm^{-2} nm^{-1} sr^{-1}). This is done by removing the dark current (interpolated from preceding and following measurement) and by multiplying the digital number values with the radiometric calibration coefficient per wavelength. Next, the at-sensor irradiance and radiance are converted to their top-of-canopy (TOC) equivalents by applying an atmospheric correction which is described in section 2.2.3.2. Afterwards, to get the TOC irradiance at the same time as the TOC radiance measurement, preceding and following TOC irradiances are linearly interpolated to the GPS time stamp of the corresponding TOC radiance measurement.

2.2.3.2. Atmospheric correction

The at-sensor irradiance and radiance must be converted to their top-of-canopy equivalents by applying an atmospheric correction. Since SIF accounts for less than 2% of the reflected radiance into the sensor and the atmosphere under the measurement altitude distorts the observed SIF signal, an atmospheric correction is critical for any accurate airborne fluorescence measurements. In this study, SIF is retrieved using the spectral region around the 760 nm O_2-A absorption feature, where the atmosphere has a high impact on the radiance. We used the *MODerate resolution atmospheric TRANsmission* (MODTRAN) algorithm to simulate the transmittance profile through the bottom 1 km of the atmosphere around the 760 nm O_2-A feature as sensed by a sensor with 0.1 nm spectral resolution (Figure 2.2). To simulate the atmospheric transmittance of the bottom 1 km of atmosphere, standard MODTRAN parameters (mid-latitude summer atmospheric profile, rural aerosol type, visibility = 23 km, sensor altitude = 1 km, and default values for water column, CO_2 and ground temperature) (MODTRAN®, Spectral Sciences, Inc) were used in the MODTRAN model.

To get a useful transmittance for a specific UAV altitude, the simulated transmittance can be converted to different thicknesses of the atmosphere ($T(d)$) using the Beer-Lambert law:

$$T(d) = \left[T\left(d_{ref}\right)\right]^{\frac{d}{d_{ref}}} \tag{2.1}$$

where d is the distance light goes through the atmosphere (i.e. UAV altitude above ground level), d_{ref} is the distance used in the simulation (1 km), and $T\left(d_{ref}\right)$ is the simulated transmittance.

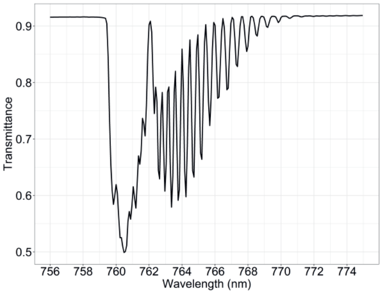

Figure 2.2. The transmittance of the bottom 1 km of atmosphere around the 760 nm O_2-A absorption feature as simulated using MODTRAN

If we consider only atmospheric transmittance, but no additive scattering, the measured at-sensor radiance (L_{sensor}) and irradiance (E_{sensor}) can be converted to their TOC equivalents (L_{toc}, E_{toc}) using:

$$L_{toc}(\lambda) = L_{sensor}(\lambda)/\left[T\left(d_{ref},\lambda\right)\right]^{\frac{d}{d_{ref}}} \tag{2.2}$$

$$E_{toc}(\lambda) = \left(E_{sensor}(\lambda)\right) * \left[T\left(d_{ref},\lambda\right)\right]^{\frac{h}{d_{ref}}} \tag{2.3}$$

where d is the distance between the target and the radiance sensor and h is the above-canopy altitude of the irradiance sensor.

Using Equations 2.2 and 2.3, we converted the at-sensor spectra to their TOC equivalents. With the FluorSpec system, d is directly measured by the laser rangefinder sensor. In downward looking measurements using this same value works also as h.

2.2.3.3. The SIF retrieval method (SSA-FLD)

The Fraunhofer Line Discriminator (FLD) principle has long been applied as the reference method to disentangle the SIF signal from the reflectance signal (James and Plascyk, 1975; Moya et al., 2004; Plascyk and Gabriel, 1975). The standard FLD-based approach utilizes two spectral bands to estimate fluorescence around each of the oxygen absorption features (O_2-B at 687 nm and O_2-A at 760 nm): one band inside and one band outside the absorption feature. A fundamental assumption of this method is that reflectance and fluorescence remain constant over the absorption feature of interest. In our study, spectra were acquired using the QE-pro spectrometer, which has an ultra-high spectral resolution (0.14 nm). To make full use of the spectral information within the oxygen absorption regions, we apply a slightly adapted FLD-based approach to retrieve SIF, called Spectral Shape Assumption FLD (SSA-FLD). Different from FLD assumptions of constant reflectance and fluorescence over the absorption feature, SSA-FLD employs a linear function to represent reflectance and a known shape of the fluorescence spectrum to describe the chlorophyll fluorescence over the spectral region around O_2-A absorption feature, where the amount of incoming radiation is more comparable to the fluorescence emission. The spectral fitting method (SFM) is another advanced technique to retrieve the fluorescence and reflected radiance from high spectral resolution radiance observations (Mazzoni et al., 2012; Meroni et al., 2010). The method relies on proper mathematical functions representing the surface reflectance (e.g. linear, polynomial, or piecewise cubic splines functions) and the chlorophyll fluorescence (e.g. Lorentzian, Gaussian or Voigt functions) within narrow spectral windows confined to the oxygen absorption bands.

Therefore, SSA-FLD can be regarded as a special case of SFM. In a parallel study we compared the two methods, and they were strongly linearly correlated ($R^2 = 0.99$) and therefore we decided to continue with SSA-FLD (results not shown).

The TOC radiance (L_{toc}) leaving the target can be written as a combination of the traditional reflected radiance and the fluorescence radiance (L_{fl}) components:

$$L_{toc}(\lambda) = \frac{1}{\pi} E_{toc}(\lambda) R'_{target}(\lambda) + L_{fl}(\lambda) \tag{2.4}$$

where $E_{toc}(\lambda)$ is the TOC incident irradiance hitting the target and R'_{target} is the apparent reflectance factor of the target without fluorescence effects.

The only two unknown items in Equation 2.4 are $R'_{target}(\lambda)$ and $L_{fl}(\lambda)$. To solve the fluorescent radiance component, the SSA-FLD model uses two assumptions. Firstly, it assumes that the fluorescence follows a known shape of the fluorescence spectrum and, secondly, that the reflectance factor spectrum of the target object behaves linearly over the used spectral region.

Thus, we split the chlorophyll fluorescent radiance ($L_{fl}(\lambda)$) into a known spectral shape component ($l_{fl}(\lambda)$) and an unknown amplitude component ($\hat{L}_{fl}$):

$$L_{fl}(\lambda) = \hat{L}_{fl}\, l_{fl}(\lambda) \tag{2.5}$$

For convenience, we can decide to scale the shape component so that $[l_{fl}(\lambda_{760nm}) = 1]$ and $[\hat{L}_{fl} = L_{fl}(\lambda_{760nm})]$.

Similarly, we need to split the reflectance factor of the target into a known spectral shape component ($r_{target}(\lambda)$ and an unknown amplitude component ($\hat{R}_{target}$):

$$R_{target}(\lambda) = \hat{R}_{target}\, r_{target}(\lambda) \tag{2.6}$$

To follow the assumption that the reflectance factor changes linearly over the oxygen absorption feature, we must solve the reflectance factor on both sides of it using equation:

$$R_{target}(\lambda) = \pi \frac{L_{target}(\lambda)}{E_{toc}(\lambda)} \tag{2.7}$$

and then linearly interpolate the $r_{target}(\lambda)$ spectrum for all sampled wavelengths in the gap area. In principle, at this stage we could solve also $\hat{R}_{target}$ but by solving only the shape component now $r_{target}(\lambda)$ improves the retrieval accuracies of both $\hat{R}_{target}$ and $\hat{L}_{fl}$ in the final solution stage.

By inserting Equations 2.5 and 2.6 into Equation 2.4, we get:

$$L_{toc}(\lambda) = \frac{1}{\pi}E_{toc}(\lambda)\hat{R}_{target}\, r_{target}(\lambda) + \hat{L}_{fl}\, l_{fl}(\lambda) \tag{2.8}$$

which can be rearranged so that all wavelength-dependent components (which are known) are separated from the non-wavelength-dependent components (which are unknown):

$$\left(\frac{L_{toc}(\lambda)}{l_{fl}(\lambda)}\right) = \hat{R}_{target}\left(\frac{E_{toc}(\lambda)\, r_{target}(\lambda)}{\pi\, l_{fl}(\lambda)}\right) + \hat{L}_{fl} \tag{2.9}$$

This is the main equation that SSA-FLD uses to solve the fluorescent radiance from observations. The equation has two unknown parameters, $\hat{R}_{target}$ and $\hat{L}_{fl}$, which could be solved simply by using data points at two or more wavelengths. In a computer environment, the $\hat{R}_{target}$ and $\hat{L}_{fl}$ are solved best using the full spectral information over the oxygen absorption band by writing the equation in matrix representation with wavelengths incrementing horizontally in the matrix cells.

By filling the matrices with the spectra over the oxygen absorption area (for example ± 5 nm), we can linearly solve the unknown parameters by matrix division:

$$\left[\hat{R}_{target} \quad \hat{L}_{fl}\right] = \frac{M_1}{M_2} \tag{2.10}$$

where

$$M_1 = \left[\frac{L_{toc}(\lambda_1)}{l_{fl}(\lambda_1)}, \quad \frac{L_{toc}(\lambda_2)}{l_{fl}(\lambda_2)}, \quad \cdots\right]$$

$$M_2 = \begin{bmatrix} \frac{E_{toc}(\lambda_1)\, r(\lambda_1)}{\pi\, l_{fl}(\lambda_1)}, & \frac{E_{toc}(\lambda_2)\, r(\lambda_2)}{\pi\, l_{fl}(\lambda_2)}, & \cdots \\ 1, & 1, & \cdots \end{bmatrix} \tag{2.11}$$

After $\hat{L}_{fl}$ has been solved, it can be converted to the full fluorescence radiance spectrum ($L_{fl}(\lambda)$) using Equation 2.5.

2.2.3.4. SIF normalization

The vegetation produces fluorescence relative to the amount of the incident photosynthetically active radiation (PAR irradiance, E_{PAR}) in energy units (μmol m^{-2} s^{-1}), which designates the spectral range of solar radiation from 400 to 700 nm. The variation in PAR absorbed by a canopy caused by different illumination conditions for a closed canopy can be considered by normalizing SIF by incident PAR (Daumard et al., 2012). Furthermore, the normalized SIF can provide more insights in the effects of pigments, leaf area, leaf inclination and physiology to variations of SIF (Van der Tol et al., 2016). The normalized SIF only represents the emission efficiency at the O_2-A band (760 nm), and only in one solid angle, therefore its unit is $\mu m^{-1} sr^{-1}$. Normalized SIF ($SIF_{normalized}$) can be expressed as

$$SIF_{normalized} = \frac{L_{fl}(760nm)}{E_{PAR}} \tag{2.12}$$

2.3. Case studies

2.3.1 Study areas

There were two study sites in our case studies. The main study site (study site 1) was located in the agricultural experimental research fields of Unifarm, Wageningen University & Research (51.987°N, 5.652°E), north to the city of Wageningen, the Netherlands. The second study site (study site 2) was a grassland field on the Campus of Wageningen University. The average altitude of the study areas is 7 m above mean sea level. The mean annual precipitation is 568 mm and the mean annual temperature is 10 °C.

Within study site 1, sugar beets (*Beta vulgaris* L., variety Urselina) and potato (*Solanum tuberosum* L., variety Aventra) were grown by using common field rotation practices (Figure 2.3). One sugar beet field (2.30 ha) and one potato field (1.22 ha) were selected as experimental targets for both ground and UAV measurements. Sugar beets grew in 2018 from April 19 (day of year (DOY): 109) to November 7 (DOY 311), and potato was planted on April 13, 2018 (DOY 103) and harvested on August 28, 2018 (DOY 240). All observations with the FluorSpec system took place under clear sky conditions while the canopies of both crops were fully closed.

Figure 2.3. Location of the study site 1 at Unifarm of Wageningen University, Wageningen, the Netherlands. For each flight, there were 4 flight lines in a potato field (L_1, L_2, L_3, and L_4) and 4 flight

lines in a sugar beet field (L_5, L_6, L_7, and L_8). The arrows indicate the UAV flying directions over the fields.

2.3.2. FluorSpec measurements for radiometric sensor calibration

The FluorSpec irradiance sensor was calibrated using the direct component of solar irradiance as reference. Data for radiometric sensor calibration were acquired with the FluorSpec mounted on a tripod over grassland on the Campus of Wageningen University on April 19, 2018 (DOY 109) on a cloud-free sunny day. Measurements for the irradiance sensor calibration were acquired at 12:40 pm Central European Time (CET) for 4 minutes (Figure 2.4a), with a tube on the top of the irradiance sensor which pointed directly at the sun. In this manuscript all time indications refer to CET. Only the raw irradiance data were used for irradiance sensor calibration.

After the irradiance optics were calibrated, the calibration was transferred to radiance optics using a white (99%) Spectralon panel. FluorSpec radiance optics were placed at 25 cm height above the horizontal reference panel (13×13 cm), resulting in a 5.5 cm radius FOV (Figure 2.4b). Spectral data were collected at 12:50 and lasted 3 minutes with the irradiance sensor pointing directly up towards the sky and the radiance sensor pointing to the panel in nadir.

To assess the calibration accuracy, FluorSpec measurements were acquired over bare soil on February 27, 2019 (DOY 58) for a cloudless condition. Data were collected at 13:01, 13:11 and 13:18 for 2 minutes and approximately 30 measurements were acquired every time.

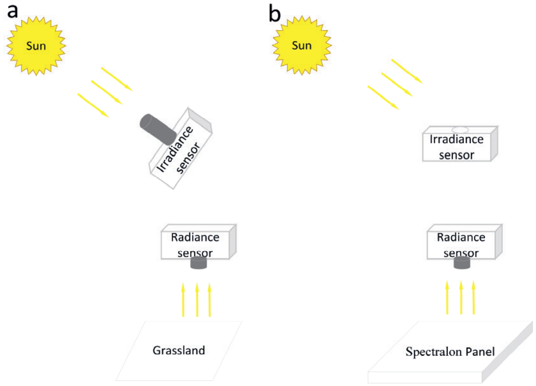

Figure 2.4. The schematic diagrams of a) irradiance sensor calibration, and b) radiance sensor calibration. Spectra for the irradiance sensor calibration were acquired with a tube on the top of the irradiance sensor pointing directly to the sun. Data for the radiance sensor calibration were acquired over a white (99%) Spectralon panel in nadir.

2.3.3. Ground measurements

2.3.3.1. FluorSpec measurements

Spectra over the potato canopy on July 23, 2018 (DOY 204) and the sugar beet canopy on August 6, 2018 (DOY 218) were measured over the full day. FluorSpec was installed at a fixed position 50 cm above the canopies, resulting in a footprint of 22 cm. FluorSpec was kept stationary acquiring measurements from nadir during the measuring day. The measurements of potato and sugar beet plants started at approximately the same time (8:28 and 8:16, respectively) and both finished at 17:06. Raw spectral data, including irradiance, dark current and radiance successively, were collected about every 25 minutes. Specifically, the time interval in the morning was 20 minutes and in the afternoon was 30 minutes. Each observation lasted 2-3 minutes and had 30-50 data records.

2.3.3.2. FluorPen measurements

The PAR-FluorPen FP 110/D (PSI, Czech), hereinafter called FluorPen, was used to obtain simultaneous measurements of variables related to ChF. The FluorPen is a portable, battery-powered Pulse amplitude-modulated fluorometer with leaf clips that enables quick and precise measurement of chlorophyll fluorescence parameters and incoming photosynthetically active radiation (PAR, μmol m^{-2} s^{-1}). Photosystem II Quantum Yield (Qy) and PAR were measured simultaneously while FluorSpec was collecting spectra diurnally. Three fully expanded young leaves from plants 30 cm away from the FOV of FluorSpec were randomly selected for the light adapted Qy measurements. The FluorPen was placed horizontally to measure the incident PAR three times per FluorSpec measurement interval.

2.3.4. UAV measurements

The FluorSpec was flown as a payload on a UAV over the study site 1 during clear sky conditions on August 2, 2018 (DOY 214). On that day, the maximum air temperature was 31 °C around 14:00 and the average wind speed was 2.48 m s^{-1}. Sunrise was at 6:00, solar noon at 13:43 and sunset at 21:26. The FluorSpec was mounted below a DJI S1000 UAV platform (DJI, China, Figure 2.5), which is powered by 8 brushless electric rotors that allow autonomous vertical take-off and landing, hovering over a target and high manoeuvre ability during in-flight operations. Flight missions were planned with a UGCS ground station, a dedicated mission planning software that matches user observation requirements and platform/payload technical parameters (i.e. flight altitude, flight speed, sampled areas, overlapping, etc). The flight mission consisted of 27 waypoints over the two fields (Figure 2.3). The UAV was programmed to fly 15 m AGL with a horizontal speed of 3 m s^{-1} from waypoint to waypoint. In this configuration, the spectrometer sampled a circular area with a diameter of 6.6 m on the ground for every measurement and the sampling interval was 10.5 m. To follow the diurnal cycle, four flights following a diurnal cycle were carried out at 9:45, 11:38, 14:15 and 16:28. Each flight lasted around 12 minutes under clear blue sky and stable light conditions. The acquired data were processed according to the processing steps described in section 2.2.3.

A Parrot Sequoia+ was mounted to the DJI Mavic drone (DJI, China) to collect multispectral measurements over the two crop fields around 11:00 on the same day (DOY 214). The Parrot Sequoia+ is a multispectral camera with green, red, red-edge and near-infrared (NIR) bands. The flight height was 60 m AGL and the flying speed was 5 m s^{-1}. Data processing was done using the Pix4D software, including photo alignment, digital surface model building, orthomosaic creation and calculation of the normalized difference vegetation index (NDVI).

Figure 2.5. DJI S1000 octocopter UAV platform with the FluorSpec mounted. "A" refers to the FluorSpec irradiance sensor and "B" refers to the radiance sensor.

2.4. Results

2.4.1. Radiometric and spectral characterization of the FluorSpec

The calibration result over the Spectralon panel is shown in Figure 2.6a. The irradiance curve had the same trend as the radiance curve, and their difference in magnitude is almost constant over the 630-800 nm range. There were four ranges where this difference varied: 654-659 nm, 686-697 nm, 717-734 nm, and 758-770 nm. The difference between the irradiance and radiance curves was smallest at 760 nm (O_2-A absorption feature), followed by 687 nm (O_2-B absorption feature). The panel reflectance was nearly 1.0 within the 630-800 nm range. Some spectral bands showed a large noise level, especially within 717-734 nm and 758-770 nm. Even though the reflectance was evenly distributed around 1.0, the peak reached 1.2 while the lowest value was approximately 0.9 in the range of 758-770 nm.

Similarly, the spectral shape of bare soil radiance was analogous to that of irradiance (Figure 2.6b). However, the difference between them became slightly smaller as wavelength increased from the red to the NIR range, because bare soil reflectance increased gradually from 0.24 at 630 nm to 0.34 at 800 nm. The irradiance acquired over the Spectralon panel was higher than that over bare soil because of different acquisition dates (12:50 on April 19, 2018, and 13:11 on February 27, 2019, respectively).

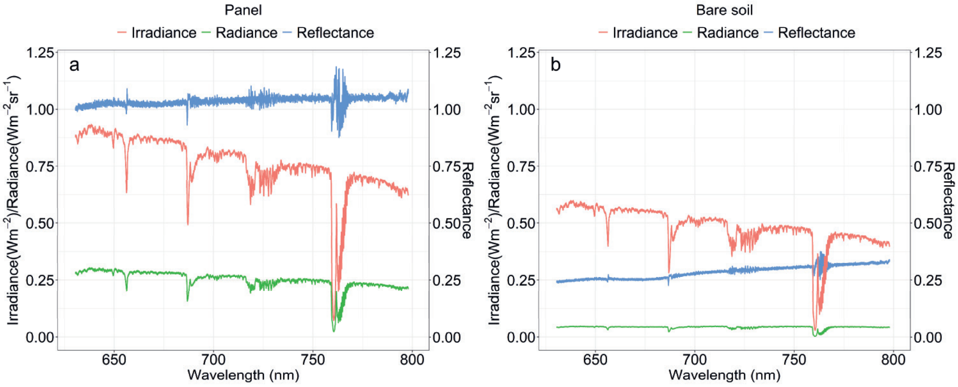

Figure 2.6. Calibrated irradiance (Wm^{-2}), radiance (Wm^{-2}sr^{-1}) and reflectance over a white (99%) Spectralon panel on April 19, 2018 (a) and a bare soil sample on February 27, 2019 (b).

2.4.2. SIF retrievals in the O_2-A band from a non-vegetation target

In this paper, we only report SIF at 760 nm (O_2-A band) that corresponds to fluorescence emission in the far-red region because in the wider O_2-A absorption band this fluorescence flux is easier to quantify than in the O_2-B absorption band. To assess the ability of SSA-FLD to retrieve SIF, SIF of bare soil was calculated from collected raw FluorSpec data. SIF values were all close to zero, but slightly negative (Table 2.1). Vegetation SIF values usually fall in a range of -0.15 ~ 3 mWm^{-2}sr^{-1}nm^{-1} (Rascher et al., 2015; Garzonio et al., 2017).

Table 2.1. The descriptive statistics of bare soil SIF measured on February 27, 2019 ($mWm^{-2}sr^{-1}nm^{-1}$).

Measuring time	Maximum	Minimum	Mean	Standard deviation
13:01	-0.009	-0.110	-0.056	0.0212
13:11	-0.009	-0.086	-0.053	0.0181
13:18	-0.022	-0.088	-0.050	0.0193

2.4.3. Diurnal SIF and normalized SIF patterns at the ground level

2.4.3.1. FluorPen PAR and FluorSpec PAR

FluorSpec PAR (Wm^{-2}) was calculated within the 630-700 nm interval from the diurnal canopy FluorSpec measurements of potato on July 23, 2018, and of sugar beets on August 06, 2018. FluorPen PAR ($\mu molm^{-2}s^{-1}$) was measured over the whole 400-700 nm interval simultaneously with the diurnal FluorSpec measurements. Figure 2.7 shows the comparison between averaged FluorSpec PAR and averaged FluorPen PAR. During the two experimental days, FluorPen PAR and FluorSpec PAR had a strong linear relation, with high R^2 (0.99). Therefore, it can be concluded that incident PAR can be calculated with FluorSpec irradiance measurements within the 630-700 nm range to normalize SIF. Therefore, E_{PAR} used to normalize SIF was calculated as:

$$E_{PAR} = \left(3.91 * PAR_{FluorSpec} - 135\right)/4.56 \tag{2.13}$$

Division by a factor of 4.56 (Sager and McFarlane, 1997) was used to convert the FluorPen unit of E_{PAR} into Wm^{-2}.

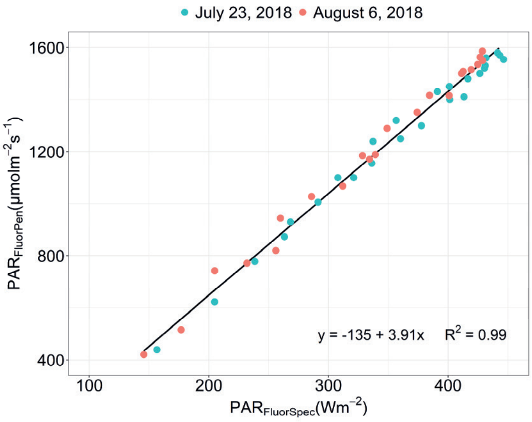

Figure 2.7. The linear relations between FluorSpec PAR and Fluorpen PAR for potato on July 23, 2018 (DOY 2014) (green dots) and for sugar beet on August 06, 2018 (DOY 218) (red dots).

2.4.3.2. Diurnal SIF cycles

The spectral and radiometric characteristics of the FluorSpec system (Figure 2.6) and the good performance of SSA-FLD (Table 2.1) allow the quantification of SIF at 760 nm. Figure 2.8 shows the diurnal cycles of SIF values of potato and sugar beet canopies, which were measured at regular intervals on July 23, 2018 and August 06, 2018, respectively. SIF exhibited a pronounced diurnal pattern with the highest average values measured close to midday. Potato SIF increased quickly till it reached the highest value around 12:30, and in the afternoon potato SIF experienced a sharp decline (Figure 2.8a). In comparison, in Figure 2.8b, SIF values of the sugar beet crop increased slowly until approximately 12:30. Interestingly, sugar beet SIF decreased gradually in the early afternoon unlike potato, but afterwards it went down steeply (Figure 2.8b). Both the range and the variations in SIF of potato were larger than those of sugar beets, despite their similar SIF diurnal patterns. PAR from FluorSpec on both days had clear diurnal patterns. PAR increased in the morning and peaked around local noon (around 13:30 pm) (Figure 2.8). Afterwards, PAR decreased. For both crops, the peaks of SIF values appeared earlier than those of PAR.

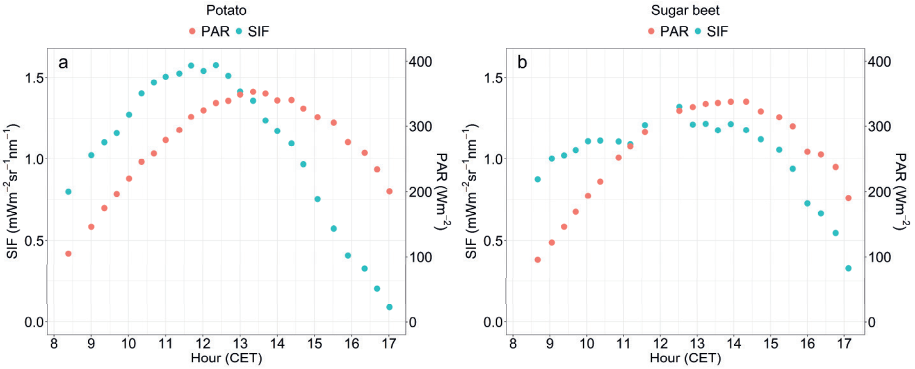

Figure 2.8. Diurnal dynamics of SIF and PAR for potato on July 23, 2018 (DOY 204) (a) and for sugar beet on August 06, 2018 (DOY 218) (b). Each value represents mean SIF and mean PAR values collected at this time.

2.4.3.3. Diurnal normalized SIF

The normalized SIF was calculated at 760 nm with PAR, which was calculated using the FluorSpec PAR-based linear model that was introduced in section 2.4.3.1 (Figure 2.7). The diurnal changes of $SIF_{normalized}$ are shown in Figure 2.9a, b. The graphs show that there has been a steady decrease in $SIF_{normalized}$ values of both crops during the day. Overall,

$SIF_{normalized}$ values of potatoes were lower than those of sugar beets. FluorPen Qy was compared to assess the reliability of $SIF_{normalized}$ (Figure 2.10a, b). Qy indicates the quantum yield of linear electron flux through the Photosystem II (PSII) reaction centres, which can be used to represent the PSII operating efficiency under different environmental conditions (Baker et al., 2008). In this study, FluorPen Qy was measured in light-adapted leaf samples. Both potato and sugar beet crops showed significant positive correlations between $SIF_{normalized}$ and Qy in Figure 2.10. Potatoes had a higher correlation than sugar beets, with R^2 values of 0.81 and 0.63, respectively.

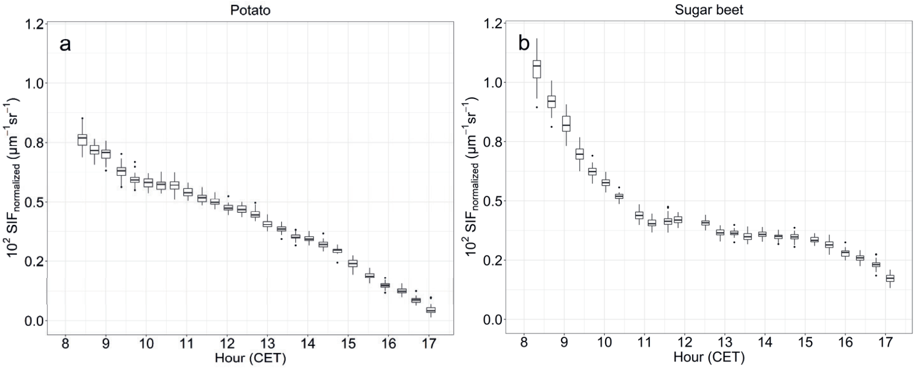

Figure 2.9. Diurnal patterns of the normalized SIF by E_{PAR} ($SIF_{normalized}$) over potatoes (a) and sugar beets (b). $SIF_{normalized}$ values were multiplied by 100. Each box with whiskers represents all $SIF_{normalized}$ calculated using SIF values acquired during the measuring time.

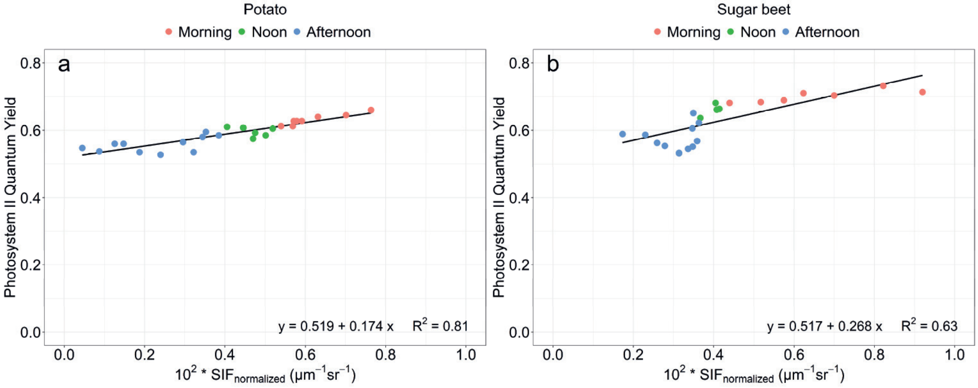

Figure 2.10. Relationships between averaged normalized SIF ($SIF_{normalized}$) and FluorPen Photosystem II Quantum Yield (Qy) for potatoes (a) and for sugar beets (b). $SIF_{normalized}$ values were multiplied by 100.

2.4.4. Diurnal dynamics of UAV-based SIF

Maps of SIF acquired from the UAV platform over the two selected crop fields clearly show novel information on plant structure and function (Figure 2.11). SIF performed differently in different fields at the same time. For instance, at11:38, SIF in the potato field (towards the south) changed over a larger range from 0.23 to 1.42 $mWm^{-2}sr^{-1}nm^{-1}$, while for sugar beets (towards the north) it varied from 0.51 to 1.34 mWm^{-2} $sr^{-1}nm^{-1}$. Some areas had fluorescence values close to zero, e.g. the senescent potato areas covered by the 4th flight line (L_4 in Figure 2.11).

The lower SIF (blue points) was consistent with low NDVI values in the potato field (particularly the headlands). Large variation could be observed within the same field. For the 2nd flight at 11:38, SIF from different flight lines shows clear variations either in potato or sugar beet fields. In the potato field, L_1 has consistently the highest fluorescence values reaching 1.42 $mWm^{-2}sr^{-1}nm^{-1}$, whereas the maximum value of L_2 was 1.05 $mWm^{-2}sr^{-1}nm^{-1}$ (Figure 2.11). Furthermore, SIF was observed to be highly variable within the same flight line. For example, L_2 of the 2nd flight within the potato field ranged from 0.35 to 1.06 $mWm^{-2}sr^{-1}nm^{-1}$.

Clear diurnal cycles of SIF in the two fields were shown by comparing the four maps over the day. The overall SIF went up in the morning and went down in the afternoon, which is in line with SIF diurnal cycles at the canopy level (Figure 2.8). SIF values at 9:44 and at 16:28 were lower than those at 11:38 and 14:45. SIF performed similarly in the 2nd and 3rd flights as their observing times were both close to solar noon when the incoming radiation was highest. This is different from the diurnal performance of potato SIF at the ground level, where SIF around 11:40 was higher than that around 14:00.

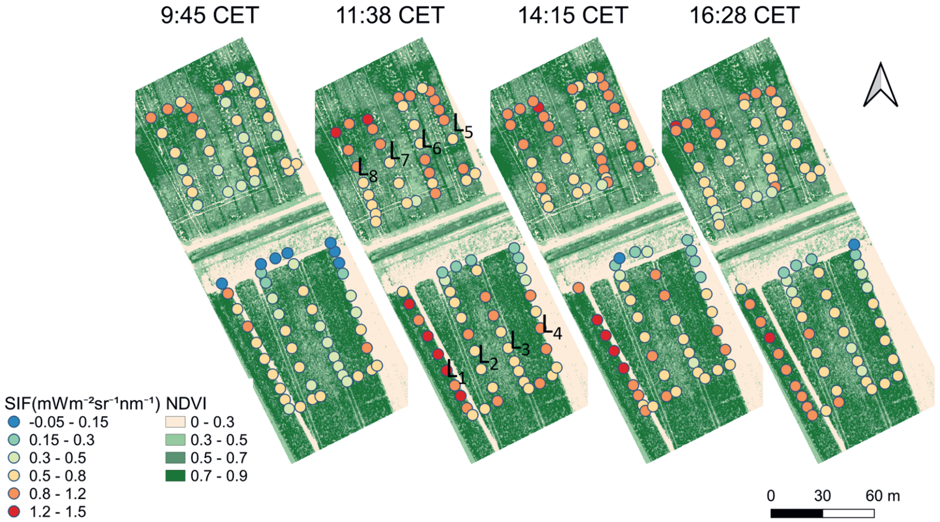

Figure 2.11. Performance of SIF in potato and sugar beet fields based on UAV measurements as obtained on August 02, 2018 (DOY 214) over the experimental area in Wageningen, the Netherlands. L_1, L_2, L_3, and L_4 were flight lines over the potato field and L_5, L_6, L_7, and L_8 were over the sugar beet field. The basemap shows NDVI values derived from a Sequoia+ multi-spectral image.

2.5. Discussion

This study introduced a UAV-based fluorescence measuring system, FluorSpec, whose measurements can be used as proxy for crop photosynthesis and stress occurring in crops both at the ground and the field level. Some earlier studies have shown the potential of UAV mounted systems to measure SIF with a non-imaging spectrometer (Bendig et al., 2019; Garzonio et al., 2017; MacArthur et al., 2014). Compared with these studies, the current study has two advantages. First, the FluorSpec FOV is 25°, which is larger than that of the systems used in the above-mentioned literature (largest FOV of 15°). Optionally, FluorSpec can be mounted with fore optics, reducing the FOV to any narrower opening angle. As Gautam et al. (2018) pointed out, increasing the FOV can compensate the footprint area loss and increase the signal strength. Thus, the 25° FOV provides stable and reliable signals. No matter what flight mode is applied, e.g. stop and go (hovering) or continuous mapping, FluorSpec SIF signals can provide a better understanding of crop photosynthetic performance due to the larger footprint. In our study, the continuous mapping flight mode was applied and enabled us to have more insights into SIF performance of larger areas within and between fields. Secondly, the atmosphere between the sensor and target affects airborne SIF retrieval (Damm et al., 2014) and adds uncertainties in SIF observations even at short distances of 10 m such as tower and UAV observations (Sabater et al., 2018). In our study, atmospheric correction was applied to FluorSpec measurements, which increases the reliability of the SIF retrieval.

2.5.1 The performances of radiometric correction and SSA-FLD

The white Spectralon panel and bare soil show the expected spectral behaviour after radiometric calibration and atmospheric correction (Figure 2.6a, b). In the spectral range from 630 to 800 nm, the reflectance of the white panel was constant while the reflectance of bare soil increased from 0.24 to 0.34. This demonstrates that the FluorSpec system was well calibrated and provided realistic reflectance values at very high spectral resolution. SIF of bare soil shows very small negative values close to zero (Table 2.1), indicating no fluorescence as should be. The negative SIF values from non-vegetation targets have also been observed in other studies (Alonso et al., 2008; Damm et al., 2014; Garzonio 2017; Pinto et al., 2016). For example, Alonso et al. (2008) found that SIF values retrieved from bare soil by the iFLD method, one of the most popular methods to provide reasonable fluorescence values, were also negative and most of them varied from -0.25 - 0 $mWm^{-2}sr^{-1}nm^{-1}$. Negative SIF values could result from the combined effect of sensor noise and the retrieval assumption of a known shape of the fluorescence spectrum over vegetation, whereas this assumption is not suitable for non-vegetation targets (bare soil). The similar performance of SSA-FLD shows its capability to separate SIF from reflectance.

In the future, the measured SIF values over canopies as obtained with FluorSpec need to be validated by comparing them with a well-calibrated system like the airborne HyPlant system as a reference. A special campaign has been defined for this.

2.5.2 Diurnal cycles of ground-based SIF and $SIF_{normalized}$

Our results are in agreement with findings of previous studies (Rascher et al., 2015; Zarco-Tejada et al., 2016): (i) crop SIF values are in the range of 0 to 3 mW m^{-2} sr^{-1} nm^{-1}, both at the ground level and at the UAV level; (ii) SIF increased in the morning and decreased in the afternoon, which is mainly driven by PAR. As illustrated, for both potato and sugar beet crops, the peak of SIF occurred about an hour earlier than that of PAR (Figure 2.8). There are three possible explanations for this. One explanation is that the incoming irradiance was high around 12:30 and light energy absorption already might have exceeded the capacity for light utilization in photosynthesis, in which case photoinhibition would be triggered. Excess of absorbed light energy was dissipated into heat by nonphotochemical chlorophyll fluorescence quenching

(NPQ), which is the primary mechanism to dissipate the absorbed energy when light intensity is high. Secondly, the summer of 2018 brought a heatwave to the Netherlands, therefore there was increased heat stress and drought. The maximum temperatures were 30 ºC and 32 ºC on July 23, 2018 (DOY 204) and August 6, 2018 (DOY 218), respectively. The enzymes of the Calvin cycle involved in the carbon assimilation system are heat labile. For example, Rubisco activase, which affects Rubisco activity, is very sensitive to the elevated temperature. Thus, the carbon fixation process is sensitive to elevated temperature and gets strongly inhibited by heat stress (Berry and Bjorkman, 1980). In addition, stressed by drought, the crops had to close leaf stomata to prevent water vapor loss. Since stomata act as a gateway for water and CO_2, their closure limits the transport of CO_2 into leaves for use in carbon fixation and consequently affects the electron transport chain in light-dependent reactions. As a result, most incoming sunlight could not be processed in photochemical ways and was emitted as heat. To further reduce water vapor loss, crop leaves wilted, and PAR absorption decreased. The energy used to emit fluorescence was out of sync with incoming irradiance acquired by the FluorSpec upward sensor. Another possible reason could be the short sensor-target distance. The FluorSpec was positioned 50 cm above both crop canopies and as a result covered a 22cm-diameter circular area. The close distance could have made the SIF signal vulnerable to the solar zenith angle and BRDF effects. The small footprint also only allowed SIF acquisition over a limited canopy area, which could be affected by leaf inclination angle, canopy structure, soil background, and the plant shadow caused by the direct sunlight around solar noon.

In this study, PAR from the FluorPen is not ideal for SIF normalization for the following two reasons. Firstly, the starting time of the FluorSpec and PAR FluorPen measurements is slightly different, resulting in differences between the acquired incoming irradiance. Secondly, FluorPen measurements may not be always available due to the experimental purposes and set-ups, for example, when many other parameters need to be acquired at the same time with FluorPen. Therefore, FluorSpec data was used to model FluorPen PAR using the equation in Figure 2.7. For both crops, $SIF_{normalized}$ decreased during the measuring period (Figure 2.9). At the middle of the morning, although the ChF emission increases with PAR (Figure 2.8), normalized SIF strongly decreased because the stressed plant was not able to cope with the increasing light intensity. This decrease indicates that most of the incoming sunlight was not used for photosynthesis, which is consistent with observations in other work (Amoros-Lopez et al., 2008; Xu et al., 2018). According to Amoros-Lopez et al. (2008), in their study the fluorescence yield rose again in the late evening after 17:00, matching the decrease in the light intensity. In our study, the field experiments ended around 17:00 when the plants were still suffering from the heat wave and NPQ remained active. Although having similar declining trends, normalized SIF values of potatoes were lower than those of sugar beets. This could be caused by the different canopy structure (e.g. leaf angles and leaf size), physiological factors (different growth stages), or the combination of these or more factors. Since SIF represents a small amount of the radiance measured by the sensor, small differences in these factors can result in different performances of SIF and SIF normalization. Further research is needed to determine main reasons. The Photosystem II Quantum Yield (Qy) measured with the Fluorpen was used to validate the normalized SIF. The resulting high R^2 (0.81 for potatoes and 0.63 for sugar beets, Figure 2.10) for the relationship between Qy and $SIF_{normalized}$ shows that SIF normalized by PAR modelled from FluorSpec irradiance is a good indicator of crop photosynthesis. For sugar beets, the relationship between $SIF_{normalized}$ and Qy from 14:00 and 16:00 was seriously off and under the regression line (Figure 2.10). One possible explanation could be that the physiological response to the high light intensity and drought stress at the leaf level is different for different crops. For example, in the early afternoon, leaves of stressed sugar beet plants wilted more obviously than the stressed potato leaves. In addition, compared with potato plants, there were fewer sugar beet leaves in the FluorSpec footprint due to the larger size of sugar beet leaves. The FluorSpec captured SIF from fewer individual leaves compared to potato, which were less representative for the canopy SIF.

2.5.3 Diurnal cycles of UAV-based SIF

The value range and the diurnal cycle of UAV-based SIF proves the feasibility of the FluorSpec system to acquire SIF at the field level. The value range of FluorSpec SIF in the O_2-A band (Figure 2.11) is in a strong agreement with those from other UAV-based and airborne systems, which varies between 0~3 $mWm^{-2}sr^{-1}nm^{-1}$ depending on the characteristics of different target surfaces (Bendig et al., 2019; Garzonio, 2017; Rascher et al., 2015). Like SIF at the ground level, SIF derived from a UAV platform showed clear diurnal patterns both in a potato field and a sugar beet field. This further confirms the ability of a UAV platform to capture SIF changes diurnally at a low attitude. However, at the field level, potato SIF values from the 1st flight at 11:38 were slightly higher but close to those from the 3rd flight at 14:15, which was different from potato SIF changes at the ground level. This mismatch could be caused by the spatial scales. This is because that, at the ground level, the canopy structure within in the FluorSpec footprint, the solar zenith angle and the BRDF effect had a stronger influence on SIF values and its changes.

SIF of potato plants varied more than that of sugar beets (Figure 2.11). This could be a physiological difference, because the two crops were at different growing stages. Sugar beet was still growing in the 2018 survey period and had a dense fully mature canopy in late summer 2018. However, potatoes already approached senescence during the time of observation (beginning of August 2018). Despite the still green leaf material and a dense vegetation cover, the growing conditions of potato plants were less uniform compared to the sugar beet plants.

2.5.4. Limitations at the UAV level

Although the UAV-based FluorSpec system can capture the SIF signal and bridge the spatial gap with airborne SIF, some aspects of the study remain challenging. First, accurately geolocating the footprint of FluorSpec measurements is a challenge. This is a common problem for UAV-based point observations. An example is the study of MacArthur et al. (2014), in which their UAV platform not only lacked positioning and orientation of sensors but also the associated geometric processing workflow for an accurate ground projection of the spectroradiometer's FOV. UAV movements like pitch and roll caused variations of the footprint areas sampled by the non-imaging spectrometer at the ground (Garzonio et al., 2017). Similarly, Bendig et al. (2019) pointed out that it is challenging to obtain the weak SIF signal from a UAV-based QE-Pro spectrometer. In their study, the footprints between repetitive UAV flights spatially misaligned, which was also the case in our study. From Figure 2.11 we can see that flight lines did not always overlap perfectly and there was a recognizable spatial variation in the SIF values. One reason is that the flights were conducted without gimbal mounted to the UAV. The movements of the UAV (roll, yaw, and pitch) change the pointing directions of the two optics, resulting in non-nadir point observations. Also, the absence of an inertial measurement unit (IMU) made it less feasible to correct drone movements. The GPS sensors both on the drone and the FluorSpec sensor were not free of positioning errors, and thereby increased the uncertainty of the measurement locations.

In addition, the lean of the system caused by the UAV in-flight movements would also influence the downwelling irradiance measurements (Bendig et al., 2018, 2019), since the irradiance cosine corrector was not mounted on a gimbal. According to Bendig et al. (2019), when the flying speed is 2-3 m s^{-1} or even lower in low wind conditions (< 5.6 m s^{-1}), there is less need for motion correction. In our case, the flying speed was 3 m s^{-1} and the wind speed during the flights was less than 5.3 m s^{-1}. Therefore, in this study we ignored the influence from the system tilt on the irradiance. To address this problem in future studies, irradiance measurements taken before and after the flights can be averaged to replace the in-flight irradiance, since the flights are conducted under clear sky weather conditions. Alternatively, on a windless day, the tilting can average out over all the flight lines, and in that case the average of all irradiance spectra over the whole flight can be used.

Another drawback is that no validation data for the UAV-based SIF were available. We only have one QE-pro spectrometer and it was not feasible to collect ground-based and UAV-based field level SIF measurements at the same time or immediately after the flights as four flights were carried out within a day. As stated before, the UAV-based SIF values over canopies will be validated in a follow-up study by comparing it with a well-calibrated reference system, like the airborne HyPlant system.

2.5.5 Ways to improve the data quality of the UAV-based FluorSpec

This point-measuring UAV spectroscopy system can be improved in three aspects. First, a good flight mission plays a key role in improving SIF retrieval accuracy by acquiring high-quality data. Thus, the inputs into the ground station, such as the flight height and flight speed, should be carefully considered while designing the flight mission. For example, Garzonio et al. (2017) found that the lower flying altitude (10 m AGL) allows retrieving fluorescence in absolute units and a high-flying UAV setup (20 m AGL) enables the radiometric signal sampled during repeated measurements to be less subject to small changes of the platform location, roll and pitch angles. The decision of feasible flying parameters should take the scientific question and objective into account. Secondly, pairing the FluorSpec with a Real-Time Kinematic (RTK) enabled GNSS IMU device and installing the system on a stabilized gimbal could potentially improve the georectification accuracy down to centimetre-level positioning. Thirdly, a co-registered RGB camera can help to identify the footprint centre of the point measurements. RGB images can be processed by the Structure from Motion (SfM) algorithm (Westoby et al., 2012), which enables the reconstruction of the UAV orientation information (pitch and roll angles). RGB images can also support a visual identification of targets within the footprints and improve the understanding of SIF performance.

2.5.6 Suggestions on improving SIF comparison with other studies

Technical advantages of UAVs include the capability for highly customized deployments, quick response and turn-around for planning and investigation (Mohammed et al., 2019). Currently, more efforts are being invested in this research topic. For different UAV-based fluorescence measuring systems, protocols to acquire good and comparable measurements are necessary. This would allow testing different systems, combining data from different sensors (e.g. AirSIF, FluorSpec and HyUAS), and comparing SIF observations from different spatial scales with airborne SIF. According to our knowledge, some points can be added to the protocols. First, good and similar weather conditions are key to compare SIF values, since the SIF signal is weak and vulnerable to weather changes. Secondly, SIF is highly dynamic and sensitive, and thus a similar take-off time increases the reliability of the comparison. For instance, solar noon is a good time, as it can reduce the impact of solar angles. Thirdly, the flight pattern is also important. The two main flight modes are a hovering pattern and a continuous flying pattern. To obtain reliable data, the same flight mode should be applied all the time. In addition, a well-equipped UAV-based SIF measuring system is needed for an accurate geo-location of SIF measurements, e.g. with a gimbal and an IMU installed if possible.

2.6. Conclusions

This study demonstrated the system set-up and the processing chain of a novel UAV-based system, FluorSpec, to measure SIF at the O_2-A band for different crops at a low flying altitude. FluorSpec can collect high spectral resolution data, repeatedly over time, providing strong support for novel scientific approaches in monitoring crop photosynthetic activities and growth conditions (e.g. heat stress and drought stress), for instance within the context of precision agriculture. Within this application field it can be considered a flexible, low-cost system with clear potential.

The FluorSpec can acquire reliable spectral measurements after radiometric sensor calibration. The near-zero SIF values from the non-fluorescence emitting bare soil confirmed SSA-FLD's capability of disentangling the fluorescence signal from canopy reflectance. Ground-based SIF over potato and sugar beet canopies exhibited obvious diurnal patterns, and their differences demonstrated that SIF varied depending on the crop types. These differences could also be seen in the diurnal changes of the normalized SIF, the reliability of which was indicated by the good correlation with Qy. The fact that SIF is dominated by incoming irradiance but also influenced by other factors (e.g. heat stress) was further supported by the differences of diurnal SIF and PAR patterns and the decreasing trend of the normalized SIF. The great potential of a UAV platform to obtain SIF information at a low flying altitude and to combine this with airborne SIF products was proven by the reasonable value range of SIF at the field scale and the pronounced temporal dynamics of both studied crops. The variations shown in the same flight mainly due to the crop species, growth status and spatial heterogeneity were consistent with previous studies, which shows that the UAV-based FluorSpec system is a reliable system to measure actual SIF values.

In conclusion, the FluorSpec system, equipped with a cost-effective non-imaging instrument aboard a UAV, contributes to exploring crop SIF and photosynthetic activities in precision farming and upscaling the SIF measuring from the ground level to the field level by providing accurate, high resolution and flexible spectral measurements.

Chapter 3

UAV-based far-red sun-induced chlorophyll fluorescence plant canopy measurements for different crops

This chapter is based on:
Na Wang, Bastian Siegmann, Uwe Rascher, Jan G.P.W. Clevers, Onno Muller, Harm Bartholomeus, Juliane Bendig, Dainius Masiliūnas, Ralf Pude, Lammert Kooistra. "UAV-based far-red sun-induced chlorophyll fluorescence plant canopy measurements for different crops". *Under review.*

Abstract

Sun-induced chlorophyll fluorescence (SIF) is a direct indicator used for tracking the crop photosynthesis process, which is essential for estimating the crop growth status and for taking measures to increase crop yield. Unmanned Aerial Vehicles (UAVs) are flexible and cost-effective for acquiring SIF data at high temporal and spatial resolution. However, it is still unknown whether UAV-based SIF observations can provide reliable information within agricultural fields. To answer this question, in this paper the UAV-based point spectrometer FluorSpec was compared with the high-performance airborne imaging spectrometer HyPlant using diurnal far-red SIF measurements over different crop fields, which were acquired by almost simultaneous airborne and UAV flights during a clear sky day in 2019. After improving the footprint geolocation of FluorSpec measurements using concurrent red-green-blue (RGB) images, we compared the FluorSpec and HyPlant SIF measurements, their diurnal developments, and spatial distributions for different crop types. The results from both systems show consistent, clear diurnal patterns positively correlated with photosynthetically active radiation (PAR) over most crop types. Similar SIF spatial patterns were shown within crop fields as well. UAV-based FluorSpec SIF showed a good linear correlation with HyPlant SIF with an R^2 up to 0.76. The good agreement confirms that the UAV-based FluorSpec system is able to measure meaningful SIF values at the field scale and thus stimulates SIF applications in agriculture. This study further provides insights into the potential of UAV-based SIF to support SIF upscaling from small-scale field to airborne level.

3.1. Introduction

In the 21st century, global agriculture must produce more food to meet the rapid increase in food demand (Beddington et al., 2012). However, the quantity of photosynthesis places an upper limit to food production (Long et al., 2006). Photosynthesis is a complex physiological process depending on various biophysical processes and chemical reactions, and it is highly regulated by changing environmental conditions (Farquhar et al., 2001; Schurr et al., 2006; Turner et al., 2003). Thus, improving our knowledge on crop photosynthesis and the influence of various kinds of stresses is of the utmost importance for crop yield prediction and for taking management actions to increase yield. Solar quanta absorbed by plant chlorophyll are distributed in three competitive pathways, which consist of photosynthesis (photochemical quenching, PQ), heat dissipation (non-photochemical quenching, NPQ), and chlorophyll fluorescence (ChF). This unique functional connection to photosynthesis makes ChF a direct and powerful indicator of vegetation photosynthetic dynamics (Krause and Weis, 1991). Intensive studies at the leaf level have contributed significantly to our understanding of plant PQ and NPQ regulation mechanisms at the subcellular to leaf scales using active fluorometers (Cendrero-Mateo et al., 2016; Porcar-Castell et al., 2014; Zarco-Tejada et al., 2016, 2000). However, this approach of artificially exciting fluorescence is impractical over large distances and large areas.

Thus, the measurement of ChF excited by the sun as a natural source, sun-induced ChF (SIF), has been explored for remote sensing applications. SIF offers a unique possibility to monitor terrestrial vegetation photosynthesis from canopy to global scale (Tagliabue et al., 2019). During the last decades, innovative sensing efforts have shown the potential of SIF at the plant canopy level as an indicator of photosynthesis (Goulas et al., 2017; Pérez-Priego et al., 2015) and stress effects (Daumard et al., 2010; Xu et al., 2018). Ground-based setups usually range from a few metres to tens of metres above the canopy (Aasen et al., 2019; Gu et al., 2019; Mohammed et al., 2019; Campbell et al., 2019; Yang et al., 2018b), which can be used to track the diurnal and seasonal changes in SIF. However, most current systems have a high temporal resolution but lack the flexibility to monitor SIF at a large scale, e.g. at the field level for crop phenotyping research and crop management.

The potential of satellite-based SIF as an indicator of photosynthesis by monitoring global SIF patterns and dynamics has also been recognized (Frankenberg et al., 2011; Jeong et al., 2017; Joiner et al., 2013). Many studies have highlighted the strong relationship between SIF and gross primary productivity (GPP) (Guan et al., 2016; Sun et al., 2017; Wood et al., 2017;

Zhang et al., 2016). Some other studies have shown the potential of far-red SIF to indicate stress, e.g. temperature and water stress, and to track the dynamics of photosynthesis at ecosystem scale (He et al., 2020; Koren et al., 2018; Sun et al., 2015; Song et al., 2018; Yang et al., 2018a). One of the future Earth Explorer missions of the European Space Agency, the FLuorescence EXplorer (FLEX) mission, has been designed specifically to map vegetation fluorescence at local to ecosystem scales (Drusch et al., 2016). However, mixed pixel effects caused by the low spatial resolution of the satellite-based sensors (from hundred metres to tens of kilometres) are an unavoidable confounding factor for the space-based fluorescence signal interpretation (Colombo et al., 2018), especially within areas of high heterogeneity, such as small-scale farmlands.

Airborne systems can provide intermediate-scale observations (covering the spatial scale from metres to kilometres), allowing to map SIF at ecological and management-relevant scales (Rascher et al., 2015). This solution addresses spatial scaling issues from in-situ to satellite footprints and supports spatial measurements through enhanced validation and interpretation of satellite SIF. Case studies of airborne SIF have provided relevant and interesting insights into the spatial and spatio-temporal variability of SIF (Colombo et al., 2018; Rascher et al., 2015; Zarco-Tejada et al., 2013), SIF-based GPP estimates (Tagliabue et al., 2019; Wieneke et al., 2016; Zarco-Tejada et al., 2013), as well as stress detection, such as water shortages (Panigada et al., 2014; Wieneke et al., 2016), plant diseases (Zarco-Tejada et al., 2018), and herbicide stress (Rossini et al., 2015). An innovative combination between aerial observations and radiative transfer modelling approaches has been used to explore the effects of confounding factors on the scaling of SIF-GPP relationships (Damm et al., 2015), and to separate physiological effects from structural and leaf optical factors (Yang et al., 2019, 2020).

However, airborne platforms can be costly for measuring SIF at small-scale field level and therefore they lack the flexibility of measuring SIF at a high temporal resolution, for example, acquiring timely information on crop photosynthesis over the day and the season. As an alternative, unmanned aerial vehicles (UAVs) equipped with miniaturized and lightweight sensors offer efficient ways to monitor crop fields with high spatial and temporal resolution at a low flying altitude, e.g. to perform diurnal measurements for specific areas. This is of utmost importance to understand photosynthesis processes in plant phenotyping and precision agriculture (Tsouros et al., 2019), where measuring certain plant traits every few days and managing crop performance related to different crop varieties and management practices is needed.

To the best of our knowledge, only a limited number of studies have demonstrated the retrieval of SIF from UAV platforms (Vargas et al., 2020). A fixed-wing UAV equipped with a micro-hyperspectral imager has been applied to acquire SIF in orchards for detecting biotic/abiotic stress, e.g. water deficiency (Zarco-Tejada et al., 2013, 2012) and disease infection (Calderón et al., 2013; Zarco-Tejada et al., 2018). Garzonio et al. (2017) developed the HyUAS system, which could retrieve SIF at a low flying altitude (10-120 m) and showed that the accurate geo-location of spectra on a digital surface model greatly enhanced SIF interpretation. Maseyk et al. (2018) used the Piccolo Doppio spectrometer system to gain insight into canopy-level photosynthetic responses to CO_2 in a mature *Quercus robur* woodland. A case study of alfalfa and grass canopies was carried out with the AirSIF system by Bendig et al. (2020), in which sensor etaloning and platform motion correction was introduced to achieve accurate geolocation and footprint shape reconstruction of the SIF measurements. Chang et al. (2020) designed a new unmanned aerial system to simultaneously acquire SIF and hyperspectral reflectance for crop monitoring, where SIF acquired by this system was found to emulate and correlate well with that measured by a tower system. Recently, FluorSpec was introduced as a low-cost system for providing SIF measurements both at the canopy scale (ground-based) and at the field scale (UAV-based), and it was used to measure UAV-based SIF over different crop fields and to explore diurnal patterns and spatial distributions of crops within fields (Wang et al., 2021).

Beyond the valuable advances achieved so far, SIF measurements from UAV-based non-imaging spectrometers lack a robust validation (Vargas et al., 2020). Some studies validated UAV-based SIF products using ground truth (Chang et al., 2020; Bendig et al., 2020; Garzonio et al., 2017). However, robust validation of UAV -based SIF estimations up to now has been hindered by the spatio-temporal discrepancies of ground-based and UAV-based information, since their comparability is not fully resolved due to the differences of a few meters and/or minutes between sensor observations (Vargas et al., 2020). Well-characterized airborne SIF systems have the potential to test the ability of UAV-based methods of SIF retrieval at the field scale.

In this study, we compared the performance of the UAV-based FluorSpec and the airborne HyPlant systems in retrieving SIF over different crops. HyPlant is a high-performance airborne instrument specially designed to measure SIF and has provided spatial SIF information of different ecosystems in many airborne surveys (Rascher et al., 2015; Tagliabue et al., 2019, 2020; Wieneke et al., 2016). The experiment in this study enables comparing spatio-temporal far-red SIF patterns within agricultural fields, offering a more robust validation dataset for UAV-based data, than comparing with a single ground or tower-based reference data point. The two systems acquired data almost simultaneously four times following a diurnal pattern on one day over an agricultural area. The main goal was to assess the performance of the FluorSpec UAV-system in acquiring far-red SIF by comparing with the well-characterized airborne Hyplant system. Specifically, diurnal far-red SIF patterns and their spatial distributions were analyzed for different crop types.

3.2. Materials and methods

3.2.1. Study area

The study was carried out during the 2019 FLEX Sentinel Tandem Campaign (FLEXSense 2019) on a cloud-free day on June 26, 2019. The study site was located at the agricultural research station Campus Klein-Altendorf (CKA) that is affiliated with the University of Bonn (50°37' N, 6°59' E) and located near Rheinbach, in North Rhine-Westphalia, Germany. The analysis focused on an area of 1.5 ha covered with a variety of crops in different stages of development. The average altitude of the study site is 173 m above sea level, the average annual rainfall is 603 mm, and the mean annual temperature is 9.4 °C. On June 26, 2019, the maximum air temperature was 32 °C around 14:00 and the maximum wind speed was 3.9 m s^{-1}. Sunrise was at 5:20, solar noon around 13:40, and sunset at 21:50 Central European Summer Time (CEST). In this manuscript, all time indications refer to CEST.

In the overpass area of the FluorSpec system (Figure 3.1), the following crops were grown: winter wheat1 (*Triticum aestivum* L., sowing date: November 29, 2018), winter wheat2 (*Triticum aestivum* L., October 31, 2018), spring barley1 (*Hordeum vulgare* L., January 4, 2019), spring barley2 (*Hordeum vulgare* L., March 27, 2019), spring wheat (*Triticum aestivum* L., January 4, 2019), bean (*Glycine max* L., April 16, 2019), and maize (*Zea mays* L, May 31, 2019). For all crops, common field rotation practices were used.

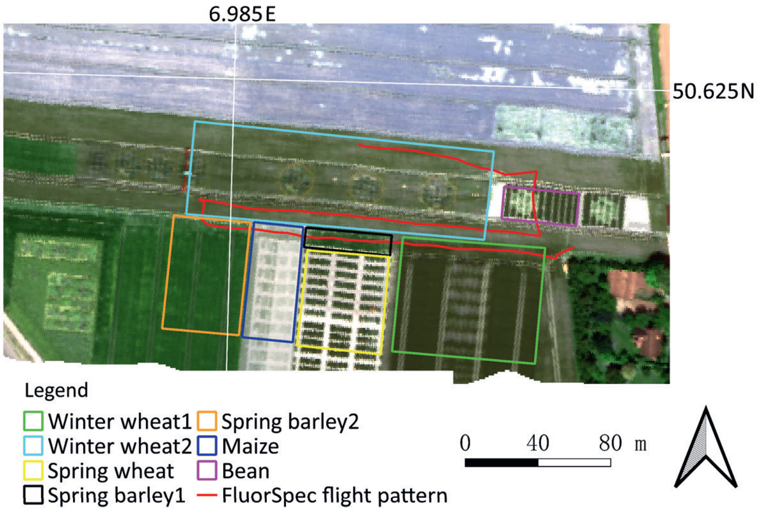

Figure 3.1. Overview of the study site (Campus Klein-Altendorf, Germany), the flight plan on June 26, 2019, and distributions of different crop types within the study area. The background image is a pseudo-RGB composite using three bands (665.6 nm, 560.7 nm, and 490.6 nm, respectively) of HyPlant DUAL data acquired at 12:58 CEST.

3.2.2. Field campaign

3.2.2.1. UAV measurements

The FluorSpec was flown over the study site under clear weather conditions on June 26, 2019. It can be used both as a ground-based SIF measurement device and as a UAV payload. The FluorSpec consists of a QE-Pro spectroradiometer (Ocean Insight, USA), a Global Navigation Satellite System (GNSS) receiver (Kendau), a laser rangefinder sensor (LightWare, Hungary), and a Sony A6000 RGB camera (Sony, Japan). The QE-Pro is a sub-nanometer spectral resolution point spectrometer, configured with two channels to measure the downwelling irradiance and the upwelling radiance in the wavelength range 630-800 nm, with a full-width-at-half-maximum (FWHM) spectral resolution of 0.3 nm and a spectral sampling interval of 0.15 nm. It covers both the O_2-A absorption band at 760 nm and the O_2-B absorption band at 687 nm that are needed for the SIF retrievals. The field-of-view (FOV) of the downward-looking radiance optics is 25°. The irradiance channel is equipped with a cosine corrector to collect solar irradiance from a hemispherical FOV (180°). The QE Pro is designed to stabilize the detector using a built-in thermoelectric cooler, keeping the detector temperature at -10°C. The actual temperature of the sensor (-10°C) is reported in the raw data file while the FluorSpec is acquiring data. The Sony RGB camera is a standard RGB-camera that is automatically triggered together with the spectroradiometer and records high-resolution images of 6000 × 4000 pixels (24 Megapixels). For more details on the FluorSpec system, see Wang et al. (2021).

The FluorSpec was mounted below a DJI S1000+ UAV platform (DJI, China, Figure 3.2), which is powered by 8 brushless electric motors that allow autonomous vertical take-off and landing, hovering over a target and high manoeuvrability during in-flight operations. The flight mission was planned with the universal ground control software (UgCS). The flight mission consisted of 6 waypoints. The UAV was programmed to a flying height of 20 m and a horizontal speed of 2 m s^{-1} from waypoint to waypoint. In this configuration, the spectroradiometer sampled a circular area with a diameter of 8.8 m on the ground for every measurement, with a sampling distance of 7 m (determined by the flight speed). This footprint size enabled capturing single crop observations within the partially narrow fields e.g. 20 m width while flying high enough the footprint would cover an area with several crop types in one flight (Figures 3.1, 3.3). The RGB camera captures an area of 30 × 20 m with a pixel resolution of 2.5 cm. The flight was repeated four times during the experimental day and the FluorSpec starting time flying over the study site was 10:35, 11:42, 13:15, and 15:32 CEST, respectively. Each flight lasted around 5 minutes while the FluorSpec passed over the study region of interest (Figure 3.1).

On the same day, a Phantom 4 RTK UAV (DJI, China) was flown over the study area at 40 m AGL. The imagery was collected with the built-in RGB camera at 1 cm ground resolution with a front overlap of 60 % and a side overlap of 40 %.

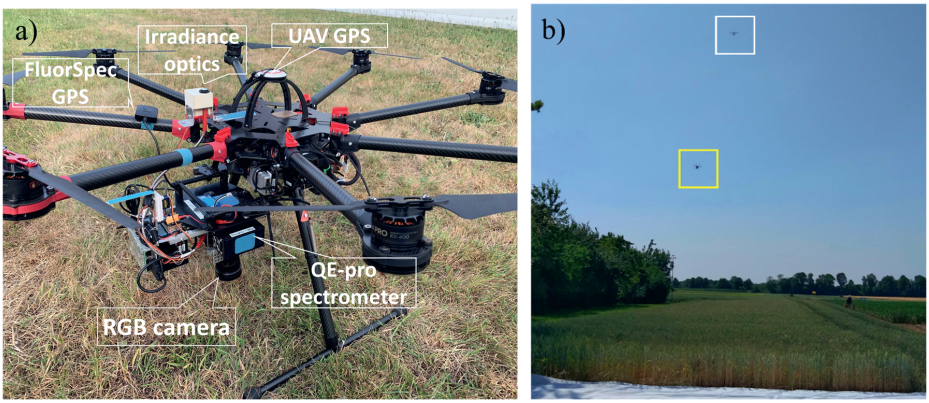

Figure 3.2. a) FluorSpec mounted below the DJI S1000+ octocopter UAV platform; b) UAV-based FluorSpec (in the yellow box) and HyPlant (in the white box) flying simultaneously over the study site (Campus Klein-Altendorf) on June 26, 2019.

3.2.2.2. Airborne HyPlant measurements

Four HyPlant flights were carried out under clear sky conditions over the study site on June 26, 2019, at 10:02, 11:32, 12:58, and 15:28 CEST with a flying altitude of 350 m, resulting in a spatial resolution of 1.0 × 0.5 m per pixel.

The HyPlant sensor is a high-performance airborne imaging spectroradiometer and was specifically designed for vegetation monitoring and to retrieve sun-induced fluorescence (Rascher et al., 2015). It consists of two modules: DUAL and FLUO. The DUAL module measures reflected radiance within the wavelength range of 380 to 2500 nm, with an FWHM of 3 nm in the visible and near-infrared regions and a spectral resolution of 10 nm in the short-wave infrared region. The FLUO module measures radiance from 670 to 780 nm, with a spectral resolution of 0.29 nm at the O_2-B (687 nm) and 0.28 nm at the O_2-A (760 nm) absorption bands. Such a high spectral resolution in the red and far-red spectral range enables fluorescence retrievals at the O_2-B and O_2-A absorption bands. Further technical details and sensor calibration are documented in Rascher et al. (2015) and Siegmann et al. (2019).

3.2.2.3. Auxiliary field data

After the 3rd overflight of the UAV, leaf area index (LAI) and relative chlorophyll concentration (Cab) were collected. For each crop field, an area of 1 × 1 m within or close to the areas sampled by FluorSpec was selected to measure LAI and Cab. Within each sample site, one LAI measurement was conducted using an LAI-2200C Plant Canopy Analyzer (LI-COR, USA) and five Cab measurements were acquired with a SPAD 502 Plus Chlorophyll Meter (Konica-Minolta, Japan). Each Cab measurement was an average from five random measurements collected from the top leaves of individual plants. SPAD-502 readings were converted to Chl concentrations using the calibration equations in Markwell et al. (1995) and Uddling et al. (2007). Photosynthetically active radiation (PAR) was measured by a weather station located within the area of CKA. This station continuously recorded meteorological data every 10 minutes.

3.2.3. Data processing

3.2.3.1. FluorSpec data preprocessing

The FluorSpec data processing chain from raw digital numbers (DN) to top of canopy (TOC) radiance ($Wm^{-2}\ sr^{-1}\ nm^{-1}$) includes four steps as described in detail in Wang et al. (2021). First, measured raw spectra were converted to at-sensor irradiance and radiance by removing the dark current, dividing by integration time, and multiplying the DN values with the radiometric calibration coefficient per wavelength. Second, laser rangefinder and the FluorSpec GNSS data were processed to obtain target-sensor distance and sensor position information, respectively. Next, the at-sensor irradiance and radiance were converted to their TOC equivalents by applying an atmospheric correction using the MODerate resolution atmospheric TRANsmission (MODTRAN6) algorithm (MODTRAN®, Spectral Sciences, Inc). Since in this paper the focus for SIF retrieval is on the O_2-A absorption feature, the adopted MODTRAN model implementation simulates the transmittance profile through the bottom 1 km of the atmosphere around the far-red 760 nm O_2-A feature. To get a useful transmittance for a specific UAV altitude, the simulated transmittance can be converted to different thicknesses of the atmosphere using the Beer-Lambert law. Preceding and following TOC irradiances are linearly interpolated using the GPS timestamp of the corresponding TOC radiance measurement to precisely get TOC irradiance at the same time as the TOC radiance measurement. More details are described in Wang et al. (2021).

3.2.3.2. Phantom RGB image processing

Using the acquired Phantom RGB images, an orthophoto was produced by photogrammetric processing with the software Metashape (AgiSoft LLC, Russia, Version 1.5.2), using 15 ground control points (GCPs) for exact geolocation. GCPs were measured with a Real Time Kinematic (RTK) GNSS. The final orthophoto had an overall accuracy of 1 cm.

3.2.3.3. Improved geolocation of the FluorSpec measurement footprints

Spatial characterization of a UAV non-imaging spectroradiometer footprint consists of footprint extent (e.g. shape) and location determination. According to Gautam et al. (2020), multiple instantaneous footprints merge and produce an elongated footprint of the spectroradiometer in case of a continuous flight mode. The integration time of the FluorSpec system is 500 ms and the log time in each radiance spectrum message is in the middle of the exposure. Therefore, for one SIF measurement during a single integration time, the time difference between the first and last instantaneous footprint is 250 ms, resulting in a 0.5 m distance between the first and last footprint centre with a flying speed of 2 m s^{-1}. Considering the large size of the FluorSpec footprints (8.8 m), we decided not to correct this elongation effect but applied a circular shape for simplicity. However, the FluorSpec system is not equipped with an RTK GNSS, so it has an estimated location accuracy of ~5 m. Therefore, simultaneously recorded RGB images were used to improve the radiance measurement footprint geolocation. The distance between the centre of the RGB camera lens and the centre of the radiance optics of the QE-Pro spectrometer was 13.5 cm and the viewing directions of both instruments were accurately aligned. Bendig et al. (2018) suggest that typical in-flight platform pitch and roll angles produce a zenith angle offset of up to 6° in low wind conditions for a comparable UAV system. If we assume that the zenith angle offset in our case was 6°, the projected distance on the ground between the centre of the RGB camera lens and the radiance optics was 13.6 cm. The influence of this projected distance for determining the relative location of the FluorSpec footprint in RGB images was negligible compared to the FluorSpec footprint size. Therefore, the footprint centre of the FluorSpec measurements was assumed to be the same as the centre of the corresponding RGB images.

To perform the geolocation correction, the FluorSpec RGB images were manually georectified by matching them with the Phantom 4 RTK orthomosaic. Afterwards, the centre coordinates of the FluorSpec RGB image determined in the previous step were assigned to the footprint locations of corresponding SIF measurements.

3.2.3.4. HyPlant FLUO data preprocessing

The HyPlant automated processing chain consists of several steps to process hyperspectral image cubes recorded by the FLUO module from raw data to TOC SIF maps. First, the FLUO raw data were converted to at-sensor radiance data (W m^{-2} sr^{-1} nm^{-1}), in which the dark frame subtraction, the radiometric correction of the image cube, the boresight correction, and the generation of the geographic lookup table file for the geometric correction were performed by the software CaliGeoPro (SPECIM, Oulu, Finland). Next, SIF was retrieved based on calibrated at-sensor radiance images. Afterwards, SIF maps were geo-rectified in the software CaliGeoPro using navigation information recorded by the global positioning system/inertial navigation system (GPS/INS) unit, which is also part of the HyPlant sensor system. For more information, the reader is referred to Siegmann et al. (2019). The positional accuracy of HyPlant SIF products after geometric correction was checked visually by comparison with the well-geolocated Phantom 4 RTK RGB orthomosaic image with a positional accuracy of 1 cm. HyPlant SIF maps were 1-2 pixels deviating geometrically from the RGB orthomosaic, resulting in a 1-2 m spatial uncertainty of HyPlant SIF images**.**

3.2.4. SIF retrieval methods

Top of canopy radiance $L_{toc}(\lambda)$ detected by sensors is a combination of true canopy reflected radiance (without fluorescence contribution) and emitted fluorescence radiance, which can be written as

$$L_{toc}(\lambda) = {}^{1}/_{\pi}\left(E_{toc}(\lambda)R'_{target}(\lambda)\right) + L_{fl}(\lambda) \tag{3.1}$$

where $E_{toc}(\lambda)$ is the TOC incident irradiance hitting the target, $R'_{target}(\lambda)$ is the apparent reflectance factor of the target without fluorescence effects, and $L_{fl}(\lambda)$ is the emitted fluorescence radiance.

The spectral fitting method (SFM) was used to retrieve SIF from HyPlant measurements. SFM was originally proposed by Mazzoni et al. (2012) and Meroni et al. (2010) and it is an advanced technique to decouple SIF and reflectance from high spectral resolution radiance observations. This method combines the atmospheric correction of the airborne data with the decoupling of reflectance and fluorescence based on the spectral fitting technique. SFM applies proper mathematical functions (Lorenzian, Gaussian or Voigt) to represent the apparent surface reflectance (linear, polynomial, or more complex piecewise cubic splines) and ChF within narrow spectral windows confined to the oxygen absorption bands. The parameters of the functions applied to represent $L_{fl}(\lambda)$ and $R'_{target}(\lambda)$ are optimized through a non-linear least square optimization process, by comparing the at-sensor radiance computed according to Equation 3.1 and instrument TOC observations, until the best match is found between the simulated and the observed radiance. For HyPlant FLUO data, SFM employs the Lorentzian function to model the fluorescence emission peak and polynomial or piece-wise cubic splines to fit the reflectance within the O_2-A spectral window of 750–780 nm (Siegmann et al., 2019). In this study, SIF at 760 nm was selected for the comparison with the SIF measurements by the FluorSpec.

For the FluorSpec instrument, the Spectral Shape Assumption Fraunhofer Line Discrimination (SSA-FLD) method as introduced by Wang et al. (2021) was used to retrieve SIF around the 760-nm oxygen absorption band of the FluorSpec measurements. SSA-FLD is a slightly adapted FLD-based approach to retrieve SIF and can use the ultra-fine spectral information within the oxygen absorption regions. It has two assumptions: (i) the fluorescence follows a known shape of the fluorescence spectrum; and (ii) the reflectance factor spectrum of the target object behaves linearly over the 760-nm oxygen absorption region. Thus, chlorophyll fluorescent radiance and true reflected radiance can both be split into a known spectral shape component and an unknown amplitude component. The unknown amplitude components are best solved using the full spectral information within the O_2-A spectral window. Therefore, SSA-FLD can be regarded as a special case of SFM. However, the general SFM function cannot be applied to UAV-based FluorSpec measurements directly without any parameter adjustment. The SFM algorithm applied to HyPlant measurements was specifically developed for the HyPlant system and inspired by the original version (Siegmann et al., 2019). Moreover, in a parallel study we compared the two methods, and they were strongly linearly correlated with an R^2 of 0.99 (Figure S3.1), which is referred to in Wang et al. (2021). Therefore, we decided to apply the SSA-FLD method to the FluorSpec data for retrieving SIF.

3.2.5. Comparison between the FluorSpec and HyPlant SIF

The comparison between FluorSpec and HyPlant SIF was carried out according to the following steps:

1. Circular footprints (8.8 m in diameter) of the FluorSpec measurements were created before the improved geolocation and after the improved geolocation.
2. SIF values of approximately 120 pixels of the HyPlant map falling within original Fluorspec footprints (before improved geolocation) and within footprints with improved geolocation were averaged as HyPlant SIF$_{\mathrm{original}}$ and HyPlant SIF$_{\mathrm{improved}}$, respectively. It was assumed that the spectroradiometer signal within a footprint polygon has a uniform distribution (Bendig et al., 2020; Garzonio et al., 2017).
3. FluorSpec SIF was compared with HyPlant SIF$_{\mathrm{original}}$ and HyPlant SIF$_{\mathrm{improved}}$, respectively, using a linear regression analysis. Scatter plots and the coefficient of determination (R^2) with p-values were used as indicators of the linear correlation between the two systems. Based on FluorSpec SIF and HyPlant SIF$_{\mathrm{improved}}$, root mean square error (RMSE), systematic error (bias), and the standard deviation of the random errors (σ_{ε}) were calculated to assess uncertainties in FluorSpec SIF measurements.

   $$Bias = \textstyle\sum_1^N (SIF_{HyPlant\_i} - SIF_{FluorSpec\_i})/N \tag{3.2}$$

   $$RMSE = \sqrt{\textstyle\sum_1^N (SIF_{HyPlant\_i} - SIF_{FluorSpec\_i})^2/N} \tag{3.3}$$

   $$\sigma_{\varepsilon} = \sqrt{RMSE^2 - Bias^2} \tag{3.4}$$

   Where N is the number of SIF observations, whereas $SIF_{HyPlant\_i}$ and $SIF_{FluorSpec\_i}$ are the HyPlant SIF and FluorSpec SIF values within the i$^{\mathrm{th}}$ footprint, respectively.
4. The follow-up steps were carried out based on FluorSpec SIF and HyPlant SIF$_{\mathrm{improved}}$. Spatial maps of the study area were generated to visually compare the SIF spatial patterns retrieved from FluorSpec and HyPlant. Diurnal patterns of SIF values were analysed for each crop type and for each overpass to evaluate the performance of the two systems.

3.3. Results

3.3.1. Improved geolocation of FluorSpec footprints

Figure 3.3 shows the change in the location of the FluorSpec measurement footprints projected on the ground before and after improved geolocation. For all flights, there was an obvious shift from the original flight path to the one with improved geolocation. The distance between the original and improved footprint centres varied for different flights, e.g. 2.58-8.15 m for the 2nd flight (11:32) and 0.24-2.77 m for the 3rd flight (12:58). The footprints after improved geolocation between repeated UAV flights misaligned spatially. For the flight path over the bean field, there was a large shift between the first flight and the other three flights. This is because during the 1st flight it was visually observed that the FluorSpec was flown over the edge between two bean plots. Since bean was one of the target crops, this flight path was adjusted by shifting the location of the fourth and fifth waypoint right after the 1st flight.

R^2 values of the linear regressions between the FluorSpec and HyPlant SIF before and after improved geolocation are presented in Table 3.1. These results show that SIF values from the two systems were more linearly correlated for flight 2 and 3 than for flight 1 and 4 whether the footprint correction was applied or not. The footprint correction improved the linear relationship between FluorSpec and HyPlant SIF for three flights as expected, but R^2 for the 3rd flight remained the same (Table 3.1). In flights 1, 2, and 4, the intercept decreased and slope increased after the improved geolocation, while these two coefficients did not show a significant change in flight 3.

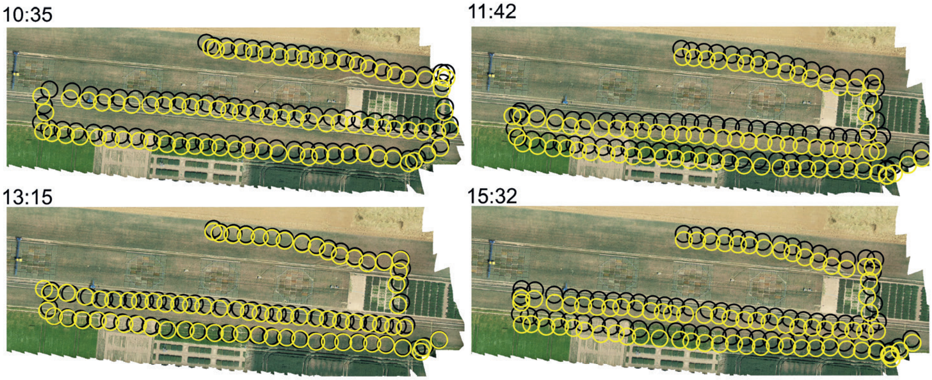

Figure 3.3. Ground projected footprints of the FluorSpec measurements before improved geolocation (circles in black) and after improved geolocation (circles in yellow). FluorSpec measurements were acquired at 10:35, 11:42, 13:15, and 15:32 CEST on June 26, 2019. The background map is the orthophoto image acquired by a Phantom 4 RTK UAV at 11:19 CEST on the same day.

Table 3.1. R^2, intercept (m), and slope of the linear relationships between FluorSpec SIF and HyPlant SIF before and after the improved geolocation and mean/minimum/maximum shift distance (m) of footprint centres of the FluorSpec measurements before and after the improved geolocation.

Flight	**Before improved geolocation**			**After improved geolocation**			**Shift distance**		
	R^2	Intercept	Slope	R^2	Intercept	Slope	Mean	Minimum	Maximum
Flight 1	0.54	0.21	0.68	0.65	0.17	0.82	3.11	1.61	5.45
Flight 2	0.73	0.39	0.90	0.76	0.32	0.99	4.77	2.58	8.15
Flight 3	0.71	0.30	0.99	0.71	0.31	0.98	1.56	0.24	2.77
Flight 4	0.48	0.49	0.63	0.68	0.30	1.00	3.94	1.57	5.57

3.3.2. SIF comparison between FluorSpec and HyPlant

3.3.2.1. Spatial variations of FluorSpec and HyPlant SIF

The spatial distribution of SIF derived from the two systems over the study site is shown in Figure 3.4. Overall, HyPlant SIF ranged from 0 to 2.4 mWm^{-2} sr^{-1} nm^{-1}. Within the flying area of the FluorSpec, HyPlant SIF values fell in the range of 0.0 to 1.75 mWm^{-2} sr^{-1} nm^{-1}. Both HyPlant and FluorSpec fluorescence show similar and clear patterns within different fields. Different crop types had different SIF values. Winter wheat1 and spring barley2 fields (Figure 3.1) exhibited higher SIF where the total canopy chlorophyll content (LAI × Cab) of the plants was larger (Table 3.2). Lower SIF values appeared in the maize field due to a low fractional vegetation cover (Table 3.2). At that time maize canopy was so sparse that its LAI could not be determined. In addition, SIF from both systems showed spatial variations within the same field. For example, for the 3rd flight within the winter wheat1 field, FluorSpec SIF varied from 0.65 to 1.28 mW m^{-2} sr^{-1} nm^{-1} and HyPlant SIF ranged from 1.06 to 1.49 mW m^{-2} sr^{-1} nm^{-1}.

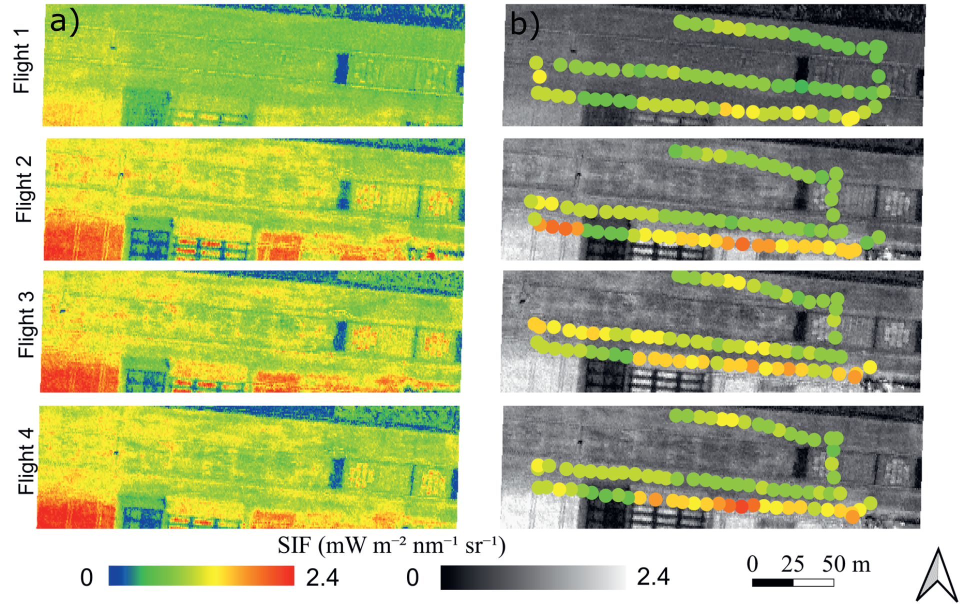

Figure 3.4. Diurnal and spatial patterns of a) HyPlant SIF, and b) FluorSpec SIF, both retrieved at 760 nm (O_2-A) at Campus Klein-Altendorf on June 26, 2019. The SIF maps in Figure 3.4 (column a) were obtained from HyPlant measurements at 10:02, 11:32, 12:58, and 15:28 CEST. In Figure 3.4 (column b), circles represent the FluorSpec SIF values within sampled areas acquired at 10:35, 11:42, 13:15, and 15:32 CEST, and the background maps are HyPlant SIF images in a grey colour scheme.

Table 3.2. Average leaf area index (LAI, $cm^2\ cm^{-2}$) values and relative chlorophyll content (C_{ab}) ($g\ m^{-2}$) of the six studied crop types.

Crop variety	Spring barley1	Spring barley2	Bean	Maize	Winter wheat1	Winter wheat 2
LAI	2.53	5.46	3.50	-	4.46	5.46
Cab	0.62	0.42	0.54	0.56	0.63	0.26
LAI×Cab	1.57	2.29	1.89	-	2.81	1.41

3.3.2.2. Diurnal dynamics of the FluorSpec and HyPlant SIF

Figure 3.4 shows the consistent diurnal patterns of SIF acquired by the two systems. Both the FluorSpec and HyPlant SIF show lower fluorescence values in the morning and higher fluorescence values around solar noon. However, within the spring barley2 field, SIF values acquired during the 2nd flight (11:32, hereafter flight time in brackets refers to HyPlant flight time) were highest among all flights due to a closed vegetation canopy within the footprints in comparison to the other flights where the footprint partially contained soil information from the headland of the field. Some SIF measurements from the 2nd and 4th flights (11:32 and 15:28) in part of the winter wheat1 field were also higher than those from the 3rd flight (12:58).

The diurnal dynamics of SIF over the six crop types were analysed in more detail in Figure 3.5. During the measuring day, both the FluorSpec and HyPlant SIF showed similar diurnal trends for the same crop type and this diurnal change was consistent with the overall trend shown in Figure 3.4. For most crops, SIF developed in an expected diurnal pattern, similar to that of PAR, including two winter wheat varieties, spring barley1, and bean, while this diurnal pattern was more pronounced for the HyPlant system. Maize and spring barley2 showed a deviating pattern. For both systems, the diurnal SIF of spring barley2 presented a sine-like curve, where SIF reached the highest values around noon, decreased around 13:00, and increased again slightly around 15:30. In maize, the lowest SIF was observed around noon, contrary to the overall trend of the other crop types. Furthermore, some differences between the two systems could be observed. For the FluorSpec, among all varieties, the mean SIF values over winter wheat1 were highest over the day except for flight 2 where spring barley2 had the highest SIF value. For HyPlant spring barley2 presented the highest mean SIF, except for flight 3 where its mean SIF values were close to those for winter wheat1. Overall, winter wheat1 showed higher SIF values than winter wheat2 for both platforms, which coincides with the larger canopy chlorophyll content (LAI × Cab) as can also be observed in Figure 3.4. Similarly, spring barley2 had higher SIF and higher canopy chlorophyll content than spring barley1. Beans had similar SIF as winter wheat2, although structurally they are different crops and had different canopy chlorophyll contents.

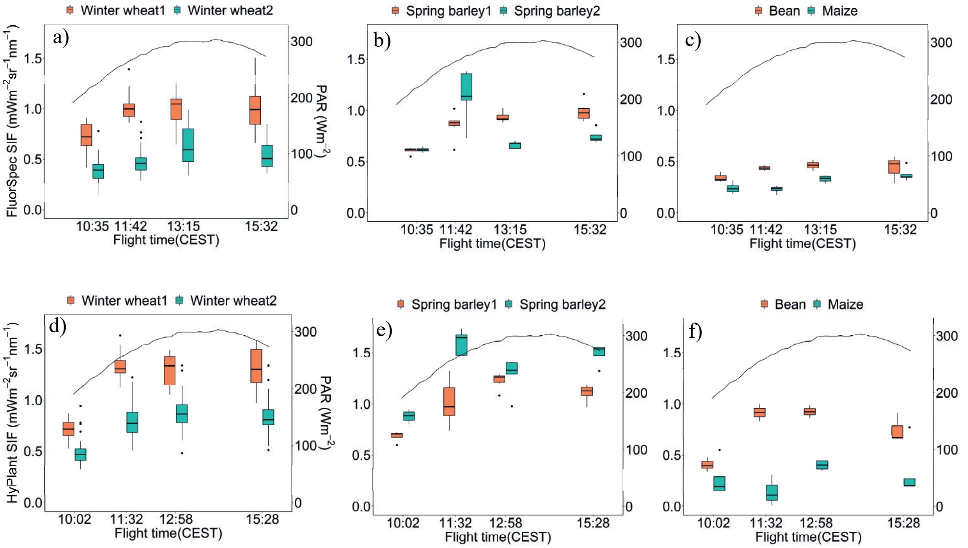

Figure 3.5. Diurnal patterns of a) ~c) FluorSpec SIF and photosynthetically active radiation (PAR) over the six crop varieties, and d) ~e) HyPlant SIF and PAR over the six crop varieties, grouped by crop type for four flights carried out on June 26, 2019, in Campus Klein-Altendorf. PAR data were taken from a weather station in Campus Klein-Altendorf.

3.3.2.3. Statistical relationships between FluorSpec SIF and HyPlant SIF

The relationship between FluorSpec SIF and HyPlant SIF was further evaluated using the RMSE, bias, and standard deviation of random effect (σ_{ε}) (Table 3.3). Flight 2, 3, and 4 had similar RMSE, bias, and σ_{ε} values. In contrast, the three statistics of flight 1 were lower, particularly for RMSE and bias, due to the narrower value range, i.e. lower far-red SIF, compared to flights 2-4. The positive bias shows that the airborne SIF values were systematically higher than the UAV-based SIF values and is generally larger than the random error contribution from σ_{ε}. This effect can be seen as well in the scatterplot of Hyplant SIF and FluorSpec SIF for each flight, where datapoints for flight 1 are closer to the 1:1 line compared to flights 2-4 (Figure 3.6). For all flights, SIF from the two different systems not only had a significant relationship (p-value < 0.001), but also were correlated well, with R^2 ranging from 0.65 to 0.76. Flight 2 had the highest R^2 (0.76), followed by flight 3 (0.71). The data points below the trend line in the bottom-left part of the scatterplot were located in the young maize field, which had a low vegetation coverage.

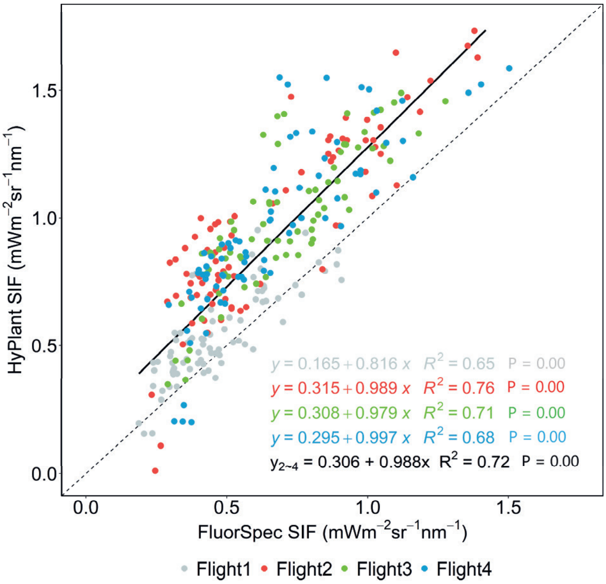

Figure 3.6. Linear relationships of the FluorSpec SIF and HyPlant SIF for the four flights over Campus Klein-Altendorf (CKA) on June 26, 2019. The linear equations per flight are listed in color and the equation for the combined SIF from flights 2, 3, and 4 is shown in black. FluorSpec UAV data were acquired at 10:35, 11:42, 13:15, and 15:32 CEST. HyPlant data were collected at 10:02, 11:32, 12:58, and 15:28 CEST.

Table 3.3. RMSE, bias, and standard deviation of random effect (σ_ε) between HyPlant SIF and FluorSpec SIF after the improved geolocation of the FluorSpec footprints. RMSE, bias, and σ_ε are shown in the unit of mWm^{-2} sr^{-1} nm^{-1}.

Statistics	Flight1	Flight2	Flight3	Flight4
RMSE	0.137	0.350	0.328	0.346
Bias	0.076	0.302	0.293	0.293
σ_ε	0.114	0.177	0.147	0.184

3.4. Discussion

3.4.1. Geometric accuracy

Accurate spatial characterization and geolocation of UAV observation footprints are essential to unravel the origin and spatial variability of optical signals acquired within the extent of airborne and satellite pixels (Gautam et al., 2020). It is critical to precisely locate both the

UAV-based and airborne SIF measurements before any comparison can be made. According to Siegmann et al. (2019), the positioning and orientation information recorded by an Oxford GPS/INS unit is used for the geometric correction of HyPlant data. This led to a precise internal image geometry with only minor deviations of less than 2 pixels. According to Siegmann et al. (2019), the absolute geometric accuracy of HyPlant imagery may be improved in the future by a high-resolution RGB snapshot camera, which has been operated in the aircraft together with HyPlant. In this study, the geometric accuracy of HyPlant SIF maps was evaluated by visually comparing them to a Phantom 4 RTK-based orthomosaic, which had a precise geometric accuracy (1 cm). HyPlant SIF maps had a high absolute positioning precision with maximum deviations of 1-2 pixels and the positioning error should thus be 1- 2 m, with the pixel size of 1 × 0.5 m.

Spatial uncertainties in UAV-based FluorSpec measurements could originate mainly from GNSS inaccuracies and the in-flight movements of the UAV. Firstly, UAV movements, i.e. pitch and roll, caused deviations in the spatial extent (e.g. shape and size) and the spatial location of the footprint areas sampled by the QE-Pro point-based spectrometer projected onto the ground (Garzonio et al., 2017; Gautam et al., 2020). According to Bendig et al. (2020), when flying with a speed lower than 3 m s^{-1} in good wind conditions (< 6.1 m s^{-1}), the in-flight movement correction of UAV pitch and roll angles has little effect on SIF retrieval. In our case, the UAV flew at a speed of 2 m s^{-1} and the maximum wind speed was 4 m s^{-1}. Therefore, we chose not to carry out UAV movement correction. In addition, the elongation of the FluorSpec footprint did not need to be corrected as the distance between the first and last footprint centre of one measurement (0.5 m) could be ignored compared to the footprint size with a diameter of 8.8 m. Secondly, there were two GNSS units included in the UAV-based FluorSpec system. The GNSS of the UAV guided the aircraft to the waypoints and the FluorSpec GNSS recorded the positional information, which is used for the initial positioning of the FluorSpec SIF observations. Both GNSS instruments have positioning errors, resulting in an uncertainty of the measurement location. In the future, FluorSpec could be paired with a Real-Time Kinematic (RTK) enabled GNSS IMU device and be installed on a stabilized gimbal to improve the georectification accuracy down to centimeter-level.

A co-registered RGB camera helps to identify the footprint centre of the point measurements. Garzonio et al. (2017) and Gautam et al. (2020) used the digital surface model (DSM) created with co-registered RGB images using the structure-from-motion (SfM) technique (Mancini et al., 2013; Ullman, 1979) to assist an accurate geo-location of a non-imaging sensor mounted on a multirotor UAV platform. In this study, high-resolution RGB photos from the camera on the UAV were used to support the footprint geolocation of the FluorSpec measurements. However, due to the short battery life, the low flying speed, and the flying height of the UAV, it was not feasible to both acquire SIF over a larger area (several fields with different crops) and at the same time guarantee a large side overlap of the RGB images. As a result, photogrammetry software like Agisoft Metashape or Pix4D could not be used to process these RGB images from the FluorSpec. This problem was solved by using the Phantom 4 RTK photos to meet the requirements of photogrammetry (see section 3.2.3.2 for details). As explained in section 3.2.3.3, the footprint centre of the FluorSpec measurement could be assumed to be the same as the centre of the corresponding RGB image. Therefore, it was feasible to manually correct the geolocation of the FluorSpec footprint.

The improved geolocation of the FluorSpec footprint enhanced the linear correlations between the FluorSpec and HyPlant SIF values for all flights (Table 3.1), indicating that the geolocation correction improved the spatial accuracy of the FluorSpec footprints. The mean R^2 increased from 0.62 to 0.70, which proves the feasibility of the geolocation method and confirms the importance of accurate footprint geolocation of the non-imaging FluorSpec measurements. However, the increase in R^2 varied for different flights. We consider the distance between the original and the corrected footprints to be a major reason. Firstly, the R^2 improved considerably for flight 1 and 4 by 0.11 and 0.20, respectively. The average shift distance between footprint centres before and after improving geolocation was 3.11 m and 3.94 m, respectively (Table 3.1), resulting in different HyPlant pixels falling within these footprints. The improved geolocation of the footprints did not lead to a higher linear correlation for the 3rd flight. This is mainly ascribed to the shorter distance (maximum 2.77 m) between the original and corrected footprints. The sampled areas of the FluorSpec before and after geolocation correction for this flight largely overlapped, which can be seen in Figure 3.3. Interesting is that for the 2nd flight, R^2 only rose by 0.03 despite the largest maximum shift distance of 8.15 m, which emphasizes the necessity to have improved geolocation of the footprint for a UAV-based point sensor, even though the linear relationship between the FluorSpec and HyPlant SIF was not improved distinctly.

3.4.2. SIF retrieval and comparison

In this study, SIF values derived from FluorSpec and HyPlant within FluorSpec footprints fell in the range of 0 to 1.75 mW m^{-2} sr^{-1} nm^{-1}, which was in accordance with the expected value range of remotely retrieved SIF (Siegmann et al., 2019). Comparison of SIF values from the two systems showed similar spatial patterns (Figure 3.4), consistent diurnal changes (Figures 3.4 and 3.5), and a strong linear correlation (Figure 3.6).

All flights performed using the two systems showed similar spatial patterns (Figure 3.4), where winter wheat1 and spring barley2 crops had higher SIF among all crops, while the maize field exhibited the lowest values. The meaningful spatial patterns constitute a direct proxy of the vegetation functional state (Rascher et al., 2015; Wieneke et al., 2016; Tagliabue et al., 2019). However, SIF observations from remote sensing are sensitive to crop structure (e.g. LAI and leaf orientation), biochemical constituents (e.g. Cab), illumination condition, sun-target-viewing geometry (Pinto et al., 2017; Lu et al., 2020), and physiological status (Van der Tol et al., 2016; Verrelst et al., 2015). The first three factors jointly determine the amount of radiative energy absorbed by plants, and the first two can affect the scattering and reabsorption of SIF within the canopy. For example, far-red SIF in the observation direction is strongly affected by canopy structural variation due to canopy scattering (Migliavacca et al., 2017; Porcar-Castell et al., 2014). Changes in sun-target-viewing geometry influence the BRDF effect on directional SIF observations (Zhang et al., 2018). Finally, physiological status regulates the partitioning of absorbed solar energy into the three pathways, as mentioned in the introduction (PQ, NPQ, and ChF). In this study, the variations of SIF could be partly explained by LAI, Cab, and the product of both (LAI × Cab) (Table 3.2). Observed SIF is a joint result of multiple factors, which is indicated by low SIF values in the maize field with high Cab and in the winter wheat2 field with high LAI. Agricultural fields with a higher product of Cab and LAI (e.g. winter wheat1 and spring barley2, as seen in Table 3.2) usually exhibited higher SIF. In addition, some other structural factors such as the leaf angle distribution (e.g. planophile, erectophile, and spherical) and the structure of the canopy (horizontal or vertical) could have an influence on the canopy scattering of SIF and sun-target-view geometry within different crop fields. It should be noted that only one LAI measurement per crop type is a limitation of the study, which may affect the interpretability of SIF in relation to LAI due to a lack of information about the spatial variability of LAI.

Figure 3.5 also shows a clear difference in SIF for different crop varieties, e.g. spring barley 1/2, which differed in genetic varieties and sowing time, indicating the potential of SIF for crop phenotyping. Both FluorSpec and HyPlant SIF showed diurnal trends as expected over most crop types, consistent with the diurnal changes of the incoming PAR (Figure 3.5). Incidental lack of a clear diurnal pattern for some crops could be potentially explained by the geometry difference within the FluorSpec footprint as the same flight path of different flights did not completely overlap. For instance, for both systems during flight 2, spring barley2 had the highest SIF values over the day, while the maize SIF was the lowest. This could be largely attributed to crop canopy structure. The areas within the spring barley2 field sampled by FluorSpec had high LAI, while areas within the very sparse maize field (Figure 3.3) had a weak vegetation signal that included more bare soil, and a strong effect of structure (shadows, leaf angles, and gap fractions) would contribute to lowering the SIF values. A model-based study (Verrelst et al., 2015) showed, a large part of the variability in SIF was related to variations in LAI and leaf angle distribution (LAD). Another possible reason could be angular dependencies of SIF (Van der Tol et al., 2009; Zhang et al., 2020; Pinto et al., 2017). The angles between the sun, the target, and the sensor in a continuous mapping mode were changing with flight movements, which changed fractions of sunlit and shaded leaves within the FOV of a sensor (He et al., 2017), contributing to the bidirectionality of SIF observed by the sensor (Biriukova et al., 2020). More investigation addressing angular effects in SIF is needed, as variations in sun-target-viewing geometries affect directional SIF interpretation, particularly for diurnal flights.

Further consistency of HyPlant and FluorSpec SIF was indicated by the linear models shown in Figure 3.6. Except for the first flight before mid-day, slopes and intercepts of the regression equations, as well as bias and σ_ε for the last three flights, were similar. The similar linear regression coefficients for these flights underline the stable performance of the FluorSpec to capture SIF at a low flying altitude and indicate its high capacity to assist the interpretation of airborne SIF measurements. The larger difference in flight1 may be due to the mismatch in flying time (30 mins), which would change the illumination geometry, e.g, solar zenith angle (SZA), which in turn would cause variations in sun-canopy-sensor geometry and further affect directional SIF observations.

Relating SIF values from both systems (Figure 3.6, Table 3.3) not only shows a strong linear relationship but also a strong bias between the two measurement systems (particularly for the flights at mid-day). HyPlant-derived fluorescence values were overall higher than the FluorSpec-derived fluorescence. For the last three flights, HyPlant SIF was consistently about 0.3 $mWm^{-2}\ sr^{-1}\ nm^{-1}$ higher than FluorSpec SIF. According to Tagliabue et al. (2019), HyPlant SIF was also shown to exhibit higher values than the ground-retrieved SIF values over different canopies within a sampling area of 1.7 - 2.3 m diameter, with a bias of 0.26 $mW\ m^{-2}\ sr^{-1}\ nm^{-1}$. In our study, this systematic offset between the two systems ranged from 0.076 to 0.302 $mW\ m^{-2}\ sr^{-1}\ nm^{-1}$. The last three flights had almost the same difference in the average SIF between the two systems, which was around 0.29 mW m^{-2} sr^{-1} nm^{-1}. The 1st flight had an average mean SIF difference of 0.076 mW m^{-2} sr^{-1} nm^{-1}, which we consider to be realistic and related to a short time delay between data acquisitions. The FluorSpec flight was performed roughly 30 minutes after the HyPlant flight, and the incoming irradiance increased rapidly from 190 to 220 W m^{-2} due to a higher sun elevation angle, resulting in higher SIF values acquired by the FluorSpec. Bias values were much larger than the random error components (Table 3.3), indicating that most of the uncertainties in FluorSpec measurements are systematic and can be accountable. Several reasons could account for the constant difference. Firstly, the FluorSpec is equipped with a point spectrometer while HyPlant has an imaging sensor. Although both sensors were well calibrated (Rascher et al., 2015; Wang et al., 2021), the technical differences in the spectral sampling interval (SSI), signal-to-noise ratio (SNR), FWHM, point-spread function (PSF), and field of view (FOV) could have caused variations in the raw spectra and form the basis for the subsequent SIF retrieval differences (Cendrero-Mateo et al., 2019; Pacheco-Labrador et al., 2019). Secondly, SFM and SSA-FLD were applied to retrieve HyPlant SIF and the FluorSpec SIF, respectively. Different interpolation strategies to estimate fluorescence and reflectance at wavelengths affected by O_2 absorption could lead to some uncertainties (Cendrero-Mateo et al., 2019). SFM applies the Lorentzian function to model the fluorescence emission peak and polynomial or piece-wise cubic splines to fit the reflectance within the O_2-A spectral window of 750-780 nm, while SSA-FLD assumes that the fluorescence follows a known shape of the fluorescence spectrum and employs a linear function to model the reflectance factor within the 750-780 nm interval. It is recommended to use the same methods to retrieve SIF from different systems for more robust conclusions. In addition, different flight heights of two platforms and different atmospheric correction schemes would also contribute to our reported agreement and disagreement of SIF from UAV and HyPlant. These aforesaid factors are worthy to be further explored in future studies.

The consistent performances between HyPlant and FluorSpec SIF confirm the capability of the UAV-based FluorSpec to measure reliable SIF values. This finding enables UAV-based SIF to provide valuable information to facilitate the elucidation of mechanistic relationships between photosynthesis and SIF at the field level and for real-time crop monitoring, e.g. crop stress detection. The good agreement achieved between these two systems also highlights the potential of UAV-based SIF to provide complementary information to airborne SIF and bridge the existing gap between small-scale field and airborne observations, which thereby further support the interpretation and validation activities of satellite-based SIF, e.g. the upcoming FLEX satellite.

3.5. Conclusions

The goal of this paper was to evaluate SIF measurements from a UAV-based non-imaging spectrometer (FluorSpec) in comparison to SIF observations from the high-performance airborne HyPlant system. By comparing SIF of different crops recorded by the UAV-based FluorSpec system and SIF retrieved from the airborne imaging spectrometer HyPlant, we found a strong linear relationship (R^2 up to 0.76), consistent diurnal patterns over different crop canopies, and similar spatial variations within crop fields. However, FluorSpec recorded systematically higher far-red SIF of up to 0.3 mW m^{-2} sr^{-1} nm^{-1}, indicating that quality of geometric co-registration, technical differences of the sensors, sun-target-viewing geometry, and SIF retrieval algorithms affect far-red SIF measured from different platforms, and have to be either improved or corrected for. Our results prove the capacity of the UAV-based FluorSpec as a flexible and cost-effective system to measure reliable SIF in absolute values at a low flying altitude. The findings further indicate the potential of UAV-based SIF for plant phenotyping and precision farming and to facilitate the versatility and flexibility for SIF analysis at different spatial and temporal scales.

SUPPLEMENTARY MATERIALS

SSA-FLD and SFM

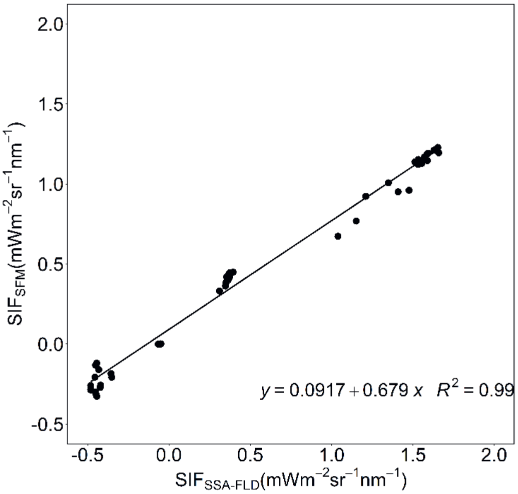

Figure S3.1. The linear relationship between SSA-retrieved and SFM-retrieved far-red SIF over vegetation targets (low green grass and green winter wheat) and non-fluorescence targets (bare soil and 99% white panel).

Chapter 4

Potential of UAV-based sun-induced chlorophyll fluorescence to detect water stress in sugar beet

This chapter is based on:
Na Wang, Jan G.P.W. Clevers, Sebastian Wieneke, Harm Bartholomeus, Lammert Kooistra "Potential of UAV-based sun-induced chlorophyll fluorescence to detect water stress in sugar beet". *Under review.*

Abstract

Sun-induced chlorophyll fluorescence (SIF) is considered a direct measurement of the functional status of photosynthesis and can potentially indicate plant physiological changes caused by water stress. Unmanned Aerial Vehicles (UAVs) are flexible and cost-effective options to acquire SIF data at a high temporal resolution. The direct effect of water stress on the SIF response in agricultural crops at the field level still needs further research in order to clearly understand the involved mechanisms. In this study, we assessed whether UAV-based SIF can detect water deficit within a sugar beet field. We acquired SIF measurements at the oxygen absorption bands A (760 nm, SIF_{760}) and B (687 nm, SIF_{687}) over irrigated and non-irrigated sugar beet plots using a UAV platform. SIF normalized by photosynthetically active radiation (PAR) ($SIF_{760norm}$, $SIF_{687norm}$) and SIF normalized by absorbed PAR ($SIF_{760yield}$ and $SIF_{687yield}$), and the ratio between SIF_{687} and SIF_{760} (SIF_{ratio}) were evaluated for water deficit detection. To better interpret the response of SIF indices to water stress, additional UAV-based hyperspectral and thermal data were acquired. We found that $SIF_{760norm}$, $SIF_{687norm}$, $SIF_{687yield}$, and SIF_{ratio} showed a significant response to the recovery of sugar beet after irrigation (p-value < 0.05) on June 28 when sugar beet plants were exposed to water stress. On the other hand, only $SIF_{760norm}$, $SIF_{687norm}$, and SIF_{ratio} weakly tracked the changes induced by the irrigation (p-value < 0.1) on July 24 when both water stress and heat stress affected the crop. Differences in response to irrigation were found between SIF indices at 760 nm and at 687 nm on both dates. The findings of this study suggest that SIF indices could potentially indicate water stress at field level, but its value to detect the changes of photosynthetic activity under severe stress might be limited and needs more investigation.

4.1. Introduction

Due to changing climate, water shortage for plants (water stress) has been exacerbated by reduced rainfall and changed precipitation patterns (Lobell et al., 2011). Water shortage causes physiological, biochemical, and morphological changes that induce a reduction in photosynthesis and thus is a critical abiotic stressor limiting crop growth and yield and is therefore threatening global food security (Lesk et al., 2016). For better management and minimizing harmful effects on crop production, it is critical to detect water stress timely and accurately.

Remote sensing provides spatiotemporal monitoring of crop structural, biochemical, and physiological changes induced by water stress at different scales (Atzberger, 2013). Vegetation indices (VIs) are sensitive to changes in crop canopy structure, leaf pigments, or leaf water content under water stress conditions and may serve as indicators of water stress (Govender et al., 2009; Zarco-Tejada et al., 2013). However, most VIs cannot reveal physiological responses to environmental stressors. This is because they lack a direct connection with photosynthetic functioning. As a result, greenness-based VIs cannot capture short timescale changes (Xu et al., 2021). Therefore, Calderón et al. (2013) suggested that structural and pigment indices were good only to assess damage. Plants can be irreversibly affected before visible symptoms of water stress appear (Jones and Schofield, 2008; Mahajan and Tuteja, 2005). To avoid severe crop damages, a pre-symptomatic or pre-visual detection of plant physiological changes can essentially contribute (Chaerle and Van Der Straeten, 2000). The photochemical reflectance index (PRI) can indicate the short-term changes in xanthophyll pigments under stress conditions (Gamon et al., 1992; Gamon et al., 1997), thus it can be a potential pre-visual indicator of water stress. However, PRI has been shown to be strongly affected by canopy structure and leaf pigmentation (Gitelson et al., 2017). The initial plant response to water stress is stomatal closure to prevent water loss via transpiration (Chaves et al., 2002; Jones and Schofield, 2008), resulting in an overall increase of plant leaf and canopy temperature compared to a well-watered plant. Thermal remote sensing of leaf and canopy temperature has therefore become an established method to detect pre-visual water stress (Jackson et al., 1981; Maes and Steppe, 2012). However, the major limitation of the temperature-based approach is that the use of leaf or canopy temperature values alone cannot directly estimate the physiological status of plants (Gerhards et al., 2019).

Plant photosynthesis is one of the key physiological phenomena which is strongly affected by water stress (Chaves et al., 2002; Farooq et al., 2009). Annual broadleaf crop photosynthesis is in particular sensitive to moisture stress due to leaf stomatal closure, improper photosynthetic machinery, reduced leaf expansion, and decreased leaf pigment concentration, resulting in strong downregulation of photosynthesis (Fu and Huang, 2001; Wahid et al., 2007). However, photosynthesis is a complex physiological process depending on various biophysical parameters and chemical reactions, and it is highly regulated by changing environmental conditions (Farquhar et al., 2001; Schurr et al., 2006; Turner et al., 2001).

Chlorophyll fluorescence (CF) is considered a direct and powerful measurement of the functional status of photosynthesis (Lichtenthaler and Rinderle, 1988). Light energy absorbed by plant chlorophyll has three main dissipating pathways, which consist of photosynthesis (photochemical quenching, PQ), heat dissipation (non-photochemical quenching, NPQ), and fluorescence emission in a wavelength between 650-800nm characterized by two peaks at approximately 685 and 740 nm. Any alteration in the efficiency of one of the pathways can affect the other two (Porcar-Castell et al., 2014). Sun-induced CF (SIF), a continuous emission signal from photosystem II and I, has been intensively studied to further understand vegetation photosynthetic activities on a large scale (Frankenberg and Berry, 2018; Goulas et al., 2017; Guanter et al., 2021; Pérez-Priego et al., 2015; Rascher et al., 2009; Yang et al., 2015). Physiological responses of SIF during stress have been explored at ground level (e.g. Helm et al., 2020; Marrs et al., 2020; Paul-Limoges et al., 2018; Xu et al., 2018), at airborne level with medium- or high-altitude systems (e.g. Camino et al., 2018; Gerhards et al., 2018; Panigada et al., 2014; Pinto et al., 2020; Wieneke et al., 2016; Zarco-Tejada et al., 2012), and at ecosystem scale using satellite observations (e.g. Chen et al., 2021; Lee et al., 2013; Sun et al., 2015; Wang et al., 2019; Yoshida et al., 2015).

Ground-based SIF measurements (e.g. tower-based) cannot assess spatial variation in SIF within the crop field. Although medium- or high-altitude airborne-based measurements can provide valuable spatial information on stress levels over a particular study area, these platforms are costly, and they lack the flexibility of measuring SIF at a high temporal resolution. As an alternative, unmanned aerial vehicles (UAVs) offer cost-efficient ways to monitor crop fields with high spatial and temporal resolution at a low flying altitude. This low-cost approach also provides an option to bridge the gap between in situ and airborne observations, enhancing stress detection at different spatial scales. Therefore, low-altitude UAV-based SIF can be of great potential for monitoring water stress within crop fields.

The SIF signal is relatively small compared to reflected sunlight (about 1- 5% in the near-infrared region, NIR) and is affected by various factors such as physiological status (Porcar-

Castell et al., 2014), canopy structure (Dechant et al., 2020), biochemical constituents (Verrelst et al., 2015), illumination condition (Van der Tol et al., 2016), and sun-target-viewing geometry (Lu et al., 2020; Pinto et al., 2017). In addition, plant response to water stress is expressed by a variety of physiological changes (e.g. stomatal behaviour, and leaf water content), biophysical changes (energy balance, leaf, and canopy structure), and photochemical processes (Gerhards et al., 2019). These factors complicate the response of SIF and reduce the predictability of actual crop photosynthetic status under water shortage. Some studies found SIF at the leaf level or proximal level may not indicate the photosynthetic changes caused by water stress (Helm et al., 2020; Marrs et al., 2020), which are discrepant from some satellite SIF observations (Sun et al., 2015). This emphasizes the necessity of evaluating the potential of SIF in water stress detection at the field level.

An approach using optical reflectance, thermal imagery, and SIF enables us to obtain useful information about the current plant status and it can also provide a better understanding of how different factors may affect the dynamics of SIF under stress (Pinto et al., 2020). Because near and shortwave infrared hyperspectral remote sensing provides information on vegetation composition and canopy structure. Some studies have investigated the potential of combining SIF, visible and near-infrared (VNIR), and thermal indices in water stress detection or in the context of water stress at different spatial levels (Alonso et al., 2017; Calderón et al., 2013; Camino et al., 2018; Gerhards et al., 2018; Panigada et al., 2014; Xu et al., 2018; Zarco-Tejada et al., 2012), some of them focusing on agricultural crops. Xu et al. (2018) assessed the responses of diurnal SIF, PRI, and the difference between air temperature and canopy temperature to water stress for maize using a tower-based platform. They found that the optimal detection time of water stress by SIF indicators is around midday and by PRI is in the afternoon. In Panigada et al. (2014), the potential of remote indices like PRI, far-red SIF, and canopy temperature calculated from airborne VNIR and thermal imageries were investigated to discriminate water treatments in maize and sorghum plots. SIF and T_c were found sensitive to water stress for both crops.

This study aims to explore the potential of UAV-based SIF indices to detect water stress within a sugar beet field. We utilized additional remotely sensed signals of the canopy temperature, canopy structure, and leaf pigments to improve the interpretation of SIF at the wavelength of 687 nm (SIF_{687}) and 760 nm (SIF_{760}) under drought conditions. During the two measurement campaigns, sugar beet plants were affected by drought (June 2019) and by a combination of drought and heat stress (July 2019). A combination of temperature indices, VIs, and soil moisture measurements was used to determine the stress conditions and plant status. We hypothesize that i) SIF_{760} and SIF_{687} and their indices can track the plant responses to drought in June and the combined heat and drought stress in July, and ii) SIF indices react differently under the two different stressed conditions.

4.2. Materials and methodology

4.2.1. Study area

The dataset used in this study was acquired within a sugar beet field (*Beta vulgaris L., Urselina*) during the 2019 growing season (Figure 4.1). The study site is located at Unifarm, the agricultural experimental research farm of Wageningen University & Research, the Netherlands. The experiment was located at latitude 51° 59' 17.64" N and longitude 5° 39' 21.17" E. Soil texture is sandy loam. Sugar beet was sown with 50 cm between rows and 18 cm within a row on April 1, 2019 (day of year (DOY): 91) and harvested on November 15, 2019 (DOY 319). Canopy closure was reached on June 15 (DOY 166) at BBCH stage 39 (Meier et al., 1993).

Since water deficits in the middle of the growing period tend to strongly affect sugar yields (Steduto et al., 2012), we decided to conduct the field experiment in June and July. Figure 4.2 shows precipitation, minimum and maximum air temperature (T_a) in June and July 2019. In June, precipitation occurred only before June 22 and the total precipitation amount in June was 77.8 mm. The peak of the maximum air temperature (T_{max}) occurred on June 25 (34 °C) followed by June 24 and June 29 both around 31 °C. In July, total precipitation was 31.5 mm, less than half the amount of June. A heat wave occurred from July 23 to July 26 with the maximum T_{max} on July 25 (38 °C).

To explore crop response to water stress, two treatments with three repetitions were applied in three blocks. Each block randomly consisted of 2 plots (12 m × 30 m), one treatment with three sprinklers for irrigation treatment and the other treatment without irrigation as the control plot (Figure 4.1). To determine the required irrigation moment, soil moisture (volumetric water content, vol%) at a depth of 65 mm was measured using an ML3 ThetaProbe Soil Moisture Sensor (Delta-T Devices, UK) and plant status was assessed visually once a week. The averaged soil moisture on June 22 was 8.4 vol% in irrigated plots and 7.8 vol% in non-irrigated plots and decreased to 3.5 vol% and 3.81 vol%, respectively, on June 25 and sugar beet leaves visually showed wilting effects. According to two reports on the soil properties in the study field in 2018 from Wageningen Research Unifarm, crops should be irrigated when the soil moisture was below 7.5 vol%. 90 minutes of irrigation was applied to the irrigation plots on the evening of

June 27. Average soil moisture was 2.7 vol% in the irrigation plots and 2.9 vol% in non-irrigation plots on June 27 before irrigation and 16.3 vol% in the irrigation plots on June 28 after irrigation. Soil moisture values on July 16 were 5.1 vol% and 5.5 vol% in irrigation and non-irrigation plots, respectively. Despite precipitation at an amount of 13 mm on July 20, there was a visual symptom of water stress (leaf wilting) on July 22. Therefore, we decided to irrigate the sugar beet on the evening of July 23. After the watering, the average soil moisture was 9.5 vol% in the irrigation plots and 2.8 vol% in the non-irrigation plots on July 24. Same management operations were applied to the six plots during the whole growing season except for the two irrigations.

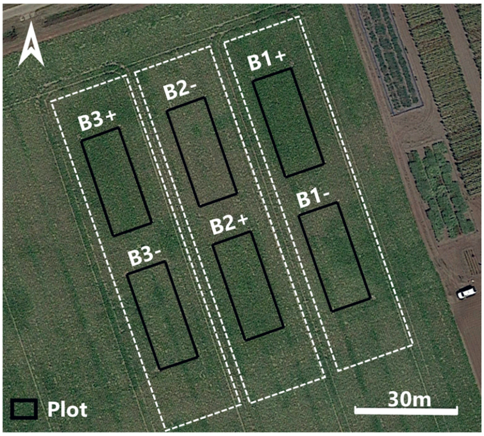

Figure 4.1. Location of the experimental plots at Unifarm of Wageningen University, Wageningen, the Netherlands. B1, B2, B3 refer to block1, block2, and block3 in the sugar beet field (dotted frames in white). + indicates an irrigation treatment applied to the plot and – indicates no irrigation treatment in the plot (control). The base map is a satellite image from Google Earth acquired on July 24, 2019.

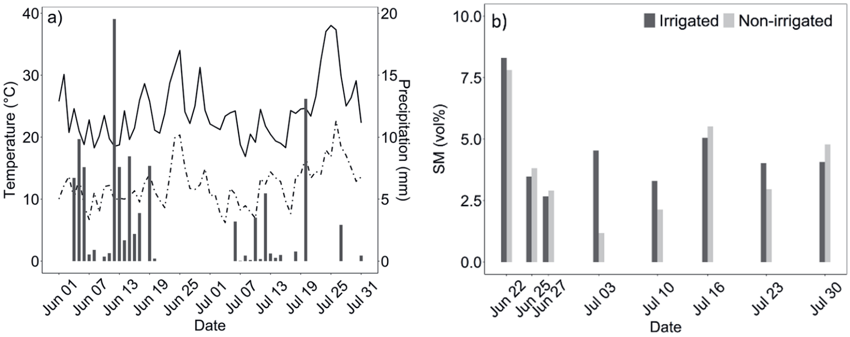

Figure 4.2. a) Daily minimum (T_{min}, °C), daily maximum air temperature (T_{max}, °C), and daily precipitation (mm) in June and July measured by Weather Station "De Veenkampen" (2.6 km from the

study site), and b) soil moisture (SM, vol%) measured in both irrigated and non-irrigated plots in June and July 2019.

4.2.2. UAV data acquisition and processing

A UAV campaign was conducted in 2019 on June 27, June 28, July 23, and on July 24 close to solar noon under clear sky conditions. The flight campaign lasted about 1 hour on each date. During the flights, the temperature was approximately 21.8 °C and wind speed was 3.6 ~ 4.7 m s^{-1} on June 27, 23.3 °C and 2.4 ~ 3.4 m s^{-1} on June 28, 31.5 °C and 1.7 ~ 2.7 m s^{-1} on July 23, and 36.8 °C and 3.7 ~ 4.7 m s^{-1} on July 24.

4.2.2.1. FluorSpec fluorescence observations

Fluorescence measurements were acquired by the FluorSpec mounted below a DJI S1000+ UAV platform (DJI, China). FluorSpec consists of a QE-Pro spectroradiometer (Ocean Insight, USA), a Global Navigation Satellite System (GNSS) receiver (Kendau), a laser rangefinder sensor (LightWare, Hungary), and a Sony A6000 RGB camera (Sony, Japan). The QE-Pro is a sub-nanometer spectral resolution point spectrometer, configured with two channels to measure the downwelling irradiance and the upwelling radiance in the wavelength range 630–800 nm, with a full-width-at-half-maximum (FWHM) spectral resolution of 0.3 nm and a spectral sampling interval of 0.15 nm. This allows SIF retrieval in the O_2-A absorption band at 760 nm (SIF_{760}) and in the O_2-B absorption band at 687 nm (SIF_{687}). The field-of-view (FOV) of the downward-looking radiance optics is 25°. The irradiance channel is equipped with a cosine corrector to collect solar irradiance from a hemispherical FOV (180°). The Sony RGB camera is a standard RGB camera that is automatically triggered together with the spectroradiometer and records high-resolution images of 6000 × 4000 pixels (24 Megapixels). At a flying height of 20 m above ground level (AGL), the camera captures an area of 30 × 20 m with a pixel resolution of 0.5 cm. For more details on the FluorSpec system, see (Wang et al., 2021).

FluorSpec flight mission was planned with the universal ground control software (UgCS). The flight mission consisted of three flight lines over the centre line of each block and each flight line had three waypoints. The UAV was programmed to fly 20 m AGL, with a horizontal speed of 1 m s^{-1} from waypoint to waypoint. In this configuration, the spectroradiometer sampled a circular area with a diameter of 8.8 m on the ground for every measurement and the sampling distance was 3.5 m. Each flight lasted around 5 minutes while the FluorSpec passed over the six sugar beet plots (Figure 4.1).

The FluorSpec data processing chain from raw digital numbers (DN) to top of canopy (TOC) radiance (Wm^{-2} sr^{-1} nm^{-1}) includes four steps as described in detail in Wang et al. (2021).

First, measured raw spectra were converted to at-sensor irradiance and radiance by removing the dark current, dividing by integration time, and multiplying the DN values with the radiometric calibration coefficient per wavelength. Secondly, laser rangefinder and the FluorSpec GNSS data were processed to obtain target-sensor distance and sensor position information, respectively. Next, the at-sensor irradiance and radiance were converted to their TOC equivalents by applying an atmospheric correction using the atmospheric transmittance of the bottom 1 km of atmosphere derived from the MODerate resolution atmospheric TRANsmission (MODTRAN6) algorithm (MODTRAN®, Spectral Sciences, Inc). To get a useful transmittance for a specific UAV altitude, the simulated transmittance can be converted to different thicknesses of the atmosphere using the Beer-Lambert law. Afterward, preceding and following TOC irradiances are linearly interpolated using the GPS timestamp of the corresponding TOC radiance measurement to get TOC irradiance at precisely the same time of the TOC radiance measurement. More details are described in Wang et al. (2021). To improve the geolocation of FluorSpec footprints, the FluorSpec RGB images were manually georectified by matching them with a pseudo-RGB composite using three bands (670 nm, 550 nm, and 514 nm, respectively) of the processed Rikola (Preprocessing of Rikoa data refers to section 4.2.2.2). Afterward, the centre coordinates of the FluorSpec RGB image determined in the previous step were assigned to the footprint locations of corresponding SIF measurements (chapter 3).

4.2.2.2. Rikola hyperspectral measurements

Hyperspectral images were acquired on the four measuring dates using a lightweight hyperspectral frame camera (Rikola Ltd., Oulu, Finland) onboard the same DJI S1000+ UAV platform. The camera used is based on a Fabry-Perot interferometer (FPI) (Honkavaara et al., 2013) and was programmatically configured to register 16 narrow spectral bands in a range of 515–870 nm with full width at half maximum (FWHM) varying between 13 and 17 nm (Table S4.1). These bands were chosen due to their importance to describe changes in biochemical (leaf chlorophyll content) and biophysical (e.g. leaf area index, ground cover, etc.) traits of vegetation at leaf and canopy levels (Clevers and Kooistra, 2011).

The UGCS ground station software was used to plan the flight mission. The study area was captured in 10 flight lines, parallel to the longest side of the area. The flight height was 50 m and the flying speed was 2 m s^{-1}. The overlap between flight lines was approximately 80%, within the flight line the overlap between images was approximately 60%. To calibrate the data to reflectance factors, dark current measurements and images of a reflectance reference panel (gray 50% Spectralon panel (LabSphere Inc., North Sutton, NH, USA)) were taken before and after the flight. The flight duration was around 8 minutes. The HyperspectralImager 2.0 software converted the raw images in digital numbers (registered with 12-bit radiometric resolution) to radiances (Wm^{-2} sr^{-1} nm^{-1}). The radiance images were then transformed into reflectance factor images using the empirical line method and the measurement of the Spectralon panel. The images were aligned and ortho- and georectified in Agisoft Metashape using ground control points (GCPs) that were surveyed with a real-time-kinematic (RTK)-enabled rover, following the data processing protocol described by Roosjen et al. (2017).

4.2.2.3. WIRIS thermal data

Thermal images were acquired by the Workswell WIRIS 640 (Workswell s.r.o., Praha, Czech Republic) mounted to a gimbal on board an Altura AT8 octocopter. The thermal camera has a temperature sensitivity of 0.05 °C and a resolution of 640 × 512 pixels in a spectral range of 7.5-13.5 μm. It captures images recording actual temperature in a TIFF radiometric image format. The system also is equipped with a RGB camera with a resolution of 1600 × 1200 pixels.

The WIRIS flight pattern consisted of 10 flight lines parallel to the longest side of the blocks. The flight height was 40 m above ground level and the flight speed was 2 m s^{-1}. Images were acquired with a pixel resolution of 0.5 cm. The period of thermal camera calibration was 30 minutes and each flight lasted 7 minutes.

The calibrated TIFF images were processed and an orthomosaic for the whole trial was constructed with Agisoft Metashape. The geo-referencing of the mosaic image was done manually in ArcMap 10.2 using the GCPs measured by RTK. On July 24, the thermal camera did a calibration in the middle of the flight due to a late take-off, resulting in a temperature difference of 6-7 °C in the same area captured before and after the recalibration. It was assumed that the histogram was the same within overlapping areas. Histogram matching (HM) is commonly applied to find a monotonic mapping between a pair of histograms (Gonzalez and Woods, 2006). To solve this mismatch, we applied HM to the overlapping areas of two radiometric images taken exactly before and after the recalibration and used the last image before the calibration as a reference. The returned function was applied to all images taken after the recalibration. The temperature difference in the same area was reduced to less than 0.5 °C. This mismatch was corrected using the histMatch function in R.

4.2.2.4. Ground measurements

Leaf area index (LAI), chlorophyll concentration (Cab), and soil moisture (SM) observations were collected after the flights on the four measuring dates. On June 27 and July 24, these three types of measurements were measured from six plots, and on June 28 and July

23 ground measurements were acquired only in the three irrigation plots: 8-10 areas of 1 m × 1 m were evenly sampled along the long side of the block. Within each sample site, one LAI measurement was conducted using the LAI-2200C Plant Canopy Analyzer (LI-COR, USA) and five Cab measurements were acquired with a SPAD 502 Plus Chlorophyll Meter (Konica-Minolta, Japan). Each Cab measurement was an average of five random measurements collected from the top leaves of individual plants. SPAD-502 readings were converted to Cab concentrations using the calibration equations in Malnou et al. (2008). SM was conducted at a soil depth of 65 mm with the ML3 ThetaProbe Soil Moisture Sensor.

4.2.3. Indices applied in water stress detection

4.2.3.1. Optical vegetation and temperature indices

For optical vegetation indices on canopy structure, we selected the normalized difference vegetation index (NDVI) due to its relationship with the leaf area index (Rouse et al., 1973; Carlson and Ripley, 1997). The ratio of the transformed chlorophyll reflectance index and the optimized soil-adjusted vegetation index (TCARI/OSAVI) has been demonstrated to successfully minimize soil background and leaf area index variation in crops, providing predictive relationships for chlorophyll concentration estimation with hyperspectral imagery in closed crops (Haboudane et al., 2002). The photochemical reflectance index (PRI) has shown promise to remotely estimate dynamics in xanthophyll pigment interconversion at short timesteps and can be used to detect dynamic variations of NPQ (Gamon et al., 1992). Canopy temperature (T_c) has been considered a reliable proxy for plant water status monitoring due to leaf stomatal closure (Jackson et al., 1981). To get pure vegetation canopy temperature (T_{cveg}), the canopy temperature image was masked using the NDVI image to remove the effect from soil surface temperature. Only pixels with NDVI greater than 0.3 were used for deriving T_{cveg}. T_c and T_{cveg} had very similar values in the six plots and therefore we used T_c in this study.

4.2.3.2. SIF indices

Related to physiological plant processes, changes in SIF can be potentially related to stress-induced variations in photosynthesis. SIF observed above the canopy can be expressed as

$$SIF = APAR * \Phi F * f_{esc} \tag{4.1}$$

where APAR (W m^{-2}) is the photosynthetically active radiation absorbed by chlorophyll in green leaves, ΦF is the physiological SIF emission yield of the whole canopy, and f_{esc} is the fraction of all SIF photons emitted from all leaves and escaped from the canopy (Guanter et al., 2014).

Since APAR can be calculated as

$$APAR = PAR * fAPAR \quad (4.2)$$

where fAPAR is the fraction of PAR absorbed by vegetation, Equation 4.1 can be reformulated as

$$SIF = PAR*fAPAR* \Phi F * f_{esc} \quad (4.3)$$

In this paper, SIF_{687} and SIF_{760} were estimated using the Spectral Shape Assumption Fraunhofer Line Discrimination (SSA-FLD) method (Wang et al., 2021). SSA-FLD is a slightly adapted FLD-based approach to retrieve SIF and can use the ultra-fine spectral information within the oxygen absorption regions. It has two assumptions: (i) that the fluorescence follows a known shape of the fluorescence spectrum; and (ii) that the reflectance factor of the target object behaves linearly over the utilized spectral region. SSA-FLD can be regarded as a special case of the spectral fitting method (SFM) (Mazzoni et al., 2012; Meroni et al., 2010). The SFM function cannot be applied to UAV-based FluorSpec measurements without any parameter adjustment. Moreover, in a parallel study, we compared the two methods and they were strongly linearly correlated (R^2 = 0.99 at 760 nm (Wang et al., 2021) and R^2 = 0.91 at 687 nm (Figure S4.1)).

According to Equation 4.3, SIF normalization by incident PAR can remove the effect of variations in PAR caused by different illumination conditions (Van der Tol et al., 2016). PAR in this study was calculated using FluorSpec irradiance measurements acquired before the UAV took off. FluorSpec PAR was firstly calculated within the 630-700 nm interval using 20 consecutive irradiance measurements and then converted to incoming PAR within 400-700 nm using the equation in Wang et al. (2021). The flight duration was 5 minutes under stable blue-sky illumination conditions. Therefore, PAR measurements before take-off can be applied to normalize SIF and to calculate APAR during the flight.

SIF_{yield} represents the ratio of the fluorescence and the absorbed PAR (APAR). According to Equation 4.3, this index can provide further insights into canopy scattering and leaf re-absorption and physiology effects to variations of SIF (Sun et al., 2015). We applied a wide dynamic range vegetation index (WDRVI, defined in Equation 4.4) proposed by Gitelson et al. (2005) to calculate fAPAR (Equation 4.5), which has proved to be linearly correlated with fAPAR (Viña and Gitelson, 2005; Liu et al., 2019).

$$WDRVI = (\alpha *R_{nir} - R_{red})/ (\alpha *R_{nir} + R_{red}) \quad (4.4)$$

$$fAPAR = 0.516*WDRVI + 0.726 \quad (4.5)$$

In Equation 4.4 R_{nir} and R_{red} are the reflectance at the near-infrared and red band and they were represented by Rikola reflectance at 800 nm and 670 nm, respectively. α is a weighting coefficient with a value of 0.1-0.2 (Gitelson et al., 2014). fAPAR was estimated using the linear regression (Equation 4.5) established by Liu et al. (2019) with α at 0.1 and it correlated well with LAI ground measurements (Figure S4.2), confirming the reliability of the fAPAR estimate using WDRVI and the feasibility of SIF_{yield} calculation with the estimated APAR. SIF_{yield} at 687 nm and 760 nm were calculated.

Since SIF_{687} and SIF_{760} have different sensitivity to the photosynthetic activity, their ratio (SIF_{687}/SIF_{760}) may be related to physiological changes introduced by a changing contribution of fluorescence emission from Photosystem I (PSI) and Photosystem II (PSII) in response to plant stress (Wieneke et al., 2016; Porcar-Castell et al., 2014).

Table 4.1. Indices were compared and evaluated in this study. R represents Rikola reflectance at a specific wavelength. The VIs and Tc were averaged per plot using pixel level values.

Category	VIs	Formula	References
Canopy structure	NDVI	$(R_{800} - R_{670}) / (R_{800} + R_{670})$	Rouse et al. (1973)
Xanthophyll pigments	PRI	$(R_{570} - R_{531}) / (R_{570} + R_{531})$	Zarco-Tejada et al. (2013)
Chlorophyll concentration	TCARI/ OSAVI	$3*((R_{700}-R_{670})-0.2*(R_{700}-R_{550}) *(R_{700}/R_{670}))/ ((1+0.16) (R_{800}-R_{670})/(R_{800}+R_{670}+0.16)$	Haboudane et al. (2002)
Temperature	T_c	T_c	Jackson et al. (1981)
Photosynthesis	SIF_{norm}	SIF/PAR	Rossini et al. (2010)
	SIF_{yield}	SIF/APAR	Sun et al. (2015)
	SIF_{ratio}	SIF_{687}/SIF_{760}	Ač et al. (2015)

4.2.4. Statistical analysis

To investigate the irrigation effect on the selected indices (Table 4.1), first, we calculated per plot the difference between the average value of an index on date 1 (before irrigation) and on date 2 (after irrigation) (hereafter called the delta index, Δindex). The null hypothesis (H_0) was that irrigation treatment had no significant effect on the delta index value as compared to the non-irrigation plots per block, which was tested with a paired t-test (Hsu and Lachenbruch, 2014). Spatial heterogeneities might exist between blocks, e.g. due to planting and management history. With a paired t-test, the irrigation and non-irrigation plots per block were compared and therefore the block effect was taken into consideration. Furthermore, to investigate the effect from the changes of the selected VIs and T_c caused by irrigation treatment on SIF indices, we applied linear regression to ΔSIF indices and ΔVIs and ΔT_c.

4.3. Results

4.3.1. Field measurements

Table 4.2 shows an overview of ground measurements on four experimental dates. On June 27, LAI, Cab, and SM had similar values in irrigation and non-irrigation plots. On June 28, SM in the irrigation plots had increased to 16.24 vol% and LAI had increased from 2.84 to 3.95 (not statistically significant, p-value = 0.22). From July 23 to July 24, for irrigation plots, SM also had a considerable increase from 4.03 to 9.48 vol%, but less than the increase on June 28. The irrigation effect was not noticeable due to a small decrease in LAI (p-value = 0.40). A decrease in Cab was observed both on June 28 and July 24, which was not statistically significant.

Table 4.2. Descriptive statistics (mean values ± standard deviations) of leaf area index (LAI, $cm^2\ cm^{-2}$), chlorophyll contents (Cab, $\mu g\ cm^{-2}$), and soil moisture (SM, vol%) in irrigated and non-irrigated plots during the field campaign. NA indicates no ground measurements were acquired. + indicates an irrigation treatment applied to the plot and – indicates no irrigation treatment in the plot.

Date	LAI		Cab		SM	
	B+	B–	B+	B–	B+	B–
June 27	2.84±0.87	3.19±1.12	52.50±6.73	51.71±7.23	2.67±0.12	2.91±1.05
June 28	3.95±1.08	NA	46.24±6.40	NA	16.24±2.01	NA
July 23	2.08±0.91	NA	62.83±7.42	NA	4.03±0.22	NA
July 24	1.86±0.45	0.67±0.38	48.50±13.66	46.58±17.58	9.48±0.29	2.78±0.78

4.3.2. Index maps

To visually evaluate the spatial variation of water stress conditions in the study field, we selected two commonly used indices for water deficit detection, canopy structural parameter NDVI and canopy temperature T_c (Figures 4.3 and 4.4). Maps of $SIF_{760norm}$ and $SIF_{687norm}$ (Figures 4.5 and 4.6) show the variability of the signals under drought and drought/heat stress conditions. The average values within each plot are shown in Tables S4.2 and S4.3. Maps for the other indices are not shown, but in the statistical analysis, all indices were included.

4.3.2.1. NDVI and T_c mapping

Figure 4.3 shows spatial patterns of NDVI and T_c measurements within the six plots. On June 27 we found higher NDVI values within B1- ad areas around the central axis in B3- and lower values in B2- (Figure 4.3a), T_c values in block 1 were lower than in the other two blocks. After irrigation, NDVI showed an increase in the irrigation plots and NDVI in non-irrigation plots all decreased slightly on the second day (Figure 4.3c). Canopy temperature for irrigated areas had a decrease on June 28 and a rise within non-irrigation plots (Figure 4.3d). Higher T_c was observed within non-irrigation plots ranging from 25.3 (B1–) to 30.3 °C (B2–).

On July 23, NDVI values were lower than those observed on June 27 (except B1+) and T_c values were higher overall. Irrigation did not largely affect NDVI values within irrigation plots, whereas NDVI within non-irrigation plots had a noticeable decrease, particularly within B2– (Figure 4.4c). Figure 4.4d shows a clear difference in the spatial pattern of T_c on July 24. Highest T_c appeared in non-irrigation B2– up to 44.0 °C followed by T_c in B1– (40.3 °C).

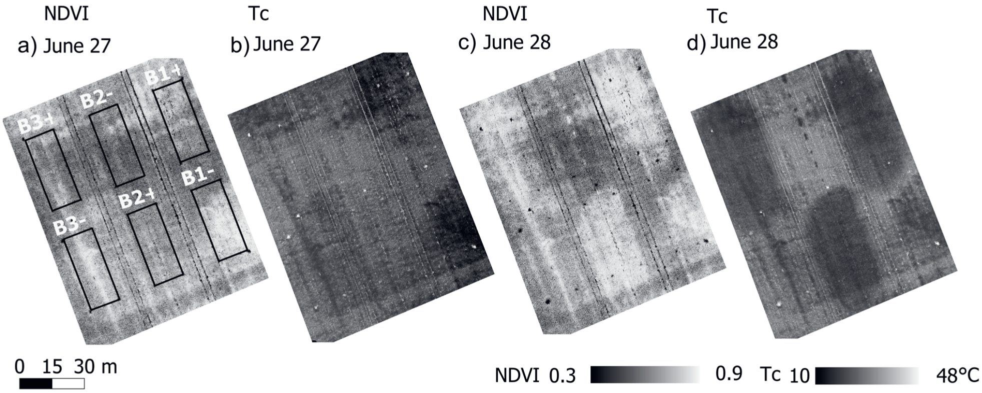

Figure 4.3. Maps of NDVI on June 27 (a) and on June 28 (c). Maps of canopy temperature (T_c) on June 27 (b) and on June 28 (d). B1, B2, B3 refer to block1, block2, and block3 in the sugar beet field. + indicates an irrigation treatment applied to the plot and – indicates no irrigation treatment in the plot. Irrigation of 90 minutes was given to B1+, B2+, and B3+ on the evening of June 27.

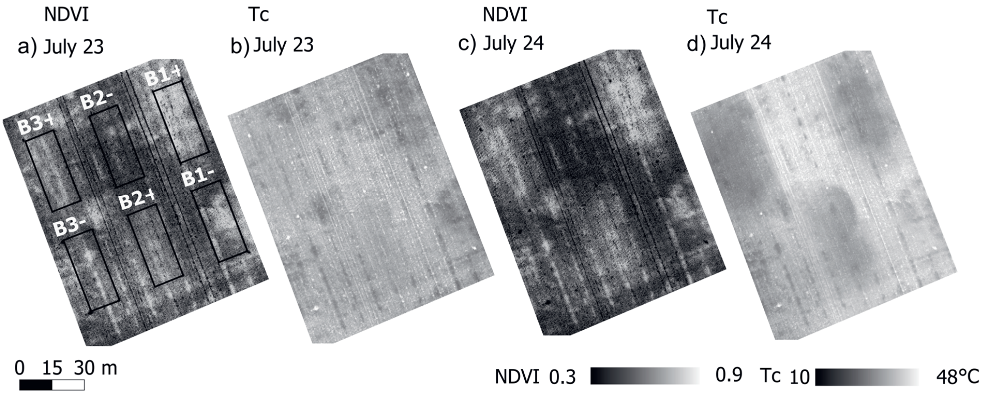

Figure 4.4. Maps of NDVI on July 23 (a) and on July 24 (c). Maps of canopy temperature (T_c) on July 23 (b) and on July 24 (d). B1, B2, B3 refer to block1, block2, and block3 in the sugar beet field. + indicates an irrigation treatment applied to the plot and – indicates no irrigation treatment in the plot. Irrigation of 90 minutes was given to B1+, B2+, and B3+ on the evening of July 23.

4.3.2.2. Spatial patterns of $SIF_{760norm}$ and $SIF_{687norm}$

The spatial patterns of $SIF_{760norm}$ and $SIF_{687norm}$ on four measuring dates are shown in Figures 4.5 and 4.6. In general, $SIF_{760norm}$ values were higher than $SIF_{687norm}$ values per plot, particularly on June 27 and June 28. Both metrics showed field heterogeneity which was not easy to be noticed in NDVI and T_c maps. Higher spatial variations can be found in $SIF_{760norm}$ observations. Clear differences can be noticed within each plot, e.g. within B2– on June 27 $SIF_{760norm}$ varied from 0.50 to 0.73, and $SIF_{687norm}$ ranged within 0.34 ~ 0.54 (Figure 4.5a, b).

On June 27, the $SIF_{760norm}$ map (Figure 4.5a) shows a spatial pattern similar to NDVI but opposite to T_c. The highest $SIF_{760norm}$ values were found within B1– and lowest $SIF_{760norm}$ values were observed within B2–. $SIF_{687norm}$ distributed more evenly and the highest and lowest values appeared in B1+ and B3– (Figure 4.5b). On June 28, both SIF indices decreased within all three blocks despite the irrigation given to half of the plots.

On July 23, both values of $SIF_{760norm}$ and $SIF_{687norm}$ were lower than those on June 27 (Figure 4.6a, b). Averaged $SIF_{760norm}$ ranged from 0.30 (B2–) to 0.49 (B1+) and averaged $SIF_{687norm}$ varied from 0.31 (B2–) to 0.38 (B3+). After irrigation on July 24, $SIF_{760norm}$ increased in irrigation plots, particularly within B1–, and decreased in non-irrigation plots (Figure 4.6c), whereas all plots had increased $SIF_{687norm}$.

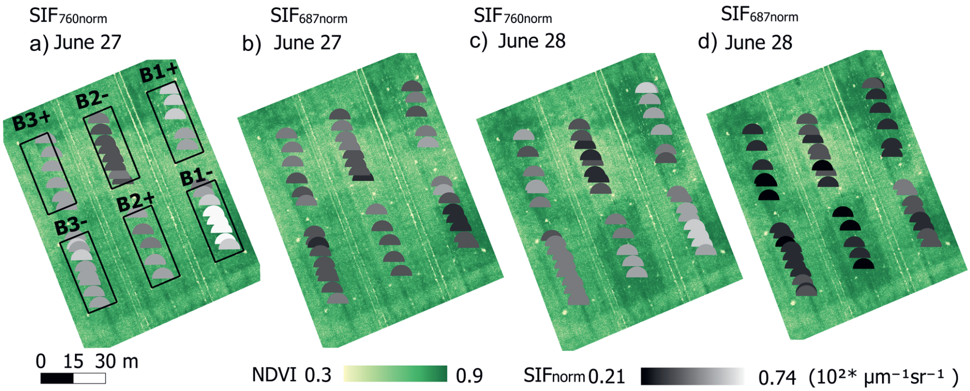

Figure 4.5. Maps of SIF$_{760norm}$ on June 27 (a) and on June 28 (c). Maps of SIF$_{687norm}$ on June 27 (b) and on June 28 (d). B1, B2, B3 refer to block1, block2, and block3 in the sugar beet field. + indicates an irrigation treatment applied to the plot and – indicates no irrigation treatment in the plot. Irrigation of 90 minutes was given to B1+, B2+, and B3+ on the evening of June 27.

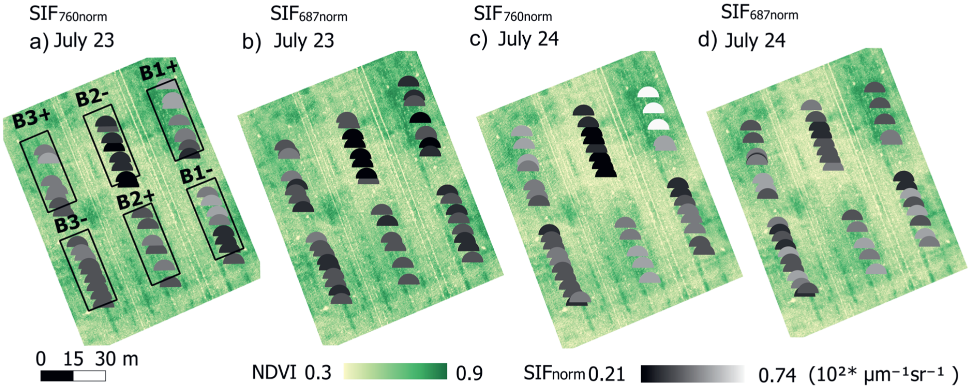

Figure 4.6. Maps of SIF$_{760norm}$ on July 23 (a) and on July 24 (c). Maps of SIF$_{687norm}$ on July 23 (b) and on July 24 (d). B1, B2, B3 refer to block1, block2, and block3 in the sugar beet field. + indicates an irrigation treatment applied to the plot and – indicates no irrigation treatment in the plot. Irrigation of 90 minutes was given to B1+, B2+, and B3+ on the evening of July 23.

4.3.3. Change analysis

Figures 4.3~4.6 show the spatial patterns of NDVI, T$_c$, and SIF$_{norm}$ and provide a visual evaluation of changes in these indices mainly induced by the imposed irrigation treatment. However, it takes effort to quantify these changes and to better assess the effect of irrigation on these metrics. To compare the response difference between irrigation and non-irrigation plots, we investigated the changes in values of each index acquired on two consecutive experimental days (delta index).

4.3.3.1. ΔNDVI, ΔPRI, and ΔT_c

Figures 4.7 and 4.8 present delta values in NDVI, PRI, and T_c on two consecutive measuring days in June and July, respectively. As shown in Figure 4.7a, after irrigation on June 28 NDVI values increased strongly while the NDVI in the non-irrigation plots slightly decreased. PRI increased in all plots, but the increase was larger within non-irrigation plots. T_c observed from the irrigated plants canopy decreased and from the non-irrigated plants canopy increased. The smallest decrease and largest increase were both observed in block1.

On July 24, NDVI declined in all plots (Figure 4.8a). Figure 4.8b shows that except for an increase in B1–, PRI showed a small decrease in other plots. T_c decreased in B2+ and B3+ and had a substantial increase in B1– and B2–. T_c measurements in B1+ and B3– remained almost unchanged before and after the water treatment (Figure 4.8c).

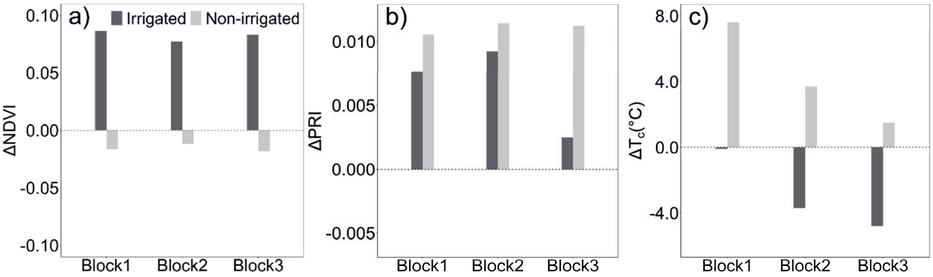

Figure 4.7. Delta values (June 28 minus June 27) in NDVI (ΔNDVI) (a), in PRI (ΔPRI) (b), and in T_c (ΔT_c) (c) in three sugar beet blocks. Irrigated refers to irrigated plots B1+, B2+, and B3+, and non-irrigated refers to non-irrigated plots B1–, B2– and B3–. Irrigation was given to irrigated plots on the evening of June 27.

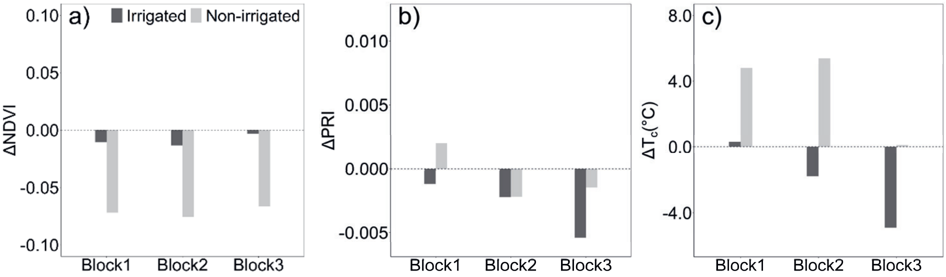

Figure 4.8. Delta values (July 24 minus July 23) in NDVI (ΔNDVI) (a), in PRI (ΔPRI) (b), and in T_c (ΔT_c) (c) in three sugar beet blocks. Irrigated refers to irrigated plots B1+, B2+, and B3+, and non-irrigated refers to non-irrigated plots B1–, B2– and B3–. Irrigation was given to irrigated plots on the evening of July 23.

4.3.3.2. ΔSIF indices

To test whether the irrigation effect can also be observed in SIF measurements, the changes (delta) for different SIF indices on the consecutive days are presented in Figures 4.9 and 4.10. SIF$_{760\mathrm{norm}}$ and SIF$_{687\mathrm{norm}}$ both decreased on June 28 and their decline between irrigated and non-irrigated plots varied remarkably (Figure 4.9a, b). SIF$_{760\mathrm{norm}}$ emitted from irrigated plants reduced less per block than the non-irrigated ones. For SIF$_{687\mathrm{norm}}$ the reduction for the irrigated plots was stronger. SIF$_{760\mathrm{norm}}$ had only a slight drop in B2+, whereas SIF$_{687\mathrm{norm}}$ had a remarkable and similar decrease within all irrigation plots. SIF$_{\mathrm{yield}}$ at both 687 nm and 760 nm had a similar trend as SIF$_{687\mathrm{norm}}$ from June 27 to June 28 overall (Figure 4.9c, d). Except for a small increase in SIF$_{687\mathrm{yield}}$ within B1–, both SIF$_{760\mathrm{yield}}$ and SIF$_{687\mathrm{yield}}$ experienced a reduction in all blocks. There was no obvious difference in ΔSIF$_{760\mathrm{yield}}$ between the irrigated and control plots per block, particularly in block2, while this difference in ΔSIF$_{687\mathrm{yield}}$ was much larger. SIF$_{\mathrm{ratio}}$ decreased substantially within irrigation plots and slightly increased within non-irrigation plots. The largest decrease in SIF$_{\mathrm{ratio}}$ appeared in B2+ (Figure 4.9e).

On July 24, SIF$_{760\mathrm{norm}}$ increased in irrigation plots with the largest increase up to 0.15 in B1+, while it decreased slightly in non-irrigation plots (Figure 4.10a). SIF$_{687\mathrm{norm}}$ increased within all plots but more in irrigation plots, resulting in an obvious difference in ΔSIF$_{687\mathrm{norm}}$ between irrigated and non-irrigated plots per block (Figure 4.10b). Figure 4.10c, d both showed an increase in SIF$_{760\mathrm{yield}}$ and SIF$_{687\mathrm{yield}}$ on July 24. SIF$_{760\mathrm{yield}}$ showed a larger increase in irrigated plots in comparison to non-irrigated plots per block, but little difference in the increase is seen in block3. SIF$_{687\mathrm{yield}}$ increased slightly less in irrigation plots, making it difficult to differentiate the changes in ΔSIF$_{687\mathrm{yield}}$ in the irrigated plot from the non-irrigated one per block. Although SIF$_{\mathrm{ratio}}$ increased in all plots, the change was larger in non-irrigated plots (Figure 4.10e).

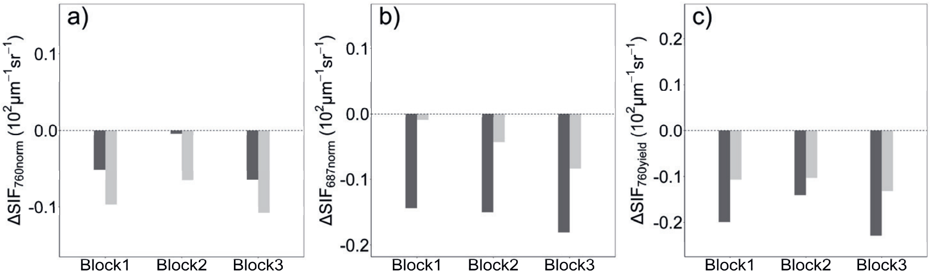

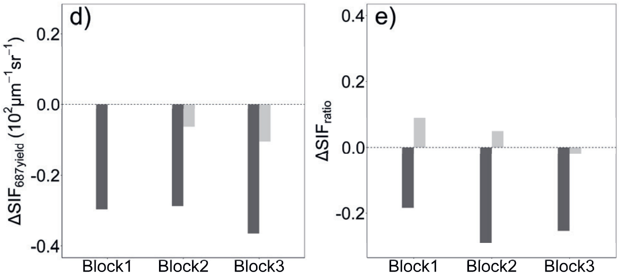

Figure 4.9. Delta values (June 28 minus June 27) in $SIF_{760norm}$ ($\Delta SIF_{760norm}$) (a), in $SIF_{687norm}$ ($\Delta SIF_{687norm}$) (b), in $SIF_{760yield}$ ($\Delta SIF_{760yield}$) (c), in $SIF_{687yield}$ ($\Delta SIF_{687yield}$) (d), and in SIF_{ratio} (ΔSIF_{ratio}) (e) in sugar beet blocks. Irrigated refers to irrigated plots B1+, B2+, and B3+, and non-irrigated refers to non-irrigated plots B1–, B2– and B3–. Irrigation was given to irrigated plots on the evening of June 27.

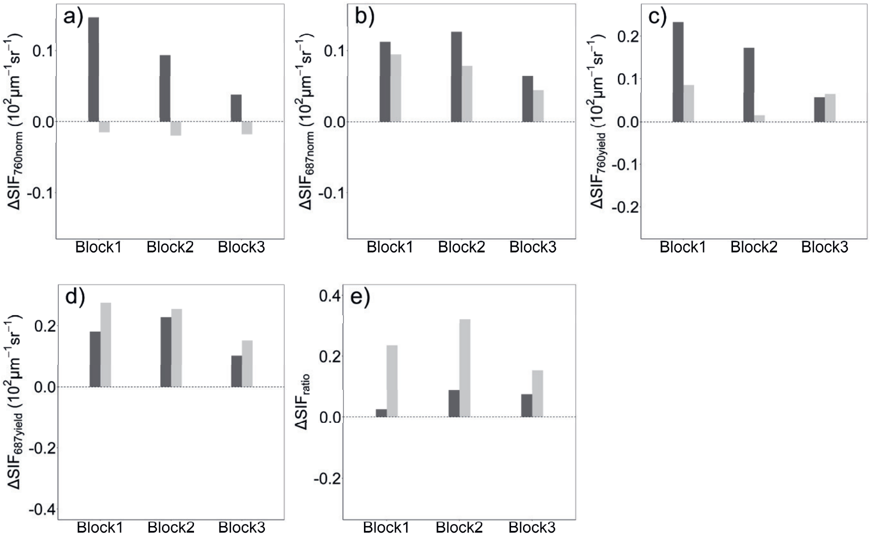

Figure 4.10. Delta values (July 24 minus July 23) in $SIF_{760norm}$ ($\Delta SIF_{760norm}$) (a), in $SIF_{687norm}$ ($\Delta SIF_{687norm}$) (b), in $SIF_{760yield}$ ($\Delta SIF_{760yield}$) (c), in $SIF_{687yield}$ ($\Delta SIF_{687yield}$) (d), and in SIF_{ratio} (ΔSIF_{ratio}) (e) in three sugar beet blocks. Irrigated refers to irrigated plots B1+, B2+, and B3+, and non-irrigated refers to non-irrigated plots B1–, B2– and B3–. Irrigation was given to irrigated plots on the evening of July 23.

4.3.4. Statistical analysis

Table 4.3 shows an overview of the effect of irrigation on delta values of NDVI, PRI, and T_c and five SIF-based metrics. To better evaluate the potential of SIF indices, we also tested the irrigation effect on TCARI/OSAVI.

Both in June and July, NDVI was significantly affected by irrigation treatment, which is in line with the significant changes of NDVI shown in Figures 4.3c and 4.5c. This finding indicated that the irrigation treatment had a clear effect on the canopy structure of sugar beet plants in our experimental set-up. The pigment-related index TCARI/OSAVI was also found to be affected significantly by the given irrigation. Irrigation had a significant impact on canopy temperature T_c (Figures 4.3d and 4.4d) and this impact was greater in June as shown by the higher significance in Table 4.3.

In June, irrigation significantly affected SIF indices except for $SIF_{760yield}$. $SIF_{760norm}$ and SIF_{ratio} were less affected in comparison to $SIF_{687norm}$ and $SIF_{687yield}$. However, in July the irrigation effect was weak on $SIF_{760norm}$, $SIF_{687norm}$, and SIF_{ratio}. SIF_{yield} both at 760 nm and 687 nm were hardly influenced by the irrigation treatment.

Table 4.4 shows the significance of the linear regression between delta values of these VIs and canopy temperature and SIF indices. All selected VIs and T_c had a significant correlation with $SIF_{687norm}$ and $SIF_{687yield}$, and most of them were significantly related to SIF_{ratio}, whereas the correlation with $SIF_{760norm}$ and $SIF_{687norm}$ was much weaker. In July, except for SIF_{ratio}, ΔVIs and ΔT_c did not significantly correlate to ΔSIF indices. SIF_{ratio} was significantly related to ΔNDVI and ΔT_c.

Table 4.3. Irrigation effects on different indices for water stress detection (numbers are statistical significance, ***p < 0.001, **p < 0.01, *p < 0.05, . 0.05 < p < 0.1, and ns p > 0.1).

Indices		June 28-June 27	July 24 -July 23
SIF indices	$\Delta SIF_{760norm}$	0.0128 *	0.0705 .
	$\Delta SIF_{687norm}$	0.0095 **	0.0989 .
	$\Delta SIF_{760yield}$	0.1314 ns	0.1360 ns
	$\Delta SIF_{687yield}$	0.0084 **	0.1853 ns
	ΔSIF_{ratio}	0.0121 *	0.0680 .
Vegetation indices	ΔNDVI	0.0019 **	8.12e-05 ***
	ΔPRI	0.1560 ns	0.1860 ns
	ΔTCARI/OSAVI	0.0079 **	0.0119 *
Temperature	ΔT_c	0.0035 **	0.0215 *

Table 4.4. Significance of the linear regression between vegetation indices and canopy temperature and SIF indices (numbers are statistical significance, ***p < 0.001, **p < 0.01, *p < 0.05, . 0.05 < p < 0.1, and ns p > 0.1)

	$\Delta SIF_{760norm}$	$\Delta SIF_{687norm}$	$\Delta SIF_{760yield}$	$\Delta SIF_{687yield}$	ΔSIF_{ratio}
June 28-June 27					
ΔNDVI	0.0987.	0.0111 *	0.0883.	0.0024 **	0.0058 **
ΔPRI	0.6460 ns	0.0682.	0.0279 *	0.0564.	0.1278 ns
ΔTCARI/OSAVI	0.0716.	0.0110 *	0.1287 ns	0.0027 **	0.0093 **
ΔT_c	0.1843 ns	0.0016 **	0.1995 ns	0.0060**	0.0039 **
July 24 -July 23					
ΔNDVI	0.0428 *	0.4237 ns	0.1130 ns	0.3650 ns	0.0172 *
ΔPRI	0.7240 ns	0.6020 ns	0.9690 ns	0.1345 ns	0.4810 ns
ΔTCARI/OSAVI	0.1140 ns	0.4150 ns	0.2250 ns	0.4766 ns	0.0799.
ΔT_c	0.3540 ns	0.9064 ns	0.5062 ns	0.0844.	0.0485 *

4.4. Discussion

The objective of this research was to explore the response of UAV-based SIF indices to water stress in a sugar beet field. VNIR hyperspectral and thermal data were used to assist the interpretation of the SIF indices. Our results showed that SIF indices responded to the irrigation treatment when plants were under water stress (in June) whereas they could not indicate the irrigation effect under combined water and heat stress (in July). The responses of SIF indices retrieved at 760nm were different from those of SIF indices at 687nm.

4.4.1. Field conditions

Plant responses to water stress are complex (Chaves et al., 2002; Yardanov et al., 2003) and under field conditions, these responses appear synergistically or antagonistically and are modified by simultaneous plant stresses. For example, heat stress commonly coincides with water scarcity under field conditions. Crop protective mechanisms only under water deficit may be insufficient to dissipate the excess of excitation energy (Krause, 1988), which can complicate the response of SIF to water stress. Generally, water loss under heat stress is larger during daytime, mainly due to an increased rate of transpiration, ultimately impairing certain important physiological processes in plants (Fahad et al., 2017). At optimal temperatures (25 °C) photosynthetic capacity only decreased at leaf relative water contents (RWC) around 60 %. However, when the temperature rose above the optimum (35 °C), photosynthetic capacity was affected at a higher leaf water status (RWC = 80 %) (Chaves et al., 2002). In our study, low soil moisture values before irrigation (Table 4.2) indicated a water deficit occurring in the sugar beet plants on both June 27 and July 23. Sugar beet performs best in a range of temperatures from 17 to 25°C (Ober and Rajabi, 2010). The maximum air temperature during the observation period did not exceed 24 °C on June 27 and June 28. Therefore, we may assume that temperature was not a limiting factor. In contrast, the extremely high air temperature on July 23 (31.5 °C) and July 24 (36.8 °C) imposed extra heat stress on the existing water stress. Irrigation eased the stress conditions in irrigated plots both on June 28 and July 24, indicated by the increase in SM and LAI (Table 4.2). The observed decrease in Cab after irrigation also evidenced the irrigation effect. Under water deficit conditions on June 27, Cab was mostly measured from the standing young leaves. Relocation of mobile nutrients, such as nitrogen, to the younger top canopy leaves promotes increased chlorophyll contents (Yang et al., 2001). The two different field stress conditions could be further indicated by SM values and the recovery of sugar beet plants in irrigated plots on June 28 and July 24. The irrigation did not reduce the stress on July 24 as much as that on June 28, indicated by lower SM and NDVI and higher T_c on July 24 (Figures 4.3, 4.4, and S4.3; Table S4.2).

4.4.2 Response of SIF indices to water stress on June 27 and 28

We found that $SIF_{760norm}$, $SIF_{687norm}$, $SIF_{687yield}$, and SIF_{ratio} could significantly indicate the differences between irrigated and non-irrigated sugar beet plants (Table 4.3). The decrease in SIF_{norm} and SIF_{yield} in non-irrigated plots agrees with the findings from some previous studies (Ač et al., 2015; Gerhards et al., 2018; Xu et al., 2021, 2018; Zarco-Tejada et al., 2012). The meta-analysis study carried out by Ač et al. (2015) suggests that water stress, in general, induces a decline in red and far-red fluorescence signal intensity measured at both leaf and canopy levels. The decline could be explained by the activation of non-photochemical mechanisms and the reduction in APAR. As the first and foremost response of almost all the C3 plants to water stress, stressed plant stomata closure occurs to prevent water vapor loss via transpiration under water deficit and this results in a decrease of evaporating cooling and therefore an increase in leaf temperature (Chaves et al., 2002; Jones and Schofield, 2008), evidenced by the higher T_c measured over non-irrigated plants on June 28 (Figures 4.3d and 4.7c). Reduced stomatal conductance limits CO_2 intake and consequently increases the generation of reactive oxygen species (ROS) and also affects the electron transport chain in light-dependent reactions (Flexas et al., 2002). Photorespiration increases to prevent oxidative damage in chloroplasts caused by ROS (Voss et al., 2013). NPQ is also upregulated as the dominant way to thermally dissipate the photon energy absorbed, which cannot be processed in photochemical ways. Both the two energy dissipation mechanisms result in a decrease both in photosynthesis rate and fluorescence emission (Porcar-Castell et al., 2014)). PRI is directly related to the pH-dependent NPQ which has the main protection function of photosystem II (Goss and Lepetit, 2015). The increased PRI in non-irrigation plots on June 28 (Figure 4.7b) indicates an increase in NPQ. In addition, sugar beet leaves rolled and wilted to reduce water loss, resulting in a decrease in effective LAI, which was indicated by the decreased NDVI and fAPAR (Figures 4.7a and S4.2). As incoming shortwave irradiance on June 27 and 28 were the same (798.85 W m^{-2}), APAR in non-irrigation plots decreased and thus could contribute to the decline in fluorescence emission.

SIF_{norm} and SIF_{yield} also decreased in irrigation plots on June 28. One possible reason is the higher air temperature on the 2nd day. The lower intensity of fluorescence emission could probably result from the increased photosynthesis and increased NPQ. The optimal temperature for photosynthesis for well-watered sugar beet is around 25°C (Ober and Rajabi, 2010). The air temperature was 23.8 °C on June 28 which would benefit sugar beet photosynthesis. In addition, stronger NPQ was triggered to cope with the higher temperature on June 28, indicated by the increased PRI within irrigated plots. Another possible reason could be that irrigated sugar beet plants physiologically partly or even fully recovered from the water stress, suggested by the decreased T_c (Figure 4.7c). Therefore, the quantum yield of PSII increased and fluorescence emission efficiency decreased.

Differences in response to irrigation were found between SIF indices at 760nm and 687nm (Figures 4.9 and 4.10). First, changes of $SIF_{760norm}$ and $SIF_{687norm}$ differed in irrigation and non-irrigation plots. Canopy structure differences may be the main reason for different change pattern as it affects the scattering and reabsorption throughout the canopy after emissions (Verrelst et al., 2015). Table 4.4 also shows that ΔNDVI was significantly related relate to $SIF_{760norm}$ and $SIF_{687norm.}$ $SIF_{760norm}$ had a smaller decrease in the irrigation plots than in non-irrigation plots, which could be explained by the stronger scattering effect within the dense canopy of recovered sugar beet plants. Similarly, the structural recovery effect also contributed to stronger reabsorption for $SIF_{687norm}$ detected from irrigated plants, resulting in a larger decrease in $SIF_{687norm}$ compared with non-irrigation plants. SIF_{yield} can give further insights into fluorescence emission efficiency (ΦF) and the fraction of emitted SIF that escapes from the canopy (f_{esc}) by removing the effect of APAR (Sun et al., 2015). In contrast to $SIF_{760norm}$,

$SIF_{760yield}$ observed from irrigated plants decreased more, which might imply that the scattering effect within the irrigated plant canopies enhanced f_{esc} at 760nm. f_{esc} at 760 nm can be estimated using observations of FCVI and NIRv (Yang et al., 2020; Zeng et al., 2019). Since both FluorSpec and Rikola data do not fully cover the range from 400 to 700 nm used for the calculation of FCVI, f_{esc} was estimated using NIR_{V}. However, we found the f_{esc} estimate not reasonable (results not shown) and we attributed this to the scale of observation. Zeng et al. (2019) tested the SIF-NIRv relationship using satellite measurements and we suggest more research should focus on the f_{esc} at proximal and field levels. The similar decline within non-irrigation plots both in $SIF_{760norm}$ and $SIF_{760yield}$ indicated that the irrigation treatment had a significant effect on $SIF_{760yield}$. The similar trends of $SIF_{687yield}$ and $SIF_{687norm}$ might indicate that the canopy structural changes less affect the reabsorption of SIF_{687}. Irrigation treatment had a significant effect on $SIF_{687yield}$ (p-value < 0.05; Table 4.3). SIF_{ratio} can significantly distinguish the irrigated and non-irrigated sugar beet plants and SIF_{ratio} of stressed sugar beets showed a significant increase on June 28 (Figure 4.9e, Table 4.3). A higher SIF_{ratio} appearing in sugar beet fields under water deficit was also observed by Wieneke et al. (2018). Even though we cannot exclude that the significant change of the SIF_{ratio} was due to the reduced re-absorption of $SIF_{687norm}$ and decreased scattering of $SIF_{760norm}$., this signal might be a potential indicator of sugar beet actual physiological status as this ratio varies in response to the changes in the photosynthetic activity of the two photosystems (Agati et al., 1995; Yang et al., 2019).

4.4.3. Response of SIF indices to combined water and heat stress on July 23 and 24

SIF indices did not significantly track the changes induced by the irrigation treatment on July 24 when sugar beet plants were stressed by the water shortage and extremely high temperature. Different from findings on June 28, we observed an increase in SIF_{norm} and SIF_{yield} at both 687nm and 760nm over both irrigated and non-irrigated sugar beet canopies, except for a slight decrease in $SIF_{760norm}$ within non-irrigated plots. The different physiological/biochemical effects of sugar beet plants caused by the combined stress could be the main reason. On July 23 and 24, the combined stress could be considered a short term “flash” drought, induced by a rainfall reduction and abnormally high temperatures (Mo and Lettenmaier, 2015). We speculate that to cope with the flash drought, sugar beet plants reduced their stomatal conductance, leading to an increase both in photorespiration and NPQ, and a substantial decrease in the photochemistry in the light reaction centre of photosynthesis (PQ) (Flexas and Medrano, 2002; Helm et al., 2020). Some studies at proximal tower level showed a clear response of stomatal conductance and net photosynthesis to water stress at leaf level or proximal tower level, but they found SIF may not track changes in photosynthesis in response to drought stress (Helm et al., 2020; Marrs et al., 2020). Fluorescence relates to the photochemistry in the light reactions of photosynthesis. At the leaf level, the response of the light reactions may be muted compared to the stomatal response, as increases in NPQ and the proportion of open PSII reaction centres compensate for decreases in photochemistry, dampening the impact on SIF (Gu et al., 2019; Schlau-Cohen and Berry, 2015). According to Helm et al. (2020), the complementarity between PQ and NPQ likely dominates this trade off under drought stress, and the decrease in PQ may be compensated by the increase in NPQ, thus affecting fluorescence relatively little. On the other hand, severe heat stress can induce damage to chlorophyll pigments, a decline in leaf nitrogen content, blockage of PSII reaction centre and decrease in quantum efficiency of electron flow, and down-regulation of PSII photochemistry, all of which can result in a reduction in photosynthesis. PSII is very responsive to temperature and its activity is greatly influenced and even partially terminated under high-temperature stress (Camejo et al., 2006). Photodamage caused by the combined stress might be a possible reason to explain why $SIF_{687norm}$, $SIF_{760yield}$, and $SIF_{687yield}$ increased in both irrigation and non-irrigation plots.

The response of SIF to the combined stress could also be affected by the canopy structural changes of sugar beet plants. Due to the heat wave, sugar beet plants did not structurally recover from the severe stress after the irrigation (Figures 4.8a and S4.3f, h), resulting in a reduction in APAR which probably decreased fluorescence emission. We assume leaf physiological changes might dominate the response of SIF under heat stress in July. In plot B2–, sugar beet plants were largely damaged (Figure S4.3h). This can affect fluorescence emission efficiency and decouple the relationship between fluorescence and photosynthesis. The decoupling relationship might explain the increase in most SIF indices, and it might be further inferred that under this severe stress, more absorbed energy was emitted as fluorescence. Some other factors might also contribute to the lack of significance in July, e.g. measurement uncertainty in UAV observations, spatial variation of SIF due to heterogeneity in soil properties and the limited number of repetitions (and plots).

It is hard to explain the performances of SIF indices in response to severe stress (e.g. the combined stress in July) since SIF is a subtle signal. Even at leaf level, the response of SIF to water stress is complicated by several factors (Helm et al., 2020). As suggested by Marrs et al. (2020), to take full advantage of the information provided by remotely measured chlorophyll fluorescence, a full picture of energy partitioning on the ground is needed. This includes a need to better characterize energy dissipation dynamics. As drought stress leading to an upregulation of NPQ is a relatively well-estimated phenomenon, we expected increased PRI in non-irrigated plots. Interestingly, except for a slight increase in PRI in B1–, PRI decreased somewhat in other plots (Figure 4.8b). PRI also did not respond significantly to the irrigation treatment. Note that PRI is strongly affected by canopy structure and leaf pigmentation and can confound links to NPQ behaviour (Gitelson et al., 2017; Schickling et al., 2016). Therefore, PRI should be carefully interpreted to avoid an ill-conditioned situation while exploring the vegetation's physiological response to water stress. More information is needed to assist SIF and PRI interpretation, e.g. field measurements related to leaf water vapor and NPQ. NDVI, TCARI/OSAVI, and temperature index (T_c) significantly tracked the changes of the irrigated sugar beet plants under both different stress conditions. In June, the significance of the correlation between these indices and SIF indices also indicated the potential of SIF indices to detect water deficit, particularly SIF_{687} and its indices and SIF_{ratio} (Table 4.4). However, on July 24, the severe stress might already damage the photosynthetic apparatus of the sugar beet plants. Therefore, as discussed in the introduction, our results also show that the structural, pigment, and temperature index could not provide direct and timely information on crop photosynthetic functioning (Table 4.4).

4.4.4. Implications

There is no universal relationship between photochemistry and fluorescence emission under stress conditions, meaning that fluorescence can either increase or decrease depending on the nature of the stressor and the physiological status of the plants (Porcar-Castell et al., 2014). Structural factors further contribute to TOC SIF observations and complicate their interpretation. Our findings suggest that the used SIF indices could indicate early stress but might not be able to provide added value to track changes of photosynthesis under severe stress. Calderón et al. (2013) also found that SIF had a significant response to verticillium wilt (p-value < 0.05) at the early stage of disease development only at canopy level. The provided information might depend on the imposed environmental stress levels and to what extent SIF responds to the stress remains unclear. As Helm et al. (2020) suggested, the value of SIF as an accurate estimator of photosynthesis may decrease during mild stress events of short duration, especially when the response is primarily stomatal and not fully coupled with the light reactions of photosynthesis. Additional measurements could give further insight into the ongoing processes. First, leaf measurements of photosynthetic parameters, e.g. gas exchange, the quantum yield of PSII, and NPQ, can provide insights into the mechanism linking fluorescence and photosynthesis under different severity levels of water stress. Second, ground SIF or active leaf fluorescence measurements can validate UAV-SIF, which increases the robustness of the results as SIF observations from remote sensing are subtle and complicated by several factors (Pinto et al., 2017; Lu et al., 2020). Future studies on water stress at different levels and combined water deficit and high-temperature stress at different levels can provide more insights into the potential of UAV-based SIF to detect environmental stress. Furthermore, modelling approaches can describe SIF-relevant processes including absorption, emission, scattering, and re-absorption, and therefore can also provide deeper insights into the effects of plant canopy structural, biochemical, and physiological factors on SIF response to water stress (Yang et al., 2019).

4.5. Conclusion

The main purpose of this work was to understand the response of UAV-based SIF indices (SIF_{norm} and SIF_{yield} at two O_2 absorption bands and SIF_{ratio}) and to evaluate their potential for water stress detection. Additional remote sensing information such as canopy temperature and vegetation indices including NDVI, PRI, and TCARI/OSAVI were used to characterize the stress status and assist the interpretation of the response of SIF indices to the irrigation treatment. On June 28, irrigated plants and non-irrigated plants showed significant differences in $SIF_{760norm}$, $SIF_{687norm}$, $SIF_{687yield}$, and SIF_{ratio}. This significant irrigation effect was also observed in the vegetation index and canopy temperature measurements. Apparently, water stress was not so severe in June that irrigation had an immediate effect on canopy structure and temperature, not only on photosynthesis. On July 24, the situation was quite different. In addition to water stress, a heat wave also caused severe heat stress. Only $SIF_{760norm}$, $SIF_{687norm}$, and SIF_{ratio} weakly tracked the changes induced by irrigation in July. Irrigation effects on the vegetation index and canopy temperature measurements also were less significant in comparison to June. This study further confirms the capacity of SIF acquired by a UAV system to detect early stress at the field level. Further investigations are necessary to give a comprehensive understanding of the potential of UAV-based SIF to detect environmental stress at different levels and to support crop management in the context of precision agriculture.

SUPPLEMENTARY MATERIALS

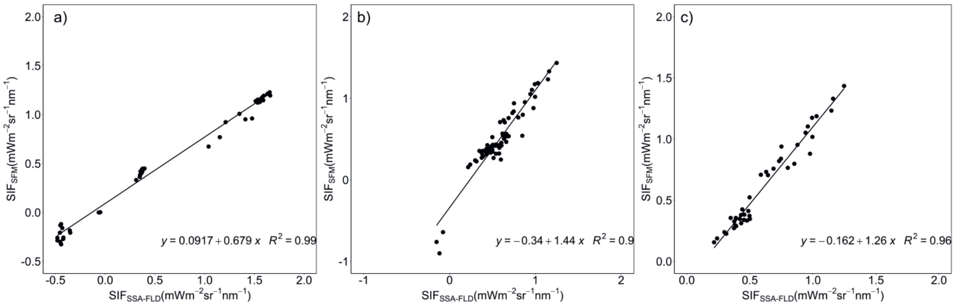

Figure S4.1. The linear relationship between SIF retrieved by SSA-FLD ($SIF_{SSA-FLD}$) and SIF retrieved by SFM (SIF_{SFM}) at O_2-A over vegetation targets (low green grass and green winter wheat) and non-fluorescence targets (bare soil and 99% white panel) (a), at O_2-B over vegetation canopies (low green grass, green winter wheat, well-watered sugar beets and stressed sugar beets) and non-fluorescence targets (bare soil) (b), and at O_2-B over vegetation canopies (green winter wheat, well-watered sugar beets and stressed sugar beets) (c).

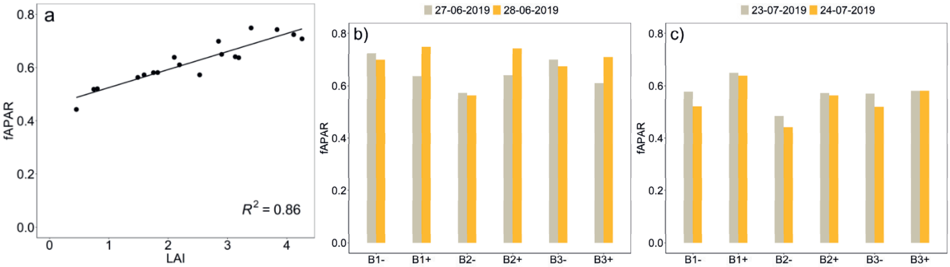

Figure S4.2. Correlation between fAPAR and LAI field measurements for the four measurement dates combined (a), fAPAR on June 27 and on June 28 (b), and fAPAR on July 23 and July 24 (c). B1, B2, B3 refer to block1, block2, and block3 in the sugar beet field. + indicates an irrigation treatment applied to the plot and – indicates no irrigation treatment in the plot. Irrigation was given to B1+, B2+, and B3+ on the evenings of June 27 and July 23.

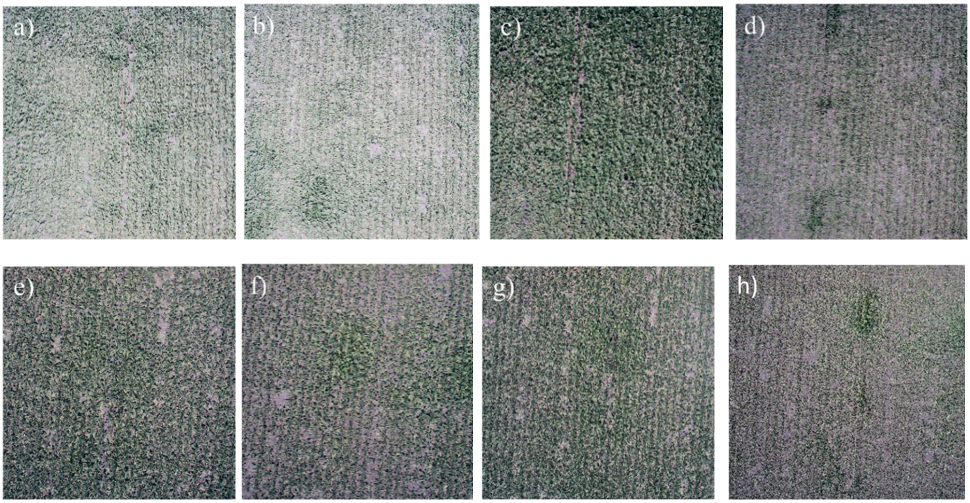

Figure S4.3. Sugar beets within B2+ and B2- on June 27 (a) and (b), on June 28 (c) and (d), on July 23 (e) and (f), and on July 24 (g) and (h). Irrigation was given to B1+, B2+, and B3+ on the evenings of June 27 and July 23.

Table S4.1. Spectral band centres (BC, nm) and full width at half maximum (FWHM, nm) of Rikola camera.

BC	515	530	550	570	630	670	680	700	710	720	730	740	750	780	800	870
FWHM	14	14	13	13	13	13	13	13	13	13	13	13	13	13	13	17

Table S4.2. Descriptive statistics (mean values ± standard deviations) of NDVI and T_c at the plot level on June 27, June 28, July 23, and July 24. B1, B2, B3 refer to block1, block2, and block3 in the sugar beet field. + indicates an irrigation treatment and – indicates non-irrigation treatment in the plot. Irrigation was given to B1+, B2+, and B3+ on the evenings of June 27 and July 23.

Plots	June 27		June 28		20190723		20190724	
	NDVI	T_c	NDVI	T_c	NDVI	T_c	NDVI	T_c
B1+	0.740±0.083	20.7±4.5	0.827±0.053	20.6±2.3	0.752±0.075	33.2±2.4	0.742±0.081	33.5±2.0
B1-	0.806±0.076	17.7±4.3	0.789±0.074	25.3±3.7	0.674±0.110	35.5±3.0	0.602±0.115	40.3±2.1
B2+	0.747±0.069	24.5±3.2	0.824±0.048	20.8±2.1	0.676±0.085	36.8±1.7	0.663±0.095	35±1.3
B2-	0.674±0.091	26.6±4.0	0.662±0.094	30.3±4.1	0.549±0.109	38.6±2.5	0.473±0.106	44.0±1.9
B3+	0.716±0.083	27.1±3.7	0.798±0.060	22.3±2.2	0.685±0.087	37.6±1.2	0.681±0.100	32.7±1.5
B3-	0.792±0.064	24.5±3.3	0.774±0.064	26.0±3.6	0.670±0.100	37±2.3	0.603±0.106	37.1±2.1

Table S4.3. Descriptive statistics (mean values ± standard deviations) of $SIF_{760norm}$ and $SIF_{687norm}$ at the plot level on June 27, June 28, July 23, and July 24. SIF_{norm} was multiplied by 100 to better discriminate the differences in the small values, and the unit is $10^2*\mu m^{-1}\ sr^{-1}$. B1, B2, B3 refer to block1, block2, and block3 in the sugar beet field. + indicates an irrigation treatment applied to the plot and – indicates non-irrigation treatment in the plot. Irrigation was given to B1+, B2+, and B3+ on the evenings of June 27 and July 23.

Plot	June 27		June 28		July 23		July 24	
	$SIF_{760norm}$	$SIF_{687norm}$	$SIF_{760norm}$	$SIF_{687norm}$	$SIF_{760norm}$	$SIF_{687norm}$	$SIF_{760norm}$	$SIF_{687norm}$
B1+	0.600±0.028	0.471±0.054	0.549±0.065	0.328±0.030	0.491±0.083	0.338±0.057	0.638±0.092	0.451±0.044
B1-	0.655±0.074	0.407±0.071	0.558±0.058	0.398±0.060	0.436±0.085	0.352±0.043	0.421±0.066	0.447±0.097
B2+	0.520±0.043	0.415±0.025	0.516±0.034	0.265±0.032	0.430±0.034	0.362±0.035	0.523±0.031	0.488±0.059
B2-	0.428±0.032	0.415±0.062	0.363±0.024	0.372±0.053	0.301±0.064	0.314±0.076	0.282±0.027	0.392±0.063
B3+	0.557±0.023	0.455±0.053	0.492±0.055	0.274±0.026	0.459±0.043	0.384±0.052	0.496±0.049	0.448±0.071
B3-	0.585±0.035	0.394±0.031	0.477±0.030	0.311±0.034	0.429±0.027	0.372±0.042	0.412±0.054	0.416±0.082

Chapter 5

Decoupling crop physiological and non-physiological responses to water stress from UAV-based sun-induced fluorescence observations with a radiative transfer model

This chapter is based on:
Na Wang, Peiqi Yang, Jan G.P.W. Clevers, Sebastian Wieneke, Lammert Kooistra. "Decoupling crop physiological and non-physiological response to water stress from UAV-based sun-induced fluorescence observations with a radiative transfer model". *Under review.*

Abstract

Sun-induced chlorophyll fluorescence (SIF) can potentially indicate plant physiological changes caused by water stress due to its physiological connection with photosynthesis. SIF response to crop physiological alterations under water stress is complicated by the concurrent changes in biochemistry and morphology. This study aims to disentangle the physiological effect from the non-physiological effect on SIF variations caused by water stress, providing more direct insights into the mechanism of SIF response to stress. We parameterized the radiative transfer model SCOPE with measurements of top of canopy (TOC) reflectance and SIF to decouple the joint effects on TOC SIF in a sugar beet crop. SIF and reflectance data were acquired over irrigated and water-stressed plots using an Unmanned Aerial Vehicle (UAV) on two consecutive days. The non-physiological response was quantified with SCOPE by fitting the model parameters to the TOC reflectance measurements. Subsequently, SIF emission yield (ΦF) was estimated using SIF measurements to represent the actual physiological status. The results demonstrate that SIF variation caused by water stress both at 687 nm and 760 nm was co-affected by the physiological alterations in ΦF and non-physiological changes in canopy structure and leaf biochemistry. Changes in ΦF had a significant effect on variations in TOC SIF caused by water stress (p-value < 0.05 at both 687 nm and 760 nm). In contrast, non-physiological contribution to SIF variations was lower and this was mainly due to the weak co-effect of the fraction of absorbed photosynthetically active radiation (fAPAR) and the fluorescence escape fraction (f_{esc}) on SIF responses. This study provided further insights into plant physiological status under water stress and into the scalable quantitative use of SIF from the leaf to the ecosystem level.

5.1. Introduction

Plant photosynthetic activity is affected by many adverse environmental stress factors (Evans and Fischer, 1999; Saibo et al., 2009). Limited water supply causes physiological, biochemical, and morphological changes in plants that induce a reduction in photosynthesis (Lesk et al., 2016; Reddy et al., 2004), and thereby it is a major abiotic factor that adversely affects agricultural crop production worldwide. The drastic and rapid changes in the global climate have aggravated this situation (Lobell et al., 2011). There is an urgent need for remote sensing products that track the photosynthetic changes in space and in time for sustainable crop management. Vegetation indices (VIs) based on the visible and near-infrared (VNIR) spectral region can be used to quantify crop responses by mapping variation in canopy structure and leaf biochemistry caused by water stress (Atzberger, 2013). A limitation of this approach is that they do not provide a direct link to photosynthetic functioning. For instance, greenness-based VIs cannot capture rapid and short-term adaptations in the photosystems to changing environmental conditions (Meroni et al., 2011; Porcar-Castell et al., 2014; Wieneke et al., 2016; Xu et al., 2021).

Sun-induced chlorophyll fluorescence (SIF) is considered as a direct measure of the photosynthetic rate (Frankenberg and Berry, 2018; Meroni et al., 2009; Porcar-Castell et al., 2014). SIF emission is one of the three main pathways of the light energy absorbed by leaf chlorophyll, the other two being photosynthesis (photochemical quenching, PQ) and heat dissipation (non-photochemical quenching, NPQ) (Krause and Weis, 1991; Lichtenthaler and Rinderle, 1988). Responses of SIF during water stress have been largely explored at the ground level (e.g. Helm et al., 2020; Marrs et al., 2020; Paul-Limoges et al., 2018; Xu et al., 2018), at low altitude with Unmanned Aerial Vehicles (UAVs) (e.g. Xu et al., 2021), at airborne level (e.g. Panigada et al., 2014; Pinto et al., 2020; Wieneke et al., 2016), and at satellite level (e.g. Lee et al., 2013; Sun et al., 2015; Yoshida et al., 2015).

However, variations in SIF observations cannot be directly interpreted as physiological changes because of the confounding effects of vegetation structure and biochemistry and of incoming radiation (Damm et al., 2015; Migliavacca et al., 2017; Van der Tol et al., 2016; Verrelst et al., 2015; Yang et al., 2020). This applies in particular to the interpretation of SIF under water stress, as plant response to water stress can be expressed by a variety of physiological, structural, and biochemical changes (Farooq et al., 2009; Gerhards et al., 2019). The observed top-of-canopy (TOC) SIF is the product of three processes, absorption of photosynthetically active radiation (APAR) by leaf chlorophylls, re-emission of a part of the absorbed energy as SIF, and the re-absorption and scattering of SIF within the canopy (Porcar-Castell et al., 2014; Van der Tol et al., 2014). In analogy to the conceptual scheme of the Light Use Efficiency (LUE) model (Monteith, 1977, 1972), the observed TOC SIF can be expressed as

$$SIF = PAR \times fAPAR_{chl} \times \Phi F \times f_{esc} \tag{5.1}$$

$fAPAR_{chl}$ is the fraction of PAR absorbed by chlorophyll in green leaves. ΦF is the fluorescence emission yield from all leaves in the canopy. It represents the fraction of absorbed energy that is not used for PQ and NPQ and is modulated by changes in the physiological status of plants (Porcar-Castell et al., 2014). f_{esc} is the fraction of the emitted fluorescence that escapes from the canopy in the viewing direction (Guanter et al., 2014b).

For a mechanistic interpretation of SIF under water stress, it is essential to differentiate effects of non-physiological variation from effects of photosynthetic functional variation on SIF. According to the LUE model, plant structure and leaf biochemistry control TOC SIF through $fAPAR_{chl}$ and f_{esc} (Dechant et al., 2020; Rossini et al., 2016; Yang et al., 2019), while the physiological status of photosynthesis affects TOC SIF via ΦF (Porcar-Castell et al., 2014; Wieneke et al., 2018). Therefore, to understand SIF variations under stress, $fAPAR_{chl}$ and f_{esc} can represent the plant structural and biochemical (non-physiological) effect (Dechant et al., 2022, 2020; Guanter et al., 2014), and ΦF can indicate the physiological effect (Celesti et al., 2018; Porcar-Castell et al., 2014).

Some reflectance-based physical approaches have been explored to elucidate the confounding factors of SIF. The normalization of SIF by $APAR_{chl}$ (often referred to as SIF yield) provides more direct information on the vegetation physiological status by excluding the impact of PAR absorption ($fAPAR_{chl}$) and incoming radiation (PAR) (Equation 5.1) (Dechant et al., 2020; Miao et al., 2018; Sun et al., 2015). Wieneke et al. (2018) and Li et al. (2020) attempted to empirically correct for canopy structure effects in SIF yield by dividing it by the modified triangular vegetation index 2 (MTVI2), which is related to LAI. More recently, f_{esc} at 760 nm was estimated using the fluorescence correction vegetation index (FCVI) and the near-infrared reflectance of vegetation (NIR_v) (Yang et al., 2020; Zeng et al., 2019) to account for canopy structural effects due to the scattering on far-red SIF (Chang et al., 2021; Dechant et al., 2020; Xu et al., 2021). ΦF can be derived using SIF and NIRv×PAR, allowing evaluating its contribution to SIF variations under stress (Chen et al., 2021; Kimm et al., 2021). These approaches allow rapid decoupling of the canopy structural and functional regulation of SIF and have enhanced our understanding of the physiological information in SIF. The SIF radiative transfer within a canopy complicates the quantification of ΦF and f_{esc} from canopy level measurements, with increasing complexity when moving from field to airborne and satellite observations (Celesti et al., 2018; Van der Tol et al., 2019). However, these approaches are derived by radiative transfer modelling with a number of assumptions and simplifications or with semi-empirical approaches (Liu et al., 2019; Yang et al., 2020; Zeng et al., 2019). In addition, they cannot easily disaggregate red SIF into the physiological and non-physiological signals due to the within-leaf scattering and re-absorption of red SIF within the leaf or inside a plant canopy (Van der Tol et al., 2019; Van Wittenberghe et al., 2015; Yang and Van der Tol, 2018).

Radiative transfer models (RTMs) offer a comprehensive complementary method to facilitate the exploitation of SIF (Verrelst et al., 2015) and may serve to disentangle the physiological effect from other effects. An approach of using RTMs and TOC reflectance has been applied to explore the physiological information contained in TOC SIF (Celesti et al., 2018; Van der Tol et al., 2016; Yang et al., 2019). Vegetation biochemical and structural parameters can be retrieved by means of inverting an RTM using measured reflectance data (Jacquemoud et al., 2009), and further are used in a fluorescence RTM to simulate TOC SIF (Van der Tol et al., 2016). The model called Soil-Canopy Observation Photosynthesis and Energy fluxes (SCOPE) describes the radiative transfer processes of incoming radiation and emitted SIF in a canopy, and therefore can estimate $fAPAR_{chl}$, f_{esc}, and ΦF (Van der Tol et al., 2009; Yang et al., 2021b). SCOPE has provided a better understanding of leaf biochemical and canopy structural effects on SIF (Verrelst et al., 2015; Yang et al., 2019). Van der Tol et al. (2016) successfully inverted vegetation leaf and canopy parameters from TOC reflectance using SCOPE and subsequently simulated far-red SIF with the inverted parameters. They concluded that this approach reproduced the far-red SIF response to the chemical blocking of photosystem II. Yang et al. (2019) estimated the biochemical and structural effects on TOC SIF with a constant ΦF using a combination of SCOPE and TOC reflectance. Celesti et al. (2018) quantified ΦF as a direct product of a numerical inversion of the SCOPE model using hyperspectral reflectance and effectively discriminated the effects of pigment content and leaf/canopy structural properties from physiological properties. Their findings showed that RTMs, hyperspectral reflectance, and the SIF signal together can reveal both the dynamics of vegetation structure and of functioning in a given situation.

The goal of this study is to decouple and quantify physiological and non-physiological responses of a sugar beet crop to water stress using an RTM modelling approach. Hyperspectral reflectance and SIF observations were acquired with a UAV platform over a sugar beet field before and after irrigation. We utilized SCOPE, TOC reflectance, and SIF observations to estimate canopy structural and leaf properties and the physiological factor (ΦF). The estimated vegetation biophysical parameters and ΦF were then used to simulate TOC SIF for four synthetic scenarios to unravel the physiological and non-physiological effects induced by water stress on SIF response.

5.2. Materials and methods

5.2.1. Experimental setup

A field experiment was conducted within a sugar beet field (*Beta vulgaris* L., var. Urselina) during the 2019 growing season. The study site was located at Unifarm, the agricultural experimental research farm of Wageningen University & Research, the Netherlands (51° 59' 17.64" N, 5° 39' 21.17" E). The soil texture was sandy loam. Sugar beet (50 cm between rows and 18 cm within a row) was sown on April 1, 2019 (day of the year (DOY): 91) and harvested on November 15, 2019 (DOY 319). To explore crop response to water stress, an experimental design was set up with three blocks. Each block consisted of 2 plots (12 m × 30 m). There were 3 plots with an irrigation treatment and 3 plots without it among these 6 plots (Figure 5.1a).

As water deficits in the middle of the growing period strongly decrease sugar beet yields (Steduto et al., 2012), we decided to experiment in the middle of the season. In June, rainfall occurred only before June 22. Figure 5.1b shows the peak of the maximum air temperature that occurred on June 25 (34 °C). Soil moisture (SM, volumetric water content, vol%) was measured and plant status was assessed visually once a week to determine the required irrigation moment. SM at a depth of 65 mm was measured using an ML3 ThetaProbe Soil Moisture Sensor (Delta-T Devices, UK). On June 25, the average soil moisture was 3.5 vol% in irrigation plots and 3.8 vol% in non-irrigated plots, respectively, and sugar beet leaves were visibly wilted. Two reports on the soil properties in this study field in 2018 from Wageningen Research Unifarm showed that crops should be irrigated when the soil moisture is below 7.5 vol%. Therefore, sugar beet plants within the irrigated plots were irrigated for 90 minutes on the evening of June 27. SM was measured within the six plots on June 27 (Day 1) and in the three irrigated plots on June 28 (Day 2).

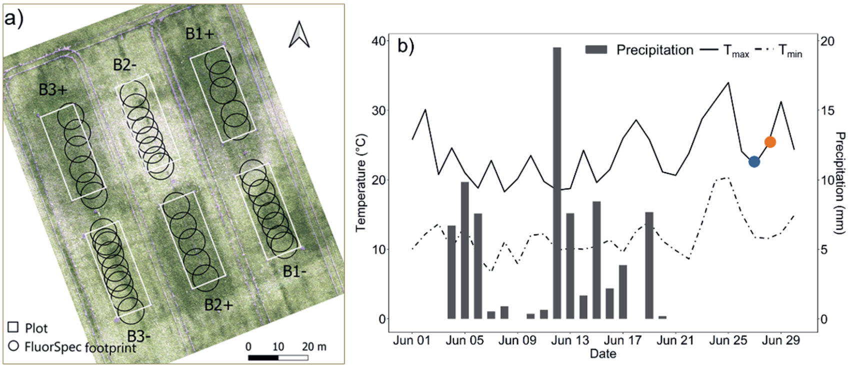

Figure 5.1. a) Location of the experimental plots at Unifarm of Wageningen University, Wageningen, the Netherlands, and b) daily minimum air temperature (T_{min}, °C), daily maximum air temperature (T_{max}, °C), and daily precipitation (mm) in June 2019 measured by the weather station "De Veenkampen" (2.6 km from the study site). In Figure 5.1a, B1, B2, B3 refer to block1, block2, and block3 in the sugar beet field. + indicates an irrigation treatment applied to the plot and – indicates no irrigation treatment. White rectangles refer to plot boundaries. Black circles refer to FluorSpec footprints (8.8 m in diameter). The background image is a pseudo-RGB composite using Rikola bands at 650, 550, and 514 nm acquired on June 28 (Day 2). Blue and yellow circles in Figure 5.1b indicate June 27 and 28, 2019, respectively.

5.2.2. UAV data acquisition and processing

UAV flights were performed on June 27 (Day 1) and 28 (Day 2), which were the days before and after the irrigation event, respectively. The flights were executed close to solar noon under clear sky conditions and lasted about 30 minutes on each date. The meteorological conditions during the UAV campaigns on the two days are shown in Table 5.1.

Table 5.1. The meteorological conditions during the UAV flights on Day 1 and Day 2. The meteorological data was from the weather station "De Veenkampen" (2.6 km from the study site).

Parameters	Day 1	Day 2
Acquisition time (local)	13:35	13:40
Sun zenith angle (SZA, °)	28.68	28.73
Air temperature (T_a, °C)	21.51	23.48
Wind speed (m s^{-1})	2.68	2.53
Incoming shortwave radiation (R_{in}, W m^{-2})	798.85	795.00
Incoming longwave radiation (R_{li}, W m^{-2})	358.19	367.71

5.2.2.1. FluorSpec fluorescence observations

Fluorescence measurements were acquired by the FluorSpec system mounted on a DJI S1000+ UAV platform (DJI, China). A QE Pro spectrometer (Ocean Insight Inc., Dunedin, FL, USA) was used for SIF retrieval, configured with a full width at half maximum (FWHM) of 0.31 nm, a spectral sampling interval of 0.16 nm, and a spectral range of 640–800 nm. This allows SIF retrieval in two O_2 absorption bands. The field-of-view (FOV) of a down-looking bare optic fiber is 25°. The irradiance channel is equipped with a cosine corrector to collect solar irradiance from a hemispherical FOV (180°). For more details on the FluorSpec system, see Wang et al. (2021).

The UAV was programmed to fly 20 m above ground level (AGL) over the centreline of each block, with a horizontal speed of 1 m s^{-1} from waypoint to waypoint. In this configuration, the spectroradiometer sampled a circular area with a diameter of 8.8 m on the ground at every measurement and the sampling distance was 3.5 m. Each flight lasted around 5 minutes as the FluorSpec passed over the six sugar beet plots (Figure 5.1).

Spectral data were converted from digital numbers (DN) to calibrated radiometric values (Wm^{-2} sr^{-1} nm^{-1}) with custom Matlab scripts (Wang et al., 2021). First, measured raw spectra were converted to at-sensor irradiance and radiance by removing the dark current, dividing by integration time, and multiplying the DN values with the radiometric calibration coefficient per wavelength. Secondly, laser rangefinder and the FluorSpec GNSS data were processed to obtain target-sensor distance and sensor position information, respectively. Next, the at-sensor irradiance and radiance were converted to their TOC equivalents by applying an atmospheric correction using the MODerate resolution atmospheric TRANsmission (MODTRAN6) algorithm (MODTRAN®, Spectral Sciences, Inc). Afterward, preceding and following TOC irradiances were linearly interpolated using the GPS timestamp of the corresponding TOC radiance measurements to obtain TOC irradiance at precisely the same time as the TOC radiance measurement.

TOC SIF at the oxygen absorption bands A (760 nm, SIF_{760}) and B (687 nm, SIF_{687}) were retrieved using the Spectral Shape Assumption Fraunhofer Line Discrimination (SSA-FLD) method (Wang et al., 2021). The spectral ranges of 685–690 nm and 750-780 nm for O_2-B and O_2-A were selected, respectively. SSA-FLD has two assumptions: (i) that the fluorescence follows a known shape of the fluorescence spectrum, and (ii) that the reflectance factor of the target object behaves linearly over the utilized spectral region. SSA-FLD can be regarded as a special case of the spectral fitting method (SFM) (Mazzoni et al., 2012; Meroni et al., 2010).

The SFM function can only be applied to UAV-based FluorSpec measurements after parameter adjustment. A strong linear correlation between SIF retrieved by SSA-FLD and by SFM can be found in Figure S5.5. More details are described in Wang et al. (2021).

5.2.2.2. Rikola hyperspectral measurements

Hyperspectral images were acquired using a lightweight hyperspectral frame camera (Rikola Ltd., Oulu, Finland) onboard the same DJI S1000+ UAV platform. This camera is based on a Fabry-Perot interferometer (FPI) and was programmatically configured to register 16 narrow spectral bands in a range of 515-870 nm with FWHM varying between 13 and 17 nm (Table 5.2). These bands were chosen due to their importance to describe changes in biochemical (leaf chlorophyll content) and biophysical (e.g. leaf area index, ground cover, etc.) traits of vegetation at leaf and canopy levels (Clevers and Kooistra, 2011).

The UAV was flown at a height of 50 m AGL and a flying speed of 2 m s^{-1}. The flight duration was around 8 minutes. The HyperspectralImager 2.0 software converted the raw images in digital numbers (DN) into radiance (Wm^{-2} sr^{-1} nm^{-1}). The radiance images were then transformed into reflectance factor images using the empirical line method and the measurement of a Spectralon panel. The images were aligned and ortho- and georectified in Agisoft Metashape using ground control points (GCPs) that were surveyed with a real-time-kinematic (RTK)-enabled rover. Spectral signatures on Day 1 and Day 2 per plot are given in Figure S5.1.

Table 5.2. Spectral band centres (BC, nm) and full width at half maximum (FWHM, nm) of the Rikola camera.

BC	515	530	550	570	630	670	680	700	710	720	730	740	750	780	800	870
FWHM	14	14	13	13	13	13	13	13	13	13	13	13	13	13	13	17

5.2.2.3. WIRIS thermal data

Thermal images were acquired by the Workswell WIRIS 640 camera (Workswell s.r.o., Prague, Czechia) mounted on a gimbal on board an Altura AT8 octocopter. The thermal camera has a temperature sensitivity of 0.05 °C and a resolution of 640 × 512 pixels in a spectral range of 7.5-13.5 µm. It captures images that record actual temperature in a TIFF radiometric image format. The flight height was 40 m above ground level and the flight speed was 2 m s^{-1}. The flight lasted 12 minutes. Images were acquired with a pixel resolution of 0.5 cm. The calibrated TIFF images were processed and an orthomosaic of canopy temperature (T_c, °C) for the whole experimental area was constructed with Agisoft Metashape. The geo-referencing of the mosaic image was done manually in ArcMap 10.2 using the GCPs measured by RTK.

5.2.3. Modelling setup

The SCOPE model was used to study the physiological and non-physiological effects on TOC SIF introducedby water stress (Figure 5.2). Three RTMs embedded in SCOPE were used. Firstly, RTMo based on the SAIL model (Verhoef, 1984) produced reflectance at the canopy level. Next, the Fluspect model (Vilfan et al., 2016) was used to simulate reflectance and fluorescence spectra inside the canopy based on the distribution of APAR modelled with RTMo. Fluspect (Vilfan et al., 2016), based on PROSPECT (Jacquemoud and Baret 1990), simulated leaf reflectance, transmittance, and fluorescence emission of both forward and backward sides of the leaf. Finally, RTMf used the output of Fluspect to scale fluorescence from the leaf to the canopy (Van der Tol et al., 2019). The soil reflectance was modelled using the “Brightness-Shape-moisture” (BSM) model (Yang et al., 2021a).

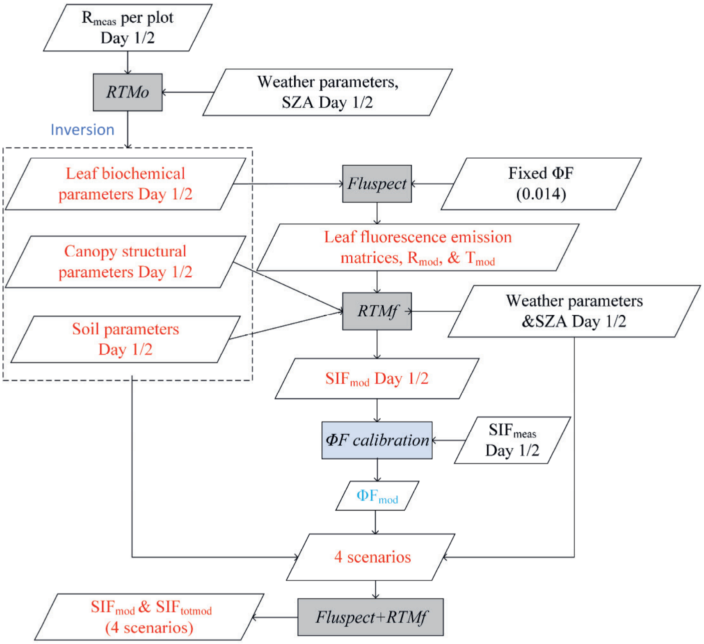

Figure 5.2. Flow diagram used for the simulation of TOC SIF scenarios. The parameters ‘R’, ‘T’, and ‘SZA’ refer to reflectance, transmittance, and sun zenith angle, respectively. RTMo, Fluspect, and RTMf (in grey-shaded background) are three submodules of SCOPE. Measurements are displayed in black and simulated variables in red. The suffixes “meas” and “mod” refer to measurements and simulations, respectively. Four scenarios (Table 5.4) were simulated to unravel the physiological and non-physiological effects on SIF response induced by water stress and are explained in section 5.2.3.3.

5.2.3.1. Retrieving leaf and canopy parameters

Soil, leaf optical, and canopy structural properties were inverted from the Rikola spectral measurements by inverting the reflectance routine of SCOPE (i.e. RTMo) per plot on Day 1 and Day 2. The model inversion routine was based on a Numerical Optimization (NO) method and minimized the cost function that estimated the differences between the measured and the simulated TOC reflectance in the Rikola spectral region from 500 nm to 900 nm (Celesti et al., 2018; Yang et al., 2019). The NO algorithm iteratively executes the RTMo model, varying all the free parameters within their range of variation (Table 5.3), until the residuals between the modelled and the measured apparent reflectance are minimized. The Root Mean Squared Error (RMSE) values were used to compare the simulated and the measured reference values.

Table 5.3 shows the key parameters used in the inversion routine. The Rikola reflectance was averaged per plot as the input in Fluspect and RTMo. Prior information is crucial to reduce the ill-posedness of the inverse problem. The average values of the soil moisture measurements on Day 1 in the irrigated and non-irrigated plots were 2.7 vol% and 2.9 vol%, respectively, and the averaged SM in irrigated plots on Day 2 was 16.2 vol%. The range of soil moisture volume percentage (SM) in the BSM model is 5 - 55 vol%. Therefore, in our model study, the initial SM was 5 vol% in all plots on Day 1 and in the non-irrigated plots on Day 2, and it was 15 vol% in the irrigated plots on Day 2. For the Fluspect model, the fluorescence emission yield (ΦF) was fixed at 0.014 (i.e. 40% above the default value of 0.01 in SCOPE for a dark-adapted leaf), which is a realistic value for steady-state fluorescence during daytime (Van der Tol et al., 2014). Dicotyledon crops have a high default leaf structure parameter (N) (Jacquemoud et al., 1996) which can range between values of 1.6 and 3 (Boren et al., 2019). Therefore, in our case, the N of the dicotyledon sugar beet was fixed at the middle value between 1.6 and 3 (2.3). Other Fluspect parameters were left free to vary during the inversion routine (Table 5.3). To reduce the ill-posedness, we narrowed the ranges of C_{ab} based on the growth stage of the sugar beet (Jay et al., 2017). We applied a spherical distribution to model the sugar beet canopy in all plots on Day 1 and in non-irrigated plots on Day 2 (LIDFa = -0.3; LIDFb = -0.15), while for the irrigated sugar beet canopy on Day 2 a distribution between spherical and erectophile (LIDFa = -0.5; LIDFb = -0.15) was applied. The leaf angle distribution was visually assessed based on the FluorSpec RGB images and available field photos (Figure S5.4), by visual comparison with six distribution functions given as examples in SCOPE documentation. Leaf area index (LAI) was left free to vary during the inversion routine.

Table 5.3. The ranges, assumed standard deviations (sd), and initial values of the main inverted parameters used in SCOPE.

Parameters	Definition	Unit	Range	Assumed sd	Initial value
C_{ab}	Chlorophyll a+b content	μg cm^{-2}	20-60	15	40
C_{ca}	Carotenoids content	μg cm^{-2}	0-25	4	10
C_{dm}	Leaf mass per unit area	g cm^{-2}	0.001-0.02	0.006	0.01
C_w	Leaf water content	cm	0-0.2	0.02	0.02
C_s	Senescent material	-	0-0.4	0.2	0.1
N	Leaf structure parameter	-	-	-	2.3
LAI	Leaf area index	cm^2 cm^{-2}	1-7	2	3
LIDFa	Leaf inclination distribution function parameter a	-	-1 - 1	0.1	-0.3/-0.5
LIDFb	Leaf inclination distribution function parameter b	-	-1 - 1	0.1	-0.15
SM	Soil moisture volume percentage	vol%	5-55	10	5/15

5.2.3.2. Estimating ΦF

The overall fluorescence emission efficiency within 650 800 nm can be estimated as the product of ΦF and a probability density function $\phi(\lambda_f)$ (Van der Tol et al., 2014; Vilfan et al., 2016). $\phi(\lambda_f)$ quantifies the probability that a fluorescence photon produced in the pigment bed has a wavelength λ_f (nm):

$$\Phi F(\lambda) = \Phi F \times \phi(\lambda_f) \tag{5.2}$$

Therefore, Equation 5.1 can be rewritten as

$$SIF_{meas}(\lambda) = PAR \times fAPAR_{chl} \times \Phi F \times \phi(\lambda_f) \times f_{esc}(\lambda) \tag{5.3}$$

We first treated ΦF as a constant in all plots on the two days. The value of ΦF was set to 0.014. To estimate ΦF, the parameters listed in Table 5.3 retrieved from section 5.2.3.1, and TOC SIF measurements per plot per day were the inputs in RTMf. According to Equation 5.3, SIF can be modelled as

$$\mathrm{SIF_{mod}}(\lambda) = \mathrm{PAR} \times \mathrm{fAPAR_{chl}} \times 0.014 \times \phi(\lambda_f) \times f_{esc}(\lambda) \quad (5.4)$$

The actual ΦF can be retrieved by combining Equations 5.3 and 5.5.

$$\Phi\mathrm{F}(\lambda) = (\mathrm{SIF_{meas}}(\lambda) / \mathrm{SIF_{mod}}(\lambda)) \times 0.014 \quad (5.5)$$

5.2.3.3. Methodology to decouple SIF responses to water stress

To unravel the physiological and non-physiological effects induced by water stress on SIF response, four synthetic scenarios were set up using the inverted vegetation and soil parameters, ΦF, and the meteorological parameters. Table 5.4 illustrates the parameters used to set up the four scenarios. Scenario 1 (S1) was calculated using these parameters of Day 1 to reproduce TOC reflectance (R_{meas}) and fluorescence (SIF_{meas}) on Day 1. Scenario 2 (S2) was calculated using these parameters of Day 2 to reproduce TOC reflectance (R_{meas}) and fluorescence (SIF_{meas}) on Day 2. Scenario 3 (S3) was set up using ΦF_{mod} of Day 1 and other inputs of Day 2 to only consider physiological changes in ΦF induced by irrigation. Scenario 4 (S4) used the retrieved canopy structural and leaf biochemical parameters on Day 1 and other inputs on Day 2 and aimed to only consider the non-physiological changes in canopy structure and leaf biochemistry caused by the irrigation.

SIF difference between two scenarios was made to decouple the joint physiological and non-physiological effects. The difference between simulated SIF in S1 (SIF_{S1}) and S2 (SIF_{S2}) (ΔSIF_{p+np}) represents the SIF changes induced by water stress considering both physiological and non-physiological effects. The difference between SIF_{S2} and SIF_{S3} (ΔSIF_{p}) represents SIF changes induced by physiological effects since the non-physiological parameters were the same in these two scenarios. The difference between SIF_{S2} and SIF_{S4} (ΔSIF_{np}) represents SIF changes induced by non-physiological effects (changes in canopy structure and leaf biochemistry) as the physiological factor ΦF_{mod} was kept the same in S2 and S4. We applied a linear regression between ΔSIF_{p} /ΔSIF_{np} and ΔSIF_{p+np} at 687 and 760 nm in all plots to evaluate the physiological and non-physiological impacts caused by water stress on SIF.

Table 5.4. Inputs in SCOPE for the four scenarios. Canopy structural and leaf biochemical parameters were inverted from the Rikola reflectance using SCOPE. ΦF_{mod} was estimated using SIF measurements. Meteorological data were measured by the weather station "De Veenkampen" (2.6 km from the study site).

Scenario (S)	Canopy structure & leaf biochemistry	ΦF_{mod}	Meteo	Aim
S1	Day 1	Day 1	Day 1	To reproduce field scenario and SIF_{meas} on Day 1
S2	Day 2	Day 2	Day 2	To reproduce field scenario and SIF_{meas} on Day 2
S3	Day 2	Day 1	Day 2	To simulate a scenario only considering ΦF changes due to water stress
S4	Day 1	Day 2	Day 2	To simulate a scenario only considering non-physiological changes due to water stress

5.2.4. SIF and SIF-related indices

Table 5.5 shows the indices used to disentangle the causes of SIF variation due to the water stress. PAR was not included as PAR values on Day 1 and Day 2 were almost the same (Table 5.1). $fAPAR_{chl}$ represents the ability of plant canopies to absorb incident PAR and can partly describe the influence of canopy structural and leaf biochemical changes caused by water stress on SIF (Asrar et al., 1984; Dechant et al., 2020). f_{esc} is the ratio of TOC SIF and total SIF (SIF_{tot}) which is emitted by all the leaves in vegetation canopies and represents the scattering and reabsorption effects within the canopy (Guanter et al., 2014). Therefore, $fAPAR \times f_{esc}$ is the non-physiological component (Dechant et al., 2020). ΦF is the physiological SIF emission yield of the canopy and can describe the physiological response of the crop under water stress. T_c has been considered a reliable proxy for plant water status monitoring due to leaf stomatal closure (Jackson et al., 1981). PRI can indicate the short-term changes in xanthophyll pigments and reflect the dynamic photoprotective mechanisms (NPQ) under stress conditions (Gamon et al., 1992, 1997). The normalized difference vegetation index (NDVI) is a proxy of leaf area index due to its relationship with the leaf area index (Rouse et al., 1973; Carlson and Ripley, 1997). T_c, PRI, and NDVI were used to assist the interpretation of SIF response under water stress.

Table 5.5. A summary of indices used in this study and the physiological/non-physiological effect indicated by the indices. All SIF-related indices were either direct outputs from the SCOPE simulation or estimated with the simulations. The photochemical reflectance index (PRI) and normalized difference vegetation index (NDVI) were calculated with Rikola reflectances. Canopy temperature (T_c) was from WIRIS thermal data. NDVI, PRI, and T_c were averaged per plot using pixel level values. P refers to the physiological effect and NP refers to the non-physiological effect.

Index	Source	Factors considered	Effects
SIF_{mod}	SCOPE output	PAR×$fAPAR_{chl}$, ΦF, and SIF scattering and absorption	P and NP
$fAPAR_{chlmod}$	$APAR_{chlmod}$/ PAR_{mod}	$fAPAR_{chl}$	NP
f_{escmod}	SIF_{mod} / SIF_{totmod}	SIF scattering or absorption	NP
$fAPAR_{mod}$*f_{escmod}	$fAPAR_{chlmod}$ × (SIF_{mod} / SIF_{totmod})	$fAPAR_{chl}$, SIF scattering and absorption	NP
ΦF_{mod}	$(SIF_{meas})/(SIF_{mod}) \times 0.014$	ΦF	P
T_c	Canopy temperature	Stomatal closure	P
PRI	$(R_{570} - R_{530})/(R_{570} + R_{530})$	Non-photochemical quenching (NPQ)	P
NDVI	$(R_{800} - R_{670})/(R_{800} + R_{670})$	Canopy structure	NP

5.2.5. Statistical analysis

To investigate the irrigation effect on simulated SIF and SIF-related indices, the difference between an index value (Table 5.5) on Day 1 (before irrigation) and Day 2 (after irrigation) was calculated per plot ($\Delta index_{mod}$). A paired t-test (Hsu and Lachenbruch, 2005) was applied to test the irrigation effect on the $\Delta index_{mod}$ value as compared to the non-irrigated plots per block. The null hypothesis (H_0) was that irrigation treatment had no significant effect on the $\Delta index_{mod}$. Spatial heterogeneities might exist between blocks, e.g. due to planting and management history. With a paired t-test, the irrigated and non-irrigated plots per block were compared and therefore the block effect was taken into consideration.

Furthermore, to investigate the mechanistic basis of the SIF response to water stress, we applied a linear regression between ΔSIF_{p+np} and the three components of SIF, i.e. modelled $\Delta APAR_{mod}$, Δf_{escmod}, and $\Delta \Phi F_{mod}$.

$$\Delta SIF_{p+np} = a1*\Delta APAR_{mod} + a2*\Delta f_{escmod} + a3*\Delta \Phi F_{mod} + a4 \quad (5.6)$$

Where a1, a2, a3, and a4 were estimated regression coefficients. The reported p-value of each explanatory variable (i.e. components of SIF) is related to its influence on ΔSIF_{p+np}.

5.3. Results

5.3.1. Response of canopy temperature, PRI, and SIF to the irrigation

On Day 1, average soil moisture (SM) in irrigated and non-irrigated plots was 2.84 and 3.19 vol%, respectively. On Day 2, SM in the irrigated plots significantly increased to 16.24 vol% (p-value < 0.05). Although no SM measurements were taken for non-irrigated plots on Day 2, SM of the non-irrigated plots was expected to vary little from Day 1 to Day 2. Canopy temperature (T_c) values on Day 1 were similar in both irrigated and non-irrigated plots. As expected, T_c of the irrigated crop decreased but increased for the non-irrigated crop from Day 1 to Day 2 (Figure 5.3a). PRI increased in both irrigated and water-stressed plots, but the increase and the variation were larger within non-irrigated plots (Figure 5.3b). Both T_c and PRI on Day 2 had a smaller variation in irrigated plots than in non-irrigated plots. SIF_{760} values were higher than SIF_{687} on both days. Both SIF_{687} and SIF_{760} declined on Day 2 in irrigated and non-irrigated plots. SIF_{687} decreased more in the irrigated plots, while SIF_{760} declined more in the non-irrigated plots. SIF_{687} and SIF_{760} on Day 2 had smaller variations in irrigated plots.

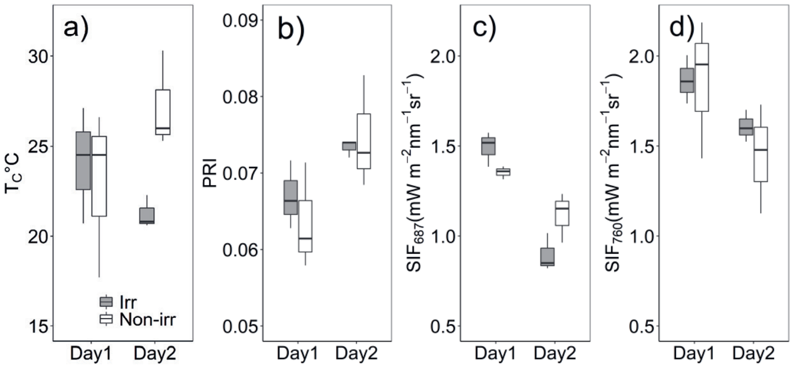

Figure 5.3. a) Canopy temperature (T_c), b) PRI, c) SIF_{687} and d) SIF_{760} in irrigated and non-irrigated plots on Day 1 and Day 2. "Irr" refers to irrigated plots and "Non-irr" refers to non-irrigated plots. An irrigation was given to the irrigated plots on the evening of Day 1. The figure was adapted from chapter 4.

5.3.2. Key parameters retrieved from Rikola reflectance

The measured TOC reflectance with Rikola was reproduced well by the SCOPE inversion approach with an RMSE between 0.006 and 0.01. As an example, the fitting between measured and simulated TOC reflectance in B1+ on Day 1 is shown (Figure 5.4a). A complete comparison of the measured and modelled reflectance spectra can be found in Figures S5.2 and S5.3. The modelled LAI correlated to NDVI derived from the Rikola camera reflectance with an R^2 of 0.90 (Figure 5.4b).

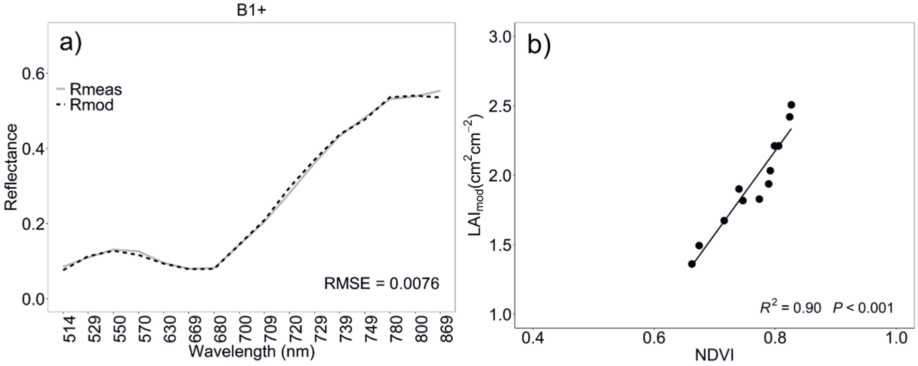

Figure 5.4. a) Example of the simulated reflectance (R_{mod}) and measured Rikola reflectance (R_{meas}) in plot B1+. b) Simple linear regression between NDVI calculated with Rikola reflectances and the modelled leaf area index (LAI_{mod}, cm^2 cm^{-2}) in SCOPE.

Figure 5.5 shows the inverted values of the key parameters that drive canopy-leaving SIF on the two days (Verrelst et al., 2015; Yang et al., 2019). On Day 2, the simulated soil moisture (SM_{mod}) in the irrigated plots increased significantly from 5.0 to 10.1 vol%, while the SM remained unchanged in non-irrigated plots, indicating the irrigation effect. LAI_{mod} was significantly different for the irrigated and non-irrigated canopies on Day 2, with an increase in the irrigated plots and a decrease in the non-irrigated plots. The other canopy structure parameter, average leaf angle (ALA) calculated from LIDFa as $ALA = 45 - 360 \times LIDFa \times \frac{1}{\pi^2}$ (Verhoef, 1998), also considerably varied between the two days. As expected, the leaf parameter C_{ab} showed no clear differences for the irrigated and non-irrigated plots on both Day 1 and Day 2.

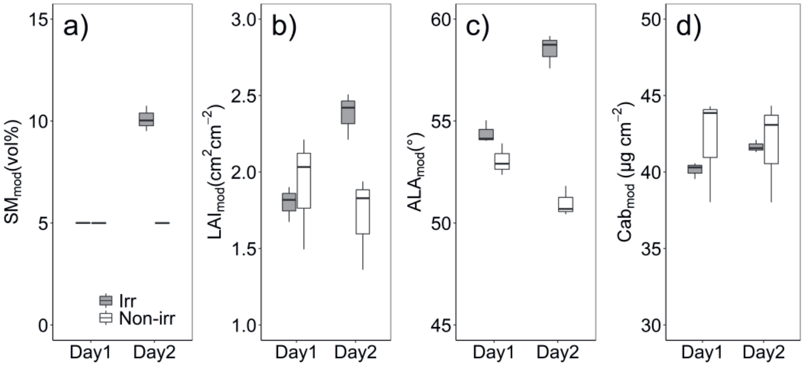

Figure 5.5. a) Modelled soil moisture (SM_{mod}), b) modelled leaf area index (LAI_{mod}), c) averaged leaf inclination angle (ALA_{mod} °) calculated from the simulated LIDFa, and d) modelled chlorophyll content (C_{abmod}) in irrigated and non-irrigated plots on Day 1 and Day 2. "Irr" refers to irrigated plots and "Non-irr" refers to non-irrigated plots. An irrigation was given to the irrigated plots on the evening of Day 1.

5.3.3. Physiological and non-physiological effects due to irrigation

Scenario 1 (S1) on Day 1 and scenario 2 (S2) on Day 2 (Table 5.4) were well reproduced. As a result, SIF_{687} and SIF_{760} simulations were the same as SIF_{687} and SIF_{760} measurements, respectively (Figure S5.7). Therefore, hereafter we used SIF_{S2} and SIF_{S1} to represent TOC SIF measurements on Day 1 and Day 2, respectively.

Figure 5.6 shows the linear regressions between ΔSIF_p or ΔSIF_{np} and ΔSIF_{p+np} at 687 and 760 nm in both irrigated and non-irrigated plots. At 687 nm, both ΔSIF_p and ΔSIF_{np} had a strong linear and positive correlation with ΔSIF_{p+np} (Figure 5.6a, b), and ΔSIF_p correlated better with ΔSIF_{p+np} than the ΔSIF_{np}. ΔSIF_p within all plots was negative and its absolute value was larger within irrigated plots. ΔSIF_{np} values were negative within irrigated plots and positive within non-irrigated plots. This distinction between irrigated and non-irrigated plots showed that SIF_{687} was able to capture both the physiological variations and non-physiological changes caused by water stress. ΔSIF_{np} values varied in a narrower range than ΔSIF_p values for both irrigated and non-irrigated plots. At 760 nm, ΔSIF_p positively correlated with ΔSIF_{p+np} ($R^2 = 0.96$) (Figure 5.6c). In contrast, ΔSIF_{np} negatively correlated with ΔSIF_{p+np} with $R^2 = 0.45$ (Figure 5.6d). ΔSIF_p within all plots were negative as ΔSIF_{p+np} and its absolute value was overall larger within non-irrigated plots, showing a physiological distinction in SIF_{760} between irrigated and non-irrigated plots. The non-physiological distinction was not clear, as ΔSIF_{np} varied over a small range from 0 to 0.2 mW m^{-2} $nm^{-1}sr^{-1}$.

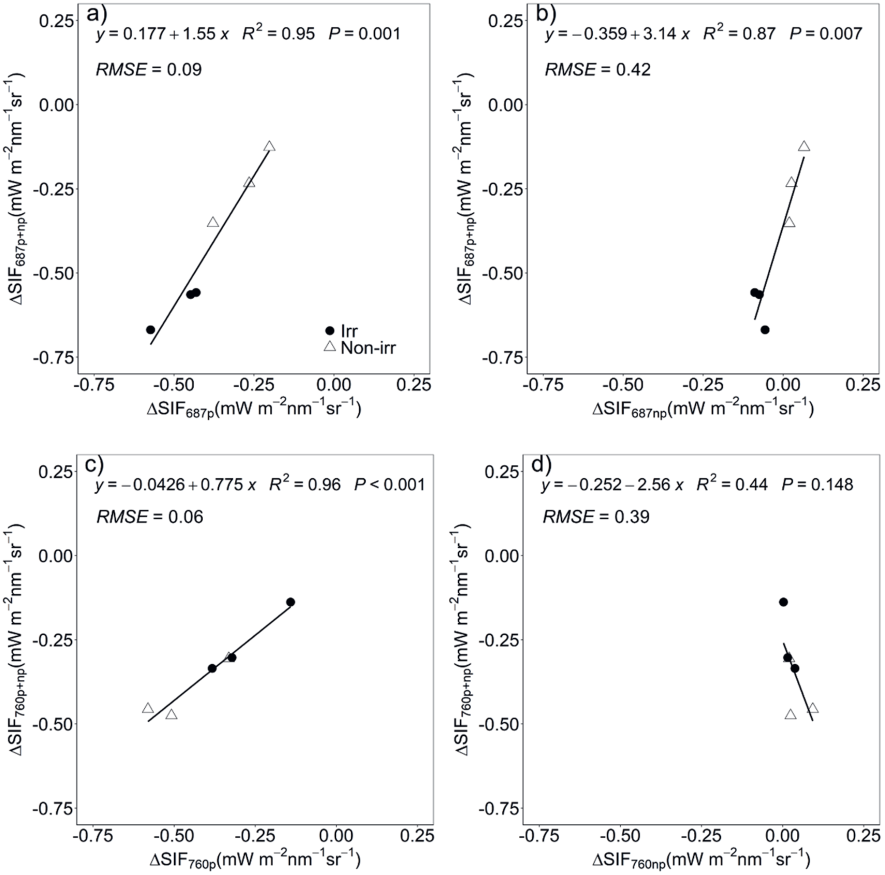

Figure 5.6. Comparison between ΔSIF caused by physiological changes (SIF_{S2}-SIF_{S3}, ΔSIF_p) and ΔSIF_{p+np} (SIF_{S2}-SIF_{S1}) a) at 687 nm and c) at 760 nm. Comparison between ΔSIF caused by non-physiological changes (SIF_{S2}-SIF_{S4}, ΔSIF_{np}) and ΔSIF_{p+np} (SIF_{S2}-SIF_{S1}) b) at 687 nm and d) at 760 nm. "Irr" refers to irrigated plots and "Non-irr" refers to non-irrigated plots. RMSE is shown in unit of mW m^{-2} $nm^{-1}sr^{-1}$

5.3.4. Modelled ΔSIF and ΔSIF-related indices and irrigation effects

Figure 5.7 shows the modelled ΔSIF and ΔSIF-related indices and the irrigation effect on them as compared to the non-irrigated plots per block. At 687 nm, the irrigation treatment had a significant impact on SIF_{687} and its indices with a p-value < 0.05 (Figure 5.7a-e). On Day 2, SIF_{mod}, and ΦF_{mod} showed a decrease in all plots, and the decrease was larger in the irrigated plots. f_{escmod} increased in non-irrigated plots and decreased in irrigated plots. As expected, $fAPAR_{chlmod}$ showed an increase in irrigated plots and a decrease in the non-irrigated plots on Day 2. At 760 nm (Figure 5.7f-j), the irrigation treatment significantly affected the SIF_{mod},

f_{escmod}, and $fAPAR_{chlmod}$ (p-value < 0.05). SIF_{mod} observed from the irrigated sugar beet plants had a smaller decrease. f_{escmod} increased in non-irrigated plots and decreased in irrigated plots. ΦF_{mod} of the irrigated plants had a smaller decrease and was slightly different from that of the water-stressed plants.

To better understand the physiological and non-physiological contribution, we tested the significance of the linear regression between the three components of SIF and ΔSIF indices (Table 5.6). At 687 nm, changes in ΦF_{mod}, f_{escmod}, and $fAPAR_{chlmod}$ all had a significant effect on ΔSIF_{p+np} and the effect of Φf_{mod} was the largest. At 760 nm, ΔSIF_{p+np} was significantly affected by the alterations in $\Delta\Phi F_{mod}$. Changes in Δf_{escmod} and $\Delta fAPAR_{chlmod}$ did not significantly relate to SIF variations from Day 1 to Day 2.

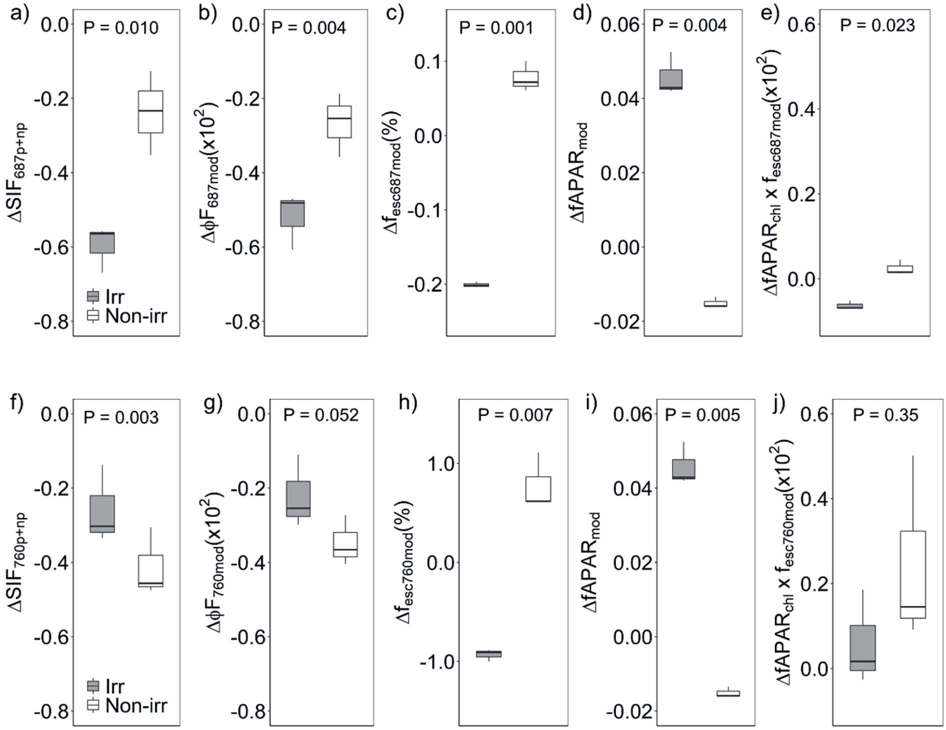

Figure 5.7. Delta values (S2 minus S1) in the modelled SIF and SIF-related indices: a-e) at 687 nm and f-j) at 760 nm. Irrigation was given to the irrigated plots on the evening of Day 1. “Irr” refers to irrigatied plots and “Non-irr” refers to non-irrigated plots. Irrigation effects on different indices were tested with a paired t-test. P are statistical significance. SIF_{mod} is shown in units of mW m^{-2} nm^{-1} sr^{-1}, f_{escmod} in % sr^{-1}, and $fAPAR_{chl} \times f_{escmod}$ in sr^{-1}. ΦF and $fAPAR_{chl}$ are unitless.

Table 5.6. Significance of the linear regression between ΔSIF-related indices ($\Delta\Phi F_{mod}$, Δf_{escmod}, $\Delta fAPAR_{chlmod}$) and ΔSIF_{p+np} (Equation 5.6) (numbers represent the statistical significance of the regression coefficients, ***$p < 0.001$, **$p < 0.01$, *$p < 0.05$, ns $p > 0.1$).

	$\Delta\Phi F_{mod}$	Δf_{escmod}	$\Delta fAPAR_{chlmod}$	$\Delta\Phi F_{mod}$	Δf_{escmod}	$\Delta fAPAR_{chlmod}$
	687 nm			760 nm		
ΔSIF_{p+np}	0.0013 **	0.011 *	0.022 *	0.023 *	0.276 ns	0.261 ns

5.4. Discussion

Our aim was to have a better understanding of the physiological and non-physiological effects of water stress on SIF and quantify their contribution to SIF variations caused by water stress in a sugar beet field. The results showed that both the physiological factor ΦF and non-physiological factors (i.e. canopy structural and leaf optical factors) adjusted in response to water stress and mediated the response of SIF both at 687 nm and 760 nm.

5.4.1. Decoupling SIF response to water stress

A decrease was observed in SIF_{687} and SIF_{760} on Day 2 in both irrigated and non-irrigated plots (Figure 5.3c, d). The decrease was caused jointly by the physiological alterations in fluorescence emission yield (ΦF) and by the non-physiological changes in canopy structure and leaf biochemistry (Figures 5.6 and 5.7). This is consistent with our expectations based on the theory behind the SIF variations (Ač et al., 2015; Dechant et al., 2020; Guanter et al., 2014; Verrelst et al., 2015). ΦF decreased on Day 2 within both irrigated and non-irrigated plots. For non-irrigated sugar beet, the ΦF reduction could be caused by the higher temperature and the high light intensity (Table 5.1), which could intensify the water stress on Day 2. To cope with water stress, leaf stomatal closures occur to prevent excessive water loss, leading to a decrease in evaporative cooling and a follow-up increase in leaf temperature due to the reduction in transpiration rates (Figure 5.3a) (Flexas and Medrano 2002) (Chaves et al., 2002; Flexas et al., 2006). The stomatal closure also limits the transport of CO_2 into leaves for use in carbon fixation and consequently affects the electron transport chain in light-dependent reactions. To prevent photoinhibition, NPQ is triggered as the photoprotective mechanism to dissipate excessive energy (Flexas et al., 2002, 2006). The increase in NPQ, as indicated by the increased PRI (Figure 5.3b), reduces fluorescence emission yield (Ač et al., 2015; Xu et al., 2021) and quantum yield of photosystem II (PSII) (Gu et al., 2019). Within irrigated plots, an irrigation effect on Day 2 was confirmed by the significant increase in soil moisture (SM_{meas}) and the decrease in canopy temperature (T_c) (Figure 5.3a). The leaf-level NPQ of irrigated plants acquired by the PAR-FluorPen FP 110/D was also lower than that of non-irrigated plots on June 29 (two days after irrigation) (Table S5.1), suggesting less water stress within the irrigated plots than non-irrigated ones. Therefore, recovery of sugar beet plants from the water stress occurred, but it was not clear to what extent. The reduction in ΦF on Day 2 suggested that the irrigated sugar beet plants might not have fully recovered from water stress. One possible reason could be that a full physiological recovery might not occur within a short time after the irrigation (less than a day). That could explain the increase in PRI within irrigated plots indicating a stronger NPQ regulation after irrigation (Figure 5.3b). Compared to the sugar beet plants on Day 1, a partial physiological recovery on Day 2 might increase photosynthetic yield and result in a lower intensity of fluorescence emission. This deduction could be supported by the higher leaf-level effective quantum yield of PSII (Qy) in the irrigated plot on June 29 (Table S5.1). Qy represents the PSII operating efficiency under different environmental conditions (Baker, 2008).

Non-physiological (canopy structural and leaf biochemical) factors also played a non-negligible role in mediating SIF variation under the water deficit (Figures 5.6b, d and S5.8). The most important canopy structural and leaf biochemical variables determining TOC SIF are leaf inclination angle distribution (LAD), leaf area index (LAI), and leaf chlorophyll content (C_{ab}) (Van der Tol et al., 2019; Verrelst et al., 2015). C_{ab} showed very small variations (Figure 5.5d). This might be due to the short recovery time after irrigation (less than a day), or the water stress was not severe enough to reduce chlorophyll content. Therefore, the non-physiological changes mainly originated from canopy structural factors. Under water stress, dynamic adjustments in leaf angle or leaf folding regulate leaf evapotranspiration and light absorbance (Chaves et al., 2003), The changes in LAI and LAD (Figure 5.5b, c) could explain the significant irrigation effect on both $fAPAR_{chl}$ and f_{esc} at both 687 and 760 nm ($p\text{-value} < 0.01$) (Figure 5.7c, d, h, i). The decrease of f_{esc} could partly explain the reduction of SIF_{687} and SIF_{760} within irrigated plots on Day 2. The decrease of f_{esc} at 687 nm was expected due to the stronger reabsorption effect within the recovered canopy. The reduction in f_{esc} of SIF_{760} within irrigated plots might be due to changes in the sugar beet leaf angle distribution. Planophile leaf orientations of the non-irrigated sugar beet have higher fluorescence than erectophile ones of the irrigated plants, similar to the higher reflectance of planophile canopies (Dechant et al., 2020; Van der Tol et al., 2019; Zeng et al., 2019).

5.4.2. The significant role of ΦF in SIF response under water stress

We found a strong effect of ΦF on SIF response to water stress (Figures 5.6b, 5.6c, and S5.8, Table 5.6). The important role of ΦF in unraveling canopy SIF-photosynthesis relationship under stress has been found at the leaf level (Flexas and Medrano, 2002; Jonard et al., 2020; Mohammed et al., 2019) and at canopy level (Celesti et al., 2018; Chen et al., 2021; Kimm et al., 2021; Van der Tol et al., 2016; Xu et al., 2021). The small contribution of the non-physiological components could be due to the joint effect of $fAPAR_{chl}$ and f_{esc}, which represents the structural effect on TOC SIF (Dechant et al., 2020). Compared with ΦF, the irrigation effect on the non-physiological proxy for SIF, $fAPAR_{chl} \times f_{esc}$, was less significant at 687 nm and 760 nm (Figure 5.7b, e, g, j). In addition, compared to ΦF, the non-physiological components $fAPAR_{chl}$ and f_{esc} had a much weaker effect on SIF at 687 nm and 760 nm, particularly at 760 nm where the changes in both $fAPAR_{chl}$ and f_{esc} did not significantly correspond to SIF variations. Some research reported that physiological signals may have a marginal contribution to SIF variations (Dechant et al., 2022, 2020; Miao et al., 2018; Yang et al., 2018). As speculated by Kimm et al. (2021), the different findings for ΦF could be attributed to two major aspects, i.e. whether physiological stresses existed and how tightly physiological stress was coupled with canopy structural or photosynthetic variation. Crops were observed without stress and, as a result, no clear signals of physiological variations were observed in TOC SIF (Dechant et al., 2020; Miao et al., 2018; Yang et al., 2018). In the absence of strong environmental stress, canopy-level SIF variations are expected to be driven predominantly by APAR and f_{esc} rather than ΦF for ecosystems where fPAR and f_{esc} show important seasonal variations compared to ΦF, (Dechant et al., 2020; Wang et al., 2020). In our case, first, water stress was present, as evidenced by low SM. The irrigation treatment largely eased the stress, as indicated by increased SM_{meas} and reduced T_c. Therefore, a significant change in ΦF caused by irrigation was observed. Second, correcting canopy structural effects and thus linking canopy- and leaf-level SIF is essential to tracking physiological canopy responses. Compared with approaches to characterize the components of canopy SIF using semi-empirical (e.g. NIR_v) or radiative transfer modelling with a number of assumptions and simplifications (e.g. FCVI) (Dechant et al., 2020; Yang et al., 2020; Zeng et al., 2019), we applied the RTM approach to characterize physiological and non-physiological factors, which could achieve a better decoupling between physiological stress and canopy structural variation. In addition, the time interval between the irrigation treatment and SIF acquisition could affect SIF response to water stress. For example, Xu et al. (2021) collected data two weeks after the onset of water exclusion. They found an important contribution of ΦF to spatial variations of SIF between irrigated and non-irrigated plots, while structural changes had a more important contribution. We explored the water stress effect on SIF observations the day after the irrigation and found ΦF dominated SIF variations, indicating that ΦF had a rapid response to photosynthetic changes caused by irrigation.

5.4.3. Modelling accuracy

RTM approaches have the advantage of offering a physiologically consistent estimate of canopy parameters that are essential for a better interpretation of fluorescence (Mohammed et al., 2019). TOC reflectance can be used to explain vegetation biochemical and structural effects on TOC SIF (Van der Tol et al., 2019; Yang and Van der Tol, 2018; Yang et al., 2019). The rationale is that TOC SIF and reflectance are connected through their common dependence on radiative transfer processes (Yang et al., 2019). They are both determined by leaf biochemistry, canopy structure, and sun-target geometry.

The modelled reflectance was well correlated with the measured TOC reflectance in all plots with RMSE between 0.006 and 0.010 (Figures 5.3a, S5.2, and S5.3), which was consistent with Yang et al. (2019). According to Yang et al. (2019) and Van der Tol et al. (2016), most of the variability of SIF could be reproduced after retrieving parameters from reflectance, and the uncertainty in modelled SIF is determined by the reflectance fitting. Therefore, the low RMSE between the simulated and the measured reference proved the robustness of our approach and the reliability of SIF simulations. The significant irrigation effect on the modelled soil moisture (SM_{mod}), LAI (LAI_{mod}) and averaged leaf angle (ALA_{mod}) further confirmed the accuracy of the inversion approach (Figure 5.5a-c). The irrigation treatment had little effect on C_{ab} (Figure 5.5d), which was reasonable and expected due to the short recovery time. C_{ab}, LAI, and leaf inclination angle are the most influential biochemical and structural parameters driving SIF (Van der Tol et al., 2016; Verrelst et al., 2015). Therefore, LAI_{mod}, ALA_{mod}, and C_{abmod} underlined a reliable inversion, laying a good foundation for SIF simulations. Ill-posedness of retrievals is a common problem in model inversions. Parameters that have little influence on reflectance may not be accurately retrieved, for example, soil moisture and LIDFb. Fortunately, these parameters have little influence on SIF simulation due to the shared sensitivities of TOC reflectance and TOC SIF (Yang et al., 2019). To reduce the ill-posedness of the inversion, we narrowed the ranges of some parameters based on the growth stage of the sugar beet, e.g. C_{ab} was confined to 30-50 $\mu g\ cm^{-2}$. We compared the modelled ΦF_{760} and the physically estimated ΦF_{760} ($\Phi F_{760meas}$) as a ratio of $SIF_{760meas}$ and NIRv×PAR (Chen et al., 2021; Kimm et al., 2021) and found that ΦF_{760mod} values were close to the $\Phi F_{760meas}$ estimates with R^2=0.95 and RMSE = 0.001 (Figure

S5.6), suggesting the reliability of the ΦF calibration approach. Both SIF retrieval from observations or SIF simulations from RTMs are challenging due to the within-leaf scattering and re-absorption of red SIF within the leaf or inside a plant canopy (Van Wittenberghe et al., 2015; Yang and Van der Tol, 2018), resulting in uncertainties in the SIF_{meas} and SIF_{mod} at 687 nm and further in the $ΦF_{687}$ calibration. The evaluation of $ΦF_{687mod}$ needs further research.

5.4.4. Implications

In this study, we used an approach of combining an RTM, observed hyperspectral reflectances, and SIF observations together to disentangle photosynthetic functional information from extraneous effects of water stress on SIF observations in a sugar beet field. The results proved that SIF variations were co-affected by ΦF and non-physiological factors. Our study demonstrated the important role of ΦF to provide direct insights into the mechanism of SIF response to stress and its link to vegetation photosynthesis. Kimm et al. (2021) also showed that SIF-derived ΦF was indicative of physiological stress with even greater sensitivity than SIF, whereas other studies found ΦF had little contribution to SIF variation (Dechant et al., 2020, 2022; Miao et al., 2018). Therefore, further detailed investigations will be necessary to evaluate the quality of ΦF estimates and better understand its variations regarding physiological mechanisms, which involves consideration of vegetation, site, and environmental factors, and the role of ancillary data at relevant spatial scales (Mohammed et al., 2019).

One limitation of this study is that its scope was constrained by limited data (only 6 plots) as we utilized the average SIF and reflectance per plot. The limited amount of data influenced the robustness of the inversion and SIF simulation as well as the separation of the concurrent effects. The results would be more inclusive if more SIF measurements per plot or more plots were involved. Another limitation is that no LAI, C_{ab}, and LAD measurements and leaf-level measurements of chlorophyll fluorescence were available for input of the model as prior knowledge or for validation of the simulated parameters. In future studies, a UAV-based Structure from Motion (SfM) photogrammetric method can be applied to the FluorSpec RGB images or Rikola images to obtain LAD directly (Xu et al., 2021, 2020). To evaluate the accuracy of the estimated ΦF, the development of an active system that measures full fluorescence spectra is a promising way forward to obtain the necessary data to validate this approach (Magney et al., 2017; Van der Tol et al., 2019).

The approach of combining RTM, TOC reflectance, and TOC SIF quantified plant physiological variation under stress conditions at the field level with UAV-based observations. The method can further support the quantification of stress effects by ΦF at ecosystem scales with airborne and satellite measurements. For example, the satellite-based FLuorescence EXplorer (FLEX) is designed to provide the complete spectrum of red and far-red chlorophyll fluorescence and will fly in tandem with Sentinel-3 (Drusch et al., 2016). Sentinel-3 reflectance can be used to retrieve important vegetation state variables like LAI, fAPAR, C_{ab}, and surface temperature. The combined retrieval of vegetation parameters from Sentinel-3 and TOC fluorescence from FLEX can feed an RTM and explore the physiological information carried by TOC fluorescence, contributing to improving our understanding of large-scale vegetation responses.

5.5. Conclusion

In this study, we investigated the effect of the physiological variation in ΦF and non-physiological variation in leaf biochemistry and canopy structure on SIF response to water stress in a sugar beet crop. We found that ΦF and biochemical and structural factors jointly control TOC SIF. However, SIF variation both at 687 nm and 760 nm caused by water stress was strongly affected by the physiological factor ΦF and positively correlated only with SIF variations caused by ΦF. At 687 nm, non-physiological changes had a weak (positive) effect on SIF variations, while at 760 nm non-physiological changes had a non-significant (negative) effect on SIF response to water stress. The findings confirm the physiological importance of SIF in water stress detection and its ability to reflect photosynthetic responses to stress. The combination of RTMs, measurements of TOC reflectance and SIF enables the physiological information quantification from field-level SIF observations and facilitates the understanding of the mechanistic reactions of SIF to changing environmental conditions at large spatiotemporal scales. In our case, the decoupling of the physiological and non-physiological information in SIF was under a specific water stress situation. This does not necessarily provide universal insight into the range of physiological conditions under which SIF may be measured. We, therefore, recommend extending the focus on the disentanglement of the concurrent effects on SIF response under different stress conditions, e.g. to different stress types and at different severity levels

SUPPLEMENTARY MATERIALS

1. Rikola reflectance measurements and simulations in 6 plots on Day1 before irrigation and Day2 after irrigation

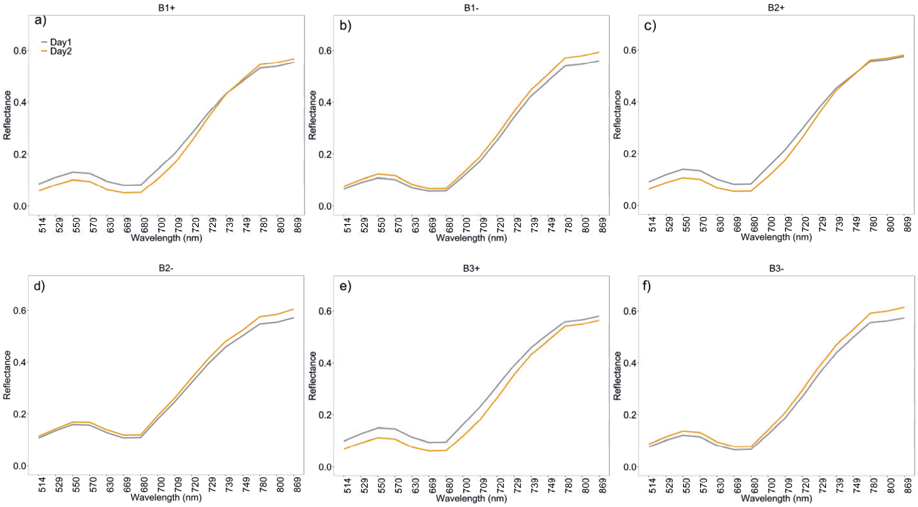

Figure S5.1. Average Rikola reflectance in six sugar beet plots on Day 1 before irrigation and Day 2 after irrigation.

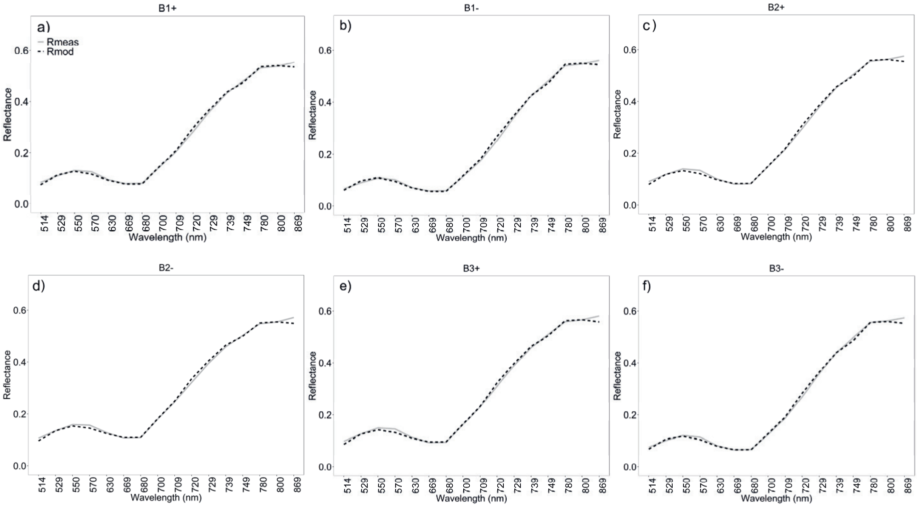

Figure S5.2. Measured Rikola reflectance and simulated reflectance in 6 plots on Day 1 before irrigation.

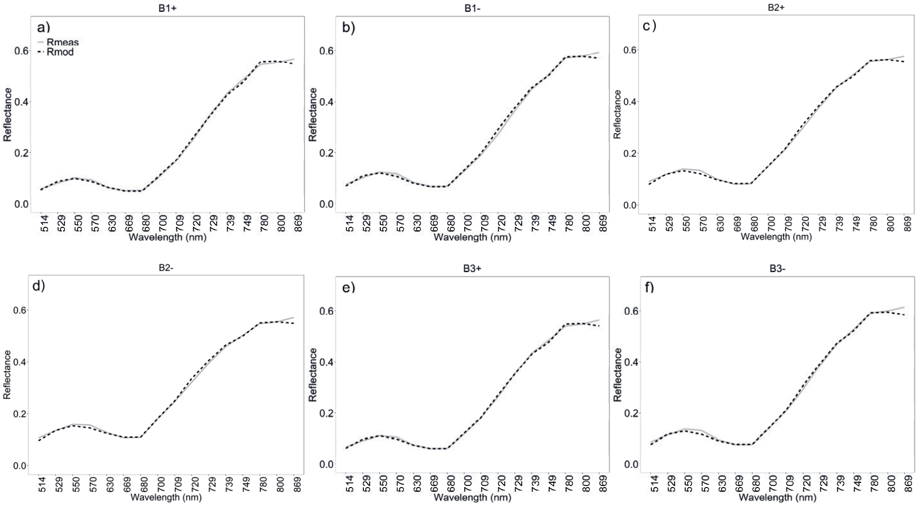

Figure S5.3. Measured Rikola reflectance and simulated reflectance in 6 plots on Day 2 after irrigation.

2. RGB images of the irrigated sugar beets and the non-irrigated sugar beets

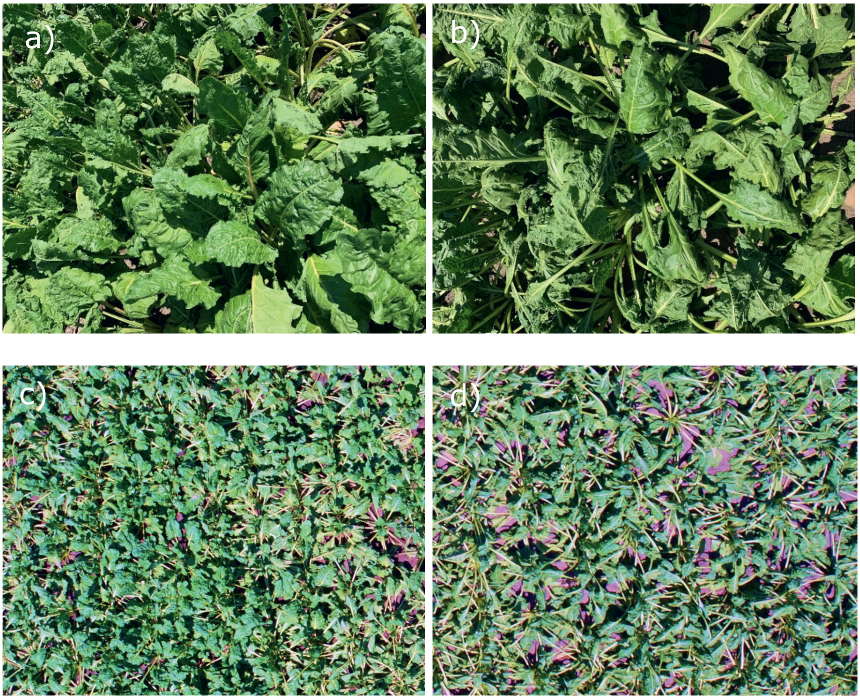

Figure S5.4. Field images of a) the irrigated sugar beets and b) the non-irrigated sugar beets on Day 2. UAV RGB images c) of the irrigated sugar beets and d) of the non-irrigated sugar beets on Day 2.

3. SSA-FLD and SFM

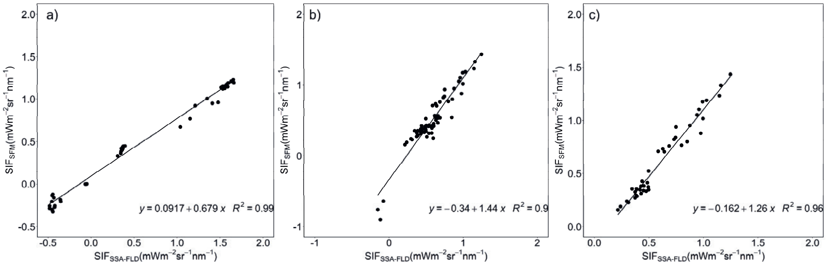

Figure S5.5. a) The linear relationship between SIF retrieved by SSA-FLD ($SIF_{SSA\text{-}FLD}$) and SIF retrieved by SFM (SIF_{SFM}) at O_2-A over vegetation targets (low green grass and green winter wheat) and non-fluorescence targets (bare soil and 99% white panel), b) at O_2-B over vegetation canopies (low green grass, green winter wheat, well-watered sugar beets and stressed sugar beets) and non-fluorescence targets (bare soil), and c) at O_2-B over vegetation canopies (green winter wheat, well-watered sugar beets and stressed sugar beets).

4. Comparison between simulated ΦF760 and estimated ΦF760 using a semi-empirical approach

ΦF at 760 nm can be estimated by a semi-empirical approach using SIF measurements (SIF_{meas}) and NIR_vP (NIR_v×PAR) (Kimm et al., 2021; Dechant et al., 2022).

$$\Phi F_{meas} = SIF_{meas} / (NIR_v \times PAR) \qquad (S5.1)$$

Where NIR_v is the product of NDVI and the reflectance at the near-infrared band.

$$NIR_v = NDVI \times R_{nir} \qquad (S5.2)$$

Where R_{nir} and R_{red} are the reflectances at the near-infrared and red bands as obtained from Rikola reflectances at 800 nm and 670 nm, respectively. PAR in this study was calculated using FluorSpec irradiance measurements acquired before the UAV took off. FluorSpec PAR was firstly calculated within the 630-700 nm interval using 20 consecutive irradiance measurements and then converted to incoming PAR within the 400-700 nm range using the equation in Wang et al. (2021). Fig. S5.6 shows a comparison between the modelled ΦF_{760} (ΦF_{760mod}) and the physically estimated ΦF760 ($\Phi F_{760meas}$).

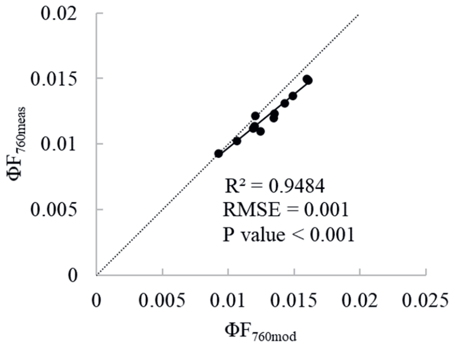

Figure S5.6. Linear regression between the modelled fluorescence emission yield at 760 nm (ΦF_{760mod}) with SCOPE and the estimated ΦF at 760 nm ($\Phi F_{760meas}$) using a semi-empirical approach.

5. SIF measurements (SIF_{meas}) and SIF simulations (SIF_{mod})

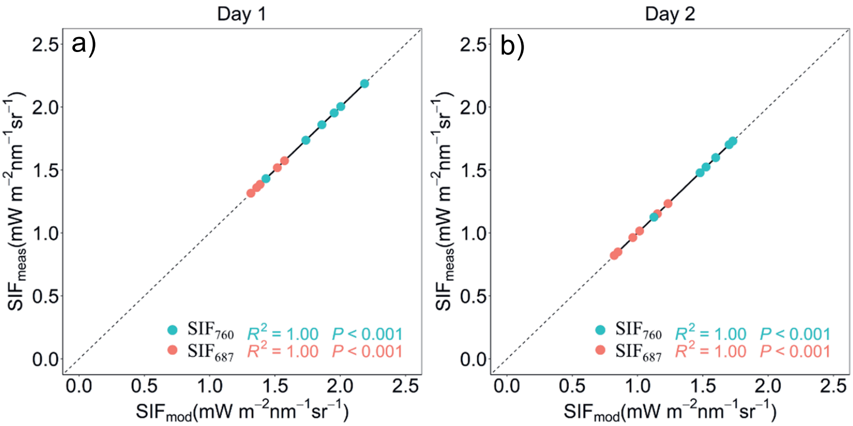

Figure S5.7. Linear regressions between a) modelled SIF (SIF_{mod}) in scenario1 and measured SIF (SIF_{meas}) on Day 1, b) SIF_{mod} in scenario 2 and SIF_{meas} on Day 2.

6. Quantification of the physiological contribution and non-physiological contribution

We defined a so-called contribution index to quantify the contribution from physiological changes (C_p) and non-physiological changes (C_{np}) to the overall changes in SIF between Day 1 and Day 2 as:

$$C_p=\Delta SIF_p/\Delta SIF_{p+np} \tag{S5.3}$$

$$C_{np}=\Delta SIF_{np}/\Delta SIF_{p+np} \tag{S5.4}$$

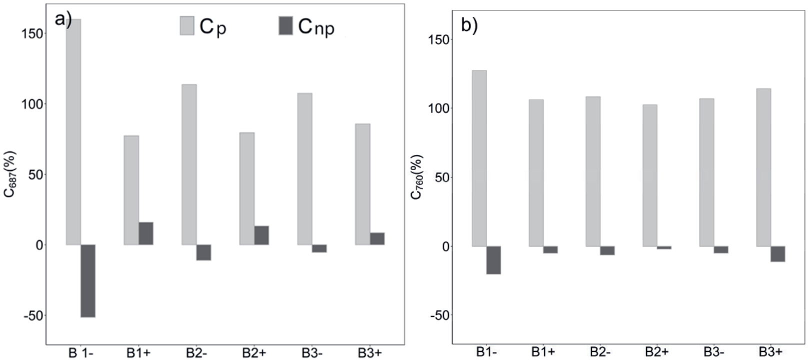

Figure S5.8. Physiological and non-physiological contribution to SIF variations in six plots at a) 687 nm and b) 760 nm. + indicates an irrigation treatment applied to the plot and – indicates no irrigation treatment in the plot. B1, B2, B3 refer to block1, block2, and block3. Irrigation was given on the evening of Day 1.

7. Active photosynthetic measurements

Table S5.1. Active measurements of photosynthetic parameters using PAR-FluorPen FP 110/D (PSI, Czech) measurements. Instantaneous chlorophyll fluorescence (Ft, a.u.), effective quantum yield of PSII (Qy, unitless), and non-photosynthetic quenching (NPQ, unitless) under steady states. All values were light-adapted under steady status.

Parameter	Ft	Qy	NPQ
B+	5788.3	0.31	1.12
B-	5377.5	0.29	1.39

Chapter 6

General discussion

6.1. Introduction

A better understanding of photosynthesis plays an important role in food security. Sun-induced chlorophyll fluorescence (SIF) is a byproduct of vegetation photosynthesis and is, therefore, a suitable candidate for monitoring vegetation photosynthetic activity (Frankenberg and Berry, 2018; Meroni et al., 2009; Porcar-Castell et al., 2014). SIF research has achieved substantial progress but mainly focused on the ground, airborne, and satellite levels. However, ground-based setups lack spatial flexibility, as they are bound to a specific location (Bendig et al., 2021). Satellite SIF signals are mixed due to the low spatial resolution and are not suitable for the monitoring of small-scale farmlands. Airborne systems can be costly to provide high-temporal SIF data that is required to capture responses of crop photosynthesis to changing light intensities and other environmental conditions, e.g. water availability (Mohammed et al., 2019). To fully explore the role of SIF in understanding photosynthetic processes in precision agriculture and plant phenotyping, there is an urgent need to acquire SIF at high temporal resolution over agricultural fields. Unmanned Aerial Vehicles (UAVs) provide possibilities to meet this demand due to their flexibility and fast data acquisition capabilities. The development of a lightweight spectrometer enables frequent SIF acquisition from a UAV at a low flying altitude. However, SIF is a weak signal and can be a result of the confounding effects from different factors. Therefore, the ability of a novel UAV SIF measuring system to provide reliable SIF information at a low altitude needs robust validation.

Water stress is a major abiotic factor adversely affecting crop photosynthetic activities and thus crop production worldwide (Lesk et al., 2016; Reddy et al., 2004). The drastic and rapid changes in the global climate have aggravated this situation (Lobell et al., 2011). It is therefore critical to understand the crop photosynthetic machinery under water stress for sustainable crop management. Due to the functional link between dynamic changes in photosynthetic activity and fluorescence emissions, UAV-based SIF can potentially indicate plant physiological changes caused by water stress at the field level. The plant response to water stress is complex and can be expressed by a wide range of changes in physiology, biochemistry, and morphology (Farooq et al., 2009). All of those changes contribute to the variations in SIF caused by water stress and complicate the physiological response of SIF to water stress. The importance to understand the sources of uncertainty in SIF-photosynthesis relationships at a range of scales was highlighted by Ryu et al. (2019). This emphasizes the necessity of evaluating the potential of SIF in water stress detection at the field level. To further understand the photosynthetic response to water stress, the changes in the physiological component of SIF should be characterized.

The overall objective of this thesis was to evaluate the potential of UAV-based SIF to understand crop photosynthesis under field conditions. For this, **chapter 2** introduced a novel UAV-based SIF measuring system, the FluorSpec, and tested its ability to characterize the diurnal variations of SIF. **Chapter 3** further evaluated the ability of the UAV-based FluorSpec to provide reliable SIF information in comparison to a well-validated airborne imaging system. **Chapter 4** and **chapter 5** focused on the evaluation and understanding of the performance of the UAV-based SIF indices in water stress detection in a sugar beet field. In this chapter, the main findings of this work, the reflection on the results, and challenges on the way are summarized. An outlook on the future study using UAV-based SIF is also presented.

6.2. Can the UAV-based FluorSpec system acquire SIF at the field level and characterize its diurnal variation?

Chapter 2 presented a novel UAV-based system, the FluorSpec, to measure the far-red SIF at the O_2-A band. The capability of the Spectral Shape Assumption Fraunhofer Line Discriminator (SSA-FLD) approach to disentangle the SIF signal from the top of canopy (TOC) reflectance was validated by FluorSpec measurements acquired over non-fluorescence emission targets (Figure 2.6b). At the ground level, TOC SIF exhibited a pronounced diurnal pattern, which was positively related to the incoming photosynthetically active radiation (PAR) (Figure 2.8). This is consistent with the findings of previous studies (Rascher et al., 2015; Zarco-Tejada et al., 2016). The divergence of diurnal patterns between SIF and PAR indicated that the crops might suffer from the mid-day depression due to intensive sunlight. Non-photosynthetic quenching (NPQ) is activated as the main way to dissipate the absorbed energy when light intensity is high (Müller et al., 2001; Porcar-Castell et al., 2014). A good correlation was found between diurnal normalized TOC SIF and leaf photosystem II quantum yield (Qy) over potato and sugar beet crops (Figure 2.10), which showed FluorSpec's ability to acquire SIF information and capture the dynamics of photosynthesis. The decrease in normalized SIF might be due to the drought brought by the heatwave and low precipitation in the summer of 2018 in the Netherlands. To cope with drought, crop stomatal closure prevents water loss and results in stronger NPQ and photorespiration, decreasing the photosynthetic yield and fluorescence emission (Porcar-Castell et al., 2014). In addition, the high temperature on the two experimental dates might result in blockage of the Photosystem II (PSII) reaction centre, decrease in quantum efficiency of electron flow, and even down-regulation of PSII photochemistry (Berry and

Bjorkman, 1980; Camejo et al., 2006). In this case, the activation of NPQ dominates the energy dissipation and reduces the fluorescence yield. The high intensity of sunlight might also increase NPQ, contributing to the decrease in fluorescence emission.

At the field level, UAV-based SIF exhibited a similar pronounced diurnal pattern and showed variations within different crop fields (Figure 2.11). We found larger variations in SIF of potato plants than that of sugar beets. This could be caused by the physiological difference as the two crops were at different growing stages in the survey period. Sugar beet was still growing and had a dense fully mature canopy in late summer, whereas potatoes already approached senescence during the time of observation and had less uniform growing conditions. These results proved the capacity of the UAV-based FluorSpec to measure SIF at the field scale and indicated the potential of UAV-based SIF in exploring photosynthetic activities in precision farming and upscaling the SIF measurements from the ground to the field level.

Two aspects remained challenging in our study. Firstly, like other UAV-based SIF measuring systems, accurate geolocation of FluorSpec footprints was also a challenge in our case (Bendig et al., 2019; MacArthur et al., 2014). A co-registered RGB camera can assist to identify the footprint centre of the point measurements. RGB images can be processed by the Structure from Motion (SfM) algorithm (Westoby et al., 2012), and UAV orientation information can be reconstructed. A RGB image was implemented to the UAV-based FluorSpec to calibrate the footprint geolocation (Chapter 3). Another challenge is that no validation data was available for the UAV-based SIF. Ground-based SIF can be used in ground-truthing and validation (Bendig et al., 2020; Chang et al., 2020; Garzonio et al., 2017), whereas the spatio-temporal discrepancies of ground-based and UAV-based information can hinder robust validation. Alternatively, UAV-based Fluorspec can be validated by comparing them with a high-performance system like an airborne system as a reference (Chapter 3).

6.3. Can the SIF measurements from the UAV-based FluorSpec system provide reliable information within agricultural fields?

Chapter 3 compared the performance of the UAV-based FluorSpec and the airborne HyPlant systems in retrieving diurnal SIF over different crops. The high-resolution RGB photos from the camera on the UAV were used to support the footprint geolocation of the FluorSpec measurements. The improved geolocation of the FluorSpec footprints (Figure 3.3) enhanced the linear correlations between the FluorSpec and HyPlant SIF for all flights (Table 3.1). SIF values derived from both systems fell in a reasonable and expected range (Siegmann et al., 2019)

(Figure 3.4). All flights performed using the two systems showed similar spatial patterns (Figure 3.4). The meaningful spatial patterns constitute a direct proxy of the vegetation functional state (Rascher et al., 2015). A clear difference in SIF existed for different crop varieties (Figures 3.4 and 3.5), e.g. two varieties of the spring barley, indicating the potential of SIF for crop phenotyping. Consistent and clear diurnal patterns over most crop types were found for both systems, positively correlated to the changes in PAR (Figure 3.5). For some crops, a lack of a clear diurnal development could be explained by the geometry difference within the FluorSpec footprint for different flights and the angular dependencies of SIF. Further consistency of HyPlant and FluorSpec SIF was confirmed by the strong linear relationship (Figure 3.6), underlining the stable performance of the FluorSpec to capture SIF at a low flying altitude, and indicated its high capacity to assist the interpretation of airborne SIF measurements.

HyPlant-derived SIF values were overall higher than the FluorSpec-derived SIF and the bias was similar for the flights at mid-day (Figure 3.6, Table 3.3), indicating the stable performances of UAV-FluorSpec in SIF acquisition. The technical differences in the point spectrometer of FluorSpec and image camera of Hyplant could partly explain the constant difference (Cendrero-Mateo et al., 2015; Pacheco-Labrador et al., 2019). Moreover, the two systems applied different interpolation strategies to retrieve SIF at the O_2 absorption wavelength (760 nm), adding some uncertainties to the retrieved SIF values (Cendrero-Mateo et al., 2019).

The findings in chapter 3 proved the ability of UAV-based SIF to provide valuable information in exploring the mechanism between photosynthesis and SIF at the field level. The consistent performances between these two systems also underline the potential of UAV-based SIF to complement airborne SIF and scale SIF from small-scale field to airborne level, which thereby further support the interpretation and validation activities of satellite-based SIF, e.g. the upcoming FLuorescence EXplorer (FLEX) satellite. The results also encourage the application of UAV-based SIF in precision agriculture, e.g. timely crop monitoring for stress detection.

6.4. Can UAV-based SIF and its indices detect water stress in a crop?

Chapter 4 assessed the value of UAV-based red SIF at 687 nm (SIF_{687}) and far-red SIF at 760 nm (SIF_{760}) and SIF-related indices in water stress detection within a sugar beet field. Two field campaigns were carried out on two consecutive days in June and July 2019. UAV-based thermal and hyperspectral reflectance data were acquired to assist the interpretation of SIF response. On June 27 and 28, sugar beets were suffering from water stress while on July 23 and 24 plants were under severe stress due to a water deficit and extremely high temperature.

Therefore, water stress in June could be considered early stress in comparison to July. The irrigation did not reduce the stress on July 24 as much as that on June 28, which was indicated by the lower soil moisture and normalized difference vegetation index (NDVI), and higher canopy temperature (T_c) on July 24 in the irrigated sugar beet plots (Figures 4.3 and 4.4, Table 4.2). Higher spatial variations can be found in SIF observations than in NDVI and T_c maps (Figures 4.3-4.6), indicating that SIF might be more sensitive to plant stress conditions. Except the SIF yield (SIF/APAR) at 760 nm, all SIF indices were found to be able to track the recovery of sugar beet after irrigation on June 28 (p-value < 0.05) (Table 4.3). This indicated the potential of SIF indices to detect water stress at the early stage. On July 24, only some SIF indices showed a weak response to the changes induced by the irrigation (p-value < 0.1) (Table 4.3). This might be because the complementarity between photosynthetic quenching (PQ) and non-photosynthetic quenching (NPQ) dominated the trade-off of energy dissipation (Helm et al., 2020). Variations in the fluorescence emission efficiency are usually small and vegetation type-specific and thus do not always correlate well with photochemical efficiency (Gu et al., 2019; Porcar-Castell et al., 2014). In addition, the severe stress might cause photodamage of PSII and thus decouple the fluorescence emission and the actual photosynthetic activity (Camejo et al., 2006). We also found that NDVI, TCARI/OSAVI, and T_c could track the plant changes induced by irrigation under both the early stress and severe stress situations (Table 4.3). This implies that the structural, pigment, and temperature indices could not provide direct and timely information on crop photosynthetic functioning (Gerhards et al., 2019; Xu et al., 2021), underlining the unique role of SIF as a physiological indicator in stress detection.

The findings suggested that the used SIF indices could indicate water stress but might not be able to provide added value to track changes of photosynthesis under severe stress. The information derived from TOC SIF might depend on the imposed environmental stress levels. To what extent SIF responds to the stress at different levels remains unclear. Further research on the UAV-based SIF response to drought stress at different severity levels over different crops should be implemented.

6.5. What are the physiological and non-physiological effects on SIF variations caused by water stress and their respective contribution?

Chapter 5 disentangled the physiological effect from the non-physiological effect on SIF variations caused by water stress. Radiative transfer models (RTMs), TOC reflectance and SIF measurements were utilized together to estimate the non-physiological properties of canopy structure and leaf biochemistry, and then the physiological factor (fluorescence emission yield,

ΦF). The estimated vegetation parameters and ΦF were subsequently used to simulate TOC SIF in four different scenarios in order to unravel the physiological and non-physiological effects on SIF response. SIF and reflectance data were acquired over irrigated and non-irrigated sugar beet plots using a UAV platform on two consecutive days under clear sky conditions.

TOC SIF was found to be jointly controlled by ΦF and non-physiological (biochemical and structural) factors (Figure 5.6), in line with our expectations based on the theory behind the SIF variations (Guanter et al., 2014; Verrelst et al., 2015; Ač et al., 2015). However, the physiological signal ΦF dominated SIF variations caused by water stress (Figures 5.6 and 5.7) and had a significant effect on variations in TOC SIF (p-value < 0.05 at both 687 nm and 760 nm) (Table 5.6). The important impact of ΦF on SIF responses to environmental stress has also been found by previous studies (Celesti et al., 2018; Chen et al., 2021; Kimm et al., 2021; Van der Tol et al., 2016; Xu et al., 2021). ΦF decreased on Day 2 within both irrigated and non-irrigated plots. For non-irrigated plots, the ΦF reduction could be caused by the higher temperature and the high light intensity (Table 5.1), which could intensify the water stress on Day 2. Plant stomatal closure occurs to cope with water stress and consequently NPQ is triggered as the photoprotective mechanism to dissipate excessive energy (Flexas et al., 2002, 2006), evidenced by the increase in PRI (Figure 5.3b), resulting in a decrease of the fluorescence emission yield (ΦF) (Ač et al., 2015; Xu et al., 2021) and the quantum yield of PSII (Gu et al., 2019). Within irrigated plots, the increased soil moisture and decreased canopy temperature indicated a recovery of sugar beet plants from the water stress but to what extent remained unclear. The reduction in ΦF of irrigated sugar beets suggested that on Day 2 the irrigated sugar beets might not fully recover from water stress, as indicated by the increased PRI (Figure 5.3b). A partial physiological recovery might increase photosynthetic yield on Day 2, lowering the efficiency of fluorescence emission. The non-physiological effect on TOC SIF variations caused by water stress was much smaller than the physiological effect (Figure 5.7). This could be due to the co-effect of the fraction of absorbed photosynthetically active radiation (fAPAR) and the fluorescence escape fraction (f_{esc}). fAPAR×f_{esc} can represents the non-physiological components of TOC SIF (Dechant et al., 2020). The irrigation effect on fAPAR×f_{esc} was weaker compared to ΦF, particularly at 760 nm (p-value > 0.1 for fAPAR×f_{esc}) (Figure 5.8). Furthermore, both variations in fAPAR and f_{esc} had weaker impacts on SIF changes induced by water stress than ΦF (Table 5.6).

The combination of RTM, TOC reflectance, and TOC UAV-based SIF quantified plant physiological variation under stress conditions at the field level with UAV-based observations.

The method can further support the stress quantification capability of ΦF at ecosystem scales with airborne and satellite measurements, e.g. the FLuorescence EXplorer (FLEX). Studies found different performance of the physiological factor (ΦF) and non-physiological factors (Dechant et al., 2022, 2020; Kimm et al., 2021; Miao et al., 2018; Xu et al., 2021). Many factors could affect the findings, e.g. the presence of stress, stress severity and duration, vegetation type, and weather conditions. In a specific situation, not all aspects might be influential or equally important (Mohammed et al., 2019). Further research is deemed necessary to better understand the role of ΦF in TOC SIF and its contribution to SIF response under stress, which involves consideration of vegetation, site, environmental factors, and ancillary data at relevant spatial scales (Mohammed et al., 2019).

6.6. Reflection and outlook

This section summarizes some challenges on the way in the interpretation and the scaling of UAV-based SIF and presents an outlook on the future study using UAV-based SIF.

6.6.1. Interpretation of UAV-based SIF data

One challenge is the meaningful interpretation of canopy SIF for a better understanding of the photosynthetic state of plants (Bendig et al., 2021). Firstly, the footprint geolocation of a UAV-based point spectrometer hinders a correct interpretation of SIF. An accurate spatial characterization of the UAV observation footprint is essential to unravel the origin and spatial variability of SIF signals (Gautam et al., 2019), including location determination and footprint extent (e.g. shape). Spatial uncertainties in UAV-based FluorSpec measurements can originate from GNSS inaccuracies and the in-flight movements of the UAV. In chapter 3, we proposed a manual geolocation calibration of FluorSpec footprints using the implemented RGB images. This approach mainly considers the GNSS inaccuracies. To achieve a precise geometric determination, UAV navigation has to be precise enough to position the sensor field of view (FOV) over an area, and the UAV movements, i.e. pitch and roll, need to be corrected. In the future, the FluorSpec can be paired with a Real-Time Kinematic (RTK) enabled GNSS IMU device and be installed on a stabilized gimbal to improve the georectification accuracy down to centimeter-level.

Second, the mixed signal within the footprint of a point measurement complicates the explanation of SIF, particularly in a small-scale heterogeneous field. In Chapters 2, 4 and 5, SIF observations were acquired within monoculture fields, whereas in chapter 3, SIF was acquired over different crop fields designed for experimental field trials. For example, the bare soil in the young maize field and the ridge between two different crop varieties (e.g. winter wheat1 and spring barley1) (Figure 3.1) could contaminate the signal acquired within the sensor FOV and therefore could increase the uncertainty in the observed SIF information. A good flight mission can reduce the uncertainty in SIF measurements by designing the flightpath. However, a UAV might not follow a pre-designed flight pattern due to the GNSS inaccuracies and the wind condition in the field. Thus, one may need to test and modify the flight mission several times to acquire high quality SIF data. The flight patterns in chapter 4 and chapter 5 were adjusted in this way to acquire data over the centreline of each sugar beet block (Figures 4.1 and 5.1). In addition, a small sensor FOV is preferable for applications in experimental field trials. However, with a small FOV, SIF retrievals may be subjected to artifacts due to the great dominance of geometric optical scattering by canopy components and a higher probability of measuring shaded canopies or soil background (Damm et al., 2015). An imaging camera with very high spectral resolution can be a future solution. In addition, an imaging sensor could more easily cover a larger field in a single flight than a point spectrometer with which the number of measurements per flight is limited (Bendig et al., 2021). The Hyperspec Fluorescence sensor (Headwall Photonics Inc.) acquires image data at high resolution within the chlorophyll fluorescence emission spectrum from 670 to 780 nm. This sensor weighs about 6 kg, however, the sensor mounted to UAVs is required to be miniaturized and lightweight for robust and operational SIF-UAV measurements (Bendig et al., 2021). In the future, a lightweight imaging fluorescence camera is needed for flexible and cost-effective measurements.

Canopy structure also has a large effect on TOC SIF interpretation by affecting APAR as the major driver of SIF and the fluorescence escape ratio (f_{esc}). SIF can be emitted by shaded or sun-lit or both areas of the canopy and can be scattered or reabsorbed within the canopy before reaching the sensor. Therefore, a detailed characterization of SIF needs the consideration of canopy structural parameters which affect SIF retrieval, e.g. leaf area index (LAI), leaf angle distribution (LAD), vegetation height, and clumping index (Verrelst et al., 2015; Zeng et al., 2019). In chapter 5, we adopted an RTM inversion approach to estimate structural parameters from TOC reflectance and better understood the biophysical effect on SIF response under water stress. Variations in sun-target-viewing geometries affect canopy SIF interpretation (Biriukova et al., 2020; Dechant et al., 2020; He et al., 2017). Angular effects in TOC SIF were not taken into consideration in this work. It is essential that future efforts investigate and correct the angular effects. The total emitted SIF from all leaves (SIF_{total}) is expected to be insensitive to canopy structure and observation direction (Yang and Van der Tol, 2018; Zeng et al., 2019) and has shown less angular dependencies compared with directional SIF observations (Zhang et al., 2020). Future research can involve both directional SIF and $\mathrm{SIF}_{\mathrm{total}}$ for a better understanding of the photosynthetic functioning.

6.6.2. UAV-based SIF scaling

The full suite of technological options allows SIF measurement at ground, UAV, airborne, and satellite scales. This contributes to exploring the full potential of SIF techniques in vegetation and crop management, and in validation and interpretation of SIF retrievals. Reliable upscaling and downscaling capabilities, therefore, are needed in both temporal and spatial dimensions for SIF processes (Mohammed et al., 2019). One motivation of this research was to bridge the gap in SIF monitoring between ground to airborne and satellite levels and provide complementary information to SIF at large scales. To achieve this, a consistent, reproducible, and comparable SIF collection at different scales is essential but challenging. In chapter 2, we specifically designed a field campaign to compare UAV-based FluorSpec and airborne HyPlant SIF observations. Relating SIF values from both systems not only shows a strong linear relationship but also a bias between the two measurement systems (particularly for the flights at mid-day) (Figure 2.6, Table 2.3). This comparison result suggests that SIF scaling analysis can be difficult due to the sensor technologies (e.g. spatial resolution, spectral range and resolution, and signal to noise ratio (SNR)) (Damm et al., 2014; Pacheco-Labrador et al., 2019), retrieval strategies (e.g. the interpolation method, the selection of appropriate wavelengths representing the absorption feature, and the appropriate definition of the reference bands (i.e. shoulders of the used absorption feature)) (Cendrero-Mateo et al., 2019), flight heights, atmospheric correction, and the specific influential factors in a given situation including meteorological and vegetation differences (Mohammed et al., 2019). These aforesaid factors are worthy to be further explored in future studies. Furthermore, studies on the relation of SIF to photosynthesis at different scales have been inconclusive, increasing the difficulties in SIF scaling. For example, the pattern of fluorescence observed on single leaves under drought does not match observations on entire canopies (Helm et al., 2020; Marrs et al., 2020; Sun et al., 2015; Xu et al., 2021). Therefore, to achieve SIF scaling, besides a simple comparison in SIF at different scales, how to combine them for comprehensive or sophisticated analysis needs more research.

Some potential approaches are indicated in this chapter to achieve SIF scaling. Integrative methods based on combined analysis of reflectance and SIF with radiative transfer models (RTMs) facilitate SIF upscaling and currently is ongoing research (Mohammed et al., 2019;

Van der Tol et al., 2016). In chapter 5, this approach was applied to simulate TOC UAV-based SIF at the field level and explored the physiological response of sugar beets to water stress. FLEX and Sentinel-3 can benefit from this approach to study vegetation photosynthetic activities. The combined vegetation parameters inverted from Sentinel-3 can feed an RTM and further explore the physiological information carried by TOC fluorescence from FLEX, enhancing our understanding of large-scale vegetation responses. Future efforts can attempt to downscale SIF using a combined machine learning and RTM approach. For example, Liu et al. (2019) proposed a practicable solution to downscale SIF from canopy level to photosystem level using a random forest model that was trained using RTM simulations. The recently proposed fluorescence correction vegetation index (FCVI) and near-infrared reflectance of vegetation (NIR_v) (Yang et al., 2020; Zeng et al., 2019) can also be applied to downscale far-red TOC SIF by determining the escape fraction of far-red SIF to account for structural effects. The FCVI has been applied to scale far-red SIF from canopy to leaf level (Siegmann et al., 2021). These downscaling approaches characterize the components of canopy SIF using semi-empirical (Liu et al., 2019; Zeng et al., 2019) or radiative transfer modelling with a number of assumptions and simplifications (Yang et al., 2020). However, they cannot be applied to red SIF due to within-leaf scattering and re-absorption of red SIF within the canopy (Van Wittenberghe et al., 2015; Yang and Van der Tol, 2018). The RTM approach, which make use of more spectral bands, is expected to be the main approach for red SIF scaling.

6.6.3. Future research

Based on the findings of this thesis and other ongoing research, several future directions for SIF research can be indicated.

1. Mapping spatial variability of SIF acquired with the UAV-based non-imaging spectrometer over the whole field

The non-imaging sensor has greatly encouraged UAV-based SIF research, due to its reduced size, high SNR, high spectral and temporal resolutions (Bendig et al., 2021; Mohammed et al., 2019). However, point measurements cannot provide the spatial variability of SIF within the entire field. The spatial pattern is not only important for the interpretation and validation of SIF imaging products at the ecosystem level, e.g. the upcoming FLEX SIF product, but also highly needed as the high dynamic temporal information in precision agriculture and phenotyping. For example, for effective crop management, the presence of stress and its severity across an agricultural field need to be evaluated to apply the right treatment in the right place at the right time.

The observed TOC SIF is determined by three processes together (i.e. the absorption of light, the emission as fluorescence, and the escape of F from the canopy), which are affected by crop properties such as structure, biochemistry, and photochemistry. TOC SIF and reflectance are connected through their common dependence on radiative transfer processes (Yang et al., 2019). Therefore, they are similarly determined by leaf biochemistry, canopy structure, and sun-target geometry. Different vegetation indices (VIs) considered as proxies of different vegetation traits can be connected to the potential SIF. For example, FCVI and NIR_v have been proposed to characterize the non-physiological component f_{esc} of far-red SIF (Yang et al., 2020; Zeng et al., 2019). NIR_vP (NIR_v×PAR) has been shown as a robust structural proxy of far-red SIF across a wide range of spatial and temporal scales (Dechant et al., 2022). Bandopadhyay et al. (2020) showed that a diverse set of VIs considered as proxies of different vegetation traits, such as biochemical, structural, and functional, can serve as a first-order proxy of SIF, with R^2 of the agreement between the modelled SIF and actual SIF at 0.69 for SIF_{760} and 0.92 for SIF_{687}.

For these reasons, a combination of area-wise VIs influencing SIF-relevant processes and point UAV-based SIF observations might be able to predict SIF across the field. This contributes to resolving the spatial heterogeneity of plant photosynthetic performance under stress conditions and provides a more in-depth look at plant functioning than point SIF measurements. Machine learning, neural networks, and model emulators may be able to support the realization of SIF scaling from the point-based footprint to the whole field level. For example, supervised machine learning approaches (e.g. random forest) trained on an appropriate training dataset are capable of building accurate prediction models (Ma et al., 2014). These models can empirically overcome the difficulties in the physical modelling (Liu et al., 2019). For example, the unavailable input parameters for the physical model can be estimated by machine learning approaches using available information. Mapping spatial variability of UAV-based SIF can provide important insights that facilitate the validation of satellite SIF and can provide complementary information to airborne and satellite SIF, e.g. HyPlant and FLEX.

2. Spatial mapping of LAI and C_{ab} for better understanding of SIF variability in the field

The structural variable LAI is the main indicator of the presence and density of vegetation and determines radiation interception by the canopy (Breda, 2003). Leaf chlorophyll absorbs the incoming sunlight for plants within the 400-700 nm spectral window as the main absorbing pigment (Lichtenthaler, 1987). LAI and C_{ab} are two of the most important variables that drive SIF emanating from vegetation canopies (Verrelst et al., 2015). Spatial maps of LAI and C_{ab} facilitate the understanding of TOC SIF observations from a UAV-based point spectrometer or imaging sensor. The spatial pattern can be mapped using RTM inversion approaches, which have been widely used to retrieve vegetation parameters such as C_{ab} and LAI from remotely sensed data (Verrelst et al., 2015). Machine learning methods can cope with the strong nonlinearity of the functional dependence between the biophysical parameter and the observed reflected radiance (Knudby et al., 2010). Therefore, machine learning methods might be alternative candidates for vegetation trait inversion. For example, the gaussian processes regression method yielded reliable LAI and C_{ab} estimates from a dataset representative of actual plant canopies and conditions as observed by the Sentinel sensors (Verrelst et al., 2012).

3. UAV-based SIF to detect water stress in a varying degree at different scales and phenological stages

A correct interpretation of SIF data is essential in water stress detection, as multiple factors can jointly influence SIF drivers and retrievals (Mohammed et al., 2019). It is essential to understand sources of uncertainty in SIF-photosynthesis relationships under water stress not only at a range of temporal and spatial scales but also in a varying severity. Water stress at varying levels affects fluorescence through their different effects on light absorption, fluorescence re-absorption, and scattering as well as PQ and photoprotective processes (e.g. NPQ and photorespiration) (Mohammed et al., 2019). In chapter 4, we found that SIF had a significant response to the slight drought in June whereas it could not track the response of sugar beet physiological response to the severe drought (Table 4.3). We speculated that the severe drought decoupled fluorescence and the functioning of photosynthesis, either via an NPQ mediation or strong photoinhibition of the photosystem II (PSII) (Helm et al., 2020; Marrs et al., 2020). Further studies are required to evaluate the potential of SIF in stress detection at the field level and better understand the mechanism between SIF and photosynthetic functioning. A controlled field experiment where water availability is limited at different levels can provide insights into to what extent SIF can track the crop physiological response and the photosynthetic adjustments.

SIF measurements from ground-based systems can reveal the SIF-photosynthesis relation at the proximal canopy level and further facilitate the interpretation and validation of UAV-based SIF observations. Active fluorescence measurements (e.g. fluorescence yield, PSII Qy, and NPQ) are already well associated with plant physiology and they can give a picture of the absorbed energy dissipation within leaves. These active parameters can be important complements to passive photosynthetic measurements including SIF. At different phenological growth stages, plants have different biophysical, biochemical, photochemical, and photosynthetic characteristics. These can result in different sources of uncertainty in SIF-photosynthesis relationships and need further research. Therefore, a combination of the leaf-level active fluorescence parameters, ground-based and field-level SIF measurements at different phenological stages under a varying stress level can provide a comprehensive understanding of the SIF-photosynthesis relationship.

4. Three-dimensional structural information assisting the interpretation of UAV-based SIF

Characterization of canopy structural effects on SIF observations facilitates the interpretation of SIF signals at local-to-regional scales (Verrelst et al., 2015; Yang and Van der Tol, 2018), particularly in understanding and diagnosing plant responses to stress. Canopy structural parameters (e.g. LAI, clumping index, leaf inclination, and canopy height) affect the absorption of PAR and SIF escape fraction (f_{esc}) from the canopy (Van der Tol et al., 2019). For example, LAI affects the production of fluorescence and the leaf inclination has a strong effect on the observed fluorescence via f_{esc} (Dechant et al., 2020). The directional UAV-based SIF observations are also angular-dependent and affected by the sun-canopy-sensor geometry (Pinto et al., 2017; Zhang et al., 2020). The analysis of plant properties can benefit greatly from three-dimensional (3D) measurements because plant responses are strongly related to their 3D structure (Omasa et al., 2007). Light detection and ranging (Lidar) has recently emerged as powerful tools for direct 3D measurements of plant structure. Miniaturization and advancement in several UAV components have prepared the ground for the construction of Unmanned Aerial Vehicle Laser Scanning (UAV-LS) systems (Brede et al., 2019). UAV-LS is able to provide a vertical profile and a horizontal distribution of plant canopy elements by illuminating a larger area (Bork and Su, 2007). Canopy 3D reconstruction can provide a better understanding of the physical effect on SIF variability under field conditions.

3D photon and flux tracing RTMs can describe SIF photon interactions with complex 3D canopy structures and support a physical characterization of SIF variability in the field. The

Discrete Anisotropic Radiative Transfer (DART) model is one of the most comprehensive physically based 3D radiative transfer models and considers the 3D structure (Gastellu-Etchegorry et al., 2017), offering more complex strategies for spatially detailed simulations in structurally complex canopies. The 3D UAV-LS information can be the input of DART and contributes to better understanding the relationships between SIF, vegetation 3D architecture, irradiance, and remote sensing configuration at canopy level (Gastellu-Etchegorry et al., 2018). Nevertheless, compared to 1-D RTMs, 3D models are generally slower and require a larger number of input parameters, and this limits their invertibility and large-scale application.

5. Synergistic sensor facilitating SIF applications

SIF is a powerful tool to mine the activity of photosynthesis and can provide information on the health status of crops (Rossini et al., 2015; Zarco-Tejada et al., 2018). However, plant responses to stress are numerous and complex. For example, plant responses to water stress can appear synergistically or antagonistically and be modified by co-occurring plant stresses under field conditions (Figure 6.1). Therefore, it is challenging to detect and monitor plant biotic/abiotic stress based on a single plant response (Gerhards et al., 2019). As shown in Figure 6.1, a multi-sensor approach using optical reflectance, thermal imagery, and SIF can be a robust stress detection framework. Synergistic sensor use can improve our understanding of plant conditions and stress, because it provides a deeper insight into the relations between spectral features and associated plant conditions and integrate the complementary strengths of different vegetation traits (Gerhards et al., 2019; Pinto et al., 2020). NIR_v and SIF captured complementary aspects of seasonal GPP dynamics across dryland ecosystem types (Wang et al., 2022). NIR_v offered better performance in GPP estimate across relatively low-productivity, sparsely non-evergreen vegetated sites, whereas SIF better captured seasonal dynamics across relatively high-productivity sites. Machine learning methods may realize the senor synergy. Reflectance-based VIs, traits inverted from hyperspectral reflectance using RTM, temperature-based indices from thermal infrared data, and SIF indices can be the input parameters of a machine learning model (Zarco-Tejada et al., 2021). The model keeps the parameters with high importance in stress detection and further combines the diverse input to monitor the presence and severity of a certain stress. This approach can be a trend for the development of global disease-detection models. Zarco-Tejada et al. (2021) successfully decoupled the biotic stress caused by vascular system-invading pathogens and abiotic stress imposed by water limitation with a random forest (RF) algorithm. The spectral traits estimated by RTM inversion, CWSI, and far-red SIF were used as inputs for the RF models. Based on the results, a library can be established for recording the high-performance indices and the applied machine learning approach in a certain situation, which involves vegetation types, sites, and environmental factors at relevant spatial scales (Mohammed et al., 2019). This approach enhances a comprehensive understanding of the value of SIF for applications. For example, the multi-senor approach assists the characterization of stress and the interpretation of SIF (Panigada et al., 2014; Pinto et al., 2020). However, it remains unclear whether the involvement of SIF can contribute to a low-input and highly efficient agriculture. The library can show the value of SIF in modern agricultural management and support decision-making on what sensors to be used in a certain condition.

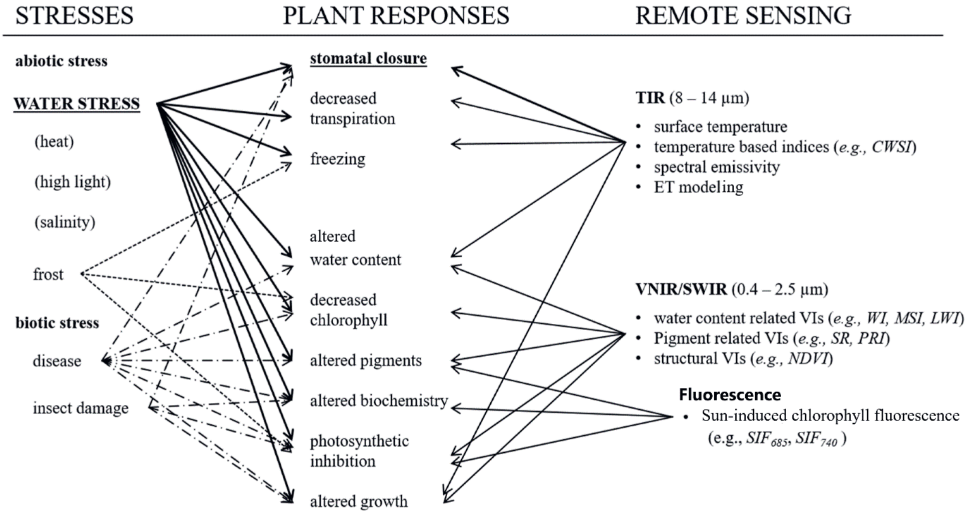

Figure 6.1. Most important relationships between primary plant stresses, the induced plant responses, and remote sensing techniques for the detection of environmental stresses. The figure was sourced from Gerhards et al. (2019) which focused on water stress detection.

SIF can be a promising signal to assist the process of high-throughput plant phenotyping in plant breeding. Plant breeding has greatly increased the grain yield of cereals via genetic manipulation (Pingali, 2012). To increase efficiency in plant breeding, plant breeders and farmers have been making selections based on phenotypes, e.g. yield potential, resistance to drought, heat tolerance, and nutrient use efficiency (Araus and Cairns, 2014). As a physiological trait, SIF is fundamentally and directly related to photosynthesis and has advantages in timely crop stress monitoring. Therefore, SIF plays an important role in crop phenotyping and can support selection-making in crop breeding.

6.7. Conclusions

This research introduced the novel UAV-based FluorSpec to measure a reliable SIF at field level and showed its ability to bridge the gap between the ground and ecosystem SIF observations and thus complement the airborne/satellite SIF information. The findings also provided further insights into the potential of UAV-based SIF to detect water stress and improved our understanding of the photosynthetic response to water stress for the presented case. This thesis gives valuable knowledge on the potential of SIF in precision agriculture and phenotyping. More studies need to be conducted to unravel the full potential of UAV-based SIF measurement though it has proved to be an exciting new tool for studying vegetation dynamics.

REFERENCES

Aasen, H., Van Wittenberghe, S., Sabater Medina, N., Damm, A., Goulas, Y., Wieneke, S., Hueni, A., Malenovský, Z., Alonso, L., Pacheco-Labrador, J., 2019. Sun-induced chlorophyll fluorescence II: review of passive measurement setups, protocols, and their application at the leaf to canopy level. Remote Sensing. 11,927. http://doi.org/10.3390/rs11080927

Ač, A., Malenovský, Z., Olejníčková, J., Gallé, A., Rascher, U., Mohammed, G., 2015. Meta-analysis assessing potential of steady-state chlorophyll fluorescence for remote sensing detection of plant water, temperature and nitrogen stress. Remote Sensing of Environment. 168,420-436. https://doi.org/10.1016/j.rse.2015.07.022

Agati, G., Mazzinghi, P., Fusi, F., Ambrosini, I., 1995. The F685/F730 chlorophyll fluorescence ratio as a tool in plant physiology: response to physiological and environmental factors. Journal of Plant Physiology. 145,228-238. https://doi.org/10.1016/S0176-1617(11)81882-1

Alonso, L., Gomez-Chova, L., Vila-Frances, J., Amoros-Lopez, J., Guanter, L., Calpe, J., Moreno, J., 2008. Improved fraunhofer line discrimination method for fluorescence quantification. IEEE Geoscience and Remote Sensing Letters. 5,620-624. https://doi.org/10.1109/lgrs.2001180

Alonso, L., Van Wittenberghe, S., Amorós-López, J., Vila-Francés, J., Gómez-Chova, L., Moreno, J., 2017. Diurnal cycle relationships between passive fluorescence, PRI and NPQ of vegetation in a controlled stress experiment. Remote Sensing. 9,770. https://doi.org/10.3390/rs9080770

Amoros-Lopez, J., Gomez-Chova, L., Vila-Frances, J., Alonso, L., Calpe, J., Moreno, J., del Valle-Tascon, S., 2008. Evaluation of remote sensing of vegetation fluorescence by the analysis of diurnal cycles. International Journal of Remote Sensing. 29,5423-5436. https://doi.org/10.1080/01431160802036391

Araus, J.L., Cairns, J.E., 2014. Field high-throughput phenotyping: the new crop breeding frontier. Trends in plant science. 19,52-61. https://doi.org/10.1016/j.tplants.2013.09.008

Asrar, G., Fuchs, M., Kanemasu, E., Hatfield, J., 1984. Estimating absorbed photosynthetic radiation and leaf area index from spectral reflectance in wheat[1]. Agronomy Journal. 76,300-306. https://doi.org/10.2134/agronj1984.00021962007600020029x

Atzberger, C., 2013. Advances in remote sensing of agriculture: Context description, existing operational monitoring systems and major information needs. Remote Sensing. 5,949-981. https://doi.org/10.3390/rs5020949

Baker, N.R., 2008. Chlorophyll fluorescence: a probe of photosynthesis in vivo. Annual Review of Plant Biology. 59,89-113. https://doi.org/10.1146/annurev.arplant.59.032607.092759

Bandopadhyay, S., Rastogi, A., Juszczak, R., 2020. Review of Top-of-Canopy Sun-Induced Fluorescence (SIF) Studies from Ground, UAV, Airborne to Spaceborne Observations. Sensors. 20,1144. https://doi.org/10.3390/s20041144

Barnabás, B., Jäger, K., Fehér, A., 2008. The effect of drought and heat stress on reproductive processes in cereals. Plant, Cell & Environment. 31,11-38. https://doi.org/10.1111/j.1365-3040.2007.01727.x

Barton, C.V.M., North, P., 2001. Remote sensing of canopy light use efficiency using the photochemical reflectance index: Model and sensitivity analysis. Remote Sensing of Environment. 78,264-273. https://doi.org/10.1016/S0034-4257(01)00224-3

Beddington, J.R., Asaduzzaman, M., Bremauntz, F.A., Clark, M.E., Guillou, M., Jahn, M.M., Erda, L., Mamo, T., Van Bo, N., Nobre, C.A., 2012. Achieving food security in the face of climate change: Final report from the Commission on Sustainable Agriculture and Climate Change. hal-02807678

Bendig, J., Chang, C., Wang, N., Atherton, J., Malenovský, Z., Rascher, U., 2021. Measuring solar-induced fluorescence from unmanned aircraft systems for operational use in plant phenotyping and precision farming. In, 2021 IEEE International Geoscience and Remote Sensing Symposium. 1921-1924. http://doi.org/10.1109/IGARSS47720.2021.9555157

Bendig, J., Gautam, D., Malenovský, Z., Lucieer, A. 2018. Influence of cosine corrector and UAS platform dynamics on airborne spectral irradiance measurements. In IGARSS 2018-2018 IEEE International Geoscience and Remote Sensing Symposium. 8822-8825. http://doi.org/10.1109/IGARSS.2018.8518864

Bendig, J., Malenovský, Z., Gautam, D., Lucieer, A., 2020. Solar-induced chlorophyll fluorescence measured from an unmanned aircraft system: sensor etaloning and platform motion correction. IEEE Transactions on Geoscience and Remote Sensing. 58(5), 3437-3444. https://doi.org/10.1109/TGRS.2019.2956194

Berry, J., Bjorkman, O., 1980. Photosynthetic response and adaptation to temperature in higher plants. Annual Review of Plant Physiology. 31,491-543.

Biriukova, K., Celesti, M., Evdokimov, A., Pacheco-Labrador, J., Julitta, T., Migliavacca, M., Giardino, C., Miglietta, F., Colombo, R., Panigada, C., 2020. Effects of varying solar-view geometry and canopy structure on solar-induced chlorophyll fluorescence and PRI. International Journal of Applied Earth Observation and Geoinformation. 89,102069. https://doi.org/10.1016/j.jag.2020.102069

Boren, E.J., Boschetti, L., Johnson, D.M., 2019. Characterizing the variability of the structure parameter in the PROSPECT leaf optical properties model. Remote Sensing. 11,1236. https://doi.org/10.3390/rs11101236

Bork, E.W., Su, J.G., 2007. Integrating LIDAR data and multispectral imagery for enhanced classification of rangeland vegetation: A meta analysis. Remote Sensing of Environment. 111,11-24. https://doi.org/10.1016/j.rse.2007.03.011

Breda, N.J., 2003. Ground-based measurements of leaf area index: a review of methods, instruments and current controversies. Journal of Experimental Botany. 54,2403-2417. https://doi.org/10.1093/jxb/erg263

Brede, B., Calders, K., Lau, A., Raumonen, P., Bartholomeus, H.M., Herold, M., Kooistra, L., 2019. Non-destructive tree volume estimation through quantitative structure modelling: Comparing UAV laser scanning with terrestrial LIDAR. Remote Sensing of Environment. 233,111355. https://doi.org/10.1016/j.rse.2019.111355

Bryant, D.A., Frigaard, N.-U., 2006. Prokaryotic photosynthesis and phototrophy illuminated. Trends in Microbiology. 14,488-496. https://doi.org/10.1016/j.tim.2006.09.001

Calderón, R., Navas-Cortés, J.A., Lucena, C., Zarco-Tejada, P.J., 2013. High-resolution airborne hyperspectral and thermal imagery for early detection of Verticillium wilt of olive using fluorescence, temperature and narrow-band spectral indices. Remote Sensing of Environment. 139,231-245. https://doi.org/10.1016/j.rse.2013.07.031

Camejo, D., Jiménez, A., Alarcón, J.J., Torres, W., Gómez, J.M., Sevilla, F., 2006. Changes in photosynthetic parameters and antioxidant activities following heat-shock treatment in tomato plants. Functional Plant Biology. 33,177-187. https://doi.org/10.1071/FP05067

Camino, C., González-Dugo, V., Hernández, P., Sillero, J.C., Zarco-Tejada, P.J., 2018. Improved nitrogen retrievals with airborne-derived fluorescence and plant traits quantified from VNIR-SWIR hyperspectral imagery in the context of precision agriculture. International Journal of Applied Earth Observation and Geoinformation. 70,105-117. https://doi.org/10.1016/j.jag.2018.04.013

Camino, C., Gonzalez-Dugo, V., Hernandez, P., Zarco-Tejada, P.J., 2019. Radiative transfer Vcmax estimation from hyperspectral imagery and SIF retrievals to assess photosynthetic performance in rainfed and irrigated plant phenotyping trials. Remote Sensing of Environment. 231,111186. https://doi.org/10.1016/j.rse.2019.05.005

Campbell, P., Huemmrich, K., Middleton, E., Ward, L., Julitta, T., Daughtry, C., Burkart, A., Russ, A., Kustas, W., 2019. Diurnal and seasonal variations in chlorophyll fluorescence associated with photosynthesis at leaf and canopy scales. Remote Sensing. 11(5). doi.org/ 488.10.3390/rs11050488

Carlson, T.N., Ripley, D.A., 1997. On the relation between NDVI, fractional vegetation cover, and leaf area index. Remote Sensing of Environment. 62,241-252. https://doi.org/10.1016/S0034-4257(97)00104-1

Celesti, M., van der Tol, C., Cogliati, S., Panigada, C., Yang, P., Pinto, F., Rascher, U., Miglietta, F., Colombo, R., Rossini, M., 2018. Exploring the physiological information of Sun-induced chlorophyll fluorescence through radiative transfer model inversion. Remote Sensing of Environment. 215,97-108. https://doi.org/10.1016/j.rse.2018.05.013

Cendrero-Mateo, M.P., Carmo-Silva, A.E., Porcar-Castell, A., Hamerlynck, E.P., Papuga, S.A., Moran, M.S., 2015. Dynamic response of plant chlorophyll fluorescence to light, water and nutrient availability. Functional Plant Biology. 42,746-757. https:// doi.org/10.1071/FP15002

Cendrero-Mateo, M.P., Moran, M.S., Papuga, S.A., Thorp, K., Alonso, L., Moreno, J., Ponce-Campos, G., Rascher, U., Wang, G., 2016. Plant chlorophyll fluorescence: active and passive measurements at canopy and leaf scales with different nitrogen treatments. Journal of Experimental Botany. 67,275-286. https:// doi.org/10.1093/jxb/erv456

Cendrero-Mateo, M.P., Wieneke, S., Damm, A., Alonso, L., Pinto, F., Moreno, J., Guanter, L., Celesti, M., Rossini, M., Sabater, N., 2019. Sun-induced chlorophyll fluorescence III: Benchmarking retrieval methods and sensor characteristics for proximal sensing. Remote Sensing. 11,962.https://doi.org/10.3390/rs11080962

Chaerle, L., Van Der Straeten, D., 2000. Imaging techniques and the early detection of plant stress. Trends in Plant Science. 5,495-501. https://doi.org/10.1016/S1360-1385(00)01781-7

Chang, C.Y., Wen, J., Han, J., Kira, O., LeVonne, J., Melkonian, J., Riha, S.J., Skovira, J., Ng, S., Gu, L., 2021. Unpacking the drivers of diurnal dynamics of sun-induced chlorophyll fluorescence (SIF): Canopy structure, plant physiology, instrument configuration and retrieval methods. Remote Sensing of Environment. 265,112672. https://doi.org/10.1016/j.rse.2021.112672

Chang, C.Y., Zhou, R., Kira, O., Marri, S., Skovira, J., Gu, L., Sun, Y., 2020. An Unmanned Aerial System (UAS) for concurrent measurements of solar-induced chlorophyll fluorescence and hyperspectral reflectance toward improving crop monitoring. Agricultural and Forest Meteorology. 294,108145. https://doi.org/10.1016/j.agrformet.2020.108145

Chaves, M.M., Maroco, J.P., Pereira, J.S., 2003. Understanding plant responses to drought—from genes to the whole plant. Functional Plant Biology. 30,239-264. https://doi.org/10.1071/FP02076

Chaves, M.M., Pereira, J.S., Maroco, J., Rodrigues, M.L., Ricardo, C.P.P., Osório, M.L., Carvalho, I., Faria, T., Pinheiro, C., 2002. How plants cope with water stress in the field? Photosynthesis and growth. Annals of Botany. 89,907-916. https://doi.org/10.1093/aob/mcf105

Chen, J., Liu, X., Du, S., Ma, Y., Liu, L., 2021. Effects of Drought on the Relationship Between Photosynthesis and Chlorophyll Fluorescence for Maize. IEEE Journal of Selected Topics in Applied Earth Observations and Remote Sensing. 14,11148-11161. https://doi.org/10.1109/JSTARS.2021.3123111

Chen, S., Huang, Y., Wang, G., 2021. Detecting drought-induced GPP spatiotemporal variabilities with sun-induced chlorophyll fluorescence during the 2009/2010 droughts in China. Ecological Indicators. 121,107092. https://doi.org/10.1016/j.ecolind.2020.107092

Cheng, Y.B., Middleton, E.M., Zhang, Q., Huemmrich, K.F., Campbell, P.K., Cook, B.D., Kustas, W.P., Daughtry, C.S., 2013. Integrating solar induced fluorescence and the photochemical reflectance index for estimating gross primary production in a cornfield. Remote Sensing. 5,6857-6879. https://doi.org/10.3390/rs5126857

Clevers, J.G., Kooistra, L., 2011. Using hyperspectral remote sensing data for retrieving canopy chlorophyll and nitrogen content. IEEE Journal of Selected Topics in Applied Earth Observations and Remote Sensing. 5,574-583. https://doi.org/10.1109/JSTARS.2011.2176468

Cogliati, S., Rossini, M., Julitta, T., Meroni, M., Schickling, A., Burkart, A., Pinto, F., Rascher, U., Colombo, R., 2015. Continuous and long-term measurements of reflectance and sun-induced chlorophyll fluorescence by using novel automated field spectroscopy systems. Remote Sensing of Environment. 164,270-281. https://doi.org/10.1016/j.rse.2015.03.027

Colombo, R., Celesti, M., Bianchi, R., Campbell, P.K., Cogliati, S., Cook, B.D., Corp, L.A., Damm, A., Domec, J.C., Guanter, L., 2018. Variability of sun-induced chlorophyll fluorescence according to stand age-related processes in a managed loblolly pine forest. Global Change Biology. 24,2980-2996. https://doi.org/10.1111/gcb.14097

Damm, A., Elbers, J., Erler, A., Gioli, B., Hamdi, K., Hutjes, R., Kosvancova, M., Meroni, M., Miglietta, F., Moersch, A., 2010. Remote sensing of sun-induced fluorescence to improve modeling of diurnal courses of gross primary production (GPP). Global Change Biology. 16,171-186. https://doi.org/10.1111/j.1365-2486.2009.01908.x

Damm, A., Guanter, L., Laurent, V.C.E., Schaepman, M.E., Schickling, A., Rascher, U., 2014. FLD-based retrieval of sun-induced chlorophyll fluorescence from medium spectral resolution airborne spectroscopy data. Remote Sensing of Environment. 147,256-266. https://doi.org/10.1016/j.rse.2014.03.009

Damm, A., Guanter, L., Paul-Limoges, E., Van der Tol, C., Hueni, A., Buchmann, N., Eugster, W., Ammann, C., Schaepman, M.E., 2015. Far-red sun-induced chlorophyll fluorescence shows ecosystem-specific relationships to gross primary production: An assessment based on observational and modeling approaches. Remote Sensing of Environment. 166,91-105. https://doi.org/10.1016/j.rse.2015.06.004

Dash, J., Curran, P., 2004. The MERIS terrestrial chlorophyll index. https://10.1080/0143116042000274015

Daumard, F., Champagne, S., Fournier, A., Goulas, Y., Ounis, A., Hanocq, J.-F., Moya, I., 2010. A field platform for continuous measurement of canopy fluorescence. IEEE Transactions on Geoscience and Remote Sensing. 48,3358-3368. https://doi.org/10.1109/TGRS.2010.2046420

Daumard, F., Goulas, Y., Champagne, S., Fournier, A., Ounis, A., Olioso, A., Moya, I., 2012. Continuous monitoring of canopy level sun-induced chlorophyll fluorescence during the growth of a sorghum field. IEEE Transactions on Geoscience and Remote Sensing. 50,4292-4300. https://doi.org/10.1109/TGRS.2012.2193131

Dechant, B., Ryu, Y., Badgley, G., Köhler, P., Rascher, U., Migliavacca, M., Zhang, Y., Tagliabue, G., Guan, K., Rossini, M., 2022. NIRVP: A robust structural proxy for sun-induced chlorophyll fluorescence and photosynthesis across scales. Remote Sensing of Environment. 268,112763. https://doi.org/10.1016/j.rse.2021.112763

Dechant, B., Ryu, Y., Badgley, G., Zeng, Y., Berry, J.A., Zhang, Y., Goulas, Y., Li, Z., Zhang, Q., Kang, M., 2020. Canopy structure explains the relationship between photosynthesis and sun-induced chlorophyll fluorescence in crops. Remote Sensing of Environment. 241,111733. https://doi.org/10.1016/j.rse.2020.111733

Drusch, M., Moreno, J., Del Bello, U., Franco, R., Goulas, Y., Huth, A., Kraft, S., Middleton, E.M., Miglietta, F., Mohammed, G., 2016. The fluorescence explorer mission concept-ESA's earth explorer 8. IEEE Transactions on Geoscience and Remote Sensing. 55,1273-1284. https://doi.org/10.1109/TGRS.2016.2621820

Du, S., Liu, L., Liu, X., Zhang, X., Zhang, X., Bi, Y., Zhang, L., 2018. Retrieval of global terrestrial solar-induced chlorophyll fluorescence from TanSat satellite. Science Bulletin. 63,1502-1512. https://10.1016/j.scib.2018.10.003

Evans, L., Fischer, R., 1999. Yield potential: its definition, measurement, and significance. Crop Science. 39,1544-1551. https://doi.org/10.2135/cropsci1999.3961544x

Fahad, S., Bajwa, A.A., Nazir, U., Anjum, S.A., Farooq, A., Zohaib, A., Sadia, S., Nasim, W., Adkins, S., Saud, S., 2017. Crop production under drought and heat stress: plant responses and management options. Frontiers in Plant Science. 8,1147. https://doi.org/10.3389/fpls.2017.01147

Farooq, M., Wahid, A., Kobayashi, N., Fujita, D., Basra, S., 2009. Plant drought stress: effects, mechanisms and management. Sustainable Agriculture. 153-188. https:// doi.org/10.1051/agro:2008021

Farquhar, G.D., Von Caemmerer, S., Berry, J.A., 2001. Models of photosynthesis. Plant Physiology. 125,42-45. http://doi.org/10.1104/pp.125.1.42

Filella, I., Porcar-Castell, A., Munné-Bosch, S., Bäck, J., Garbulsky, M., Peñuelas, J., 2009. PRI assessment of long-term changes in carotenoids/chlorophyll ratio and short-term changes in de-epoxidation state of the xanthophyll cycle. International Journal of Remote Sensing. 30,4443-4455. https://doi.org /10.1080/01431160802575661

Flexas, J., Bota, J., Escalona, J.M., Sampol, B., Medrano, H., 2002. Effects of drought on photosynthesis in grapevines under field conditions: an evaluation of stomatal and mesophyll limitations. Functional Plant Biology. 29,461-471. https://doi.org/10.1071/PP01119

Flexas, J., Medrano, H., 2002. Drought-inhibition of photosynthesis in C3 plants: stomatal and non-stomatal limitations revisited. Annals of Botany. 89,183-189. https://doi.org/10.1093/aob/mcf027

Flexas, J., Ribas-Carbó, M., Bota, J., Galmés, J., Henkle, M., Martínez-Cañellas, S., Medrano, H., 2006. Decreased Rubisco activity during water stress is not induced by decreased relative water content but related to conditions of low stomatal conductance and chloroplast CO2 concentration. New Phytologist. 172,73-82. https://doi.org/10.1111/j.1469-8137.2006.01794.x

Foley, J.A., Ramankutty, N., Brauman, K.A., Cassidy, E.S., Gerber, J.S., Johnston, M., Mueller, N.D., O'Connell, C., Ray, D.K., West, P.C., Balzer, C., Bennett, E.M., Carpenter, S.R., Hill, J., Monfreda, C., Polasky, S., Rockström, J., Sheehan, J., Siebert, S., Tilman, D., Zaks, D.P.M., 2011. Solutions for a cultivated planet. Nature. 478,337-342. https://doi.org/10.1038/nature10452

Frankenberg, C., Berry, J., 2018. Solar induced chlorophyll fluorescence: Origins, relation to photosynthesis and retrieval. Comprehensive Remote Sensing, 3, 143-162. https://doi.org/10.1016/B978-0-12-409548-9.10632-3

Frankenberg, C., Fisher, J.B., Worden, J., Badgley, G., Saatchi, S.S., Lee, J.E., Toon, G.C., Butz, A., Jung, M., Kuze, A., 2011. New global observations of the terrestrial carbon cycle from GOSAT: Patterns of plant fluorescence with gross primary productivity. Geophysical Research Letters. 38, https://doi.org/10.1029/2011GL048738

Frankenberg, C., O'Dell, C., Berry, J., Guanter, L., Joiner, J., Köhler, P., Pollock, R., Taylor, T.E., 2014. Prospects for chlorophyll fluorescence remote sensing from the Orbiting Carbon Observatory-2. Remote Sensing of Environment. 147,1-12. https://doi.org/10.1016/j.rse.2014.02.007

Fu, J., Huang, B., 2001. Involvement of antioxidants and lipid peroxidation in the adaptation of two cool-season grasses to localized drought stress. Environmental and Experimental Botany. 45,105-114. https://doi.org/10.1016/S0098-8472(00)00084-8

Gamon, J., Penuelas, J., Field, C., 1992. A narrow-waveband spectral index that tracks diurnal changes in photosynthetic efficiency. Remote Sensing of Environment. 41,35-44. https://doi.org/10.1016/0034-4257(92)90059-S

Gamon, J., Serrano, L., Surfus, J., 1997. The photochemical reflectance index: an optical indicator of photosynthetic radiation use efficiency across species, functional types, and nutrient levels. Oecologia. 112,492-501.

Garzonio, R., Di Mauro, B., Colombo, R., Cogliati, S., 2017. Surface reflectance and sun-induced fluorescence spectroscopy measurements using a small hyperspectral UAS. Remote Sensing. 9(5),472. https://doi.org/10.3390/rs9050472

Gastellu-Etchegorry, J.-P., Lauret, N., Yin, T., Landier, L., Kallel, A., Malenovský, Z., Al Bitar, A., Aval, J., Benhmida, S., Qi, J., 2017. DART: recent advances in remote sensing data modeling with atmosphere, polarization, and chlorophyll fluorescence. IEEE Journal of Selected Topics in Applied Earth Observations and Remote Sensing. 10,2640-2649. https://doi.org/10.1109/JSTARS.2017.2685528

Gastellu-Etchegorry, J.-P., Malenovský, Z., Gomez, N.D., Meynier, J., Lauret, N., Yin, T., Qi, J., Guilleux, J., Chavanon, E., Cook, B., 2018. Simulation of chlorophyll fluorescence for sun-and shade-adapted leaves of 3d canopies with the dart model. In, IGARSS 2018-2018 IEEE International Geoscience and Remote Sensing Symposium. 5995-5998. https://doi.org/10.1109/IGARSS.2018.8517576

Gautam, D., Lucieer, A., Bendig, J., Malenovsky, Z., 2020. Footprint Determination of a Spectroradiometer Mounted on an Unmanned Aircraft System. IEEE Transactions on Geoscience and Remote Sensing. 58, (5), 3085-3096. https://doi.org/10.1109/TGRS.2019.2947703

Gautam, D., Watson, C., Lucieer, A., Malenovský, Z., 2018. Error budget for geolocation of spectroradiometer point observations from an unmanned aircraft system. Sensors. 18(10), 3465. https://doi.org/10.3390/s18103465

Gerhards, M., Schlerf, M., Mallick, K., Udelhoven, T., 2019. Challenges and future perspectives of multi-/Hyperspectral thermal infrared remote sensing for crop water-stress detection: A review. Remote Sensing. 11,1240. https://doi.org/10.3390/rs11101240

Gerhards, M., Schlerf, M., Rascher, U., Udelhoven, T., Juszczak, R., Alberti, G., Miglietta, F., Inoue, Y., 2018. Analysis of airborne optical and thermal imagery for detection of water stress symptoms. Remote Sensing. 10,1139. https://doi.org/10.3390/rs10071139

Gitelson, A.A., Gamon, J.A., Solovchenko, A., 2017. Multiple drivers of seasonal change in PRI: Implications for photosynthesis 2. Stand level. Remote Sensing of Environment. 190,198-206. https://doi.org/10.1016/j.rse.2016.12.015

Gitelson, A.A., Peng, Y., Huemmrich, K.F., 2014. Relationship between fraction of radiation absorbed by photosynthesizing maize and soybean canopies and NDVI from remotely sensed data taken at close range and from MODIS 250 m resolution data. Remote Sensing of Environment. 147, 108-120. https://doi.org/10.1016/j.rse.2014.02.014

Gitelson, A.A., Vina, A., Ciganda, V., Rundquist, D. C., Arkebauer, T. J., 2005. Remote estimation of canopy chlorophyll content in crops. Geophysical Research Letters, 32, 8. https://doi.org/10.1029/2005GL022688

Godfray, H.C.J., Beddington, J.R., Crute, I.R., Haddad, L., Lawrence, D., Muir, J.F., Pretty, J., Robinson, S., Thomas, S.M., Toulmin, C., 2010. Food security: the challenge of feeding 9 billion people. Science. 327,812-818. https://doi.org/10.1126/science.1185383

Gonzalez, R.C., Woods, R.E., 2006. Digital Image Pro-cessing (3rd Edition), Prentice-Hall, Inc., Upper Saddle River, NJ, USA.

Goss, R., Lepetit, B., 2015. Biodiversity of NPQ. Journal of Plant Physiology. 172,13-32. http://doi.org/10.1016/j.jplph.2014.03.004

Goulas, Y., Fournier, A., Daumard, F., Champagne, S., Ounis, A., Marloie, O., Moya, I., 2017. Gross primary production of a wheat canopy relates stronger to far red than to red solar-induced chlorophyll fluorescence. Remote Sensing. 9,97. https://doi.org/10.3390/rs9010097

Govender, M., Govender, P., Weiersbye, I., Witkowski, E., Ahmed, F., 2009. Review of commonly used remote sensing and ground-based technologies to measure plant water stress. Water SA. 35. http://doi.org/10.4314/wsa.v35i5.49201

Gu, L., Han, J., Wood, J.D., Chang, C.Y.Y., Sun, Y., 2019. Sun-induced Chl fluorescence and its importance for biophysical modeling of photosynthesis based on light reactions. New Phytologist. 223,1179-1191. http://doi.org/10.1111/nph.15796

Gu, L., Wood, J. D., Chang, C. Y., Sun, Y., Riggs, J. S., 2019. Advancing terrestrial ecosystem science with a novel automated measurement system for sun-induced chlorophyll fluorescence for integration with eddy covariance flux networks. Journal of Geophysical Research: Biogeosciences, 124(1), 127-146. http://doi.org/10.1029/2018JG004742

Guan, K., Berry, J.A., Zhang, Y., Joiner, J., Guanter, L., Badgley, G., Lobell, D.B., 2016. Improving the monitoring of crop productivity using spaceborne solar-induced fluorescence. Global Change Biology. 22,716-726. https://doi.org/10.1111/gcb.13136

Guanter, L., Aben, I., Tol, P., Krijger, J., Hollstein, A., Köhler, P., Damm, A., Joiner, J., Frankenberg, C., Landgraf, J., 2015. Potential of the TROPOspheric Monitoring instrument (TROPOMI) onboard the Sentinel-5 Precursor for the monitoring of terrestrial chlorophyll fluorescence. Atmospheric Measurement Techniques. 8,1337-1352. https://doi.org/10.5194/amt-8-1337-2015

Guanter, L., Bacour, C., Schneider, A., Aben, I., van Kempen, T.A., Maignan, F., Retscher, C., Köhler, P., Frankenberg, C., Joiner, J., 2021. The TROPOSIF global sun-induced fluorescence dataset from the Sentinel-5P TROPOMI mission. Earth System Science Data Discussions. 1-27. https://doi.org/10.5270/esa-s5p_innovation-sif-20180501_20210320-v2.1-202104

Guanter, L., Zhang, Y., Jung, M., Joiner, J., Voigt, M., Berry, J.A., Frankenberg, C., Huete, A.R., Zarco-Tejada, P., Lee, J.-E., Moran, M.S., Ponce-Campos, G., Beer, C., Camps-Valls, G., Buchmann, N., Gianelle, D., Klumpp, K., Cescatti, A., Baker, J.M., Griffis, T.J., 2014. Global and time-resolved monitoring of crop photosynthesis with chlorophyll fluorescence. Proceedings of the National Academy of Sciences. 111, E1327-E1333. https://doi.org/10.1073/pnas.1320008111

Haboudane, D., Miller, J.R., Tremblay, N., Zarco-Tejada, P.J., Dextraze, L., 2002. Integrated narrow-band vegetation indices for prediction of crop chlorophyll content for application to precision agriculture. Remote Sensing of Environment. 81,416-426. https://doi.org/10.1016/S0034-4257(02)00018-4

Hawkesford, M.J., Araus, J.L., Park, R., Calderini, D., Miralles, D., Shen, T., Zhang, J., Parry, M.A., 2013. Prospects of doubling global wheat yields. Food and Energy Security. 2,34-48. https://doi.org/10.1002/fes3.15

He, L., Chen, J.M., Liu, J., Mo, G., Joiner, J., 2017. Angular normalization of GOME-2 Sun-induced chlorophyll fluorescence observation as a better proxy of vegetation productivity. Geophysical Research Letters. 44,5691-5699. https://doi.org/10.1002/2017GL073708

He, L., Wood, J. D., Sun, Y., Magney, T., Dutta, D., Köhler, P., Zhang, Y., Yin, Y., Frankenberg, C., 2020. Tracking seasonal and interannual variability in photosynthetic downregulation in response to water stress at a temperate deciduous forest. Journal of Geophysical Research: Biogeosciences, 125(8). http://doi.org/10.1029/2018JG005002

Helm, L.T., Shi, H., Lerdau, M.T., Yang, X., 2020. Solar-induced chlorophyll fluorescence and short-term photosynthetic response to drought. Ecological Applications. 30,e02101. https://doi.org/10.1002/eap.2101

Honkavaara, E., Saari, H., Kaivosoja, J., Pölönen, I., Hakala, T., Litkey, P., Mäkynen, J., Pesonen, L., 2013. Processing and assessment of spectrometric, stereoscopic imagery collected using a lightweight UAV spectral camera for precision agriculture. Remote Sensing. 5,5006-5039. http://doi.org/10.3390/rs5105006

Hsiao, T.C., 1973. Plant responses to water stress. Annual Review of Plant Physiology. 24,519-570.

Hsu, H., Lachenbruch, P.A., 2014. Paired t test. Wiley StatsRef: Statistics Reference Online. http://doi.org/10.1002/9781118445112.stat05929

Jackson, R.D., Idso, S., Reginato, R., Pinter Jr, P., 1981. Canopy temperature as a crop water stress indicator. Water Resources Research. 17,1133-1138. https://doi.org/10.1029/WR017i004p01133

Jacquemoud, S., Baret, F., 1990. PROSPECT: A model of leaf optical properties spectra. Remote Sensing of Environment. 34,75-91. https://doi.org/10.1016/0034-4257(90)90100-Z

Jacquemoud, S., Ustin, S., Verdebout, J., Schmuck, G., Andreoli, G., Hosgood, B., 1996. Estimating leaf biochemistry using the PROSPECT leaf optical properties model. Remote Sensing of Environment. 56,194-202. https://doi.org/10.1016/0034-4257(95)00238-3

Jacquemoud, S., Verhoef, W., Baret, F., Bacour, C., Zarco-Tejada, P.J., Asner, G.P., François, C., Ustin, S.L., 2009. PROSPECT+ SAIL models: A review of use for vegetation characterization. Remote sensing of environment. 113,S56-S66. https://doi.org/10.1016/j.rse.2008.01.026

James, A., Plascyk, J. 1975. The MK II fraunhofer line discriminator (FLD-II) for airborne and orbital remote sensing of solar-stimulated luminescence. Optical Engineering. 14 (4), 144339. https://doi.org/10.1117/12.7971842

Jay, S., Gorretta, N., Morel, J., Maupas, F., Bendoula, R., Rabatel, G., Dutartre, D., Comar, A., Baret, F., 2017. Estimating leaf chlorophyll content in sugar beet canopies using millimeter- to centimeter-scale reflectance imagery. Remote Sensing of Environment., 198, 173-186. http://doi.org/10.1016/j.rse.2017.06.008

Jeong, S.-J., Schimel, D., Frankenberg, C., Drewry, D.T., Fisher, J.B., Verma, M., Berry, J.A., Lee, J.-E., Joiner, J., 2017. Application of satellite solar-induced chlorophyll fluorescence to understanding large-scale variations in vegetation phenology and function over northern high latitude forests. Remote Sensing of Environment. 190,178-187. http://doi.org/10.1016/j.rse.2016.11.021

Joiner, J., Guanter, L., Lindstrot, R., Voigt, M., Vasilkov, A., Middleton, E., Huemmrich, K., Yoshida, Y., Frankenberg, C., 2013. Global monitoring of terrestrial chlorophyll fluorescence from moderate spectral resolution near-infrared satellite measurements: Methodology, simulations, and application to GOME-2. Atmospheric Measurement Techniques. 6,2803-2823. https://doi.org/10.5194/amt-6-2803-2013

Jonard, F., De Canniere, S., Brüggemann, N., Gentine, P., Gianotti, D.S., Lobet, G., Miralles, D.G., Montzka, C., Pagán, B.R., Rascher, U., 2020. Value of sun-induced chlorophyll fluorescence for quantifying hydrological states and fluxes: Current status and challenges. Agricultural and Forest Meteorology. 291,108088. https://doi.org/10.1016/j.agrformet.2020.108088

Jones, H., Schofield, P., 2008. Thermal and other remote sensing of plant stress. General and Applied Plant Physiology. 34,19-32.

Julitta, T., Corp, L., Rossini, M., Burkart, A., Cogliati, S., Davies, N., Hom, M., Mac Arthur, A., Middleton, E., Rascher, U., Schickling, A., Colombo, R., 2016. Comparison of Sun-Induced Chlorophyll Fluorescence Estimates Obtained from Four Portable Field Spectroradiometers. Remote Sensing. 8(2), 122. https://doi.org/10.3390/rs8020122

Kalaji, H.M., Jajoo, A., Oukarroum, A., Brestic, M., Zivcak, M., Samborska, I.A., Cetner, M.D., Łukasik, I., Goltsev, V., Ladle, R.J., 2016. Chlorophyll a fluorescence as a tool to monitor physiological status of plants under abiotic stress conditions. Acta Physiologiae Plantarum. 38,102. https://doi.org/10.1007/s11738-016-2113-y

Kalaji, M.H., Goltsev, V.N., Żuk-Gołaszewska, K., Zivcak, M., Brestic, M., 2017. Chlorophyll Fluorescence: Understanding Crop Performance — Basics and Applications, 1 ed. CRC Press, Florida.

Kimm, H., Guan, K., Jiang, C., Miao, G., Wu, G., Suyker, A.E., Ainsworth, E.A., Bernacchi, C.J., Montes, C.M., Berry, J.A., 2021. A physiological signal derived from sun-induced chlorophyll fluorescence quantifies crop physiological response to environmental stresses in the US Corn Belt. Environmental Research Letters. 16,124051.

Knudby, A., LeDrew, E., Brenning, A., 2010. Predictive mapping of reef fish species richness, diversity and biomass in Zanzibar using IKONOS imagery and machine-learning techniques. Remote Sensing of Environment. 114,1230-1241. https://doi.org/10.1016/j.rse.2010.01.007

Koren, G., van Schaik, E., Araújo, A.C., Boersma, K.F., Gärtner, A., Killaars, L., Kooreman, M.L., Kruijt, B., van der Laan-Luijkx, I.T., von Randow, C., 2018. Widespread reduction in sun-induced fluorescence from the Amazon during the 2015/2016 El Niño. Philosophical Transactions of the Royal Society B: Biological Sciences. 373,20170408. https://doi.org/10.1098/rstb.2017.0408

Krause, G., Weis, E., 1991. Chlorophyll fluorescence and photosynthesis: the basics. Annual Review of Plant Biology. 42,313-349.

Krause, G.H., 1988. Photoinhibition of photosynthesis. An evaluation of damaging and protective mechanisms. Physiologia Plantarum. 74,566-574. https://doi.org/10.1111/j.1399-3054.1988.tb02020.x

Lee, J.-E., Frankenberg, C., van der Tol, C., Berry, J.A., Guanter, L., Boyce, C.K., Fisher, J.B., Morrow, E., Worden, J.R., Asefi, S., 2013. Forest productivity and water stress in Amazonia: Observations from GOSAT chlorophyll fluorescence. Proceedings of the Royal Society B: Biological Sciences. 280,20130171. https://doi.org/10.1098/rspb.2013.0171

Lesk, C., Rowhani, P., Ramankutty, N., 2016. Influence of extreme weather disasters on global crop production. Nature. 529,84-87. http://doi.org/10.1038/nature16467

Li, Z., Zhang, Q., Li, J., Yang, X., Wu, Y., Zhang, Z., Wang, S., Wang, H., Zhang, Y., 2020. Solar-induced chlorophyll fluorescence and its link to canopy photosynthesis in maize from continuous ground measurements. Remote Sensing of Environment. 236,111420. https://doi.org/10.1016/j.rse.2019.111420

Lichtenthaler, H.K., 1987. Chlorophyll fluorescence signatures of leaves during the autumnal chlorophyll breakdown. Journal of Plant Physiology. 131,101-110. https://doi.org/10.1016/S0176-1617(87)80271-7

Lichtenthaler, H.K., Rinderle, U., 1988. The role of chlorophyll fluorescence in the detection of stress conditions in plants. CRC Critical Reviews in Analytical Chemistry. 19,S29-S85. https://doi.org/10.1080/15476510.1988.10401466

Liu, X., Guanter, L., Liu, L., Damm, A., Malenovský, Z., Rascher, U., Peng, D., Du, S., Gastellu-Etchegorry, J.-P., 2019. Downscaling of solar-induced chlorophyll fluorescence from canopy level to photosystem level using a random forest model. Remote Sensing of Environment. 231,110772. https://doi.org/10.1016/j.rse.2018.05.035

Lobell, D.B., Schlenker, W., Costa-Roberts, J., 2011. Climate trends and global crop production since 1980. Science. 333,616-620. https://doi.org/10.1126/science.1204531

Long, S.P., Zhu, X.G., Naidu, S.L., Ort, D.R., 2006. Can improvement in photosynthesis increase crop yields? Plant Cell & Environment. 29, 315-330. http:/doi.org/10.1111/j.1365-3040.2005.01493.x 315.

Lu, X., Liu, Z., Zhao, F., Tang, J., 2020. Comparison of total emitted solar-induced chlorophyll fluorescence (SIF) and top-of-canopy (TOC) SIF in estimating photosynthesis. Remote Sensing of Environment. 251,112083. http://doi.org/10.1016/j.rse.2020.112083

Ma, C., Zhang, H.H., Wang, X., 2014. Machine learning for big data analytics in plants. Trends in Plant Science. 19,798-808. https://doi.org/10.1016/j.tplants.2014.08.004

MacArthur, A., Robinson, I., 2015. A critique of field spectroscopy and the challenges and opportunities it presents for remote sensing for agriculture, ecosystems, and hydrology. International Society for Optics and Photonics. 9637, 963705. https://doi.org/10.1117/12.2201046

MacArthur, A., Robinson, I., Rossini, M., Davis, N., MacDonald, K., 2014. A dual-field-of-view spectrometer system for reflectance and fluorescence measurements (Piccolo Doppio) and correction of etaloning. Proceedings of the 5th International Workshop on Remote Sensing of Vegetation Fluorescence, Paris, France. 22-24.

Maes, W., Steppe, K., 2012. Estimating evapotranspiration and drought stress with ground-based thermal remote sensing in agriculture: a review. Journal of Experimental Botany. 63,4671-4712. http://doi.org/10.1093/jxb/ers165

Magney, T.S., Barnes, M.L., Yang, X., 2020. On the covariation of chlorophyll fluorescence and photosynthesis across scales. Geophysical Research Letters. 47,e2020GL091098. http://doi.org/10.1029/2020GL091098

Magney, T.S., Frankenberg, C., Fisher, J.B., Sun, Y., North, G.B., Davis, T.S., Kornfeld, A., Siebke, K., 2017. Connecting active to passive fluorescence with photosynthesis: a method for evaluating remote sensing measurements of Chl fluorescence. New Phytologist. 215,1594-1608. https://doi.org/10.1111/nph.14662

Mahajan, S., Tuteja, N., 2005. Cold, salinity and drought stresses: an overview. Archives of Biochemistry and Biophysics. 444,139-158. http://doi.org/10.1016/j.abb.2005.10.018

Maier, S.W., Günther, K.P., Stellmes, M., 2004. Sun-induced fluorescence: A new tool for precision farming. Digital Imaging and Spectral Techniques: Applications to Precision Agriculture and Crop Physiology, 66, 207-222. https://doi.org/10.2134/asaspecpub66.c16

Malnou, C., Jaggard, K., Sparkes, D., 2008. Nitrogen fertilizer and the efficiency of the sugar beet crop in late summer. European Journal of Agronomy. 28,47-56. http://doi.org/10.1016/j.eja.2007.05.001

Mancini, F., Dubbini, M., Gattelli, M., Stecchi, F., Fabbri, S., Gabbianelli, G., 2013. Using unmanned aerial vehicles (UAV) for high-resolution reconstruction of topography: The structure from motion approach on coastal environments. Remote Sensing. 5,6880-6898. http://doi.org/10.3390/rs5126880

Markwell, J., Osterman, J.C., Mitchell, J.L., 1995. Calibration of the Minolta SPAD-502 leaf chlorophyll meter. Photosynthesis Research. 46,467-472.

Marrs, J., Reblin, J., Logan, B., Allen, D., Reinmann, A., Bombard, D., Tabachnik, D., Hutyra, L., 2020. Solar-induced fluorescence does not track photosynthetic carbon assimilation following induced stomatal closure. Geophysical Research Letters. 47,e2020GL087956. https://doi.org/10.1029/2020GL087956

Maseyk, K., Atherton, J., Thomas, R.M., Wood, K., Tausz-Sabine, S., Mac Arthur, A., Porcar-Castell, A., Tausz, M., 2018. UAV-based measurements of solar induced fluorescence to gain insight into canopy-level photosynthesis under elevated CO_2. AGU Fall Meeting Abstracts. B34C-06

Mazzoni, M., Meroni, M., Fortunato, C., Colombo, R., Verhoef, W., 2012. Retrieval of maize canopy fluorescence and reflectance by spectral fitting in the O_2–A absorption band. Remote Sensing of Environment. 124, 72-82. https://doi.org/10.1016/j.rse.2012.04.025

Meroni, M., Barducci, A., Cogliati, S., Castagnoli, F., Rossini, M., Busetto, L., Migliavacca, M., Cremonese, E., Galvagno, M., Colombo, R., 2011. The hyperspectral irradiometer, a new instrument for long-term and unattended field spectroscopy measurements. Review of Scientific Instruments. 82,043106. https://doi.org/10.1063/1.3574360

Meroni, M., Busetto, L., Colombo, R., Guanter, L., Moreno, J., Verhoef, W., 2010. Performance of spectral fitting methods for vegetation fluorescence quantification. Remote Sensing of Environment. 114,363-374. http://doi.org/10.1016/j.rse.2009.09.010

Meroni, M., Rossini, M., Guanter, L., Alonso, L., Rascher, U., Colombo, R., Moreno, J., 2009. Remote sensing of solar-induced chlorophyll fluorescence: Review of methods and applications. Remote Sensing of Environment. 113,2037-2051. https://doi.org/10.1016/j.rse.2009.05.003

Miao, G., Guan, K., Yang, X., Bernacchi, C.J., Berry, J.A., DeLucia, E.H., Wu, J., Moore, C.E., Meacham, K., Cai, Y., 2018. Sun-induced chlorophyll fluorescence, photosynthesis, and light use efficiency of a soybean field from seasonally continuous measurements. Journal of Geophysical Research: Biogeosciences. 123,610-623. https://doi.org/10.1002/2017JG004180

Migliavacca, M., Perez-Priego, O., Rossini, M., El-Madany, T.S., Moreno, G., van der Tol, C., Rascher, U., Berninger, A., Bessenbacher, V., Burkart, A., 2017. Plant functional traits and canopy structure control the relationship between photosynthetic CO 2 uptake and far-red sun-induced fluorescence in a Mediterranean grassland under different nutrient availability. New Phytologist. 214,1078-1091. https://doi.org/10.1111/nph.14437

Mo, K.C., Lettenmaier, D.P., 2015. Heat wave flash droughts in decline. Geophysical Research Letters. 42,2823-2829. http://doi.org/10.1002/2015GL064018

MODTRAN Demo. Available online: http://modtran.spectral.com/modtran_home (last accessed on 12 October 2020)

Mohammed, G.H., Colombo, R., Middleton, E.M., Rascher, U., van der Tol, C., Nedbal, L., Goulas, Y., Pérez-Priego, O., Damm, A., Meroni, M., 2019. Remote sensing of solar-induced chlorophyll fluorescence (SIF) in vegetation: 50 years of progress. Remote Sensing of Environment. 231,111177. http://doi.org/10.1016/j.rse.2019.04.030

Monteith, J.L., 1972. Solar radiation and productivity in tropical ecosystems. Journal of Applied Ecology. 9,747-766. https://doi.org/10.2307/2401901.

Monteith, J.L., 1977. Climate and the efficiency of crop production in Britain. Philosophical Transactions of the Royal Society of London B, Biological Sciences. 281,277-294. https://doi.org/10.1098/rstb.1977.0140

Moya, I., Camenen, L., Evain, S., Goulas, Y., Cerovic, Z., Latouche, G., Flexas, J., Ounis, A., 2004. A new instrument for passive remote sensing:1. Measurements of sunlight-induced chlorophyll fluorescence. Remote Sensing of Environment91(2),186–197. https://doi.org/10.1016/j.rse.2004.02.012

Moya, I., Daumard, F., Moise, N., Ounis, A., Goulas, Y., 2006. First airborne multiwavelength passive chlorophyll fluorescence measurements over La Mancha (Spain) fields. Second recent advances in quantitative remote sensing. 820-825.

Mulla, D.J., 2013. Twenty five years of remote sensing in precision agriculture: Key advances and remaining knowledge gaps. Biosystems Engineering. 114,358-371. https://doi.org/10.1016/j.biosystemseng.2012.08.009

Müller, P., Li, X.-P., Niyogi, K.K., 2001. Non-photochemical quenching. A response to excess light energy. Plant physiology. 125,1558-1566. https:// doi.org/10.1104/pp.125.4.1558

Ober, E.S., Rajabi, A., 2010. Abiotic stress in sugar beet. Sugar Tech. 12,294-298. http://doi.org/10.1007/s12355-010-0035-3

Omasa, K., Hosoi, F., Konishi, A., 2007. 3D lidar imaging for detecting and understanding plant responses and canopy structure. Journal of Experimental Botany. 58,881-898. https://doi.org/10.1093/jxb/erl142

Pacheco-Labrador, J., Hueni, A., Mihai, L., Sakowska, K., Julitta, T., Kuusk, J., Sporea, D., Alonso, L., Burkart, A., Cendrero-Mateo, M.P., 2019. Sun-induced chlorophyll fluorescence I: Instrumental considerations for proximal spectroradiometers. Remote Sensing. 11,960. https://doi.org/10.3390/rs11080960

Panigada, C., Rossini, M., Meroni, M., Cilia, C., Busetto, L., Amaducci, S., Boschetti, M., Cogliati, S., Picchi, V., Pinto, F., 2014. Fluorescence, PRI and canopy temperature for water stress detection in cereal crops. International Journal of Applied Earth Observation and Geoinformation. 30,167-178.https://doi.org/10.1016/j.jag.2014.02.002

Paul-Limoges, E., Damm, A., Hueni, A., Liebisch, F., Eugster, W., Schaepman, M.E., Buchmann, N., 2018. Effect of environmental conditions on sun-induced fluorescence in a mixed forest and a cropland. Remote Sensing of Environment. 219,310-323. https://doi.org/10.1016/j.rse.2018.10.018

Pérez-Priego, O., Guan, J.-H., Rossini, M., Fava, F., Wutzler, T., Moreno, G., Carvalhais, N., Carrara, A., Kolle, O., Julitta, T., 2015. Sun-induced chlorophyll fluorescence and photochemical reflectance index improve remote-sensing gross primary production estimates under varying nutrient availability in a typical Mediterranean savanna ecosystem. Biogeosciences. 12,6351-6367. http://doi.org/10.5194/bg-12-6351-2015.

Pingali, P.L., 2012. Green revolution: impacts, limits, and the path ahead. Proceedings of the National Academy of Sciences. 109,12302-12308. https://doi.org/10.1073/pnas.0912953109

Pinto, F., Celesti, M., Acebron, K., Alberti, G., Cogliati, S., Colombo, R., Juszczak, R., Matsubara, S., Miglietta, F., Palombo, A., 2020. Dynamics of sun-induced chlorophyll fluorescence and reflectance to detect stress-induced variations in canopy photosynthesis. Plant, Cell & Environment. 43,1637-1654. https://doi.org/10.1111/pce.13754

Pinto, F., Damm, A., Schickling, A., Panigada, C., Cogliati, S., Müller-Linow, M., Balvora, A., Rascher, U., 2016. Sun-induced chlorophyll fluorescence from high-resolution imaging spectroscopy data to quantify spatio-temporal patterns of photosynthetic function in crop canopies. Plant, Cell & Environment. 39,1500-1512. https://doi.org/10.1111/pce.12710

Pinto, F., Müller-Linow, M., Schickling, A., Cendrero-Mateo, M.P., Ballvora, A., Rascher, U., 2017. Multiangular observation of canopy sun-induced chlorophyll fluorescence by combining imaging spectroscopy and stereoscopy. Remote Sensing. 9,415. http://doi.org/10.3390/rs9050415

Plascyk, J., Gabriel, F. 1975. The Fraunhofer Line Discriminator MKII - An airborne instrument for precise and standardized ecological luminescence measurement. IEEE Transactions on Instrumentation and Measurement 24 (4), 306-313. http://doi.org/10.1109/TIM.1975.4314448

Porcar-Castell, A., Tyystjärvi, E., Atherton, J., van der Tol, C., Flexas, J., Pfündel, E.E., Moreno, J., Frankenberg, C., Berry, J.A., 2014. Linking chlorophyll a fluorescence to photosynthesis for remote sensing applications: mechanisms and challenges. Journal of Experimental Botany. 65,4065-4095. https://doi.org/10.1093/jxb/eru191

Raczka, B., Porcar-Castell, A., Magney, T., Lee, J., Köhler, P., Frankenberg, C., Grossmann, K., Logan, B., Stutz, J., Blanken, P., 2019. Sustained nonphotochemical quenching shapes the seasonal pattern of solar-induced fluorescence at a high-elevation evergreen forest. Journal of Geophysical Research: Biogeosciences. 124,2005-2020. https://doi.org/10.1029/2018JG004883

Rascher, U., Agati, G., Alonso, L., Cecchi, G., Champagne, S., Colombo, R., Damm, A., Daumard, F., De Miguel, E., Fernandez, G., 2009. CEFLES2: the remote sensing component to quantify photosynthetic efficiency from the leaf to the region by measuring sun-induced fluorescence in the oxygen absorption bands. Biogeosciences. 6,1181-1198. http://doi.org/10.5194/bg-6-1181-2009

Rascher, U., Alonso, L., Burkart, A., Cilia, C., Cogliati, S., Colombo, R., Damm, A., Drusch, M., Guanter, L., Hanus, J., Hyvarinen, T., Julitta, T., Jussila, J., Kataja, K., Kokkalis, P., Kraft, S., Kraska, T., Matveeva, M., Moreno, J., Muller, O., Panigada, C., Pikl, M., Pinto, F., Prey, L., Pude, R., Rossini, M., Schickling, A., Schurr, U., Schuttemeyer, D., Zemek, F., 2015. Sun-induced fluorescence - a new probe of photosynthesis: First maps from the imaging spectrometer HyPlant. Global Change Biology. 21,4673-4684. https://doi.org/10.1111/gcb.13017 26146813

Reddy, A.R., Chaitanya, K.V., Vivekanandan, M., 2004. Drought-induced responses of photosynthesis and antioxidant metabolism in higher plants. Journal of Plant Physiology. 161,1189-1202. https://doi.org/10.1016/j.jplph.2004.01.013

Roosjen, P.P., Suomalainen, J.M., Bartholomeus, H.M., Kooistra, L., Clevers, J.G., 2017. Mapping reflectance anisotropy of a potato canopy using aerial images acquired with an unmanned aerial vehicle. Remote Sensing. 9,417. http://doi.org/10.3390/rs9050417

Rossini, M., Burkart, A., Cogliati, S., Davies, N., Hom, M., Mac Arthur, A., Middleton, E., Rascher, U., 2016. Comparison of sun-induced chlorophyll fluorescence estimates obtained from four portable field spectroradiometers. Remote Sensing. 8,122. https://doi.org/10.3390/rs8020122

Rossini, M., Nedbal, L., Guanter, L., Ač, A., Alonso, L., Burkart, A., Cogliati, S., Colombo, R., Damm, A., Drusch, M., 2015. Red and far red Sun-induced chlorophyll fluorescence as a measure of plant photosynthesis. Geophysical Research Letters. 42,1632-1639. https://doi.org/10.1002/2014GL062943

Rouse, J., Haas, R., Schell J., Deering, D., 1973. Monitoring Vegetation Systems in the Great Plains with ERTS. Third ERTS Symposium, NASA. 1, 309–317.

Ryu, Y., Berry, J.A., Baldocchi, D.D., 2019. What is global photosynthesis? History, uncertainties and opportunities. Remote Sensing of Environment. 223,95-114. https://doi.org/10.1016/j.rse.2019.01.016

Sabater, N., Vicent, J., Alonso, L., Verrelst, J., Middleton, E.M., Porcar-Castell, A., Moreno, J., 2018. Compensation of oxygen transmittance effects for proximal sensing retrieval of canopy–leaving sun–induced chlorophyll fluorescence. Remote Sensing. 10,1551. https://doi.org/10.3390/rs10101551

Sager, J.C., McFarlane, J.C., 1997. Radiation. Plant growth chamber handbook. 1-29.

Saibo, N.J., Lourenço, T., Oliveira, M.M., 2009. Transcription factors and regulation of photosynthetic and related metabolism under environmental stresses. Annals of Botany. 103,609-623. https://doi.org/10.1093/aob/mcn227

Schickling, A., Matveeva, M., Damm, A., Schween, J.H., Wahner, A., Graf, A., Crewell, S., Rascher, U., 2016. Combining sun-induced chlorophyll fluorescence and photochemical reflectance index improves diurnal modeling of gross primary productivity. Remote Sensing. 8,574. http://doi.org/10.3390/rs8070574

Schlau-Cohen, G.S., Berry, J., 2015. Photosynthetic fluorescence, from molecule to planet. Physics Today. 68,66-67. http://doi.org/10.1063/PT.3.2924

Schurr, U., Walter, A., Rascher, U., 2006. Functional dynamics of plant growth and photosynthesis–from steady-state to dynamics–from homogeneity to heterogeneity. Plant, Cell & Environment. 29,340-352. http://doi.org/10.1111/j.1365-3040.2005.01490.x

Siegmann, B., Alonso, L., Celesti, M., Cogliati, S., Colombo, R., Damm, A., Douglas, S., Guanter, L., Hanuš, J., Kataja, K., 2019. The high-performance airborne imaging spectrometer HyPlant—From raw images to top-of-canopy reflectance and fluorescence products: Introduction of an automatized processing chain. Remote Sensing. 11,2760. https://doi.org/10.3390/rs11232760

Siegmann, B., Cendrero-Mateo, M.P., Cogliati, S., Damm, A., Gamon, J., Herrera, D., Jedmowski, C., Junker-Frohn, L.V., Kraska, T., Muller, O., 2021. Downscaling of far-red solar-induced chlorophyll fluorescence of different crops from canopy to leaf level using a diurnal data set acquired by the airborne imaging spectrometer HyPlant. Remote Sensing of Environment. 264,112609. https://doi.org/10.1016/j.rse.2021.112609

Smorenburg, K., Courrèges-Lacoste, G.B., Berger, M., Buschmann, C., Court, A., Del Bello, U., Langsdorf, G., Lichtenthaler, H.K., Sioris, C., Stoll, M.P., Visser, H., 2002. Remote sensing of solar induced fluorescence of vegetation. International Society for Optics and Photonics. 4542,178-190. https://doi.org/10.1117/12.454193

Song, L., Guanter, L., Guan, K., You, L., Huete, A., Ju, W., Zhang, Y., 2018. Satellite sun-induced chlorophyll fluorescence detects early response of winter wheat to heat stress in the Indian Indo-Gangetic Plains. Global Change Biology. 24,4023-4037. http://doi.org/10.1111/gcb.14302

Steduto, P., Hsiao, T. C., Fereres, E., Raes, D., 2012. Crop yield response to water. Rome: Food and Agriculture Organization of the United Nations. 1028.

Sun, Y., Frankenberg, C., Wood, J. D., Schimel, D. S., Jung, M., Guanter, L., Drewry, D. T., Verma, M., Porcar-Castell, A., Griffis, T. J., Gu, L., Magney, T. S., Köhler, P., Evans, B., Yuen, K. 2017. OCO-2 advances photosynthesis observation from space via solar-induced chlorophyll fluorescence. Science, 358,6360. http://doi.org/10.1126/science.aam5747

Sun, Y., Fu, R., Dickinson, R., Joiner, J., Frankenberg, C., Gu, L., Xia, Y., Fernando, N., 2015. Drought onset mechanisms revealed by satellite solar-induced chlorophyll fluorescence: Insights from two contrasting extreme events. Journal of Geophysical Research: Biogeosciences. 120,2427-2440. https://doi.org/10.1002/2015JG003150

Tagliabue, G., Panigada, C., Celesti, M., Cogliati, S., Colombo, R., Migliavacca, M., Rascher, U., Rocchini, D., Schüttemeyer, D., Rossini, M., 2020. Sun–induced fluorescence heterogeneity as a measure of functional diversity. Remote Sensing of Environment. 247,111934. https://doi.org/10.1016/j.rse.2020.111934

Tagliabue, G., Panigada, C., Dechant, B., Baret, F., Cogliati, S., Colombo, R., Migliavacca, M., Rademske, P., Schickling, A., Schüttemeyer, D., 2019. Exploring the spatial relationship between airborne-derived red and far-red sun-induced fluorescence and process-based GPP estimates in a forest ecosystem. Remote Sensing of Environment. 231,111272. https://doi.org/10.1016/j.rse.2019.111272

Tsouros, D.C., Bibi, S., Sarigiannidis, P.G., 2019. A review on UAV-based applications for precision agriculture. Information. 10,349. https://doi.org/10.3390/info10110349

Turner, D.P., Urbanski, S., Bremer, D., Wofsy, S.C., Meyers, T., Gower, S.T., Gregory, M., 2003. A cross-biome comparison of daily light use efficiency for gross primary production. Global Change Biology. 9,383-395. https://doi.org/10.1046/j.1365-2486.2003.00573.x

Uddling, J., Gelang-Alfredsson, J., Piikki, K., Pleijel, H., 2007. Evaluating the relationship between leaf chlorophyll concentration and SPAD-502 chlorophyll meter readings. Photosynthesis Research. 91,37-46. https://doi.org/10.1007/s11120-006-9077-5

Ullman, S., 1979. The interpretation of structure from motion. Proceedings of the Royal Society of London Series B Biological Sciences. 203,405-426. http://doi.org/10.1098/rspb.1979.0006

Van der Tol, C., Berry, J., Campbell, P., Rascher, U., 2014. Models of fluorescence and photosynthesis for interpreting measurements of solar-induced chlorophyll fluorescence. Journal of Geophysical Research: Biogeosciences. 119,2312-2327. https://doi.org/10.1002/2014JG002713

Van der Tol, C., Rossini, M., Cogliati, S., Verhoef, W., Colombo, R., Rascher, U., Mohammed, G., 2016. A model and measurement comparison of diurnal cycles of sun-induced chlorophyll fluorescence of crops. Remote Sensing of Environment. 186,663-677. https://doi.org/10.1016/j.rse.2016.09.021

Van der Tol, C., Verhoef, W., Timmermans, J., Verhoef, A., Su, Z., 2009. An integrated model of soil-canopy spectral radiances, photosynthesis, fluorescence, temperature and energy balance. Biogeosciences Discussions. 6,3109-3129. http://doi.org/10.5194/bg-6-3109-2009

Van der Tol, C., Vilfan, N., Dauwe, D., Cendrero-Mateo, M.P., Yang, P., 2019. The scattering and re-absorption of red and near-infrared chlorophyll fluorescence in the models Fluspect and SCOPE. Remote Sensing of Environment. 232,111292. https://doi.org/10.1016/j.rse.2019.111292

Van Wittenberghe, S., Alonso, L., Verrelst, J., Moreno, J., Samson, R., 2015. Bidirectional sun-induced chlorophyll fluorescence emission is influenced by leaf structure and light scattering properties—A bottom-up approach. Remote Sensing of Environment. 158,169-179. https://doi.org/10.1016/j.rse.2014.11.012

Vargas, J.Q., Bendig, J., Mac Arthur, A., Burkart, A., Julitta, T., Maseyk, K., Thomas, R., Siegmann, B., Rossini, M., Celesti, M., 2020. Unmanned aerial systems (UAS)-based methods for solar induced chlorophyll fluorescence (SIF) retrieval with non-imaging spectrometers: state of the art. Remote Sensing. 12,1624. https://doi.org/10.3390/rs12101624

Verhoef, W., 1984. Light scattering by leaf layers with application to canopy reflectance modeling: The SAIL model. Remote sensing of environment. 16,125-141. https://doi.org/10.1016/0034-4257(84)90057-9

Verhoef, W., 1998. Theory of Radiative Transfer Models Applied in Optical Remote Sensing of Vegetation Canopies. Wageningen: Landbouwuniversiteit Wageningen (LUW).

Verrelst, J., Muñoz, J., Alonso, L., Delegido, J., Rivera, J.P., Camps-Valls, G., Moreno, J., 2012. Machine learning regression algorithms for biophysical parameter retrieval: Opportunities for Sentinel-2 and-3. Remote Sensing of Environment. 118,127-139. https://doi.org/10.1016/j.rse.2011.11.002

Verrelst, J., Rivera, J.P., van der Tol, C., Magnani, F., Mohammed, G., Moreno, J., 2015. Global sensitivity analysis of the SCOPE model: what drives simulated canopy-leaving sun-induced fluorescence? Remote Sensing of Environment. 166,8-21. https://doi.org/10.1016/j.rse.2015.06.002

Vilfan, N., Van der Tol, C., Muller, O., Rascher, U., Verhoef, W., 2016. Fluspect-B: A model for leaf fluorescence, reflectance and transmittance spectra. Remote Sensing of Environment. 186,596-615. https://doi.org/10.1016/j.rse.2016.09.017

Viña, A., Gitelson, A.A., 2005. New developments in the remote estimation of the fraction of absorbed photosynthetically active radiation in crops. Geophysical Research Letters. 32. https://doi.org/10.1029/2005GL023647

Voss, I., Sunil, B., Scheibe, R., Raghavendra, A., 2013. Emerging concept for the role of photorespiration as an important part of abiotic stress response. Plant Biology. 15,713-722. http://doi.org/10.1111/j.1438-8677.2012.00710.x

Wahid, A., Gelani, S., Ashraf, M., Foolad, M.R., 2007. Heat tolerance in plants: an overview. Environmental and Experimental Botany. 61,199-223. http://doi.org/10.1016/j.envexpbot.2007.05.011

Wang, C., Guan, K., Peng, B., Chen, M., Jiang, C., Zeng, Y., Wu, G., Wang, S., Wu, J., Yang, X., 2020. Satellite footprint data from OCO-2 and TROPOMI reveal significant spatio-temporal and inter-vegetation type variabilities of solar-induced fluorescence yield in the US Midwest. Remote Sensing of Environment. 241,111728. https://doi.org/10.1016/j.rse.2020.111728

Wang, N., Suomalainen, J., Bartholomeus, H., Kooistra, L., Masiliūnas, D., Clevers, J.G., 2021. Diurnal variation of sun-induced chlorophyll fluorescence of agricultural crops observed from a point-based spectrometer on a UAV. International Journal of Applied Earth Observation and Geoinformation. 96,102276. https://doi.org/10.1016/j.jag.2020.102276

Wang, X., Biederman, J.A., Knowles, J.F., Scott, R.L., Turner, A.J., Dannenberg, M.P., Köhler, P., Frankenberg, C., Litvak, M.E., Flerchinger, G.N., 2022. Satellite solar-induced chlorophyll fluorescence and near-infrared reflectance capture complementary aspects of dryland vegetation productivity dynamics. Remote Sensing of Environment. 270,112858. https://doi.org/10.1016/j.rse.2021.112858

Wang, X., Qiu, B., Li, W., Zhang, Q., 2019. Impacts of drought and heatwave on the terrestrial ecosystem in China as revealed by satellite solar-induced chlorophyll fluorescence. Science of the Total Environment. 693,133627. http://doi.org/10.1016/j.scitotenv.2019.133627

Westoby, M.J., Brasington, J., Glasser, N.F., Hambrey, M.J., Reynolds, J.M., 2012. 'Structure-from-Motion'photogrammetry: A low-cost, effective tool for geoscience applications. Geomorphology. 179,300-314. https://doi.org/10.1016/j.geomorph.2012.08.021

Wieneke, S., Ahrends, H., Damm, A., Pinto, F., Stadler, A., Rossini, M., Rascher, U., 2016. Airborne based spectroscopy of red and far-red sun-induced chlorophyll fluorescence: Implications for improved estimates of gross primary productivity. Remote Sensing of Environment. 184,654-667. https://doi.org/10.1016/j.rse.2016.07.025

Wieneke, S., Burkart, A., Cendrero-Mateo, M., Julitta, T., Rossini, M., Schickling, A., Schmidt, M., Rascher, U., 2018. Linking photosynthesis and sun-induced fluorescence at sub-daily to seasonal scales. Remote Sensing of Environment. 219,247-258. https://doi.org/10.1016/j.rse.2018.10.019

Wohlfahrt, G., Gerdel, K., Migliavacca, M., Rotenberg, E., Tatarinov, F., Muller, J., Hammerle, A., Julitta, T., Spielmann, F.M., Yakir, D., 2018. Sun-induced fluorescence and gross primary productivity during a heat wave. Scientific Reports. 8,14169. https://doi.org/10.1038/s41598-018-32602-z

Wong, C.Y., Gamon, J.A., 2015. The photochemical reflectance index provides an optical indicator of spring photosynthetic activation in evergreen conifers. New Phytologist. 206,196-208. https://doi.org/10.1111/nph.13251

Wood, J. D., Griffis, T. J., Baker, J. M., Frankenberg, C., Verma, M., Yuen, K., 2017. Multiscale analyses of solar-induced florescence and gross primary production. Geophysical Research Letters, 44(1), 533-541. http://doi.org/10.1002/2016GL070775

Wyber, R., Malenovský, Z., Ashcroft, M.B., Osmond, B., Robinson, S.A., 2017. Do daily and seasonal trends in leaf solar induced fluorescence reflect changes in photosynthesis, growth or light exposure? Remote Sensing. 9(6), 604, https://doi.org/10.3390/rs9060604

Xu, S., Atherton, J., Riikonen, A., Zhang, C., Oivukkamäki, J., MacArthur, A., Honkavaara, E., Hakala, T., Koivumäki, N., Liu, Z., 2021. Structural and photosynthetic dynamics mediate the response of SIF to water stress in a potato crop. Remote Sensing of Environment. 263,112555. https://doi.org/10.1016/j.rse.2021.112555

Xu, S., Liu, Z., Zhao, L., Zhao, H., Ren, S., 2018. Diurnal response of sun-induced fluorescence and PRI to water stress in maize using a near-surface remote sensing platform. Remote Sensing. 10(10), 1510 https://doi.org/10.3390/rs10101510

Xu, S., Zaidan, M.A., Honkavaara, E., Hakala, T., Viljanen, N., Porcar-Castell, A., Liu, Z., Atherton, J., 2020. On the Estimation of the Leaf Angle Distribution from Drone Based Photogrammetry. In, IGARSS 2020-2020 IEEE International Geoscience and Remote Sensing Symposium. 4379-4382. http://doi.org/10.1109/IGARSS39084.2020.9323498

Yang, J., Tian, H., Pan, S., Chen, G., Zhang, B., Dangal, S., 2018a. Amazon drought and forest response: Largely reduced forest photosynthesis but slightly increased canopy greenness during the extreme drought of 2015/2016. Global Change Biology. 24,1919-1934. http://doi.org/10.1111/gcb.14056

Yang, J., Zhang, J., Wang, Z., Zhu, Q., Liu, L., 2001. Water deficit–induced senescence and its relationship to the remobilization of pre-stored carbon in wheat during grain filling. Agronomy Journal. 93,196-206.http://doi.org/10.2134/agronj2001.931196x

Yang, K., Ryu, Y., Dechant, B., Berry, J.A., Hwang, Y., Jiang, C., Kang, M., Kim, J., Kimm, H., Kornfeld, A., 2018. Sun-induced chlorophyll fluorescence is more strongly related to absorbed light than to photosynthesis at half-hourly resolution in a rice paddy. Remote Sensing of Environment. 216,658-673.https://doi.org/10.1016/j.rse.2018.07.008

Yang, P., Prikaziuk, E., Verhoef, W., van der Tol, C., 2021a. SCOPE 2.0: A model to simulate vegetated land surface fluxes and satellite signals. Geoscientific Model Development. 14,4697-4712. https://doi.org/10.5194/gmd-14-4697-2021, 2021

Yang, P., van der Tol, C., 2018. Linking canopy scattering of far-red sun-induced chlorophyll fluorescence with reflectance. Remote Sensing of Environment. 209,456-467. https://doi.org/10.1016/j.rse.2018.02.029

Yang, P., van der Tol, C., Campbell, P.K., Middleton, E.M., 2020. Fluorescence Correction Vegetation Index (FCVI): A physically based reflectance index to separate physiological and non-physiological information in far-red sun-induced chlorophyll fluorescence. Remote Sensing of Environment. 240,111676. https://doi.org/10.1016/j.rse.2020.111676

Yang, P., van der Tol, C., Campbell, P.K., Middleton, E.M., 2021b. Unraveling the physical and physiological basis for the solar-induced chlorophyll fluorescence and photosynthesis relationship using continuous leaf and canopy measurements of a corn crop. Biogeosciences. 18,441-465.https://doi.org/10.5194/bg-18-441-2021, 2021

Yang, P., Van der Tol, C., Verhoef, W., Damm, A., Schickling, A., Kraska, T., Muller, O., Rascher, U., 2019. Using reflectance to explain vegetation biochemical and structural effects on sun-induced chlorophyll fluorescence. Remote Sensing of Environment. 231,110996. https://doi.org/10.1016/j.rse.2018.11.039

Yang, X., Shi, H., Stovall, A., Guan, K., Miao, G., Zhang, Y., Zhang, Y., Xiao, X., Ryu, Y., Lee, J. E., 2018. FluoSpec 2 - an automated field spectroscopy system to monitor canopy solar-induced fluorescence. Sensors. 18,2063. https://doi.org/10.3390/s18072063

Yang, X., Tang, J., Mustard, J.F., Lee, J.E., Rossini, M., Joiner, J., Munger, J.W., Kornfeld, A., Richardson, A.D., 2015. Solar-induced chlorophyll fluorescence that correlates with canopy photosynthesis on diurnal and seasonal scales in a temperate deciduous forest. Geophysical Research Letters. 42,2977-2987. http://doi.org/10.1002/2015GL063201

Yardanov, I., Velikova, V., Tsonev, T., 2003. Plant responses to drought and stress tolerance. Bulgarian Journal of Plant Physiology. 187-206. http://doi.org/10.1007/978-3-642-32653-0

Yoshida, Y., Joiner, J., Tucker, C., Berry, J., Lee, J.-E., Walker, G., Reichle, R., Koster, R., Lyapustin, A., Wang, Y., 2015. The 2010 Russian drought impact on satellite measurements of solar-induced chlorophyll fluorescence: Insights from modeling and comparisons with parameters derived from satellite reflectances. Remote Sensing of Environment. 166,163-177. https://doi.org/10.1016/j.rse.2015.06.008

Zarco-Tejada, P., Camino, C., Beck, P., Calderon, R., Hornero, A., Hernández-Clemente, R., Kattenborn, T., Montes-Borrego, M., Susca, L., Morelli, M., 2018. Previsual symptoms of Xylella fastidiosa infection revealed in spectral plant-trait alterations. Nature Plants. 4,432-439. http://doi.org/10.1038/s41477-018-0189-7

Zarco-Tejada, P., Poblete, T., Camino, C., Gonzalez-Dugo, V., Calderon, R., Hornero, A., Hernandez-Clemente, R., Román-Écija, M., Velasco-Amo, M., Landa, B., 2021. Divergent abiotic spectral pathways unravel pathogen stress signals across species. Nature Communications. 12,1-11.

Zarco-Tejada, P.J., González-Dugo, M.V., Fereres, E., 2016. Seasonal stability of chlorophyll fluorescence quantified from airborne hyperspectral imagery as an indicator of net photosynthesis in the context of precision agriculture. Remote Sensing of Environment. 179,89-103. https://https://doi.org/10.1016/j.rse.2016.03.024

Zarco-Tejada, P.J., González-Dugo, V., Berni, J.A.J., 2012. Fluorescence, temperature and narrow-band indices acquired from a UAV platform for water stress detection using a micro-hyperspectral imager and a thermal camera. Remote Sensing of Environment. 117,322-337. http://doi.org/10.1016/j.rse.2011.10.007

Zarco-Tejada, P.J., Miller, J.R., Mohammed, G.H., Noland, T.L., 2000. Chlorophyll fluorescence effects on vegetation apparent reflectance: I. Leaf-level measurements and model simulation. Remote Sensing of Environment. 74,582-595. https://doi.org/10.1016/S0034-4257(00)00148-6

Zarco-Tejada, P.J., Morales, A., Testi, L., Villalobos, F.J., 2013. Spatio-temporal patterns of chlorophyll fluorescence and physiological and structural indices acquired from hyperspectral imagery as compared with carbon fluxes measured with eddy covariance. Remote Sensing of Environment. 133,102-115. http://doi.org/10.1016/j.rse.2013.02.003

Zeng, Y., Badgley, G., Dechant, B., Ryu, Y., Chen, M., Berry, J.A., 2019. A practical approach for estimating the escape ratio of near-infrared solar-induced chlorophyll fluorescence. Remote Sensing of Environment. 232,111209. https://doi.org/10.1016/j.rse.2019.05.028

Zhang, N., Wang, M., Wang, N., 2002. Precision agriculture—a worldwide overview. Computers and Electronics in Agriculture. 36,113-132. https://doi.org/10.1016/S0168-1699(02)00096-0

Zhang, Y., Xiao, X., Jin, C., Dong, J., Zhou, S., Wagle, P., Joiner, J., Guanter, L., Zhang, Y., Zhang, G., Qin, Y., Wang, J., Moore, B., 2016. Consistency between sun-induced chlorophyll fluorescence and gross primary production of vegetation in North America. Remote Sensing of Environment. 183,154-169. http://doi.org/10.1016/j.rse.2016.05.015

Zhang, Z., Zhang, Y., Joiner, J., Migliavacca, M., 2018. Angle matters: Bidirectional effects impact the slope of relationship between gross primary productivity and sun-induced chlorophyll fluorescence from Orbiting Carbon Observatory-2 across biomes. Global change biology, 24(11), 5017-5020. https://doi.org/10.1111/gcb.14427

Zhang, Z., Zhang, Y., Zhang, Q., Chen, J.M., Porcar-Castell, A., Guanter, L., Wu, Y., Zhang, X., Wang, H., Ding, D., 2020. Assessing bi-directional effects on the diurnal cycle of measured solar-induced chlorophyll fluorescence in crop canopies. Agricultural and Forest Meteorology. 295,108147. https://doi.org/10.1016/j.agrformet.2020.108147

Summary

Monitoring photosynthesis is essential to understand the photosynthetic activity in crops for sustainable yield and thus ensure food security. Sun-induced chlorophyll fluorescence (SIF) is a byproduct of the photosynthesis process and is considered a direct measurement of the dynamic behaviour of photosynthesis. Studies on SIF at the ground, airborne, and satellite level have made important achievements in understanding the dynamic SIF-photosynthesis relationship. There is an urgent need to bridge the gap in SIF measurements between temporally continuous ground retrievals and high-altitude airborne or spatially coarse satellites and further explore the potential of SIF at field level in the context of precision agriculture. Unmanned Aerial Vehicle (UAV)-based measurements allow studying temporal SIF variation at the field scale and can potentially close the mentioned spatial gap. To minimize the risk of data artifacts and correctly understand SIF values, the ability of UAV-based SIF observations to provide reliable information within agricultural fields needs a robust evaluation. Due to the physiological connection between photosynthetic changes and fluorescence emission, UAV-based SIF has the potential to support the timely detection of water stress at the field scale. However, the direct effect of water stress on the SIF response in crops at the field level still needs further research to clearly understand the involved mechanisms. As SIF retrieval is jointly affected by multiple factors, elucidation of the confounding factors of SIF is also highly needed for a reliable interpretation of the physiological variations caused by water stress. The objectives of this research are i) to evaluate the ability of a novel UAV-based system to acquire reliable SIF under field conditions, and ii) to interpret UAV-based SIF response to water stress for a better understanding of photosynthetic activities.

Chapter 2 presented the system set-up and the processing chain of a novel UAV-based system, FluorSpec, for SIF acquisition at the field level and evaluated the potential of this system and the diurnal SIF patterns for different arable crops. To test the reliability of FluorSpec diurnal SIF measurements, canopy diurnal SIF was firstly monitored over two crops using the ground-based FluorSpec. SIF from the two crops had a pronounced and expected diurnal SIF development similar to the photosynthetically active radiation (PAR). Ground-based SIF showed a good correlation with leaf Photosystem II Quantum Yield (Qy). At the field level, UAV-based SIF exhibited a clear diurnal pattern similar to the proximal canopy SIF measurements. Clear spatial variation within different crop fields was observed within FluorSpec footprints. The obtained results showed the ability of the FluorSpec system to reliably measure plant fluorescence at ground and field level and the possibility of the UAV-based FluorSpec to bridge the scaling gap between different levels of SIF observations.

Chapter 3 further evaluated the ability of the UAV-based FluorSpec to measure reliable SIF by comparing FluorSpec with a high-performance airborne imaging spectrometer, HyPlant. Airborne HyPlant and the UAV-based FluorSpec acquired diurnal SIF measurements almost simultaneously during a clear sky day. An initial step was to improve the footprint geolocation of FluorSpec measurements using concurrent RGB images. Next, the FluorSpec and HyPlant SIF measurements, their diurnal developments, and spatial distributions for different crop types were compared. A high linear correlation was found between UAV-based FluorSpec SIF and HyPlant SIF. Both UAV and airborne-based SIF show similar and pronounced diurnal patterns for most crops. Consistent spatial patterns of SIF over different crops for both systems were also clearly observed. These findings confirm that the UAV-based FluorSpec system is able to measure meaningful SIF values at the field scale and facilitate bridging the gap in SIF monitoring between ground and ecosystem scales.

Chapter 4 assessed the value of UAV-based SIF for water stress detection in a crop field. SIF measurements by the UAV-based FluorSpec were acquired over irrigated and water-stressed sugar beet plots in June 2019 under water stress and in July 2019 under combined water stress and heat stress. SIF indices were applied to detect water stress under the two different conditions. Additionally, UAV-based hyperspectral and thermal data were acquired to assist the interpretation of SIF indices. The SIF indices showed a significant response to the recovery of sugar beet after irrigation when sugar beet plants were exposed to water stress. However, only some selected SIF indices weakly tracked the changes induced by the irrigation when the crop was under severe combined stress. SIF at 687 nm and 760 nm and their indices reacted differently to the irrigation. This study confirms the capacity of SIF acquired by a UAV system to detect water stress at the field level, but its value might be limited for severe water stress detection. Further investigations are necessary to give a comprehensive understanding of the potential of UAV-based SIF to detect crop stress at different levels and to support crop management in the context of precision agriculture.

Chapter 5 presented a modelling approach to disaggregate the induced physiological and non-physiological effects by water stress on SIF variations for a better understanding of the photosynthetic dynamics under stressed conditions. UAV-based SIF measurements were acquired over irrigated and non-irrigated sugar beet plots. Fluorescence emission yield (ΦF) and biochemical and structural factors jointly controlled TOC SIF. SIF variation both at 687 nm and 760 nm caused by water stress was strongly affected by the physiological factor ΦF and positively correlated well with SIF variations only caused by ΦF. At 687 nm, non-physiological changes had a weak effect on SIF variations, while at 760 nm non-physiological changes negatively and non-significantly mediated SIF response to water stress. The combination of RTMs, TOC reflectance, and TOC SIF measurements enables the physiological information quantification from SIF observations and supports the scalable quantitative use of SIF from leaf to ecosystem level.

From the results in this thesis, it can be concluded that 1) the UAV-based FluorSpec observations can explore crop SIF and photosynthetic activities at field level and upscale the SIF measuring from the ground level to the field level by providing accurate, high resolution, and flexible spectral measurements; 2) UAV-based SIF is capable of detecting water stress at an early stage in a crop while its potential in severe stress detection needs further research; 3) the physiological and non-physiological changes both contribute to SIF variation caused by water stress, and the physiological changes had a strong effect on SIF variations in the presented case.

Acknowledgment

It’s been a long road, but here I am at the end. This achievement would not have been possible without the support, help, and care from the lovely people I met during the journey. I would like to acknowledge and give thanks to all of you.

Firstly, I would like to express my deepest appreciation to my supervision team for your dedication, care, and support thought out my PhD project. It has been so wonderful meeting you and learning from you. Lammert, I have been such lucky to have you as my promotor. You are the guiding light of my PhD adventure. You are very responsible for my project and always give timely feedback. I appreciate your encouragement and support that enhanced my confidence in overcoming the difficulties during my PhD project. You encourage me to participate in conferences and workshops to expand my network, to give more presentations to practice my presenting skills, and to have more collaborations with people outside our group and helped me to make the connection with external organizations. You also encourage me to find a balance between work and life. For me, you are not only a promoter but also a friend.

I would like to give my warmest thanks to my co-promotor, Jan, who made my PhD adventure possible. Thanks for helping me with the application for the CSC scholarship and the procedures of enrolment. Your guidance and advice carried me through all the stages of my project. I am thankful for your critical thinking along and valuable and fast feedback on my project work, and careful edits You are always there when I have questions about the data analysis and writing. I benefit from your conscientiousness and meticulousness about work. You also encourage me to think and make a decision independently, from which I will benefit in my future career.

Many thanks to my co-promotor, Harm, who is always enthusiastic about work. Thanks for your valuable input to support me in my PhD journey. I would not have such a nice field dataset without you. I appreciate your efforts made to improve the UAV-based FluorSpec system and fly UAVs. I remember the hard but fruitful fieldwork day in Germany and the seasonal fieldwork in Unifarm. I am surprised at your magic to obtain a perfect mosaic from Rikola hyperspectral images as well as at your musical talent being a guitarist of our great GRS band.

I would also like to thank Martin for your initial role as my promotor and your support with the PhD work.

The PhD work would have not been possible without the support from other co-authors. Thank you, Juha. I could not start my project without the FluorSpec system. Thank you, Uwe. You provided me with the great opportunity to have a short-term study at Juelich Research Center and your input. Bastian, Juliane, and Onno thank you for your valuable effort to support my work. Sebastian, thank you for your critical thinking in our meetings and your valuable input on my last two chapters. Peiqi, thank you for guiding me to the fascinating world of modeling and supporting me with the analysis.

There are so many great people who assisted in my fieldwork. Thank you, Marcello, for supporting me in the 2018 and 2019 field campaigns by testing the system and conducting the flights. Thank you, Ben, Marston, and Peter R., for flying the UAVs. Thank you, Dainius and Gerjon, for collecting the ground measurements. I appreciated all your efforts to make a great dataset possible.

I would like to thank you, my colleagues. My PhD life would not be interesting and happy without the conversation, coffee break, dinner, and party with you. Thank you, Dainius. You have been greatly supporting me through my PhD life. I appreciate your help with my fieldwork, coding, data analysis, and manuscript review. Thank you, Panpan, for your company since 2018 like my sister, and your help both in my life and my work. I know I can always depend on you. Thank you, Jalal and Marston, for your kindness as you are always willing to help me out, it is a great pleasure to share the office with you. Thank you, Ben, for helping me out with the research questions at the beginning of my PhD and the fieldwork. Thank you, Mathieu. I do appreciate our coffee break and the conversion about PhD life and the suggestion you gave to deal with the toughness. Thank you, Karimon. I enjoy the Bangladeshi cuisine and the time spent with you on weekends. Thank you, Ximena, for your kindness and birthday wishes every year. Thank you, Chenglong, Lili, Linlin, Na, Qijun, Quanxing, Yang, Yaowu, Yaqing, Yunyu, and Zhen for the joyful moments we had and for your support. You made me feel at home away from home. We are a family. I would also like to express my sincere gratitude to other lovely GRS members: Adugna, Aldo, Alex, Alexander, Andrei, Anne, Anne-Juul, Arend, Arnan, Arnold, Arun, Bart, Benjamin K., Charles, Corné, David, Deborah, Devis, Diego, Eliakim, Elina, Elise, Erika R., Erika S., Eskender, Federico, Frida, George, Gonzalo, Gustavo, Harm, Hasib, Hiske, Ida, Ilan, Ioannis, Jaap-Willem, Jan V., Jens, Joao, Johannes, John, Jose, Judith, Kalkidan, Karina, Konstantin, Lisa, Lukasz, Magdalena, Margaret, Marian, Marston, Martijn, Milutin, Myke, Nandika, Natalia, Niki, Ovidiu, Patric, Paulo, Paulina, Peter V., Ricardo, Rika Ratna, Rip, Robert, Roland, Romina, Ron, Samantha, Sabina, Sarah, Shivangi, Simon, Sytze, Tom, Usha, Wanda, Willy, and anybody that I might have not mentioned here. I am grateful to our group's secretaries Antoinette and Truus for your valuable efforts to help me through various administrative formalities. I am grateful to meet lovely colleagues at Juelich Research Center and I cherish the moment we spent together.

I also thank all the lovely friends I met in the Netherlands and Germany: Anna, Awang, Barbara, Bo Zhou, Caifang, Changjun, Chenhui, Chen Zhang, Chunfeng, Danju, Fang Lyu, Federico, Feng Xue, Huaiyue, Hui Jin, Jie & Hele, Jingjing, Jin Wang, Jungo, Keli, Kelvin, Lan Zhang, Laura, Lei Deng&Yusi, Li Kang, Ke Chen&Jiyao, Meixiu, Mengting&Duanduan, Mengying, Qianrui, Qinghua&Yingying, Qi Liu&Jingjing&Jiajia, Qi Zheng, Qing Zhan&Shuiqing, Rodrigo, Shanshan, Sophie, Tomonari, Ursula, Xiangyu, Xiaohan, Xiaolu, Xiaomei&Yale, Xinxin, Xilong, Yanjie&Zezhong, Yanjun, Yingsong, Yongran, Wenjie&Zhe, Wenzhe, Zhe Zeng, Zhenyu, Zhijie&Jiajia, Zulin, and anybody that I might have not mentioned here. Thank you for meeting all of you and having lots of fun!

Special thanks to some cool friends who have taken the greater part of this PhD journey with me. Your support and friendship have meant a great deal during both the good times and those when things haven't gone so well. Firstly, my flower sisters: Shanshan, Yanjie, and Yanjun. It is going to be very difficult to start the next chapter of my life without you being there. Shanshan, I appreciate your kindness, care, and suggestions given when I feel a little lost. Yanjie, we had many happy memories in our fancy apartment which enriched my PhD life. I admire your positive attitude to life. Yanjun, I feel proud to know you before I came here and your love to research motivates me to go further. Thank you, Xiaolu, for the thought-provoking conversation. Thank you, Wenyuan, for sharing your knowledge in statistics. Thank you, Qi&Jingjing&Jiajia, for your host and delicious food. Thank you, Anna, Caifang, Hui Jin, Jie&Hele, Jin Wang, Menting, and Ursula for the lovely company and all the memorable moments. I want to you know that I am so appreciated all the times we were able to stay together.

I thank the PE&RC office, particularly Claudius and Lennart for your support and guidance. Many thanks to Chinese government scholarships for financial support, providing me this opportunity to study at Wageningen University and presume my scientific career. I am grateful to the Action CA17134 SENSECO for supporting a short-term internship in Forschungszentrum Jülich, virtual mobile collaboration with scientists from China and Germany, and physical workshops in Bulgaria.

Many thanks to my master supervisor, Qiangzi Li. Thank you for your invaluable supervision and encouragement. I thank Xin Du, Hongyan, Yuan Zhang, Huanxue, and Longcai for your support during my master study. I am also grateful to colleagues I met there: Jilei, Leilong, Wei Wu, Panpan, Qingyong, Ruonan, Yu Shen, Siyuan, Gaoliang... I appreciate the cherished time spent together in the lab and social settings.

I would also like to give special thanks to Guantao for your continuous support and understanding when undertaking my research and writing my project. Thank you for constantly listening to me rant and talk things out, for cracking jokes when things became too serious, for giving the advice to deal with the challenges both in life and research, and for the sacrifices you have made for me to pursue my PhD career. Love you! Lastly, my families deserve endless gratitude. Thank you for your unconditional, unequivocal, and loving support. Love you!

Short biography

Na Wang was born on October 2nd, 1990 in Henan, China. She obtained her bachelor's degree in Geo-information Science from Zhengzhou University in 2014 (Henan, China). For her bachelor thesis, she studied the spatio-temporal changes in the landscape pattern in a river region. From 2014 to 2017, she continued her MSc education at the Remote sensing and digital earth institute, Chinese academy of science, China (Beijing, China). Her research focused on vegetation identification and monitoring using satellite mapping. Her MSc thesis studied the effects of remote sensing data at different Spatio-temporal resolutions on feature selection for improved crop identification. She was actively involved in different projects, e.g. National Natural Science Foundation of China, and fieldwork. In 2017, she started her PhD study in the Laboratory of Geo-Information Science and Remote Sensing, Wageningen University & Research (Netherlands). During her PhD project, she was interested in exploring the relationships between sun-induced chlorophyll fluorescence and photosynthesis at the canopy and the field level. Her PhD thesis focused on the potential of UAV-based sun-induced chlorophyll fluorescence in understanding crop photosynthesis. In 2020, she had a short-term internship in IBG-2 at Juelich Research Center, Germany. She focused on the comparison between UAV-based SIF and airborne SIF.

Publications

Wang, N., Suomalainen, J., Bartholomeus, H., Kooistra, L., Masiliūnas, D., Clevers, J.G., 2021. Diurnal variation of sun-induced chlorophyll fluorescence of agricultural crops observed from a point-based spectrometer on a UAV. International Journal of Applied Earth Observation and Geoinformation. 96, 102276.

Bendig, J., Chang, C., Wang, N., Atherton, J., Malenovský, Z., Rascher, U., 2021. Measuring solar-induced fluorescence from unmanned aircraft systems for operational use in plant phenotyping and precision farming. In, 2021 IEEE International Geoscience and Remote Sensing Symposium. 1921-1924.

Wang, N., Siegmann, B., Rascher, U., Clevers, J.G., Muller, O., Bartholomeus, H., Bendig, J., Masiliūnas, D., Pude, R., Kooistra, L. UAV-based Far-red Sun-Induced Chlorophyll Fluorescence Plant Canopy Measurements for Different Crops. Under review.

Wang, N., Clevers, J.G., Wieneke, S., Bartholomeus, H., Kooistra, L. Potential of UAV-based Sun-Induced Chlorophyll Fluorescence to Detect Water Stress in Sugar Beet. Under review.

Wang, N., Yang, P., Clevers, J.G., Wieneke, S., Kooistra, L. Decoupling crop physiological and non-physiological response to water stress from UAV-based SIF observations with a radiative transfer model. Under review.

Wang, N., Li, Q., Du, X., Zhang, Y., Zhao, L., Wang, H., 2017. Identification of main crops based on the univariate feature selection in Subei. Journal of Remote Sensing, 21(04):519-530

Wang, N., Li, Q., Zhao, L., Wang, H., Li, D., 2017. Optimization Analysis in Ship Detection with High-resolution SAR Images Based on Variation Coefficient Method, Remote Sensing Technology and Application, 32(02):305-314

PE&RC Training and Education Statement

With the training and education activities listed below the PhD candidate has complied with the requirements set by the C.T. de Wit Graduate School for Production Ecology and Resource Conservation (PE&RC) which comprises of a minimum total of 32 ECTS (= 22 weeks of activities)

Review of literature (4.5 ECTS)

- The potential of UAV-based sun-induced chlorophyll fluorescence in understanding crop photosynthesis

Writing of project proposal (3 ECTS)

- Measuring sun-induced fluorescence using UAV-based remote sensing

Post-graduate courses (7.7 ECTS)

- Fundamentals of crop physiology; PE&RC & University of Florida (2018)
- Geostatistics; WUR (2018)
- Advances in intercropping: principles and implementation; WUR (2021)
- Multivariate analysis; WUR (2021)
- Mixed linear models; WUR (2021)
- R and Big data; WUR (2021)

Deficiency, refresh, brush-up courses (6 ECTS)

- Geoscripting; WUR (2019)

Laboratory training and working visits (3 ECTS)

- The potential of a UAV platform to upscale sun-induced chlorophyll fluorescence from near-canopy level to airborne level; Forschungszentrum Jülich (2020)

Competence strengthening / skills courses (4.8 ECTS)

- Project and time management; WUR (2018)
- Scientific writing; WUR (2019)
- Start to teach; WUR (2020)

Scientific integrity/ethics in science activities (0.6 ECTS)

- Science integrity; WUR (2022)

PE&RC Annual meetings, seminars and the PE&RC weekend (2.1 ECTS)

- PE&RC First year weekend (2018)
- PE&RC Day (2018)
- PE&RC Midterm weekend (2019)
- PE&RC Last year afternoon (2021)

Discussion groups / local seminars or scientific meetings (4.5 ECTS)

- R-Users meeting (2018-2019)
- Remote sensing thematic group meeting (2018-2022)

International symposia, workshops and conferences (6.2 ECTS)

- The EARSeL special interest group on imaging spectroscopy; Brno, Czech Republic (2019)
- International network on remote sensing of terrestrial and aquatic fluorescence; Davos, Switzerland (2019)
- 40th EARSeL Symposium; online (2021)
- Sensing of vegetation traits in space and time; Agricultural University Plovdiv (2021)

Societally relevant exposure (0.6 ECTS)

- Age of AI- UAV-based SIF (2018)
- SENSECO Summer school promotional video (2021)

BSc/MSc thesis supervision (3 ECTS)

- Modelling sun-induced fluorescence using broadband vegetation indices

The research described in this thesis was financially supported by China Scholarship Council under Grant 201704910780, the Action CA17134 SENSECO (Optical synergies for spatiotemporal sensing of scalable ecophysiological traits funded by COST (European Cooperation in Science and Technology), the SPECTORS project (143081) funded by the European cooperation program INTERREG Deutschland-Nederland, and by the European Space Agency (ESA) in the frame of the FLEXSense campaign (ESA Contract No. 4000125402/18/NL/NA). This work has partially been funded by the Deutsche Forschungsgemeinschaft (DFG, German Research Foundation) under Germany’s Excellence Strategy – EXC 2070 – 390732324.

Financial support from Wageningen University for printing this thesis is gratefully acknowledged.

Cover design by Na Wang

Printed by ProefschriftMaken